FRONTIERS IN PHYSICS AND APPLICATIONS

Proceedings of the
NATIONAL SEMINAR ON PHYSICS (NSP-'19)

◖*Organized by* ◗
Department of Physics & Research Centre
Women's Christian College
Nagercoil – 629001, Kanyakumari District
Tamil Nadu, India.

Seminar Photo

Organizing Committee Members

Dr. C. M. Padma, Principal & President

Dr. M. M. Latha, Head & Convenor

Dr. G. Shanthi, Organizing Secretary

Dr. D. Usha, Co-Organizing Secretary

Dr. V. Bena Jothy

Dr. S. Grace Victoria

Mrs. J. Sharmila Justus

Mrs. C.R. Shyniya

Mrs. G. Addaline Stally

Mrs. A. Jarlet Jeyaseeli

Mrs. D. Jaya Reshmi

Dr. S. Beauno

PREFACE

We are very pleased to introduce the Proceedings of **National Seminar on Physics (NSP-'19)** organized by the **Department of Physics and Research Centre, Women's Christian College, Nagercoil on March 13, 2019.** This volume of proceedings provides an opportunity for readers to engage with a selection of refereed papers that were presented during the Seminar. The pages of **Frontiers in Physics and Applications** would surely be an eye-opener for readers to detect the common challenges and discover creative solutions from diverse settings.

The Department of Physics and Research Centre has been regularly organising NSP series since 2012. One of the unique and valuable dimensions to NSP is the way it brings together experts and active researchers across the Country from various Frontiers of Physics. NSP-'19 covered a range of frontier topics across the length and breadth of Material Science, Nonlinear Dynamics, Radiation Physics, Spectroscopy, Space Physics etc. The plenary lectures bridged the gap between the different fields of Physics, making it possible for budding researchers to gain insight into new areas. The contributions in this book represent a snapshot of the recent developments in the arena of Physics and provide a permanent record of what was presented in the Seminar. This issue encompasses thirty six selected manuscripts covering both the fundamental aspects and application overviews.

It is much appropriate that we record our thanks to our fellow members of the Organizing Committee for extending support and cooperation and also securing a substantial input of papers in various fields. We are also indebted to those who served as resource persons and chair persons. We also acknowledge the authors for their significant contribution. Hope the readers find this book educative and enjoyable.

<div style="text-align:right">

G. Shanthi
D. Usha
S. Grace Victoria

</div>

CONTENTS

V.   SPECTROSCOPY

VI.   STATISTICAL ANALYSIS

EFFECT OF pH ON THE STRUCTURAL PROPERTIES OF CADMIUM SULPHIDE NANOPARTICLES

R.Arthi, M.PriyaDharshini, V.Shally, Sr.Gerardin Jayam*

Research Department of Physics, Holy Cross College (Autonomous), Nagercoil-629004.

*Corresponding author: priyadharshini065@gmail.com

ABSTRACT

Cadmium sulphide is one of the most promising materials considered for its practical applications in electronics and photonics. In the present work, cadmium sulphide is synthesized at different pH by co-precipitation method. The synthesized nanoparticles were characterized using Powder X-Ray Diffraction (PXRD) and Raman Spectroscopy. The average grain size of the synthesized cadmium sulphide (CdS) nanoparticles at pH-8 is calculated as 46.4703 nm and that of CdS nanoparticles at pH-12 as 68.6676 nm using Scherrer equation. The average grain size of the sample is increased as the pH value is increased. As the concentration of hydrogen ions (pH) is increased, there is increase in crystalline nature of the nanoparticles. PXRD pattern reveals the purity of the samples. Raman peaks at 286.09 nm and 608.97 nm for CdS nanoparticles at pH-8 and at 294.26 nm, 588.53 nm, 893.02 nm for the sample at pH-12 respectively, are due to the first, second, and third order longitudinal optical (LO) phonon vibration modes. Thus it is obvious that the concentration of hydrogen ions cause an increase in grain size but it does not produce a change in the intensity of the Raman spectra.

1. INTRODUCTION

Nanostructures of sulphides and selenides have been extensively studied with a view to establish a relationship between structure, size and optical properties. II-VI semiconductor nanoparticles are currently of great interest for their practical applications such as zero-dimensional quantum confined materials in optoelectronics and photonics [1-4]. Among these, cadmium sulphide is an important element semiconductor with many excellent physical and chemical properties. CdS has been studied due to its potential technological applications in field effect transistors, solar cells, photovoltaic, light emitting diodes, photocatalysis, photoluminescence, infrared photo detector, environmental and biological sensors [5]. In the present work, cadmium sulphide nanoparticles with two different pH values were synthesized using a simple co-precipitation method and the effect of concentration of hydrogen ions on the structural properties are analyzed.

2. EXPERIMENTAL METHOD

Cadmium acetate was used as a precursor to prepare pure CdS nanoparticles. 0.5M of cadmium acetate was taken and was dissolved in 100ml distilled water and stirred it for half an hour. To this solution, 0.5M of sodium sulphide was added. 32M of ammonium hydroxide solution was added and a pH of 8 was maintained. CdS precipitate was washed with water five times to remove the unwanted residues. At 100°C, the solution was heated in hot air oven for 24 hours. The sample thus formed was yellow in color. Then it was calcined at 500°C for 4 hours. The above mentioned method was repeated and the CdS nanoparticles at a pH of 12 was obtained by adding 32M of ammonium hydroxide solution.

3. RESULTS AND DISCUSSION

Powder X-Ray Diffraction [Pxrd] Analysis

The Powder X-Ray Diffraction pattern of cadmium sulphide (CdS) nanoparticles was recorded using XPERT-PRO Diffraction system with CuK$_\alpha$ radiation of wavelength 1.54056Å. The characteristic powder X-Ray diffraction pattern of synthesized cadmium sulphide (CdS) nanoparticles at pH-8 and pH-12 are is shown in Fig.1. and Fig.2. respectively.
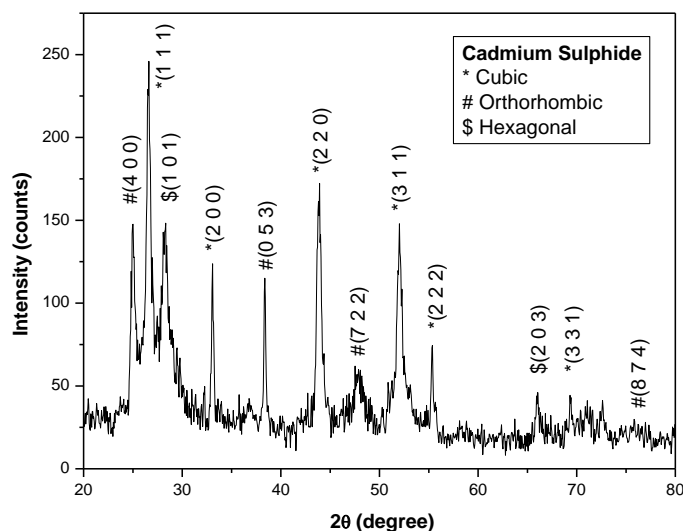
Fig.1. PXRD pattern of the synthesized CdS nanoparticles at pH-8
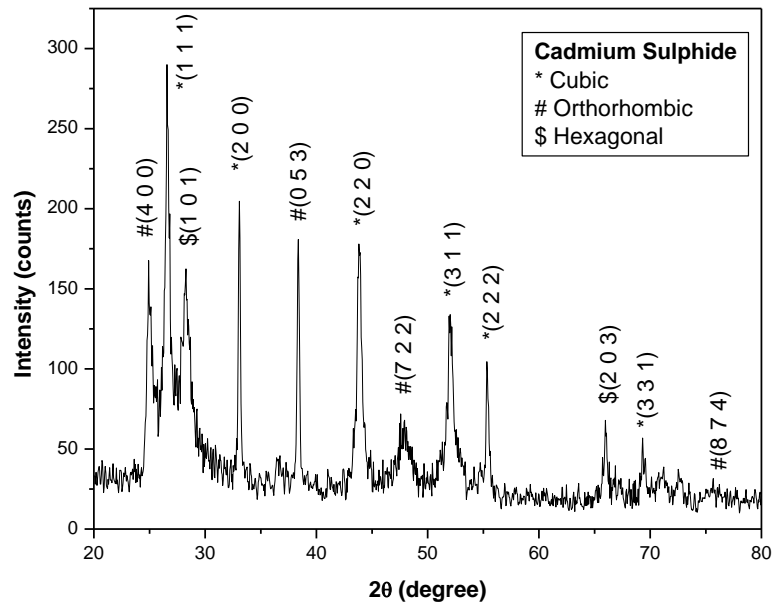
Fig.2. PXRD pattern of the synthesized CdS nanoparticles at pH-12

The average grain size of the synthesized Cadmium sulphide (CdS) nanoparticles is found out from the Powder XRD pattern using Scherer's equation,

$$D = \frac{0.9\lambda}{\beta cos\theta}(nm)$$

where, λ is the wavelength of X-Ray, β is the full width half maximum, θ is the Bragg's angle for the peak.The average grain size of the synthesized cadmium sulphide (CdS) nanoparticles at pH-8 is 46.4703nm.The average grain size of synthesized cadmium sulphide (CdS) nanoparticles at pH-12 is 68.6676nm. It is obvious that the average grain size of the sample has increased as the pH value is increased. As the concentration of hydrogen ions (pH) is increased, there is increase in crystalline nature. The "d-spacing" values given in the powder X-Ray Diffraction pattern of both the synthesized CdS nanoparticles matched well with that of the cubic (JCPDS File No.65-2887) phase. Peaks of orthorhombic (JCPDS File No.47-1179) and hexagonal (JCPDS File No.89-2944) structures are also identified in the PXRD pattern of the synthesized CdS nanoparticles. No impurity peaks are observed in the PXRD pattern.

Raman Spectra Analysis

Raman spectroscopy is considered to be vibrant tool to probe the secondary phases (or minute changes in basic structure) in various materials which are beyond the detection limit of basic characterizations tools like XRD or neutron diffraction.
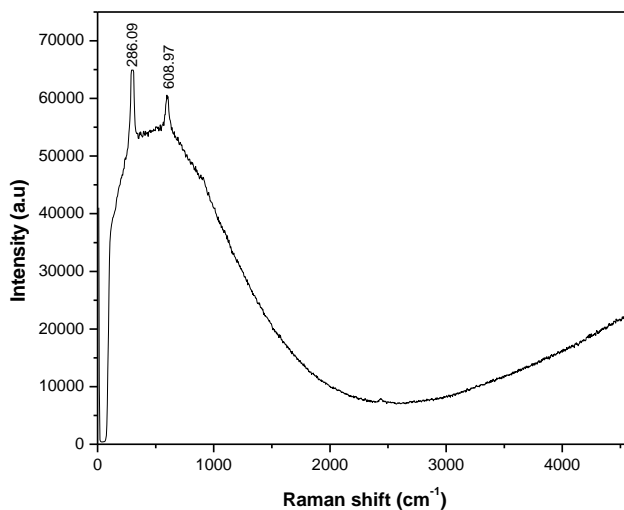
Fig.3. Raman emission spectra of the synthesized CdS nanoparticles at pH-8
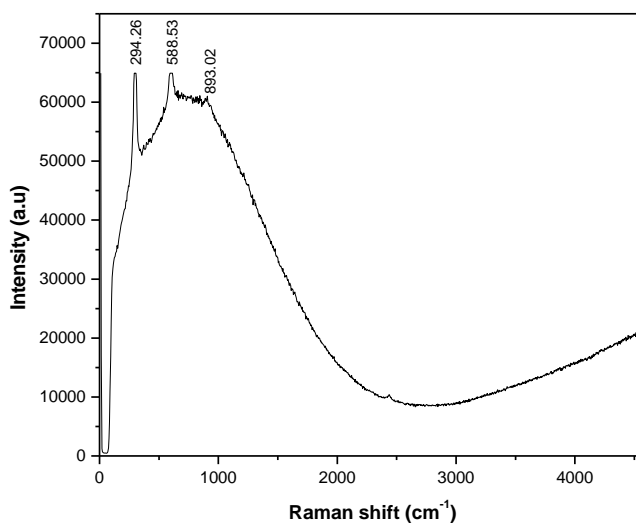
Fig.4. Raman emission spectra of the synthesized CdS nanoparticles at pH-12

Raman peaks (with decreasing order of intensity) at 286.09 nm and 608.97 nm for the sample at pH-8(Fig.3.) and at 294.26 nm, 588.53 nm, 893.02 nm for the sample at pH-12(Fig.4.) are due to the first, second, and third order longitudinal optical (LO) phonon vibration modes of the present system. Feroz A. Mir et.al (2015) have synthesized and characterized CdS nanoparticles. They observed that the Raman spectra showed first, second and third order longitudinal optical modes, and are slightly shifted to lower wave number side as compared to its bulk [1]. Rajeev R Prabhu et.al (2005) characterized CdS nanoparticles by Raman spectroscopy. Raman spectra of nanoparticles of CdS clearly show first, second and third order LO Raman peaks when excited using laser light of wavelength 514nm. The excitation of three orders of the longitudinal optical phonon modes in the Raman scattering spectrum of nanoparticles of CdS in the present study is attributed to resonance effects [4].

4. CONCLUSION

Cadmium sulphide (CdS) nanoparticles are prepared by co-precipitation method. The procedure developed in the present study offers homogenous particle distribution, good reactivity between components, nano-size particles and allows lower processing temperature. The samples are prepared with two different pH values. The obtained nanoparticles are characterized by PXRD and Raman spectroscopy. The average grain size of sample increases as the pH value is increased due to the increase in crystallinity. Absence of impurity peaks reveals the purity of the samples. From the Raman spectroscopy studies, it is observed that the Raman spectra showed first, second and third order longitudinal optical modes and is slightly shifted to lower wave number side as compared to its bulk. There is no change in the intensity of the Raman spectra due to the increase in the concentration of hydrogen ions. Thus cadmium sulphide nanoparticles can be synthesized by varying different reaction parameters for suitable applications.

REFERENCES

1) Feroz A. Mira, Indrajit Chattarjeeb, Aijaz A. Darc, K. Asokand, G.M. Bhataa, *"Preparation and characterization of cadmium sulphide nanoparticles"* ,Vol.1, pg.1240–1244, 2015.

2) B. Srinivasa Rao, B. Rajesh Kumar, V. Rajagopal Reddy, T. SubbaRao, *"Preparation and characterization of CdS nanoparticles by chemical co-precipitation technique"*, Chalcogenide Letters Vol. 8, No. 3, pg. 177 – 185, 2011.

3) R. Elilarassi, S. Maheshwari, G. Chandrasekaran, *"Structural and optical characterization of CdS nanoparticles synthesized using a simple chemical reaction route"*. Vol. 4, No. 3, pg. 309 - 312, 2010.

4) Rajeev R Prabhu and M. Abdul Khadar, *"Characterization of chemically synthesized CdS nanoparticles"*, Pramana Indian Academy of Sciences. Vol. 65, No. 5, pg. 801–807, 2005.

5) Dumbrava, C. Badea, G. Prodana, V. Ciupina, *"Synthesis and characterization of cadmium sulphide obtained at room temperature"*, Chalcogenide Letters , Vol. 7, No. 2, pg. 111 – 118, 2010.

6) F. Michael Raj, A. Jeya Rajendran, *"Synthesis and Characterization of Cadmium Sulphide Nanoparticles for the Applications of Dye Sensitized Solar Cell"*, Vol. 4, No.3, 2015.

7) Nida Qutub And Suhail Sabir, *"Characterization of Cadmium Sulphide Nanoparticles Synthesized by Chemical Precipitation Method"*, Advanced Science, Engineering and Medicine Vol. 5, pg. 1–6, 2013.

8) P. Kavitha, Suseela, R. Mary Mathelane, *"Synthesis and Characterization of Cadmium Sulphide Nanoparticles"*, The International Journal Of Engineering And Science (Ijes), Vol. 2, Issue 3, Pages 108-110, 2013.

9) Vyacheslav Kochubey, *"The Structure of Cds Nanoparticles"*, Journal of Surface Investigation X-ray Synchrotron and Neutron Techniques, Vol. 4, No.4, pg. 654-657, 2010.

10) Korimella Vijaya Raju, Bokka, Shaik, Boddeti Govindh and Annapurna, *"Synthesis and Characterization of Cadmium Sulphide (CdS) Nanoparticles Using Annona Muricata Leaf Extract as Reducing /Capping Agent"*, Vol. 5, No. 4, pg. 1035-1041, 2016.

11) Raziya, Durga, Santoshi G Rajamahanthe, Boddeti Govindh, Nowduri, *"Synthesis And Characterization Of CdS Nanoparticles"* , Vol. 4, No.4, pg. 50-57, 2016.

STRUCTURAL BEHAVIOUR OF CuO AND Pt/CuO NANOSTRUCTURED THINFILMS BY SUCCESSIVE IONIC LAYERED ADSORPTION REACTION (SILAR) TECHNIQUE

M. Janaki Devi [a], A.Lourdu Sahaya Philona[a], S.Sonia[a*], Naidu Dhanpal Jayram[b]

[a]*Department of Physics, Holy Cross College (Autonomous), Nagercoil - 629 004*
[b]*Department of Physics,Kalasalingam Academy of Research and Education,
Virudhunagar -626126*
Corresponding author: sonianst10@gmail.com

ABSTRACT

The most prominent and utilizable Platinum coated Copper Oxide nanostructured thin film is prepared using the SILAR method. It's structural properties have been studied using X-ray diffraction patten (XRD) and RAMAN spectroscopy. XRD pattern reveals the phase purity and crystallinity of CuO nanostructures. The average grain size estimated from XRD gives the diameter in the range of 14 - 27 nm. Raman spectra explains the structural information of CuO and Pt/CuO nanostructured thinfilms, in which, the peaks observed at 328 cm^{-1} , 609.32 cm^{-1} and 1141.77 cm^{-1} are the different phonon modes of CuO. The peak at 2136 cm^{-1} provides the strong evidence for the formation of plantinum on CuO nanostructures.

1. INTRODUCTION

Copper oxide, including cuprous oxide and cupric oxide is formed when copper is exposed to oxygen and oxidizes [1]. These semiconductor oxides have been studied for several reasons such as: the natural abundance of starting material (Cu); the easiness of production by Cu oxidation; their non-toxic nature and the reasonably good electrical and optical properties exhibited by CuO. Previous works showed that many of the growth methods for cuprous oxide resulted in a combined growth of copper (I) oxide Cu_2O and copper (II) oxide CuO. However CuO is widely used material than Cu_2O due to its stability. Cupric oxide (CuO) posses a monoclinic crystal structure with a band gap of 1.22–2.0 eV [2-3]. Its high optical absorption coefficient in the visible range and reasonably good electrical properties constitute important advantages and render CuO as the most interesting phase of copper oxides. CuO has been employed as heterogeneous catalysts for several environmental processes, solid state gas sensor heterostructures and microwave dielectric materials. The present report focused on the synthesis of such CuO nanostuctured thinfilms and structural properties of CuO thin films deposited by SILAR method.

2. EXPERIMENTAL TECHNIQUES

Preparation of CuO nanostructured thinfilms

- Dip the substrate in copper ammonia complex [$(Cu(NH_3)_4)^{2+}$] solution for 40 sec.

- Immerse the glass substrate in the double distilled water for 20 sec.
- Keep the substrate in anionic solution, double distilled water at 80°C for 50 sec.
- Dip the substrate in double distilled water for 20 sec.
- Dry the substrate in air for 20 sec.

Thus, one SILAR cycle is completed. Inorder to obtain the uniformity, we obtained a SILAR cycles were repeated for 20 and 40 times.

Prepartaion of Pt/CuO Nanostructured thinfilms

20 mL of 1 m M aqueous solution of $H_2PtCl_6 \cdot 6H_2O$ was added, and stirring was performed for 15 min. The redox reaction was started by adding solid tri-sodium citrate. The reaction was carried out for 120 min. All experiments were performed at room temperature. CuO nanostructured thinfilms were immersed in Platinum sol for 3h. After 3hr, Pt/CuO nanostructured thinfilms was dried in air and subjected to different characterization techniques to study their structural and surface preoperties.

3. RESULTS AND DISCUSSION

Structural Analysis

The phase purity and crystallinity of the prepared CuO and Pt/CuO nanostructured thin films were identified by X-ray diffraction analysis. The XRD patterns of the CuO and Pt/CuO nanostructured thin films are shown in Fig. 1(a and b). All the diffraction peaks of CuO nanostructured thinfilms can be readily indexed with the standard JCPDS (PDF#05-0661) file. The XRD patterns of CuO nanostructured thin films prepared by different deposition cycles consists of diffraction peaks derived from the monoclinic phase of crystalline CuO with (-111) and (111) lattice planes. Conversely, no extra diffraction peaks detected from the copper hydroxide or cuprous oxide, clearly showing only the CuO is formed in the substrate. The high intensity of peaks indicate that the prepared CuO thin films are highly crystalline in nature. Fig.2.(a and b) indicates the XRD pattern of Pt/CuO nanostructured thinfilms and shows the amorphous nature. The average crystallite size for the CuO and Pt/CuO thin films estimated from Scherrer's formula and are varying from 14 to 27 nm
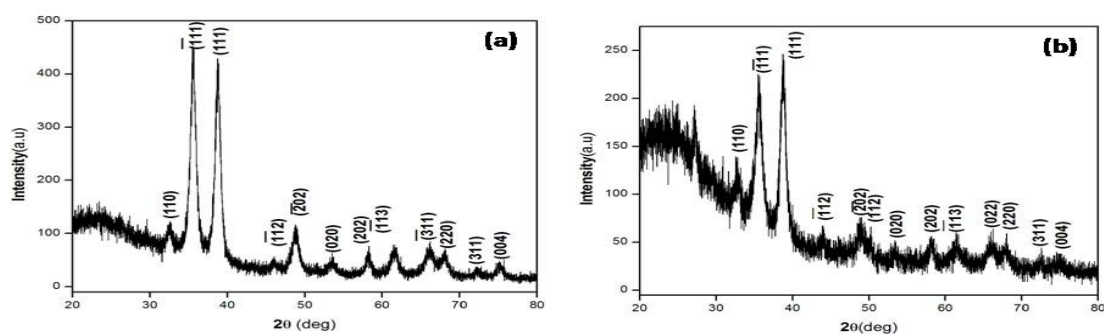
Fig. 1. XRD pattern of CuO nanostructured thinfilms prepared at a) 20 and b) 40 deposition cycles
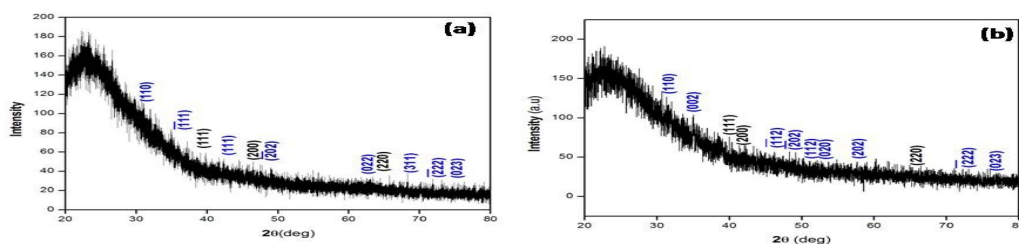
Fig.2. XRD pattern of Platinum coated CuO nanostructured thinfilms

Raman Spectra of CuO and Pt/CuO nanostructured thinfilms

Raman spectroscopy, which is a sensitive probe to the local atomic arrangements and vibrations of the materials, has been also widely used to investigate the microstructural nature of the nanosized materials in general and CuO nanomaterial in particular. Raman scattering also provides useful information about the structures and bonds of materials. Raman scattering could help to detect the existence of unintended phases such as Cu_2O or $Cu(OH)_2$ or show the crystallinity of the product. The zone center Raman active normal modes of CuO are $\Gamma RA = 4Au + 5Bu + Ag + 2Bg$. Among these vibrational modes, there are three acoustic modes (Au + 2Bu), six infrared active modes (3Au + 3Bg), and three Raman active modes (Ag + 2Bg). Three well known bands of CuO are Ag (278.81 cm^{-1}), Bg 1 (326 cm^{-1}), and Bg 2 (614.85 cm^{-1}) [4].
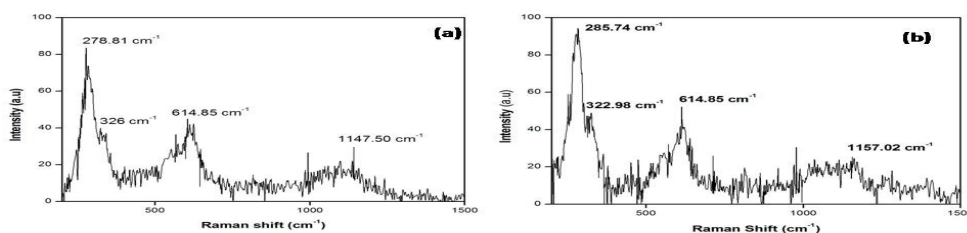
Fig. 3. Raman spectra of CuO nanostructured thinfilms prepared at a) 20 and b) 40 deposition cycles
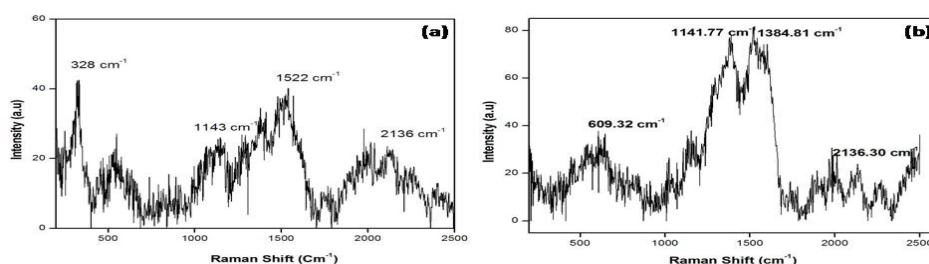
Fig. 4. Raman spectra of Platinum coated CuO nanostructured thinfilms

Fig.3 shows Raman spectra of CuO nanostructures prepared SILAR method with different deposition cycles. When increasing the deposition cycles to 40, the red shifts were occurs which is due to the phonon confinement effect in nanometer size materials. Multiphonon band of CuO nanostructures appears at wavenumber of 1130 cm^{-1}. Fig. 4 shows the Raman spectra of platinum coated CuO nanostructured thinfilms. The peaks observed at 328 cm^{-1}, 609.32 cm^{-1} and 1141.77 cm^{-1} are the different phonon modes of CuO. The peak at 2136 cm^{-1} provides the strong evidence for the formation of plantinum on CuO nanostructures.

4. CONCLUSION

Copper Oxide and Platinum coated Copper Oxide nanostructured thin films were prepared using the simple chemical method. It's structural properties have been studied using XRD, RAMAN spectroscopy. In XRD the dominating intensity of the diffracted peaks (-111), (111) reveal the improved crystallinity of CuO nanostructures. The average grain size estimated from XRD gives the diameter in the range of 14 - 27 nm. Raman Spectra explains the structural information of CuO and Pt/CuO nanostructured thinfilms, in which, the peaks observed at 328 cm^{-1}, 609.32 cm^{-1} and 1141.77 cm^{-1} are the different phonon modes of CuO. The peak at 2136 cm^{-1} provides the strong evidence for the formation of plantinum on CuO nanostructures. Being more crystalline, CuO deposited thin film may be used in semiconductor devices and in optical fibre communication system.

REFERENCES

1. The effect of hydrostatic pressure on the ambient temperature structure of CuO, Forsyth J.B., Hull S., J. Phys.: Condense. Matter 3 (1991) 5257-5261.

2. Optical Analysis of Chemical bath Fabricated CuO Thin Films;Ezenwa I.A.; Research a.Journal of Recent Sciences, Vol. 1(1), 46-50, Jan. (2012).
3. Annealing Temperature Dependence on the Physicochemical Properties of Copper Oxide Thin Films;J. Y. Park, T. H. Kwon, S. W. Koh, and Y. C. Kang; Bull. Korean Chem. Soc. 2011, Vol. 32, No. 4 1331.
4. Practical Raman spectroscopy, Gardiner, D.J. (1989)

PRESSURE INDUCED STRUCTURAL PHASE TRANSITION AND METALLIZATION IN SODIUM IODIDE (NaI)

*J. Merlinebetsy, Y.Ramola and C.Nirmala Louis**

Research Department of Physics, Holy Cross College (Autonomous),

Nagercoil – 629 004, Tamil Nadu, India.

*Corresponding author : nirmalalousis@holycrossngl.edu.in

ABSTRACT

The structural phase transition and metallization of the simple alkali iodide, sodium iodide (*NaI*) is investigated through their band structures. The band structure, density of states (DOS) and total energy are computed as a function of volume for both NaCl and CsCl phases using the full potential linear muffin-tin orbital (FP-LMTO) method. The phase transition pressure *(P_T)* and the corresponding reduced volume *(V_T)* estimated in our calculation are 0.038 Mbar and 0.89 respectively. The metallization pressure P_M is 2.6259 Mbar and the corresponding reduced volume *(V_M)* is 0.36. The results of the metallization pressure in *NaI* is compared with that of other alkali iodides potassium iodide(KI) and RbI. It is found, that the charge transfer from *s* and *p* states to the *d* state will cause metallization and the metallization pressure increases with a decrease of the lattice constant. It is also confirmed that the metallization and structural phase transition do not occur simultaneously in ionic compounds.

1. INTRODUCTION

The physical properties of materials undergo a variety of changes when they are subjected to high pressure [1]. The increase of pressure means the significant decrease in volume, which results in the change of electronic states and crystal structure [2]. The modern development in diamond anvil cell [3-11] enables the experimentalist to perform the investigation at very high value of pressure (5 Mbar). Already twenty three new elemental superconductors were found at high pressure. In this list new compounds are now being included. One such compound is the simple ionic salt CsI [3]. These results lead us to expect superconductivity in other alkali halides under high pressure, especially those alkali iodides which have already become metals [1].

2. CALCULATIVE PROCEDURE

The band structures of NaI corresponding to various pressures are obtained   in *NaCl* and *CsCl* structures using the full potential linear muffin-tin orbital (FP-LMTO) method with in generalized gradient approximation (GGA) [2]. The electronic configurations of Na is [Ne] $3s^1$ (Z=11) and for I it is [Kr]$4d^{10} 5s^2 5p^5$ (Z=53). The valence electronic configurations of Na and I are $3s^1$ and $5s^2 5p^5$ respectively. There are 8 electrons contribute to the valence band. The final energy convergence is within 10^{-5} Ry. The calculated total energies were fitted to the Birch-Murnaghan's equation of state (EOS) , to determine the phase transition pressure and other ground state properties.

Birch-Murnaghan's equation of   state is given by

$$P = 1.5B_o \ [(V_o/V)^{7/3} - (V_o/V)^{5/3} \ ] \ [1 + 0.75 \ (B_o^1 - 4) \ \{(V_o/V)^{2/3} - 1\} \ ] \qquad (1)$$

to obtain the equilibrium lattice constant   and other ground state properties. In our calculation we have chosen the NaCl structure for NaI at ambient pressure. The phase stability of the NaCl and CsCl structures of NaI is analysed using the enthalpy calculation [1]. The enthalpy *H(P)* is defined by

$$H(P) = \ E_{tot}(P) + PV(P) \qquad (2)$$

and the transition pressure corresponding to the phase transition from NaCl to CsCl is obtained from the relation

$$H_{NaCl}(P) = H_{CsCl}(P) \qquad (3)$$

where H_{NaCl} and H_{CsCl} are the enthalpies of the NaCl and CsCl phases respectively.

3. RESULT AND DISSCUSSION

The Band Structure Of NaI At Normal Pressure

The normal pressure band structure of NaI (for NaCl structure) is given in Fig:1. Fermi level is indicated by dotted horizontal line. The overall topology of the band structure at V/Vo=1 is same for previous calculation. The three bands appearing just below the Fermi energy E_F are from Na-$3s^1$ and I- $5s^2,5p^5$ electrons of NaI (Fig: 1). The empty conduction bands above the Fermi level are due to $3p^0,3d^0$ states of Na and $5d^0,6s^0,6p^0$ states of I (Fig: 1). At normal condition, the band gap Eg is found to be 0.2480Ry (3.373 eV) for NaI. The general features of

band structures are similar to previous calculations. From our calculation, NaI is a direct band gap insulator at normal pressure.

The Band Structure of NaI at High Pressure

The high pressure band structure of NaI (for CsCl structure) is given in Fig: 2. Fermi level is indicated by dotted horizontal line. The overall topology of the band structure at V/Vo=0.36 is same as Fig: 1. But Fig: 2represents metallic NaI and Fig: 1 represents insulating NaI. The triplet bands which are positioned at the bottom of valence band arise $3s^1$ electrons of Na (Fig: 2). A single band nearer to the triplet bands is due to I-$5s^2$ electrons (Fig:2). The three bands appearing just below the Fermi energy E_F and touching Fermi energy E_F are from Na-$3s^1$ and I-$5p^5$ electrons of NaI (Fig: 2).The filled conduction bands above the Fermi level are due to $3p^0,3d^0$ states of Na and $5d^0,6s^0,6p^0$states of I (Fig:2). In NaI, metallization takes place by the indirect closure (Fig:2) of band gap between valence band maxium of Γ point and conduction band minimum at the H point . The metallization volume of NaI is V/Vo=0.36, which corresponds to the pressure P_M= 2.6259 Mbar. The general features of high pressure band structure is similar to previous calculations [8-12]. From our calculation, in NaI direct closure of band gap occurs.

The variation of total energy as a function of reduced volume for NaI is shown in Fig.3. In this figure, upto V/Vo=0.89, NaCl has lowest energy. Further reduction of volume CsCl has lowest energy. The enthalpy versus pressure curve is given in Fig.4. In this figure, upto P=0.038 Mbar, NaCl has lowest energy. Further increase of pressure CsCl has lowest energy.The phase transition pressure *(P_T)* and the corresponding reduced volume *(V_T)* estimated in our calculation are 0.038 Mbar and 0.89 respectively. Our calculated phase transition pressure is in good agreement with the experimental value of 0.035 Mbar [11]. The charge transfer causes the phase transition but the mechanism for the phase transition is a geometric effect involving a change in co-ordination number from 6 in the NaCl phase to 8 in the CsCl phase. However, there are no experimental or theoretical study available for comparison at these pressures in NaI. But experimental and theoretical studies are available for comparison with alkali iodides KI and CsI [Table. 1]

4. CONCLUSION

The high pressure band structure, density of states, structural phase transition, metallization and superconductivity of NaI is investigated. When the pressure is increased there is enhanced overlapping between the wave functions of the neighbouring atoms. As a result the widths of the valence and empty conduction bands increase. These changes lead to the narrowing and closing of band gaps (metallization). The metallization reduced volume is V/V_o=0.36 (CsCl structure), and the corresponding pressure P_M is 2.6259 Mbar. In our calculation NaCl phase to CsCl phase transition occurs at 0.038 Mbar. This value is good agreement with the experimental value of 0.035 Mbar. It is also confirmed that the structural phase transition and metallization do not occur simultaneously in alkali iodide compounds [3].

Table 1: Comparison of Metallization in alkali iodides

COMPOUND	Lattice constant (au)	$(V/V0)_M$	P_M Mbar
NaI	12.212	0.36	2.626
KI [4]	13.406	0.43	1.228
RbI[1]	13.967	0.4	1.157

Figure 1: Band structure of NaI at V/Vo=1.0 (NaCl structure)
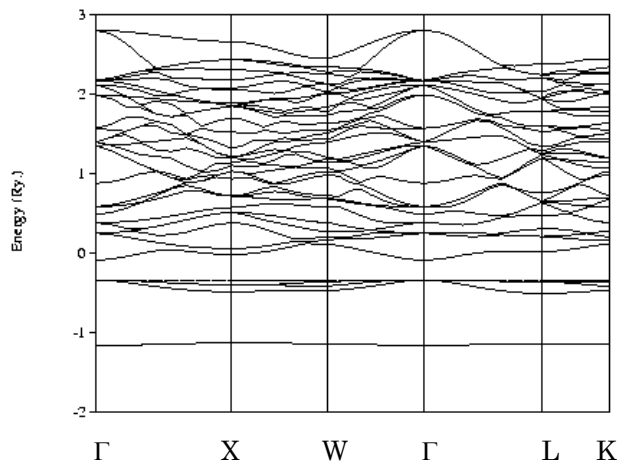
Figure 2: Band structure of NaI at V/Vo=0.36(CsCl structure)
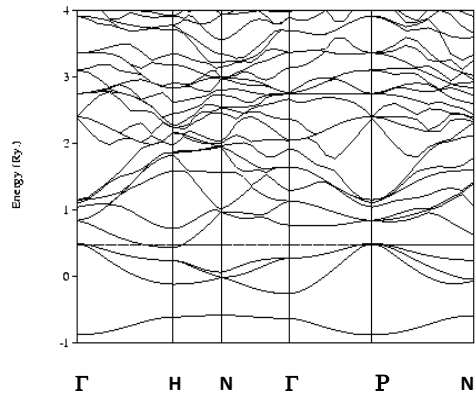
Fig.3: Total energy versus reduced volume curve for NaI (NaCl and CsCl structures)
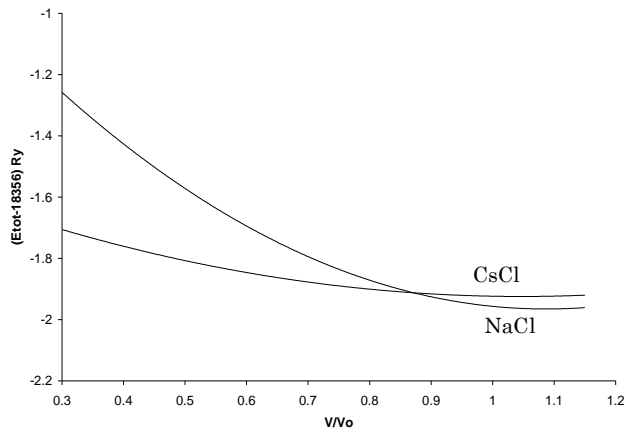
Fig 4: Enthalpy versus pressure curve for NaI in NaCl   to CsCl transition
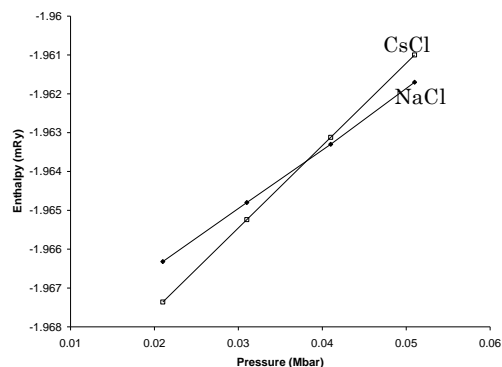
ACKNOWLEDGEMENT

REFERENCES

[1] C.Nirmala Louis and Y.Ramola,International Journal of Chemical Science,2(1),(2018) 36-41.

[2] A. Amalraj , C. Nirmala Louis and Sr. Gerardin Jayam, Journal of Theoretical and Computational Chemistry ,Vol. 6, No. 4 (2007) 833–843.

[3] M. I. Eremets, K. Shimizu and K. Amaya   Science 281(1998)1333.

[4] C. Nirmala Louis and K.Iyakutti, Physica status solidi (b), 233, 339-350 (2002).

[5] S.Q.Wang and H.Q. Ye, J. Phy. Condensed matter 14 (2002) 9579.

[6] C. Nirmala Louis, K. Iyakutti, K.S.Hema Nandhini, M. Sivakumar and E. Palaniyandi, Physica Status Solidi (b) 241, (2004) 2489-2500;

[7] U.von Barth and L. Hedin, J. Phys. C 5 (1972) 629.

[8] F. D. Murnaghan, Proc. Natl. Acad. Sci. USA 30 (1944) 244.

[9] G.D. Gaspari and B.L. Gyorffy, Phys .Rev. Lett 29 (1972) 801.

[10] W.L. Mcmillan, Phys. Rev.167(1968) 331.

[11] Y. Ramola, C.Nirmala Louis and A.Amalraj, Chemical and Materials Engineering (2017), 5(3): 65-74.

GREEN SYNTHESIS OF COPPER OXIDE NANOPARTICLES USING HENNA LEAF EXTRACT

M. Jenifer Dhas[1], J. Anto Baslis Abisha[1], P. Aji Udhaya[1*], M. Abila Jeba Queen[1],

M. Meena[2]

[1]Department of Physics, Holy Cross College, Nagercoil (Affiliated to Manonmaniam Sundaranar University, Abishekapatti, Tirunelveli 627012).

[2]Department of Physics, S.T. Hindu College, Nagercoil.

[*]**Corresponding Author : ajiudhaya@gmail.com**

ABSTRACT

In this work, we report the green synthesis of Copper Oxide nanoparticles using lawsonia inermis (henna) leaf extract by green synthesis route. Nanotechnologist nowadays adopt green synthesis widely because of its Eco friendliness.The formation of single phase Copper Oxide nanoparticles was confirmed by powder X-Ray Diffraction. Lattice parameter, volume of the unit cell and X-ray density were determined from PXRD pattern. Average crystallite size was estimated from the PXRD pattern using Scherrer equation to be around 17 nm. The optical absorption band gap of the Copper Oxide nanoparticles was estimated to be 3.149eV from the UV-Vis analysis. The composition of the as synthesized nanoparticles was confirmed by FTIR spectra analysis.

Keywords: Copper Oxide, PXRD, FTIR, lattice parameter, X-ray density, UV-Vis, band gap.

1.INTRODUCTION

Nanotechnology is considered to be the technology of the future.Nanotechnology deals with materials and systems having the dimension of about 1-100nm [1].As Green synthesis provides advancement over physical and chemical method as it is cost effective environment friendly, easily scaled up for large scale synthesis and in this method there is no need to use high pressure, temperature, energy and toxic chemical [2]. Synthesis of nanostructured oxide materials through green synthesis have been attracted considerable attention. Among the metal oxides nanostructures, copper oxide nanomaterials have attracted more attention due to some of its unique properties. Copper oxide is considered as a potential field emitter, an efficient catalytic agent, as well as a good gas sensing material. It also plays an important role in optoelectronics and solar cell [3].

2.MATERIALS AND METHODS

Copper oxide nanoparticles was prepared using the self-combustion method. In a typical procedure [4] Copper nitrate hexahydrate solution was added drop wise to the henna leaf extract and

vigorously stirred for 2 hours to obtain a well dissolved solution. Then the mixed solution was evaporated by heating on a hot pate at 80ºC for several hours. The water content gradually vaporized during heating and when a crucible temperature reached a great deal of foams was produced and a spark appeared at one corner which spread through the mass, yielding a black fluffy product. The fluffy product was was calcined at 600ºC for 2 hours. Thus Copper Oxide nanoparticles were obtained.

3. RESULT AND DISCUSSION

XRD Diffraction Analysis

Fig. 1 shows the XRD pattern for CuO nanoparticle. The prominent peak at $2\theta=36.2681°$ corresponds well to the literature value of 35.4° for the (-111) crystalline plane [5]. Also the diffraction data are in good agreement with the JCPDS file No: 80-0076. From the JCPDS file it is confirmed that the formed nanoparticles are copper oxide with formula CuO and it belongs to end – centered monoclinic crystal system. From unit cell software the lattice parameters are found to be a=4.70665 Å, b=3.41911, c=5.10996, $\alpha=\gamma=90°$ and $\beta=99.72387$ .The cell volume was found to be $V=81.0508Å^3$. The average crystallite size was calculated using the Debye Schrrer formula, $\mathbf{d = k\,\lambda\,/\beta\,\cos\theta}$ as 13.342 nm.
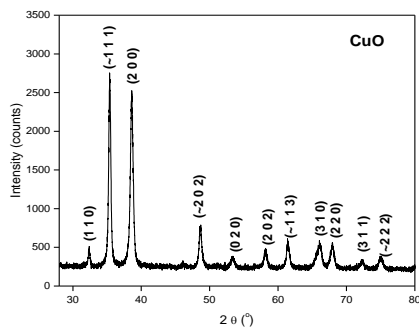
Fig. 1. PXRD pattern of CuO   Fig. 2. FTIR spectra of CuO
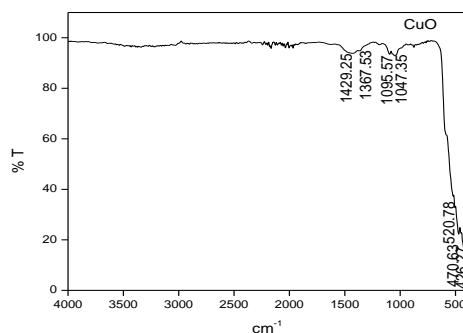
FTIR Analysis

FTIR spectra of the CuO samples as investigated in the wavenumber range of $4000-400cm^{-1}$ (Fig. 2). Some peaks are observed at 1429.25 cm^{-1}, 1367.53 cm^{-1}, 1095.57 cm^{-1}, 1047.35 cm^{-1}, 520.78 cm^{-1},470.63 cm^{-1} and 426.27 cm^{-1}. Two bands at 1429.25 cm^{-1} and 1367.53 cm^{-1} corresponds to CO_3^{2-} stretching mode, which may be due to carbon dioxide evolved at combustion process. Bands obtained at 1095.57 cm^{-1} and 1047.35 cm^{-1}corresponds to vibrational mode of N=O. Three bands at 520.78 cm^{-1}, 470.63 cm^{-1} and 426.27 cm^{-1}corresponds to Cu-O vibrational mode [6].

UV Analysis

Absorption is powerful non-destructive technique to explore the optical properties of semiconducting nanoparticles and in the present work, Energy band gap studies of the as synthesized

CuO nanoparticles have been calculated using absorption spectra and it is depicted in Fig. 3. Also the reflectance spectra of CuO nanoparticles is depicted in Fig. 4. The energy gap of the synthesized nanoparticles is found using the formula, $E_g = h\nu_g = hc/\lambda_g$, [7] Where, E_g is the optical band gap. Optical energy gap is obtained by extrapolating the linear portion of the absorption spectrum to zero. The energy band gap for CuO is calculated using $\lambda_g = 370$ nm as 3.3 eV. But the standard band gap energy for CuO nanoparticle is 3.149 eV. There is an increase in bangap value; this may be due to the synthesis method.
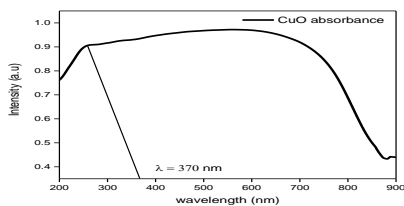
Fig. 3. UV absorption spectra of CuO
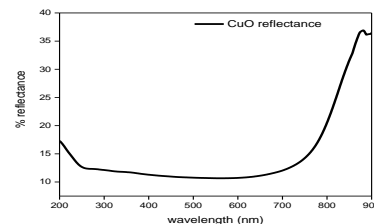
Fig. 4. UV reflectance spectra of CuO

4. SUMMARY AND CONCLUSION

In the present work, green synthesis route was adopted for the synthesis of CuO nanoparticles as green route. The XRD data of the samples are good agreement with the corresponding JCPDS file. The Copper oxide nanoparticles exhibit end – centered monoclinic crystal system. The energy gap of Copper Oxide nanoparticle was found to be 3.1 eV respectively from UV-Vis spectra. The FTIR spectral studies revealed the presence of water, nitrate, and carbon traces, which is to be avoided. The application oriented work of the prepared CuO nanoparticle is to be carried in near future.

REFERENCES

[1] Richard Booker and Earrl Boysen,Nanotechnology Wiley publishing Inc.,(2005) 10-15.

[2] C.G Granqvist, R .A. Buhrman, J. Wyns, A.J.Sievers (1976). "Far-Infrared Absorption in   Ultrafine .A1 Particles". Physt.Rev.Lett. 37(10):625-629

[3] Dwivedi P, Narvi SS, Tewari RP. International Journal of Green Nanotechnology. (2012), 4(3),1-7.

[4] Copper Oxide Nanoparticles – Properties, Applications-AZoNano.

[5] A. Rahdar, M. Aliahmad, Y. Azizib, Journal of Nanostructures, 5 (2015) 145- 151.

[6] D. S. Sheny, J. Mathew, D. Philip. Spectrochimica Acta Part A: Molecular and Biomolecular Spectroscopy. (2012), 306.

[7] Spas Nedev, Alexandar S. Urban, Andrey A, "Optical Force Stamping Lithography", Nano Letters, Vol. 11,No. 11,(2011).

ANTIBACTERIAL APPLICATIONS OF CALCIUM NANOPARTICLES

*S. K. Rinu, A. Sahaya Sabeena, M.Abila Jeba Queen, P.Aji Udhaya

Department of Physics, Holy Cross College(Autonomous), Nagercoil
*Corresponding author email id: crisrinu2@gmail.com

ABSTRACT

Inorganic nanoparticles for biomedical applications have undergone extensive investigations in recent years. Calcium carbonate nanoparticles are synthesized by wet chemical precipitation method. X-ray diffraction studies are made to determine the structural properties. The antibacterial activity was tested on Gram negative and Gram positive bacterial strains.

Keywords

Calcium carbonate, Calcium Hydrogen phosphate.

1.INTRODUCTION

Calcium derivatives are the most important natural constituents of bone and teeth. In fact, the primary tissues of bone, osseous tissue is mostly made up of a composite material consist of the inorganic mineral calcium derivatives [1]. Furthermore, tooth enamel is one of the four tissues that composes the tooth which contains the highest percentage of mineral mostly Calcium [2]. Therefore, different calcium derivatives have been shown great potentials to be applied in bone and teeth related disorders [3,4]. Filling dental caries, treatment of early dental caries lesions and generating neo-formed bone tissue using by different types of calcium derivatives has also shown notable applications.[5,6] One of the most common calcium derivatives with long history of applications in various fields is $CaCO_3$. It has been used in plastics, paint, paper, inks, food as well as pharmaceutical industries [4]. Medical applications of $CaCO_3$ in modern health care systems have attracted the attention of researches due to its great potentials and capabilities. This paper presents the preparation and characterization of calcium carbonate nanoparticles.

2. SYNTHESIS PROCEDURE

Synthesis of Calcium carbonate nanoparticles

Calcium carbonate is synthesized from egg shell. Egg shells of hen are collected in bulk. Then the egg shell is dried at room temperature. The egg shells are slightly crushed and taken in a crucible and kept in the muffle furnace at 900℃ for 2 hours. Then it is grinded into fine powder. Thus Calcium carbonate nanoparticles are synthesized.

3. CHARACTERIZATION

XRD studies for Calcium Carbonate

The diffraction data are in good agreement with the JCPDS file No:85-1108. From the JCPDS file it is confirmed that the prepared nanoparticles are Calcium Carbonate. The X-ray powder diffraction pattern of $CaCO_3$ is show in figure 1. From the JCPDS file, it was found that the prepared calcium carbonate nanoparticles belongs to Rhombohedral structure with a = 4.980Å, b =4.980Å, c = 17.018Å, $\alpha = \beta \neq \gamma = 90^0$ and Volume =365.57$Å^3$.
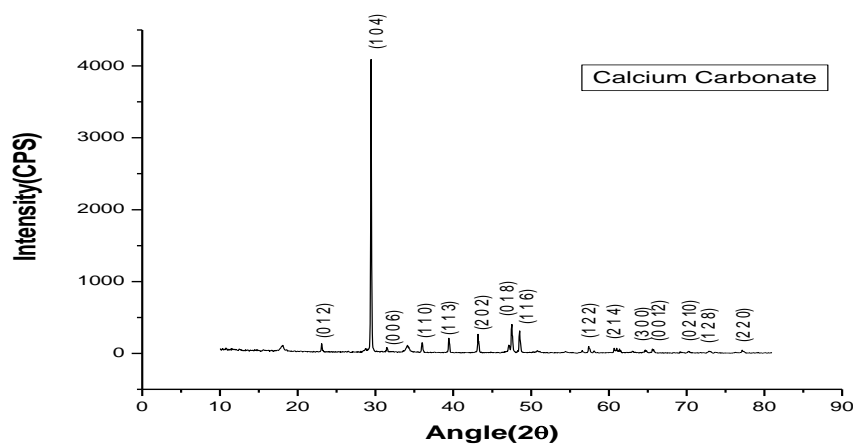
Fig. 1 The XRD pattern of Calcium Carbonate

Antibacterial Activity

The antibacterial activity was tested on Gram negative (Escherichia coli and Pseudomonas aeruginosa) and Gram positive (Enterococcus feacalis and Bacillus subtilis) bacterial strains. The qualitative assessment of the antibacterial effect was done using agar disc diffusion (KirbyBauer) method. The contact biocidal property can be determined by measuring the diameter of the zone of inhibition (ZOI) around the well. At the end of incubation, inhibition zones were examined around the disc and measured with transparent ruler in millimetres. The diameters of the ZOI are determined and these are tabulated in Table 1. The absence of growth around the nanoparticles is an indirect measure of the ability of the material to inhibit the growth.

Table.1 Diameters of the ZOI produced by the samples against the microbes

Synthesized Nanoparticles	Zone of inhibition(mm)			
	Enterococcus feacalis	Bacillus subtilis	Escherichia Coli	Pseudomonas aeruginosa
CaCO$_3$	21	20	19	21
Positive Control	17	25	20	23

4.CONCLUSION

In the present investigation Calcium nanoparticles are synthesized from egg shell by wet chemical precipitation method. From XRD studies, it is concluded that Calcium carbonate has rhombohedral structure. The antibacterial action of CaCO$_3$ nanoparticles was studied and the inhibition zones were examined around the disc are measured with transparent ruler in millimeters. It has been found that the calcium nanoparticles are highly antibacterial on gram positive bacterias.

REFERENCES

1. Bandyopadhyay-Ghosh S. Bone as a collagenhydroxyapatite composite and its repair. Trends Biomater Artif Organs 2008;22:116-124.

2. Brudevold F, Söremark R. Chemistry of the mineral phase of enamel. Struct chem organ teeth 1967;2:247-277.

3. Ohgushi H, Okumura M, Yoshikawa T, Inboue K, Senpuku N, Tamai S, et al. Bone formation processin porous calcium carbonate and hydroxyapatite. J Biomed Mat Res 1992, 26:885- 895   .

4. Biradar S, Ravichandran P, Gopikrishnan R, Goornavar V, Hall JC, Ramesh V, et al. Calcium carbonate nanoparticles: synthesis, characterization and biocompatibility. J nanosci nanotech 2011;11:6868-6874.

5. Fujihara K, Kotaki M, Ramakrishna S. Guided bone regeneration membrane made of polycaprolactone/calcium carbonate composite nano-fibers. Biomaterials 2005;26:4139-4147.

6. Hannig M, Hannig C. Nanotechnology and its role in caries therapy. Adv Dental Res 2012;24:53-57.

OPTICAL ABSORPTION AND DIFFUSE REFLECTION STUDIES ON SPRAY PYROLYSED ZnFe$_2$O$_4$ NANOSTRUCTURES

M.B. Arthina Titlin[1*], S. Mary Delphine[1]

[1]Department of Physics & Research Centre, Holy Cross College (Autonomous), Nagercoil, Tamil Nadu

*Corresponding author: arthinatitlin@gmail.com

ABSTRACT

Zinc Ferrite nanostructured thin films have been prepared by spraying 0.5 M Zn^{2-} and 1.0 M Fe^{3-} bearing nitrate solution on glass substrates maintained at four different temperatures 150, 250, 350 and 450 ºC. Thickness and the surface roughness of the prepared films were measured using the Stylus type profilometer. Crystalline nature of the prepared ZnFe$_2$O$_4$ was identified from the recorded X-ray diffraction patterns. Optical absorption spectra revealed the band gap and other charge transfer interactions. Kubelka-Munk treatment on the diffuse reflectance spectra unambiguously gave the optical band gap energy. The refractive index and packing density of ZnFe$_2$O$_4$ thin films were estimated from diffuse reflectance spectra (DRS).

Key words: Spinel, Spray pyrolysis, Optical absorption, Diffuse reflectance

1 INTRODUCTION

Estimation of optical energy gap (E_g) is essential for semiconductors that decide their applications in optoelectronic device fabrications [1]. The UV-Vis absorption spectroscopy is frequently used to characterize semiconductors thin films [2]. In normal incidence mode, dispersed light is counted as absorbed light and the technique (optical absorption) does not distinguish between the two phenomena. In order to avoid these complications, it is desirable to use DRS, which enables to obtain E_g [3]. Hence in the present study both optical absorption and DRS spectral investigation were performed to evaluate the optical constants of ZnFe$_2$O$_4$ thin films.

2 EXPERIMENTAL DETAIL

Reagent grade Fe(NO$_3$)$_3$ 9H$_2$O and Zn(NO$_3$)$_2$ 6H$_2$O were used as starting chemicals. ZnFe$_2$O$_4$ thin films were prepared by spraying the solution onto glass substrates (Corning 7059 glass) at four different substrate temperaturs, 150, 250, 350 and 450 ºC. Deposited ZnFe$_2$O$_4$ films were characterized by Mitutoya surftest SJ-301 stylus type surface roughness and thickness-measuring instrument. The structural properties of the prepared films were characterized by X-ray diffraction analysis (XRD) in XPERT-PRO diffractometer. DRS was recorded using VARIAN Cary 500 Scan spectrophotometer.

3 RESULTS AND DISCUSSION

Thicknesses of the deposited ZnFe$_2$O$_4$ thin film samples are 37.75, 104.3, 79.01 and 55.03 μm respectively for the deposition temperatures 150, 250, 350 and 450 ºC. Measured average roughness is respectively, 2.90, 5.16, 4.75, and 4.65 μm. Film prepared at 150ºC is amorphous, produced film at 250 ºC is not well crystallized. ZnFe$_2$O$_4$ films prepared with higher substrate temperatures 350 and 450 ºC are highly crystalline.

Optical absorption band slightly shifted to the lower wavelength region with deposition temperature (Fig. 1). The transitions peak around 375nm were corresponding to ligand-to-metal charge transfer ($6t_{1u}\uparrow \rightarrow 2t_{2g}\downarrow$) [4]. In addition, the peaks around 440 to 490 nm and 730 nm have been interpreted as *d-d* crystal field transition between multiplets of $3d^5$ configuration of the Fe^{3+} ion [5]. A sudden drop in absorption is observed around 550-600 nm which corresponds to band gap. In general the band structure of ferrite has O-2p orbital as the valence band and Fe-3d orbital as the conduction band [6].
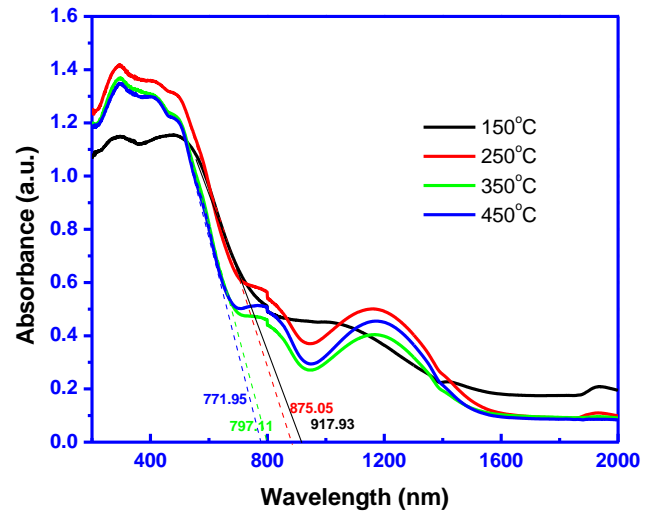
Fig. 1 Optical absorption spectra
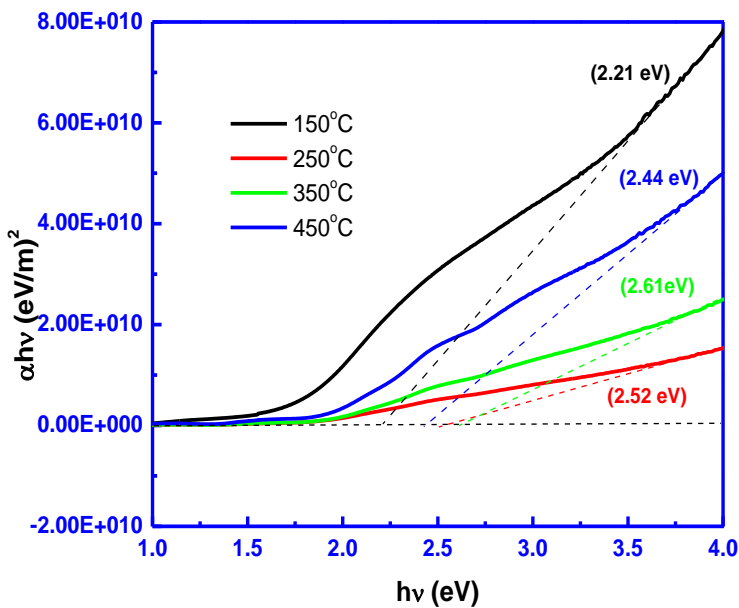
Fig. 2 Tauc plots

Fig. 2 is the constructed Tauc plots using absorption data. Obtained direct band gap values are respectively 2.21, 2.52, 2.61 and 2.44 eV for the $ZnFe_2O_4$ films deposited at 150, 250, 350 and 450 °C. Obtained band gap between O-2p and Fe-3d in $ZnFe_2O_4$ films are comparable to the reported values [7]. Obtained results revealed that the films prepared at lower temperature have higher oxygen vacancy metastable states within the energy gap and has reduced band gap [8].

Fig. 3 shows the band gap energy of the $ZnFe_2O_4$ samples analyzed from the reflectance spectra using a modified Kubelka–Munk function F(R) [36]. A graph was plotted against $[F(R) h\upsilon]^2$ and $h\upsilon$, and the intercept obtained corresponds to the direct band gap energy. The predicted band gap energies of $ZnFe_2O_4$ thin films from the reflectance specta are 2.42, 2.82, 2.33, 2.98 eV, respectively for the films processed at150, 250, 350 and 450 °C. . The band gap of the film deposited at 450 °C is 2.98 eV, which is comparatively higher than the other samples because of its bigger grain size.

The refractive index (no) can be determined from the reflectance (R). In the visible wave length region the refractive index is almost constant (1.48) and then increases suddenly in the IR region. The packing density of the prepared films was calculated and its variation with wave length is

Fig. 3 Tauc plots using DRS data

shown in Fig. 4. The packing density of bulk material has unit value [10]. the packing density can be calculated using the refractive index using the Bragg and Pippard equation [11]. In the present study, prepared $ZnFe_2O_4$ thin film prepared at 150 ℃ has the packing density in the visible region of about 1. However, the other films deposited at higher temperatures are not dense.

Fig. 4 Packing density variations

4 CONCLUSIONS

Zinc ferrite thin films have been successfully deposited using spray pyrolysis technique for four different substrate temperatures. Prepared film at low substrate temperature was amorphous and all other films deposited at higher temperature are crystalline. Optical parameters of the $ZnFe_2O_4$ thin films were evaluated using optical absorption and diffuse reflectance spectra. Reflectance data was used to find out the refractive index and hence packing density was evaluated.

REFERENCES

[1]   T. Aoki, Y. Hatanaka, and D.C. Look, Appl. Phys. Lett. 76 (2000) 3257.
[2]   U. Pal, D. Samanta, S. Ghorai, and A.K. Chaudhuri, J. Appl. Phys. 74 (1993) 6368.
[3]   D.G. Barton, M. Shtein, R.D. Wilson et al. J. Phys. Chem. B 103 (1999) 630.
[4]   L.A. Marusak, R. Messier, W.B. White, J. Phys. Chem. Solids, 41 (1980) 981.
[5]   J. J. Beltra´n, C.A. Barrero, A. Punnoose, Phys.Chem.Chem. Phys., 17 (2015) 15284.
[6]   V.R. Galakhov, E.Z. Kurmaev, et al., J. Phys. Chem. C, 114 (2010) 5154.
[7]   M. Sultan, R. Singh, J. Phys. D: Appl. Phys., 42 (2009) 115306.
[8]   Ju Hun Kim, Youn Jeong Jang, Jin Hyun Kim, et a., Nanoscale, 7 (2015) 19144.
[9]   J. Hays, K.M. Reddy, et al., J. Phys. Condens. Matter. 19 (2007) 266203.
[10]   G. Bauer, Ann. Phys. 19 (1934) 434.
[11]   R. Jacobson, Phys. Thin Films 8 (1975) 51.

AN OVERVIEW OF METAMATERIALS

Dr. Mahesh N R

Department of Physics, St.Xaviers College, Thiruvananthapuram

Email ID: mahesh.nr@hotmail.com

METAMATERIALS

Metamaterials are sub-wavelength, effectively homogenous, composite structures tailored to have properties that are yet to be found in materials that are readily available in nature. Metamaterials earn their exceptional properties mainly because of their structure rather than the physical and chemical properties of the materials they are composed of. The quest for the artificial material that can bring desired electromagnetic or mechanical properties was begun after the Second World War. These explorations gave birth to many novel materials such as photonic band gap materials, acoustic band gap materials and metamaterials. Roger M Walser, a physics professor from the University of Texas in 1999 has coined the term metamaterials for these exceptional composite structures. The possibility of a metamaterial that have essential simultaneously negative permittivity and permeability was first proposed by a Russian Physicist Victor Veselago in 1967.

Metamaterials are engineered structures, to have simultaneously negative bulk material properties of permittivity and permeability. The effective refractive index of materials can be related with their relative permittivity and permeability as

$$n = \pm\sqrt{\varepsilon_r \mu_r} \qquad (1)$$

where ε_r is the relative permittivity and μ_r is the relative permeability. Out of the two solutions of the Equation (1), for metamaterials, physically admissible one is the solution with negative sign. So materials with simultaneous negative permittivity and permeability are called negative refractive index materials (NIM). Consider the Maxwell's curl equations

$$\nabla \times \vec{E} = -\frac{\partial \vec{B}}{\partial t} \qquad (2)$$

$$\nabla \times \vec{B} = \mu\,\varepsilon\,\frac{\partial \vec{E}}{\partial t} \qquad (3)$$

where ε is the permittivity of the medium, μ is the permeability of the medium, $\vec{E}$ is the electric field and $\vec{B}$ is the magnetic field. For uniform plane waves Equations (2) and (3) can be written as

$$\vec{k} \times \vec{E} = \mu\,\omega\,\vec{H} \qquad (4)$$

$$\vec{k} \times \vec{H} = -\varepsilon\,\omega\,\vec{E} \qquad (5)$$

where $\vec{k}$ is the wave-vector and $\vec{H} = (\vec{B}/\mu)$. From Equations (4) and (5), it is clear that for ordinary materials $\vec{E}$, $\vec{B}$ and $\vec{k}$ form a right-handed triplet. For metamaterials with simultaneously negative permittivity and permeability Equations (4) and (5) can be rewritten as

$$\vec{k} \times \vec{E} = -\mu\,\omega\,\vec{H} \qquad (6)$$

$$\vec{k} \times \vec{H} = \varepsilon \omega \vec{E} \qquad\qquad (7)$$

The Equations (6) and (7) show that for metamaterials $\vec{E}$, $\vec{B}$ and $\vec{k}$ have formed a left-handed triplet. Due to this left-handedness electromagnetic metamaterial are also called as left-handed materials (LHM). But the average power per unit area carried away by an electromagnetic wave is determined by the real part of Poynting vector, and can be expressed as

$$\langle\vec{S}\rangle = \frac{1}{2\mu} (\vec{E} \times \vec{B}^*) \qquad\qquad (8)$$

The Equation (8) reminds that even for a LHM, the power transport will be in a direction as in a right-handed material (RHM). But from the Equations (6), (7) and (8), it can be concluded that phase velocity that follows the direction of wave-vector and group velocity that follows the direction of energy transport from the wave are antiparallel to each other. So in LHM electromagnetic wave has a backward propagation. Figure-1 represents the orientation of the vectors $\vec{E}$, $\vec{B}$, $\langle\vec{S}\rangle$ and $\vec{k}$ in RHM and LHM.
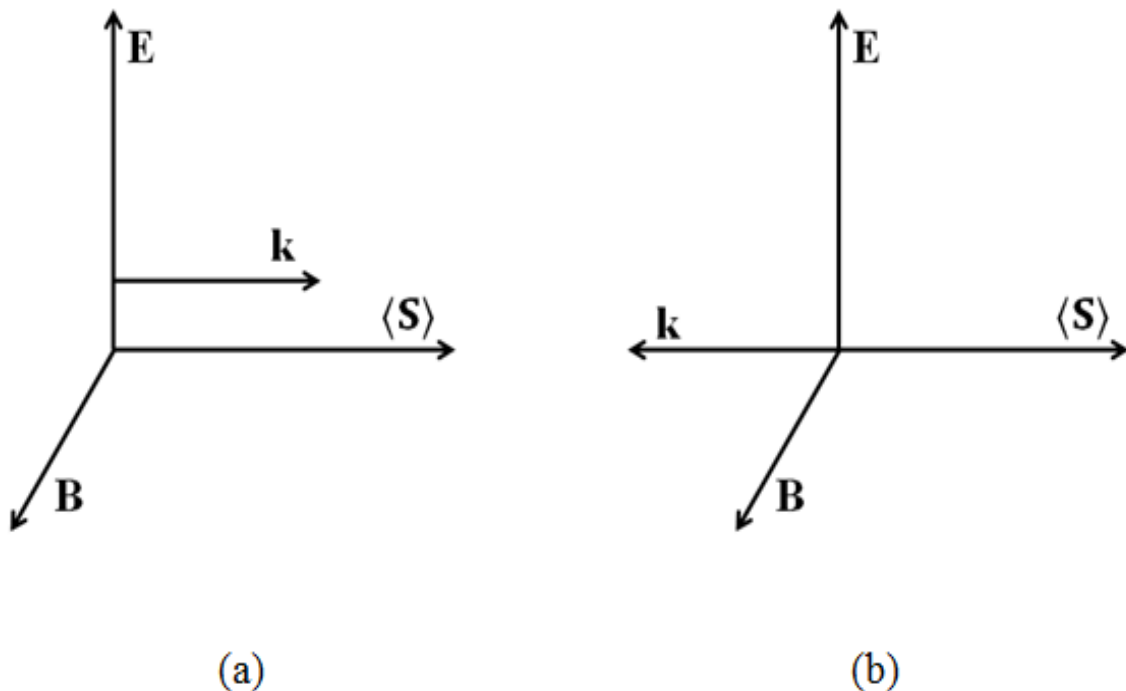
Figure-1 The orientation of the vectors $\vec{E}$, $\vec{B}$, $\langle\vec{S}\rangle$ and $\vec{k}$ in (a) RHM and (b) LHM.

The left-handedness of metamaterial affects certain laws and phenomena of electrodynamics. The reversal of Snell's law, reversal of Doppler Effect, reversal of Vavilov-Cerenkov radiation, evanescent wave propagation inside the media and beating of the diffraction limit, reversal of the focussing principles of concave and convex lenses, focussing by a flat lens, cloaking from electromagnetic waves etc. are some of the consequences of left-handedness of metamaterials.

J. B. Pendry from Imperial College, London, propounded two innovative theoretical works that propose the realization of materials with negative permittivity and permeability.

Inspired by these works Smith at University of California, fabricated and experimentally verified, an effectively homogenous medium with simultaneous negative permittivity and permeability. This medium was a composite of metal thin-wires (TW) and split-ring resonators (SRR). Figure -2 represents the periodic arrangement of metamaterial composed of TWs and SRRs.
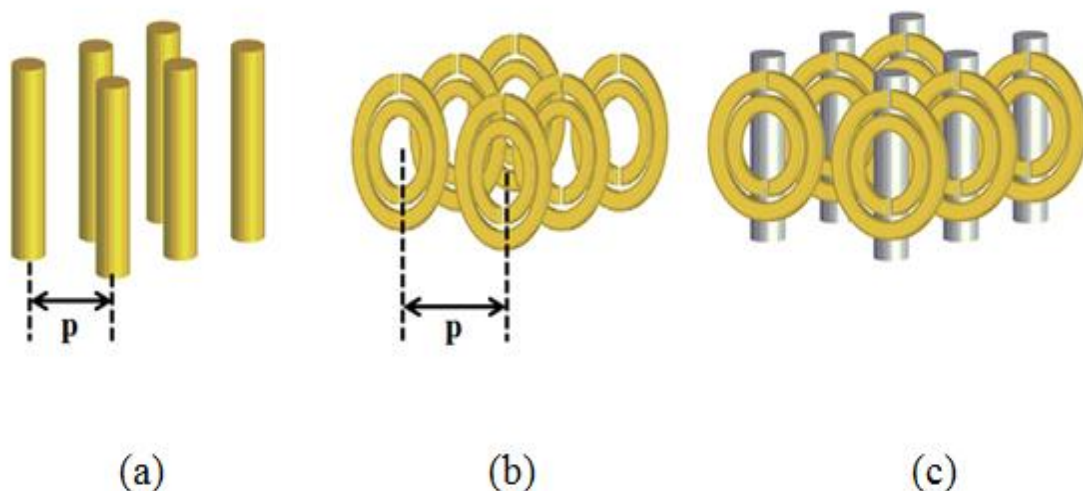
Figure 2   Periodic arrangements of (a) TWs, (b) SRRs and (c) the composite of TWs and SRRs.

An array of metallic TWs bring negative permittivity to the composite medium. When an electromagnetic wave with electric field parallel to the axis of TW excite on TWs, electric current induces in the TWs. Thus each TW effectively behaves as a dipole. This electric dipole has stationary positive charges at the one end and displaced negative charges, say electron gas, at the other end. Due to the excitation of the electric field this electron gas subjected to simple harmonic oscillation as plasmon, with a frequency and can be referred as electric plasma frequency and is expressed as

$$\omega_p = \sqrt{\frac{2\pi c^2}{p^2 \ln(p/a)}}$$
(9)

where c is the velocity of light, p is periodicity of array of TWs , a is the radius of TW. Then effective relative permittivity of the medium that formed by the sub-wavelength periodic arrangement of TWs can be expressed as

$$\varepsilon_r = 1 - \frac{\omega_p^2}{\omega^2 + \xi^2} + j\frac{\xi \omega_p^2}{\omega(\omega^2 + \xi^2)}$$
(10)

where ω is excitation frequency, $\xi = \frac{\varepsilon_o (p\omega_p/a)^2}{\pi\sigma}$, the damping factor due to metal loses, ε_o is absolute permittivity and σ is conductivity of the metal. From Equation (10), it can be concluded that real part of relative permittivity becomes negative for the condition $\omega^2 < (\omega_p^2 - \xi^2)$. Thus the medium composed of metal TWs is an effectively negative permittivity medium for the frequencies below the electric plasma frequency.

An array of metallic SRRs bring negative permeability to the composite medium. As time varying magnetic field, parallel to the axis of SRR, from an electromagnetic

wave incident on a ring, it induces electric currents in it. This electric current produce a magnetic field and ring essentially behave as a magnetic dipole. The incident field will be boosted or diminished by the induced magnetic field depending on the resonance associated with the ring. The split in the rings and the presence of the second split ring reduces the resonance frequency in a large amount. That is, split rings can achieve resonance at wavelengths larger than the diameter of the rings. For closed rings, the diameter should be at least half of the wavelength for resonance. Recently, it has been reported that dielectric nanoparticles can be a magnetic resonator as SRR. The magnetic field distributions in SRR and dielectric nanoparticle are shown in Figure- 3 (b) and (c). Figure - 3 (a) represents a single SRR and its dimensions.
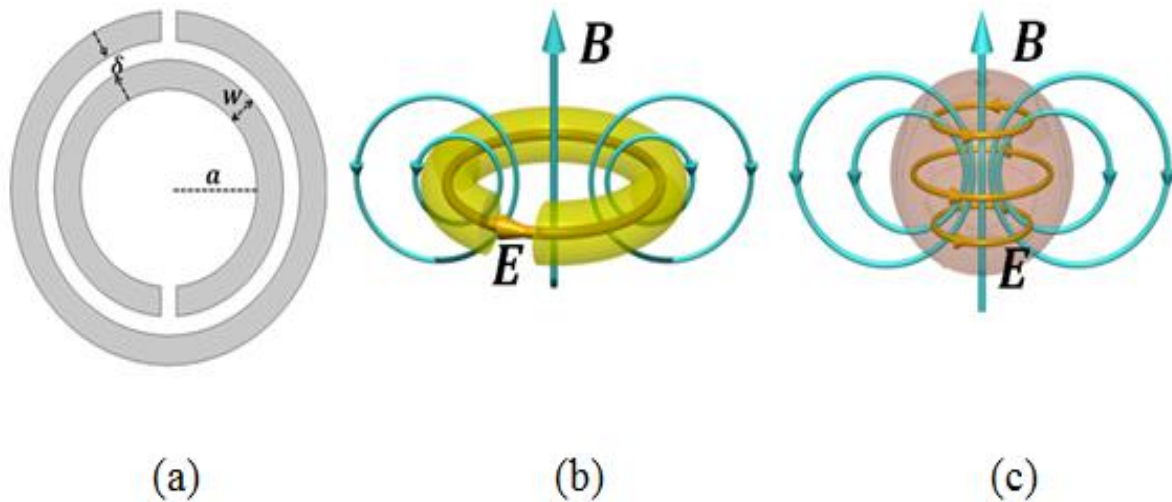
Figure 3 **(a) SRR, Magnetic Field distribution in (b) SRRs and (c) dielectric nanoparticle.**

Then effective relative magnetic permeability of the SRR medium can be expressed as,

$$\mu_r = 1 - \frac{F\omega^2(\omega^2-\omega_{om}^2)}{(\omega^2-\omega_{om}^2)^2+(\omega\xi)^2} + j\frac{F\omega^2\xi}{(\omega^2-\omega_{om}^2)^2+(\omega\xi)^2} \qquad (11)$$

where $F = \pi (a/p)^2$, a is the inner radius of the inner ring of SRR, p is periodicity of SRR, $\omega_{om} = c\sqrt{3p/\pi \ln(2wa^3/\delta)}$, the magnetic resonance frequency, w is the width of the rings, δ is the radial spacing between the rings, $\xi = 2pR'/a\mu_o$, the damping factor, R' is the metal resistance per unit length and μ_o is the absolute permeability. From the Equation (11) it can be said that there is frequency band at which real part of effective permeability become negative. For the loss-less case ($\xi = 0$), the frequency band at which relative permeability becomes negative can be expressed by the condition $\omega_{om} < \omega < \omega_{pm}$, where $\omega_{pm} = \omega_{om}/\sqrt{(1-F)}$.

By incorporating the metallic TWs and SRRs as shown in the Figure-2 (c), an electromagnetic metamaterial with double negativity can be achieved. Because of the fascinating properties metamaterial, no doubt, it will be the focus of the physics in near future.

GROWTH AND CHARACTERIZATION OF L-ALANINE SODIUM NITRATE (ASN) SINGLE CRYSTALS

L.Jothi Nirmal [*], S.Ajitha

Department of Physics, Nanjil Catholic College of Arts and Science, Kaliyakkavillai-629 153.

 *Corresponding author:jothinirmal96@gmail.com

ABSTRACT

Single crystals are used in condensed matter physics, material science etc. In the present study the preparation of L-Alanine Sodium Nitrate crystals was using slow evaporation method. The structural characterization of the grown crystal was done using X-Ray Diffraction (XRD).The LASN crystals belongs to the triclinic space group. The functional groups of the grown crystals were predicted by Fourier Transform Infrared Spectroscopy (FTIR) analysis. Optical transmittance of these grown crystals was analysed using UV- Vis-NIR studies.

Key Words: Slow evaporation technique, PXRD, FTIR, UV-Vis-NIR studies

1. INTRODUCTION

Nonlinear optical (NLO) crystals has emerged as one of the most attractive fields of current research in view of its vital applications in areas like optical modulation, optical switching, optical logic, frequency shifting and optical data storage for the developing technologies in telecommunications and in efficient signal processing [1].The development of highly efficient nonlinear optical (NLO) crystals for visible and ultraviolet region is extremely important for both laser spectroscopy and laser processing[2]. Optically active amino acids show high efficiency in optical second harmonic generation (SHG) and are promising candidates for laser and optical communication technology [3].

2. EXPERIMENTAL METHOD

Growth of L- Alanine Sodium Nitrate (LASN) crystals were carried out by slow evaporation technique. Analytical reagent (AR) grade Sodium Nitrate salt was used for the growth of L-Alanine Sodium Nitrate single crystals .Accordance with the solubility test suitable amount of Sodium Nitrate was weighted. The mixture of deionized water and Sodium Nitrate salt placed in a magnetic stirrer and is stirred well with applying mild temperature about 40°C .The stirring was continued until a homogeneous saturated solution was obtained. L-Alanine was added to the same solution was optimally covered using a thin paper sheet. Good quality transparent crystals were grown within 25 days.

Fig 1: Grown Crystal Of L-Alanine Sodium Nitrate Single Crystal

3. RESULTS AND DISCUSSION

Single crystal X-Ray Diffraction Analysis

The crystallographic parameters of L-Alanine Sodium Nitrate single crystals in the present case have been evaluated using powder XRD technique. The sharp peaks indicated the good crystalline nature of the L- ASN single crystals. The "X" PERT HIGH SCORE X-ray software was used for analysis of power XRD patterns well defined Bragg peaks are obtained at specific 2θ. Angles indicating that crystals are ordered.
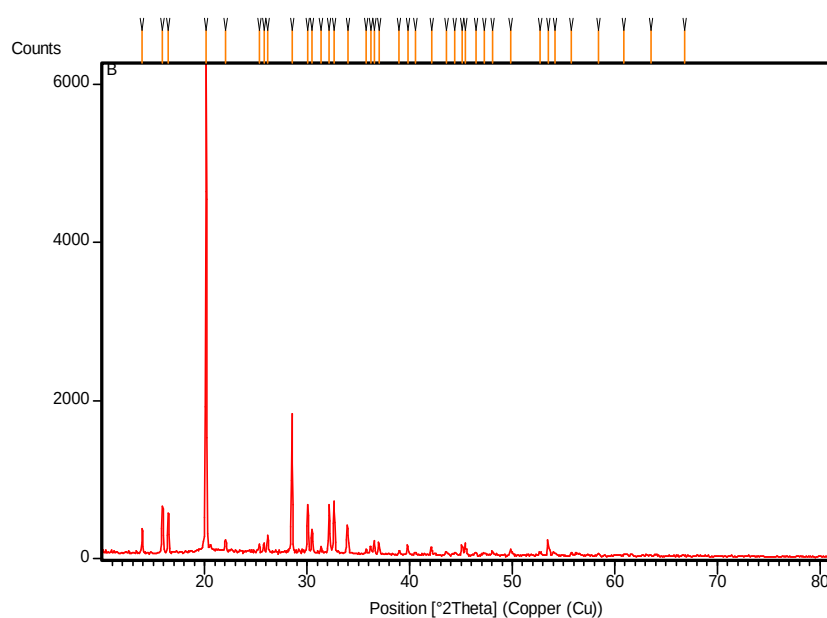
Fig 2:PXRD spectrum of L-Alanine Sodium Nitrate single crystal

Table 1 : Lattice Parameters of L-Alanine Sodium Nitrate single crystals

Crystal	L-Alanine Sodium Nitrate
Chemical formula	$C_3H_7No_2 . NaNo_3$
Crystal system	Triclinic
a($\acute{A}$)	10.83439 A^0
b($\acute{A}$.)	15.39174 A^0
c($\acute{A}$)	6.19978 A^0

Fourier Transform Infrared Spectroscopic Studies

In the present study, FTIR spectrum was recorded in order to qualitively analysed the presence of functional groups in L- Alanine Sodium Nitrate single crystals in the range 400cm^{-1} to400 cm^{-1} using Perkin Elmer grating infrared spectrophotometer.
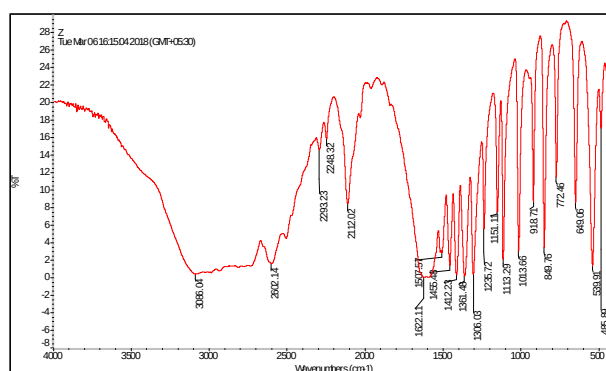
Fig 3:FTIR spectrum of L-Alanine Sodium Nitrate single crystal

Table 2: The functional groups assignments L-Alanine Sodium Nitrate single crystal

ABSORPTION WAVE NUMBERS cm^{-1}	ASSIGNMENT
3066	OH-stretching
2602	OH-stretching
2293	OH-stretching
2248	OH-stretching
2112	Over tones
1507	NH-plane bending
1361	CO_2 symmetric stretching
1306	C-O stretching
1236	C-O stretching
1151	C-CHO stretching
1013	C-CHO stretching
918	C-H out of plane bending
849	C-H out of plane bending
772	N-H out of plane bending
649	OCN deformation
539	OCN deformation

UV- Visible Spectral Analysis

UV visible study of the grown crystal was carried out by Lambda-35 UV visible spectrometer in a range 200-500nm. Optically clear L-Alanine Sodium Nitrate single crystal shows lower cut-off wavelength at around 299nm.

The band gap was calculated using the formula,

$$Eg=hc/\lambda$$

The optical band gap is found to be 299nm. For L-Alanine Sodium Nitrate single crystals. The optical transmittance spectrum of L-Alanine Sodium Nitrate single crystals is shown in figure 4.
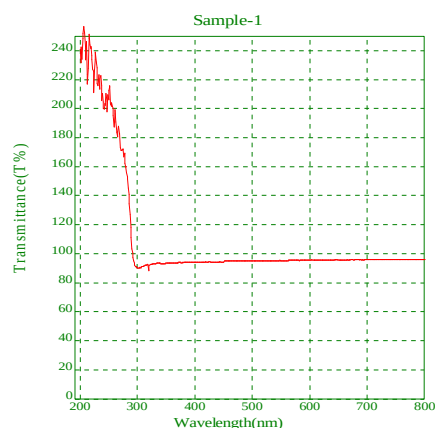
Fig 4 :UV-Visible spectrum of transmittance of L-Alanine Sodium Nitrate single crystal

4. CONCLUSION

Single crystals of L-Alanine Sodium Nitrate single crystal were grown by slow evaporation technique. Powder X-ray diffraction studies were carried out for L-Alanine Sodium Nitrate single crystals and the lattice parameters were calculated. PXRD analysis revealed that the grown crystals belong to triclinic system. The presences of functional group for L-Alanine Sodium Nitrate single crystals were studied. From FTIR spectrum we can confirm the structure ot the L-Alanine Sodium Nitrate single crystals to have both the Alanine and Sodium Nitrate molecules. The UV-visible absorption spectra shows lower cut-off wavelength at around 299nm.The optical band gap is found to be 4.169 eV.

REFERENCES

1. Marder, S.R.; Perry, J.W., Yakymyshyn, C.P. ,(1994) Chem. Mater., Vol 6, pp 1137.

2. Chemla, D.S.; Zyss, J. (1987), Nonlinear Optical Properties of Organic Molecules and crystals, Academic Press, New York,.

3. Frazier C.C, Cockerhamn, M.P, Chauchard. E.A., Lee C.H.,(1987) J. Opt .Soc. Am. Vol 4, pp 1899.

4. Gunter.P, Bosshard. Ch, Sutter. K, Arend. H, Chapuis. G, Twieg. R.J, Dobrowolski. D, (1989) ,Appl. Phys. Lett., Vol 50, pp 486.

ROASTED PADDY CHAFF AS SOLAR SELECTIVE MATERIAL FOR SPIRAL CONCENTRATORS - A SELECTIVE ANALYSIS

J.Packiam Julius[1*], T.K.Jayaleka[1],D.Usha [2]

[1]Department of Physics,Pioneer Kumaraswamy College,Nagercoil
[2]Department of Physics and Research Centre,Women's Christian College, Nagercoil,
(Affiliated to Manonmaniam Sundaranar University,Abishekappathi, Tirunelveli)
[*] Corresponding author:dr.j.pjulius@gmail.com

ABSTRACT

This study has been directed towards the study of selectivity analysis of absorbers that were used is spiral concentrating type solar cooker. New attempts were made to study the optical efficiency. Spray painting technique has been adopted for coating the selective material on the absorber. The efficiency was compared with other black coatings. It has been concluded that the spiral concentrator has the maximum efficiency with roasted paddy chaff as selective coating material.

Key words: Spiral concentrator, Selectivity

1. INTRODUCTION

In concentrating type solar cookers, the materials used for coating the absorbers are very important Selectivity is the ratio of solar radiation (absorption) to thermal infrared radiation (emission). The optimum values of absorption is 0.9 and the thermal emission is 0.10. [1,2,3]. The thickness of the coating material also decides the optical performance of the concentrator [4]. This absorber coating material is cost effective, eco friendly and efficient.

2. EXPERIMENTAL METHODS

Roasted Paddy chaff taken in a container was ground and made into a powder. It was mixed with 7% PVA and water. A colloidal solution was the resultant. It was stirred in a magnetic stirrer and sprayed on the absorber which were two aluminum & Stainless vessels. Water heating tests were carried out and the results were compared with other commercially available materials A Spiral concentrating type solar cooker was used for the investigation [5, 6,7]

3. RESULS AND DISCUSSION

The optical efficiency of the concentrator with roasted paddy chaff coating for aluminum and stainless steel absorber are tabulated

Table 1.Optical efficiency of stainless steel absorber

Temp region ºC	q loss Watt	q gain Watt	Input Ac Id	Optical efficiency %
30-38	10.3	269	618	45
38-46	25.9	344	627	44
46-52	40.9	368	633	48
52-60	56.29	254	635	47.5

60-68	70.80	240	637	46
68-76	83.85	212	635	48
76-84	83.85	212	635	48
84-91	116.87	125	619	42

Table 2.Optical efficiency of Aluminum Absorber

Temp region ºC	q loss	q gain	Input Ac Id	Optical efficiency %
30-38	16.8	250	812	50.1
38-46	29.4	330	716	40.5
46-52	50.7	350	628	42.3
52-60	64.5	207	635	44.1
60-68	70	200	645	44.1
68-76	72	211	600	46.2

Tables 1 & 2 show that roasted paddy chaff with aluminum absorber was more effective than stainless steel vessel. When the coating becomes thicker the efficiency was found to increase.

4. CONCLUSION

The roasted paddy chaff with aluminum absorber was more effective than stainless steel vessel and when the coating becomes thicker the efficiency was found to increase. It was concluded from the investigations that aluminum absorber with roasted paddy chaff retained the absorption coefficient.

REFERENCES

1. John f Glare (1998) Companion four analytic methods for calculation of irradiance in

    integrating spheres. J. Opt. Soc.Am

2. Rubin Powels (1999) Solar Energy Vol 66 PP 267

3. Sasa R. Pavlovi p(20160 design and Somulation coil Thermal Science no 4 Pp 137-1397.

4. Shib H(2008) process techn. Pp119.

5. Jeyaleka T.K (2017) Packiam Julius spectral properties of Ash for use as solar selective

    coating IJSRST PP206

6. Jayaleka T.K Packiam Julius (2017) optical efficiency of lamp black as solar selective

    Surface IJSRST PP197.

7. Trotter (1980) Spectral selectivity Applied optics Vol 19.No 5 PP71

SrO$_2$ NANOPARTICLES: STRUCTURAL, OPTICAL AND ANTIMICROBIAL STUDIES

S.Ashmitha Sailish, V.Shally*, M. Priya Dharshini, Sr.Gerardin Jayam
Research Department of Physics, Holy Cross College (Autonomous), Nagercoil-629004.

*Corresponding Author   E-mail id: **shallyregin05@gmail.com**

ABSTRACT

Strontium peroxide nanoparticles were prepared using Sr(NO$_3$)$_2$ and NaOH by simple precipitation method and the products were characterized bypowder X-ray diffraction (PXRD) and UV-DRS spectroscopy. The PXRD studies showed a tetragonal body centered structure for SrO$_2$ and is confirmed from JCPDS File No.07-0234. The UV-Vis spectra of SrO$_2$ showed a strong absorption peak at 310 nm. The SrO$_2$ nanoparticles were tested for antibacterial activity against bacteria strains and fungus.

1. INTRODUCTION

Strontium peroxide SrO$_2$ is one of the important alkaline oxides[1].It is a well-known industrially important compound and component in clay, special glass and ceramic products[2]. Strontium develops vivid colors that can improve the surface of high viscous zirconium fireproof ceramics and glazes[3]. SrO$_2$ is used as starting component in making oxide-coated cathodes for electric vacuum devices[4].SrO$_2$ is used as a feedstock to manufacture other strontium compounds, such as strontium chromate, strontium chloride, metal strontium and others. The picture tube glass in television contains about eight percent of strontium oxide[5]. SrO$_2$ grains are used in various pyrotechnic devices, flares, and tracer bullets[6-13]. SrO$_2$ is a white powder with a specific gravity of 4.56 that decomposes in water. It is made by the reaction of hydrogen peroxide with strontium oxide and is used primarily in pyrotechnics and medicines[14]. The chemical properties of strontium are intermediate between those of calcium and barium. Strontium is more reactive than calcium, less reactive than barium[15].

In the present work, strontium peroxide nanoparticles are synthesized by simple precipitation method.The preparation process has advantages of simple technology, cheap, good yield, homogeneity, low temperature and short preparation cycle. Nanoparticles with smaller particle size have been reported to show good antimicrobial activity. While growing in medium amended with nanoparticles, the bacterial population growth can be inhibited by specific nanoparticle interactions. Generally, bacterial strains are thought to present a major public health problem. Hence in this present work, antimicrobial activity of as-prepared

strontium peroxide nanoparticles is tested after the structure and optical properties are determined from the PXRD data and the UV-DRS spectroscopy respectively.

2. EXPERIMENTAL TECHNIQUES

Uniform particles are usually prepared via homogeneous precipitation reactions, a process that involves the separation of the nucleation and growth of the nucleito grow uniformly by diffusion of solutes from the solution to their surface until the final size is attained.The strontium peroxide nanoparticles are synthesized by precipitation method.Strontium nitrate was used as a precursor to prepare pure SrO_2 nanoparticles.For this, 0.45M of Strontium nitrate was taken and was dissolved in 100ml distilled water and stirred for half an hour.On the other hand, 2M of sodium hydroxide was dissolved in 100ml distilled water and stirred for half an hour and heated up to 70°C. Strontium nitrate solution is added dropwise to the sodium hydroxide solution. SrO_2 precipitate was washed with water five times to remove the impurities.It was also washed with ethanol one time to remove the unwantedresidues.At100°C,the solution was heated in hot plate until the water evaporates. SrO_2 nanoparticles thus formed was white in colour.

The structural analysis of was performed by recording the powder X-ray diffraction (PXRD) spectrum using X-ray diffractometer (PANalytical X'Pert Pro) with Cu-K$_\alpha$ as the radiation source (wavelength: 1.54056 Å) over the 2θ range of 10 ° to 90 °. The UV–DRS absorption spectra of the sample were recorded in the wavelength range of 100 to 1000 nm using a Shimadzu UV 2401 spectrophotometer in diffuse reflectance mode. Antimicrobial activities of the samples were determined by agar well diffusion method.

3. RESULTS AND DISCUSSION

X-ray powder diffraction: From the PXRD data (Fig.1), the as-prepared samples shows a tetragonal body centered structure with cell parameters a= 3.536Å, c= 6.645Å and cell volume 83.10(Å)^3 and are in good agreement with the JCPDS File No.07-0234. The average grain size of strontium oxide nanoparticles is estimated to be 32.7002 nm using the Scherrer equation

$$D = \frac{0.9\lambda}{\beta \cos \theta} \ nm$$

where, D is the mean size (diameter) of the crystallite, β is the full width half maximum intensity (in radians), λ is the wavelength of X-ray radiation used (1.54056Å) and 2θ is the angle at which maximum intensity was observed.

Using the formula $\delta = 1/D^2$, the average dislocation density is found to be $\delta = 3.9246 \times 10^{15}$ lines/m^2.
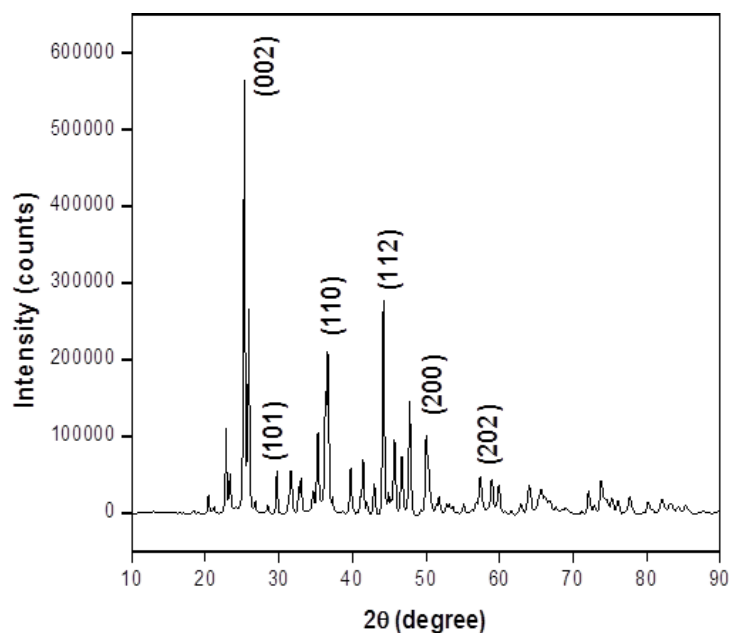
Fig.1. PXRD of SrO$_2$ nanoparticles

UV-DRS results: The absorbance of the as prepared SrO$_2$ nanoparticles is about 310 nm which shows blue shift indicating the nanocrystallinity of the as-synthesized particles.
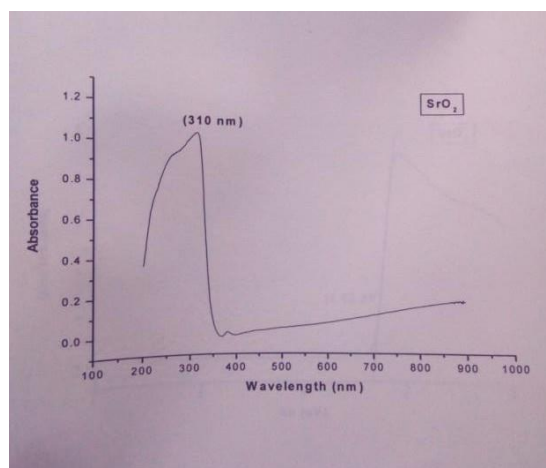
Fig.2. UV-DRS spectra of SrO$_2$ nanoparticles

Antimicrobial Activities: Fresh bacterial culture of 0.1ml having 108 CFU was spread on nutrient agar plate using swab. Wells of 6 mm diameter were punched off into medium with sterile cork borer and filled with 50µl of sample (suspended in dimethyl

sulfoxide) by using micro pipette in each well in aseptic condition. Plates were kept in a refrigerator to allow pre-diffusion of extract for 30 minutes. Further, the plates were incubated in an incubator at 37^0C for 24 hours and the antimicrobial activity (Fig.4 and Fig.5) was evaluated by measuring the zone of inhibition.
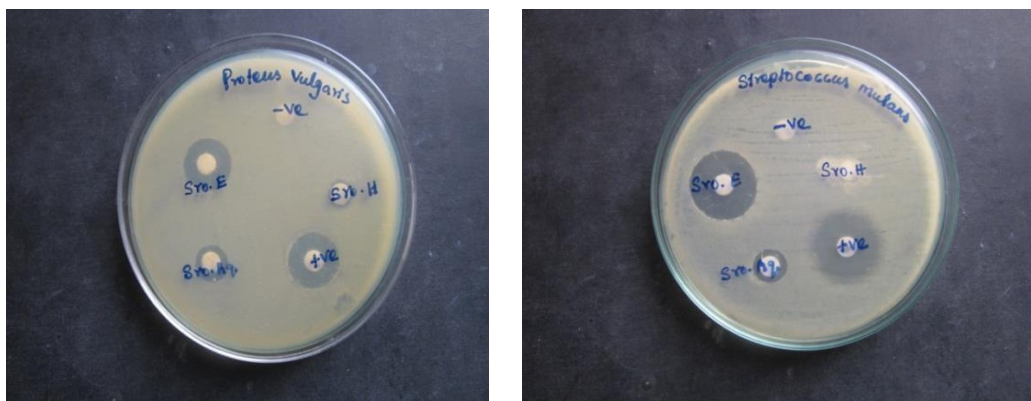
Fig.4. Antibacterial activity of SrO$_2$ nanoparticles
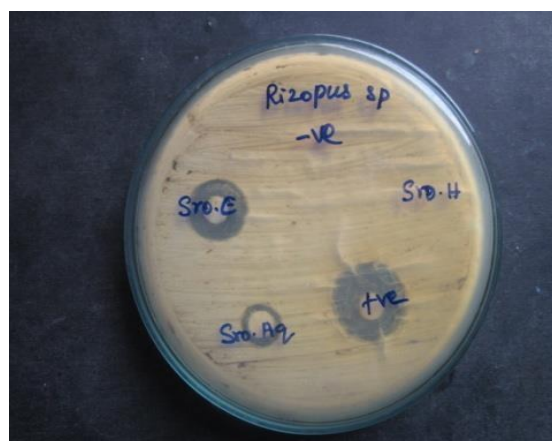
Fig.5. Antifungal activity of SrO$_2$ nanoparticles

The zone of inhibition for streptococcus mutans is 22 mm and for proteus vulgaris, it is around 10 mm. For rizopus fungus, the zone of inhibition is 8 mm.

4. SUMMARY AND CONCLUSION

The pure strontium oxide nanoparticles are synthesized by simple precipitation method. From the PXRD data the as- prepared sample shows a tetragonal body centered structure and the cell parameters are in good agreement with the JCPDS File No.07-0234. The blue shift as observed from UV-DRS studies confirms the nanosize of the particles. The antibacterial activity of as-prepared strontium oxide nanoparticles shows good antimicrobial activity so they can be used as antibacterial agents.

REFERENCES

1. J. S. Lee, Y. S. Lee, T. W. Noh, S.Nakatsuji, H. Fukazawa; *Phys. Rev.* B70 085103 (2004).

2. M. V. R. Rao, V. G. Sathe, D.Sornadurai, B. Panigrahi and T.Shripathi: *J. Phys. Chem. Solids;* 62797–806 (2001).

3. K. Maiti and R. S. Singh: *Phys. Rev*. B71 161102 (2005).

4. Y. Z. Yoo, O. Chmaissem, S. Kolesnik,B. Dabrowski, M. Maxwell, C. W.Kimball; *J. Appl.Phys*.97 ,103525(2005).

5. H. Funakubo, T. Oikawa, N. Higashi; *J.Crystal Growth* 235 401–406 (2002).

6. Q. Gan, R. A. Rao, C. B. Eom, L. Wuand F. Tsui; *J. Appl. Phys.* 85 ,5297–5299(1999).

7. FengJin ; Yan Liu ; Christopher M.Day; *Carbon'* 45, (3) 587–593 (2007).

8. Y. Hu, O. K; Tan, J. S. Pan and X. Yao, *J. Phys Chem. B*, 108 (30), 11214–11218 (2004).

9. B. Ulrici; W. Ulrici; N. N. Kovalev, *Sov.Phys.Sol. St*. 17, 2305 (1976).

10. Lin-gun Liu; William A. Bassett, *Journal of Geophysical Research*, 78,PP. 8470-8473, (1973).

11. R. J. Kearney, M. Cottini, Grilli,G.Baldini; *Basic Solid State Physics*64, 1,49–56, (1974).

12. Madelung,O;Rössler.U;Schulz,M. *TheLandolt-Börnstein-Database-*CASRegistryNumbers

13. M. Yoshimura, O. Asai, W.-S. Cho, J. Alloy. Comp. 265 (1998) 132–136

14. K. Walter, Science and Technology Review (Oct. 18, 2010).

15.Er.Rakesh Rathi, Nanotechnology: Technology Revolution of 21[st]century,First Edition (2009).

POWDER XRD AND PHOTOLUMINESCENCE STUDIES OF CdS-ZnS NANOCOMPOSITES

S.V. Suji, M. Valli Saroj, M. Priya Dharshini*, V. Shally, Sr. Gerardin Jayam

Research Department of Physics, Holy Cross College (Autonomous), Nagercoil-629004.

*Corresponding author: priyadharshini065@gmail.com

ABSTRACT

Pure CdS and CdS-ZnS nanocomposites are prepared through co-precipitation method and their structural and photoluminescent properties are analyzed. The average grain size of the synthesized pure CdS nanoparticles is around 46nm.In the CdS-ZnS nanocomposites, the observed peaks of ZnS matched well with that of the rhombohedral structure (JCPDS File No.89-2350) and the peaks of CdS observed correspond to that of hexagonal structure (JCPDS File No. 80-0006). No impurity peaks are identified in the PXRD pattern of the samples which shows the purity of the sample. The green luminescence demonstrates the good quality of the prepared products. The decrease in the intensity of PL spectrum indicates that the synthesized CdS-ZnS nanocomposites can be used as photocatalysts and antimicrobial agents.

1.INTRODUCTION

Nanocomposites of metal sulphides have been used extensively as catalysts, sensors, solar cells, photo detectorsand light emitting diodes[1]. Wet chemical synthetic methods like homogeneous precipitation, sonochemical and sol-gel methods have been employed for the synthesis of metal sulphide nanocomposites for their simplicity and good yield [2]. Among the group II-VI compound semiconductor nanoparticles, CdS and ZnS are the most promising materials. CdS, one of the most studied photoluminescent nanomaterial with a direct bandgap of 2.42 eV (515 nm). ZnS is a good material for detecting ultraviolet due to its bandgap of 3.68 eV (345 nm) and high sensitivity. Both the materials have potential applications in optics, optoelectronics and solar energy [3, 4]. In the present work, pure CdS nanoparticles and CdS-ZnS nanocomposites are prepared through co-precipitation method and the structural, and photoluminescent properties of these samples are investigated.

2. EXPERIMENTAL METHOD

Synthesis

Pure cadmium sulphide nanoparticles were synthesized using co-precipitation method. 0.5M of cadmium acetate and 0.5M of sodium sulphide were dissolved in double distilled water separately and mixed together. Ammonium hydroxide solution was added and the CdS precipitate was washed thoroughly. The solution was heated in hot air oven At 100°C for 24 hours. Then it was calcined at 500°C for 4 hours.

Preparation of CdS-ZnS nanocomposites

Cadmium acetate (0.5M), zinc acetate (0.5M), and sodium sulphide (0.5 M) solutions were stirred separately. Cadmium acetate solution was added dropwise to the sodium sulphide solution followed by zinc acetate solution and stirred magnetically for 30 minutes. Ammonium hydroxide solutionwas added andthe precipitate obtained was washed using double distilled water and ethanol. The final product was dried in hot air oven at 100°C for 6 hours and was calcined at 500°C for 2 hours. The prepared sample was finely powdered in agate mortar and thus CdS-ZnS nanocomposites were obtained.

CHARACTERIZATION

The structural analysis of pure CdS nanoparticles and CdS-ZnS nanocomposites was performed by recording the powder X-ray diffraction (PXRD) spectrum using X-ray diffractometer (PANalyticalX'Pert Pro) with Cu-K_α as the radiation source (wavelength: 1.54056Å). Photoluminescence (PL) studies were carried out using a photoluminescence spectrophotometer (Varian Cary Eclipse) and the spectra were recorded at a scan rate of 600 nm/min using an excitation wavelength of 325 nm.

3. RESULTS AND DISCUSSION

Powder X-Ray Diffraction

The characteristic powder X-Ray diffraction pattern of synthesized CdS nanoparticles and CdS-ZnS nanocomposites are shown in Fig.1.and Fig.2.respectively.
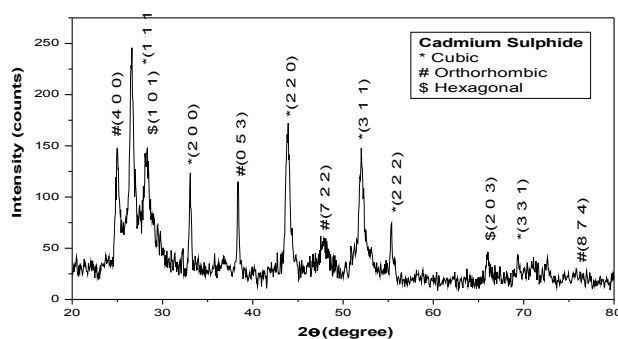
Fig.1. PXRD pattern of the synthesized pure CdS nanoparticles
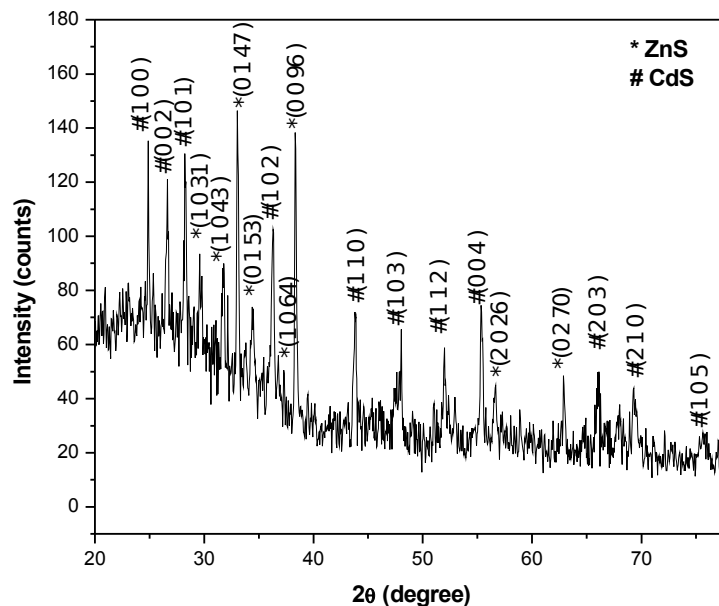
Fig.2. PXRD pattern of CdS-ZnS nanocomposites

The average grain size of the pure CdS nanoparticles is found out from the powder XRD pattern using Scherrer equation:

$$D = \frac{0.9\lambda}{\beta cos\theta} \; (nm)$$

where,

λ is the wavelength of X-Ray

β is the full width half maximum

θ is the Bragg's angle for the peak.

The average grain size of the synthesized pure CdS nanoparticles is around 46nm.Cubic (JCPDS File No.65-2887), orthorhombic (JCPDS File No.47-1179) and hexagonal (JCPDS File No.89-2944) structures are identified in the PXRD pattern of the synthesized CdS nanoparticles. No impurity peaks are observed in the PXRD pattern.

Fig.2 shows the PXRD pattern of the CdS-ZnS nanocomposites. The observed peaks of ZnS matched well with that of theJCPDS File No.89-2350 and the peaks of CdS observed corresponding to that ofJCPDS File No. 80-0006. No impurity peaks are identified in the PXRD pattern of CdS-ZnS nanocomposites which shows the purity of the sample. The polycrystalline nature of the nanocomposites is observed from the PXRD pattern. Thus the structure of CdS is found to be hexagonal and that of ZnS is found to be rhombohedral. The peaks assigned to CdS are in good agreement with that obtained by Tariq Abdulhamid Abbas et al. [5]. Similarly the peak assignment of ZnS is similar to that obtained by Nida Qutub [6].

Photoluminescence Analysis

Photoluminescence (PL) studies for the synthesized nanostructures were carried out using a photoluminescence spectrometer (Varian Cary Eclipse) and the emission spectra were recorded at an excitation wavelength of 325 nm.
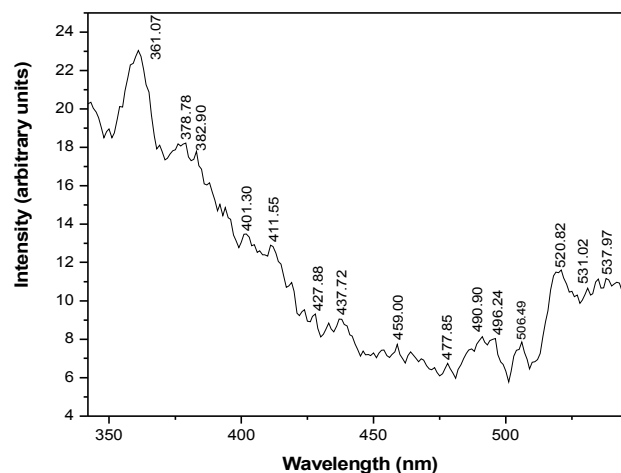
Fig.3. Room temperature PL emission spectrum of pure CdS nanoparticles
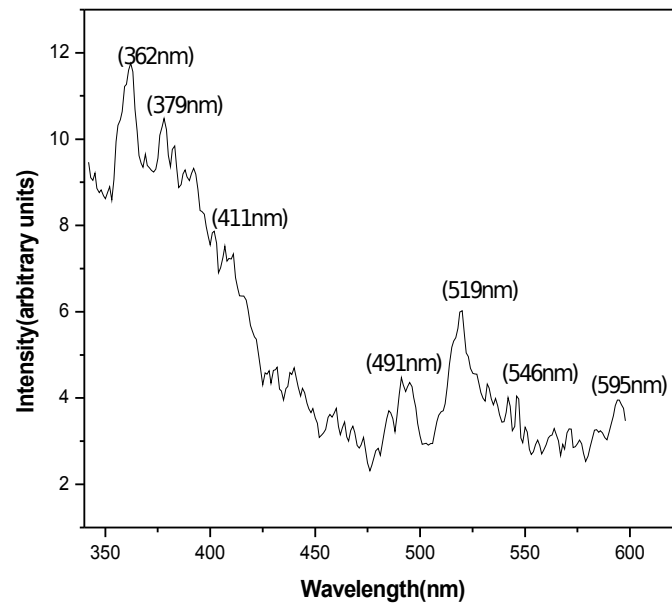
Fig.4. Room temperature PL emission spectrum of CdS-ZnS nanocomposites

The visible emission from CdS nanocrystalline particles is due to a transition of a photo-generated electron from the conduction band to a deeply trapped hole. The rate of this hole-trapping must be much faster than the radiative recombination rate of the excitonic emission. Because of the large surface-to-volume ratio of nanoparticles, efficient and fast trapping of photo-generated holes at surface sites can be expected. Trapping of a photo-generated hole at the surface is also in agreement with the size-dependence of the emission intensities [7].

The PL emission peaks in both Fig.3. and Fig.4. have been observed covering the whole 340-550nm visible region of the electromagnetic spectrum.An excitation wavelength of 325nm is used in both the samples.The green luminescence demonstrates the good quality of the prepared nanoparticles. Such low energy emissions are assigned to the surface states. The density of surface states in the nanocrystals would increase with a decrease in the size ofcrystallites of the prepared nanocrystals, due to the increased surface to volume having smaller crystallites. This would reduce the probability of excitonic emission via non-radiative surface recombination. B.Srinivasa Rao et.al reported the photoluminescence (PL) spectrum of CdS nanoparticles with excitation wavelength of 328nm and the PL peak is about 410nm. The luminescence from the surface states (around 800nm) has also been observed. Photoluminescence analysis in 400-650nm emission wavelengths shows the 'well known' green emission band in CdS nanoparticles[8].The PL emission spectrum of CdS-ZnS nanocomposites (Fig.4) which shows prominent peaks at 362 nm, 379 nm, 411 nm, 491 nm, 519 nm, 546 nm and 595 nm. The sample exhibits a strong ultra violet emission band near 362 nm and weak bands are detected in the UV-Vis region [9].The intensity of the PL peak is decreased when composite of ZnS is formed.

4. CONCLUSION

Pure CdS nanoparticles and CdS-ZnS nanocomposites are synthesized using precipitation method. PXRD confirmed the synthesis of the synthesized nanoparticles and composites. From the PL analysis, it is obvious that for the efficient visible emission of the samples, a step must be involved in which the photo-generated holeis trapped efficiently somewhere in the particle. The green luminescence demonstrates the good quality of the prepared products. The decrease in the intensity of PL spectrum indicates that the synthesized CdS-ZnS nanocomposites can be used for studying photocatalytic and antibacterial activities in future.

REFERENCES

[1]   Olumide Oluwole Akinwunmi, Gabriel O. Egharevba, Ezekiel Oladele Bolarinwa Ajayi, Synthesis and Characterization of CdS, ZnS and Cd-ZnS Nanoparticles Embedded in Polystyrene, Journal of Modern Physics, (2014), 5: 257-266.

[2]   M. Sreenivas, G. S. Harish, P. Sreedhara Reddy, Synthesis and Characterization of Mn, Ce Co-Doped CDS Nanoparticles Synthesized Via Co-Precipitation Method, International, Journal of Modern Engineering Research, (2014), 4(9): 10-16.

[3]   Y. Kashiwaba, J. Sato, T. Abe, Emission of lights of various colors from p-CdS:Cu/n-CdS thin-film diodes, Applied Surface Science, (2003), 212-213: 162-165.

[4]   A.I. Iorgu, D. Berger, L. Alexandrescu, B. S. Vasile, C. Matei, Synthesis of photoluminescent pure and doped cadmium sulphide by reverse micro emulsion method, Chalcogenide Letters, (2013), 10(12): 525- 531.

[5]   Tariq Abdulhamid Abbas, Jala Muhamed Ahmad, The Effect of Copper Doping on some Physical Properties of Chemical Sprayed CdS Thin Films, Journal of Electron Devices, (2013), 17:1413-1416.

[6]   Nida Qutub, Synthesis and Characterization of nanomaterials, Ph.D. Thesis, Aligargh Muslim University, India, (2013), 139.

[7]   Feroz A. Mira, Indrajit Chattarjeeb, Aijaz A. Darc, K. Asokand, G.M. Bhataa, "Preparation and characterization of cadmium sulphide nanoparticles" , (2015), 1:1240–1244.

[8]   B. Srinivasa Rao, B. Rajesh Kumar, V. Rajagopal Reddy, T. Subba Rao, "Preparation and characterization of CdS nanoparticles by chemical co-precipitation technique", Chalcogenide Letters, (2011), 8(3):177 – 185.

[9]   T.R. Heera and V. Balasubramanian, NiS/CdS Core-shell Embedded Polyaniline Composite: Synthesis and Characterization, Biosciences Biotechnology Research Asia, (2014), 11:349-356.

[10]   Shaik Raziya, Bokka Durga, Santoshi G Rajamahanthe, Boddeti Govindh, Nowduri Annapurna, "Synthesis and Characterization of CdS Nanoparticles", (2016), 4: 50-57.

STABILITY ANALYSIS OF CUBIC QUINTIC SEPTIC DUFFING OSCILLATOR

S. K. Remmi[a], M. M. Latha[b*]

[a] Department of Physics, Women's Christian College, Nagercoil - 629 001, India (Affiliated to Manonmaniam Sundaranar University, Abishekapatti, Tirunelveli- 627 012, Tamilnadu, India)
[b]Department of Physics, Women's Christian College, Nagercoil 629 001, India
* Corresponding author: lathaisaac@yahoo.com

ABSTRACT

This paper investigates the local stability of Cubic Quintic Septic equation governing Duffing oscillator describing a 3-spring system arranged in a critical geometric parameter. The practical stability properties using Lyapunov function is examined which shows that the system is asymptotically stable around the equilibrium points.

1. INTRODUCTION

Duffing oscillators are nonlinear in nature and have received remarkable attention in recent decades to study and research due to the basis for many mathematical models of different systems and variety of their engineering applications. The Cubic Quintic Septic Duffing equation can as well be used to model the nonlinear spring-mass system with stiffness and damping coefficients [1]. The sudden change in the values of the coefficients can be represented as a piecewise linear or nonlinear function. To the best of our knowledge from literature, in the last three decades, much attention has been paid to the investigation of stability of solutions of nonlinear differential equations of higher orders. Stability of a dynamical system with or without forcing units is a fundamental requirement for its practical value, typically in most real-world applications. Strictly speaking, stability means the system output is in the equilibrium state.

The basic concept of stability emerged from the study of an equilibrium state of a mechanical system. The Lagrangian formulation of stability theorem states that if the potential energy of a conservative system subject to some simple constraints, has a minimum, then this equilibrium position of the system is stable [2, 3]. The evolution of the fundamental concepts of system and trajectory stabilities then went through a long history, with many fruitful advances and developments, until the celebrated Ph.D. thesis of A. M. Lyapunov, The General Problem of Motion Stability, finished in 1892 [4]. This monograph is so fundamental that its ideas and techniques are virtually leading all kinds of basic research and applications regarding stabilities of dynamical systems today. In fact, the dynamical behavior analysis and the controllers design in modern physics and in engineering systems

uses the principles of Lyapunov's stability theory.

Local stability analysis tells us how a system behaves near an equilibrium point where as the Lyapunov stability analysis can be used to determine the stability of the system both near and far from the equilibrium point. A full picture of the dynamics can be generally determined by the local stability analysis combined with Phase-plane analysis, but things become much more difficult in higher-dimensional spaces.

This paper is devoted to a brief description of the local as well as Lyapunov stability of the fixed points of free nonlinear Cubic Quintic Septic Duffing equation under Quasi Zero Stiffness condition.

2. PROBLEM FORMULATION AND ANALYSIS

Fixed Points And Local Stability Analysis

A conservative Duffing equation described by a second order ordinary differential equation of mass holding odd nonlinear forces truncated to seventh power is considered as

$$\ddot{x}(t) + \xi\dot{x}(t) + \omega_0^2 x(t) - \beta x^3(t) + \gamma x^5(t) - \delta x^7(t) = F cos\Omega t, \tag{1}$$

where ξ is the damping coefficient, $\alpha = \frac{k}{m}$ is the linear coefficient and $\beta = \frac{k}{md_0^2}$, $\gamma = \frac{3k}{4md_0^4}$, $\delta = \frac{15k}{24md_0^6}$ are the cubic, quintic and septic power coefficients respectively. Ω is the external excitation frequency, F is the amplitude of the external force. This equation is termed as Cubic Quintic Septic Duffing equation which normally describes the real dynamics of the three-spring model under Quasi Zero Stiffness condition. This system exhibits many different qualitative phenomena, depending on the linear and nonlinear parameters. The presence of nonlinear stiffness β, γ, δ gives rise to nontrivial fixed points and affects their stability.

The unforced and damped Cubic Quintic Septic Duffing oscillator from Eq. 1 is given by,

$$\ddot{x} + \xi\dot{x} + \alpha x - \beta x^3 + \gamma x^5 - \delta x^7 = 0. \tag{2}$$

From Eq. 2, we obtain the autonomous dynamical system,

$$u = \dot{x}, \dot{u} = -\xi\dot{x} - \alpha x + \beta x^3 - \gamma x^5 + \delta x^7. \tag{3}$$

From the condition $u = \dot{u} = 0$, the system yields

$$\dot{x}_f = 0, -\xi\dot{x}_f - \alpha x_f + \beta x_f^3 - \gamma x_f^5 + \delta x_f^7 = 0. \tag{4}$$

where $(x_f, \dot{x}_f)$ denotes fixed points. Therefore, at the fixed points $\dot{x}_f = 0$ and x_f satisfies

$$x_f[\alpha - \beta x_f^2 + \gamma x_f^4 - \delta x_f^6] = 0. \tag{5}$$

In the case of $\alpha\beta\gamma\delta > 0$, there is only one trivial fixed point $(x_f, \dot{x}_f) = (0,0)$. In the case of $\alpha\beta\gamma\delta < 0$, there are six nontrivial fixed points in addition to the trivial one. The nontrivial fixed points are $(x_f, \dot{x}_f) = (x_{1f,2f\pm}, 0), (x_f, \dot{x}_f) = (x_{3f,4f\pm}, 0)$ and $(x_f, \dot{x}_f) = (x_{5f,6f\pm}, 0)$. The local stability of these fixed points is now examined by introducing small perturbation $x(t) = x_f + \Delta x(t), (|\Delta x| << 1)$ and $\dot{x}(t) = \dot{x}_f + \Delta\dot{x}(t), (|\Delta\dot{x}| << 1)$ into the system that changes the Eq. 3 to

$$\Delta\dot{x} = \Delta X, \Delta\dot{X} = -[\alpha + 3\beta x_f^2 - 5\gamma x_f^4 + 7\delta x_f^6]\Delta x - 2\xi\Delta X. \tag{6}$$

The Jacobian matrix for the system (6) is given by,

$$J = \begin{pmatrix} -\lambda & 1 \\ -\alpha + 3\beta x^2 - 5\gamma x^4 + 7\delta x^6 & -2\xi - \lambda \end{pmatrix}$$

Eq. 6 can be rewritten as the second-order system of the variable

$$\Delta\ddot{x} + (\alpha - 3\beta x^2 + 5\gamma x^4 - 7\delta x^6)\Delta x + 2\xi\Delta\dot{x} = 0 \tag{7}$$

and the corresponding characteristic equation is

$$\lambda^2 + 2\lambda\xi + \alpha - 3\beta x^2 + 5\gamma x^4 - 7\delta x^6 = 0. \tag{8}$$

The solution of this equation gives the eigen values λ_1 and λ_2 that determine the stability of the fixed points. The dependence of the stabilty of the above system whose natural frequency ω_n on ξ is examined.

Lyapunov Function

The most important type of stability of differential equation concerning near to a point of equilibrium is discussed by the theory of Lyapunov. The Lyapunov technique determines the stability near and far from the equilibrium point. Lyapunov's

method is based on the function which decrease in some neighbourhood of the equilibrium point. At the equilibrium point function is minimum and the fixed point is stable. Such function with this property is called as Lyapunov function.

In mechanical systems with friction, the total energy is often a Lyapunov function. The total energy of the system is obtained as

$$E = \alpha\frac{x^2}{2} - \beta\frac{x^4}{4} + \gamma\frac{x^6}{6} - \delta\frac{x_8}{8} + \frac{1}{2}mv^2. \tag{9}$$

The total energy is a positive function which means E is zero at the equilibrium point and increasing away from this point.

Now consider

$$\dot{E} = \frac{\partial E}{\partial x}\frac{dx}{dt} + \frac{\partial E}{\partial v}\frac{dv}{dt} \tag{10}$$

$$= -\xi\dot{x}^2 < 0. \tag{11}$$

since E decreases everywhere except at the equilibrium point itself.

3. RESULTS AND DISCUSSION

As the damping ratio ξ changes, the eigenvalues of the characteristic equation change. Setting $\alpha = \omega_n{}^2$, the dependence of the stability on ξ is examined:

1) $\xi < -\omega_n$.There are two positive eigen values and the trivial fixed point is an unstable node, as shown in Fig. 1(a).

2) $-\omega_n < \xi < 0$. There are complex conjugate eigen values with a positive real part and the trivial fixed point is an unstable focus, depicted in Fig. 1(b), self-excited oscillation is produced.

3) $\xi = 0$. There are pure imaginary complex conjugate eigen values and since the trivial fixed point is a centre, illustrated in Fig. 1(c), x is oscillatory with no damping.

4) $0 < \xi < \omega_n$. There are complex conjugate eigen values with a negative real part and because the trivial fixed point is a stable focus, shown in Fig. 1(d), x is oscillatory and damped.
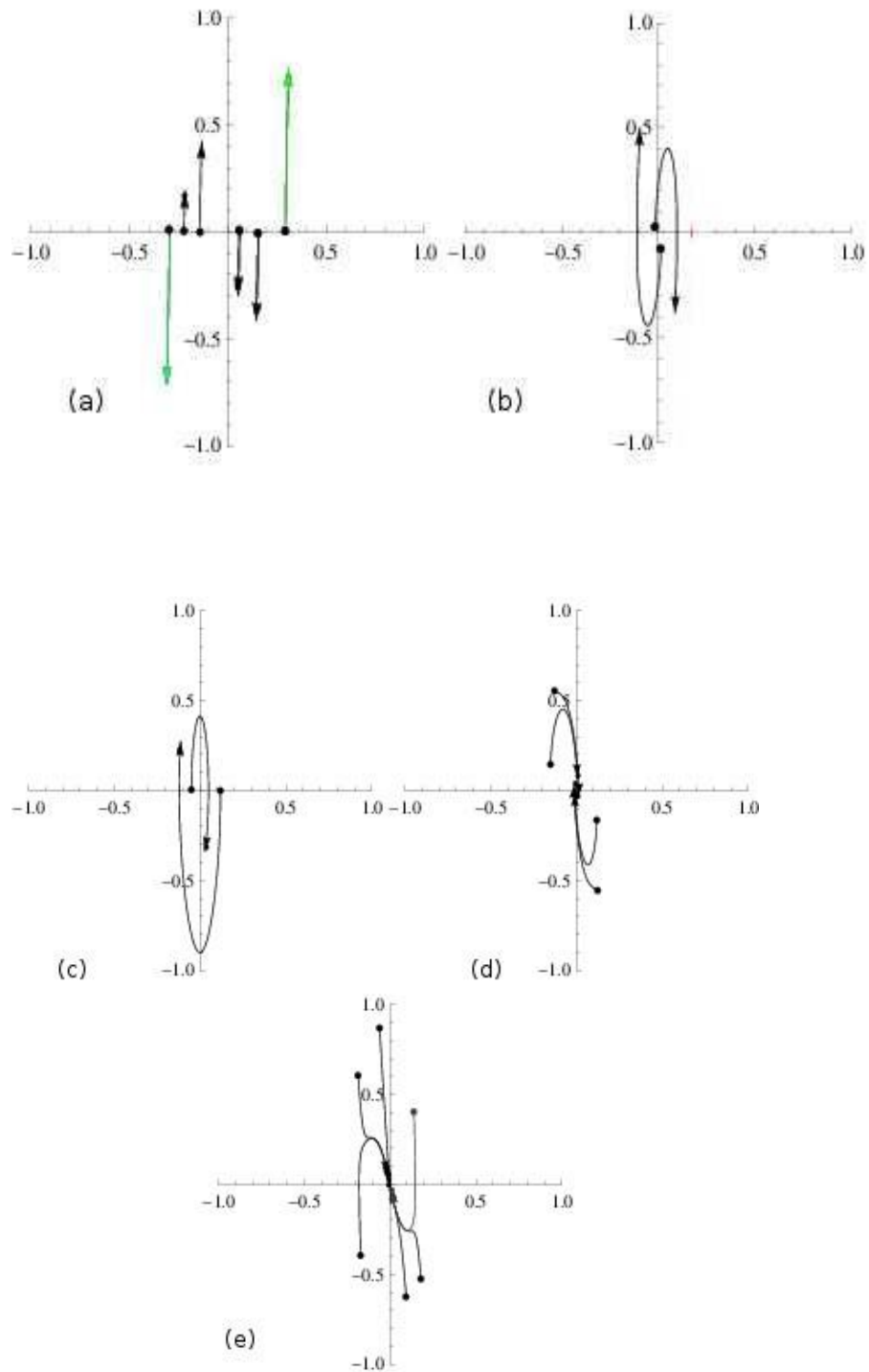
Figure 1: Phase Portraits for the case $\alpha\beta\gamma\delta > 0$: (a) $\xi < -\omega_n$; (b) $-\omega_n < \xi < 0$; (c) $\xi = 0$; (d) $0 < \xi < \omega_n$; (e) $\xi > \omega_0$

4. $\xi > \omega_0$. There are two negative eigen values and the trivial fixed point is a stable node, which is plotted in Fig. 1(e).

The nontrivial fixed points exists only if $\beta\gamma\delta < 0$.

In the case of Lyapunov stability, the energy decreases away from the fixed points. This shows the equilibrium point is globally asymptotically stable. In otherwords starting from any initial conditions, we will eventually reach the equilibrium point. The system is stable in the sense of Lyapunov.

4. CONCLUSION

In the present work, the local stability analysis of the fixed points of a nonlinear Cubic Quintic Septic Duffing equation is conducted. The variation of the fixed points with the nonlinear stiffness is examined. The Lyapunov stability analysis is performed. Since the Lyapunov function decreases everywhere except at the equilibrium point, the system is asymptotically stable.

REFERENCES

1. S. K. Remmi, M M Latha, Cubic Quintic Septic Duffing Oscillator: An analytical study, Chinese Journal of Physics, 56 (2018) 2094.

2. D. R. Merkin , Introduction to the Theory of Stability (1997) Springer-Verlag, New York.

3. Y. Ueda, Steady Motions Exhibited by Duffing's Equation: A Picture Book of Regular and Chaotic Motions (1980) SIAM, Philadelphia.

4. A. M. Lyapunov, The General Problem of Stability of Motion (1992) Taylor and Francis, London.

A STUDY ON SPIN WAVE INTERACTION IN A 2-D FERROMAGNETIC SYSTEM

L. Malkija, M. M. Latha[*]

Department of Physics, Women's Christian College, Nagercoil - 629 001, India (Affiliated to Manonmaniam Sundaranar University, Abishekapatti, Tirunelveli- 627 012, Tamilnadu, India)

* Corresponding author: lathaisaac@yahoo.com

ABSTRACT

A Ferromagnetic spin system with bilinear interaction is investigated. The quasi classical treatment is used to arrive at the nonlinear equation of motion. The nonlinear spin excitations and spin deviation along the site is studied. The results are mapped to find the maximum spin deviation along the site and study the frequency amplitude response of the system.

1. INTRODUCTION

The Earth is a huge magnet and the geomagnetic field is responsible for the sustainability of it. The study of magnets, magnetic energy and magnetic systems remain to be an active area of research all through the times and will persist as long as the earth evolves. Magnetic systems are fascinating nonlinear dynamical systems, where the structure of the system depends on the kind of interactions involved. Though, many researches have been done, the world of magnetism is not fully explored. The nonlinear spin excitations in magnetic materials have drawn considerable attention for the past few years due to its applications in fields such as microwave communication systems and nonlinear processing devices [1]. A number of theories have been developed to analyse these excitations [2]. Among the proposed methods Semi Classical approach helps in the realization of the system practically. In the spin coherent representation [3], the spin operators can be used without any change in Hamiltonian to get a nonlinear equation [4]. The coherent Holstein-Primakoff [H-P] takes a severely truncated H-P expansion for $s_l^{\pm}$, the Glauber Representation [5] is used for making small amplitude and long wave approximation whereby we get a result similar to classical one which is called the Semi Classical Treatment. Moreover, the spin excitation in a square lattice is not expressed completely. Drawn by this hint, in this paper we study the spin excitation in a square lattice model for a Ferromagnetic system with bilinear interaction.

The outline of the paper is as follows, The Hamiltonian for square lattice model of Heisenberg Ferromagnetic spin system with bilinear, anisotropic interactions is considered to obtain the

equation of motion in the semi classical limit whereby the spin wave character is studied in section 2. Section 3 is concluded with the frequency amplitude response of the system.

2. MODEL AND EQUATION OF MOTION

In a Ferromagnetic system, spin of all atoms in the ground state are oriented in one direction. The bilinear nearest neighbor spin-spin interaction is responsible for the parallel alignments of spins and is called 'exchange interaction'. Electrons obey Fermi Dirac statistics and the overall wave function of the system of electrons must be anti symmetric. Let $(-J_{i,j})$ be the energy associated between the nearest neighbor interactions.

The Hamiltonian associated with a 2-D ferromagnetic spin system is

$$\tilde{H} = -\sum_{n,m}[\tilde{J}(\vec{S}_{n,m}\cdot\vec{S}_{n+1,m}) + \tilde{J}_1(\vec{S}_{n,m}\cdot\vec{S}_{n,m+1}) + \tilde{J}_2(\vec{S}_{n,m}\cdot\vec{S}_{n+1,m+1}) - \tilde{A}(\vec{s}_{n,m}^z)^2],\qquad(1)$$

Where n, m→ lattice site

$s_{n,\,m} = (s_{n,m}^x,\ s_{n,m}^y,\ s_{n,m}^z) \rightarrow$ spin operator at lattice the site.

$J,\ J_1,\ J_2 \rightarrow$ coefficient of bilinear exchange interaction.

$A \rightarrow$ crystal field anisotropic interaction.

Now we represent the spin Hamiltonian in the dimensionless form by introducing the dimensionless spin $\hat{s}_{n,m} = \frac{\vec{S}_{n,m}}{\hbar}$ and by defining the spin ladder operator $\hat{s}_{n,m}^+$ as $\hat{s}_{n,m}^+ = \vec{s}_{n,m}^x \pm i\vec{s}_{n,m}^y$ the Hamiltonian becomes,

$$H = -\sum_{n,m}[\frac{J}{2S^2}(\hat{S}_{n,m}^+\cdot\hat{S}_{n+1,m}^- + \hat{S}_{n,m}^-\cdot\hat{S}_{n+1,m}^+ + 2\hat{S}_{n,m}^z\cdot\hat{S}_{n+1,m}^z) + \frac{J_1}{2S^2}(\hat{S}_{n,m}^+\cdot\hat{S}_{n,m+1}^-$$

$$+ \hat{S}_{n,m}^-\cdot\hat{S}_{n,m+1}^+ + 2\hat{S}_{n,m}^z\cdot\hat{S}_{n,m+1}^z) + \frac{J_2}{2S^2}(\hat{S}_{n,m}^+\cdot\hat{S}_{n+1,m+1}^- + \hat{S}_{n,m}^-\cdot\hat{S}_{n+1,m+1}^+$$

$$+ 2\hat{S}_{n,m}^z\cdot\hat{S}_{n+1,m+1}^z) - \frac{A}{S^2}(\hat{S}_{n,m}^z)^2],\qquad(2)$$

Here we assigned $H = \frac{\tilde{H}}{\hbar^2 S^2}$; $J = \tilde{J}$; $J_1 = \tilde{J}_1$; $J_2 = \tilde{J}_2$ and $A = \tilde{A}$. In order to study the spin dynamics of the 2-Dimentional Ferromagnetic system in the semi classical limit, the Hamiltonian is bosonised using H-P representation of spin operators given by $\hat{s}_{n,m}^+ = \frac{\vec{s}_{n,m}^x \pm i\vec{s}_{n,m}^y}{S}$ and $s_{n,m}^z = \frac{s_{n,m}^z}{S}$ which obeys the usual commutation relation $[S_{n,m}^\pm, s_{n,m}^z] = \mp S_{n,m}^\pm$, $[S_{n,m}^+, S_{n,m}^-] = 2s_{n,m}^z$.

In order to investigate spin deviations from the ground state, we define $s_{n,m}^{\pm} = \frac{\vec{s}_{n,m}^{x} \pm i \vec{s}_{n,m}^{y}}{S}$

and $s_{n,m}^z = \frac{s_{n,m}^z}{S}$ the usual way. The nonlinear equation of motion for the operator $S_{n,m}^+$ is found to be

$$i\hbar \frac{\partial S_{n,m}^+}{\partial t} = -\frac{1}{2}[J[s_{n,m}^z(S_{n-1,m}^+ + S_{n+1,m}^+) + S_{n,m}^+(S_{n-1,m}^z + S_{n+1,m}^z)] + J_1[s_{n,m}^z(S_{n,m+1}^+ + S_{n,m-1}^+) +$$
$$S_{n,m}^+(S_{n,m+1}^z + S_{n,m-1}^z)] + J_2(\hat{S}_{n,m}^+ \cdot \hat{S}_{n+1,m+1}^- + \hat{S}_{n,m}^- \cdot \hat{S}_{n+1,m+1}^+ + 2\hat{S}_{n,m}^z \cdot \hat{S}_{n+1,m+1}^z) -$$
$$A(S_{n,m}^+ S_{n,m}^z)], \qquad (3)$$

In the quasi classical approximation for these classical spins.

$$S_{n,m}^z = (S^2 - S_{n,m}^+ S_{n,m}^-)^{\frac{1}{2}} = (S^2 - S_{n,m}^+ S_{n,m}^+)^{\frac{1}{2}}.$$

The equation of motion admits time dependent solutions which we write as

$$S_{n,m}^+ = SS_{n,m}e^{-i\omega t} \text{and} (S_{n,m}^z = S\sqrt{1 - S_{n,m}^2} . \qquad (4)$$

Using these solutions in the equation of motion we get the time independent equation for the amplitude $S_{n,m}$ as

$$\Omega s_{n,m} = -ASS_{n,m}\sqrt{1 - S_{n,m}^2} - JS(\sqrt{1 - S_{n,m}^2}(S_{n-1,m} + S_{n+1,m}) + S_{n,m}(\sqrt{1 - S_{n-1,m}^2} +$$
$$\sqrt{1 - S_{n+1,m}^2})) - J_1 S(\sqrt{1 - S_{n,m}^2}(S_{n,m-1} + S_{n,m+1}) + S_{n,m}(\sqrt{1 - S_{n,m-1}^2} + \sqrt{1 - S_{n,m+1}^2})) -$$
$$J_2 S(\sqrt{1 - S_{n,m}^2}(S_{n-1,m-1} + S_{n+1,m+1}) + S_{n,m}(\sqrt{1 - S_{n-1,m-1}^2} + \sqrt{1 - S_{n+1,m+1}^2}), \qquad (5)$$

Where $\Omega = \hbar\omega$. The above equation determines the envelope of spin modes which is plotted against the site number $S_{n,m}$ and spin deviation S_R using recursion method to study the amplitude frequency response.

3. RESULTS AND DISCUSSION

Figure 1(a) of 2-D ferromagnetic system in the square lattice model shows the spin deviation for $\Omega = -3.95$. It is observed that the maximum spin deviation is 0.4, the spin envelope follows a highly nonlinear pattern where the amplitude is increasing from minimum and reaches the maximum in the positive and negative axis and then suddenly decreases. The frequency pattern repeats itself. The minimum spin deviation is at $S_{n,m} = 12$. Further increase in the value of Ω in Figure 1 (b) indicates an increase in spin deviation, where the maximum amplitude is 1. In Figure 1(c) when the value of Ω is made more positive the amplitude changes a little in the beginning but later resembles the same pattern as in Figure 1 (b).
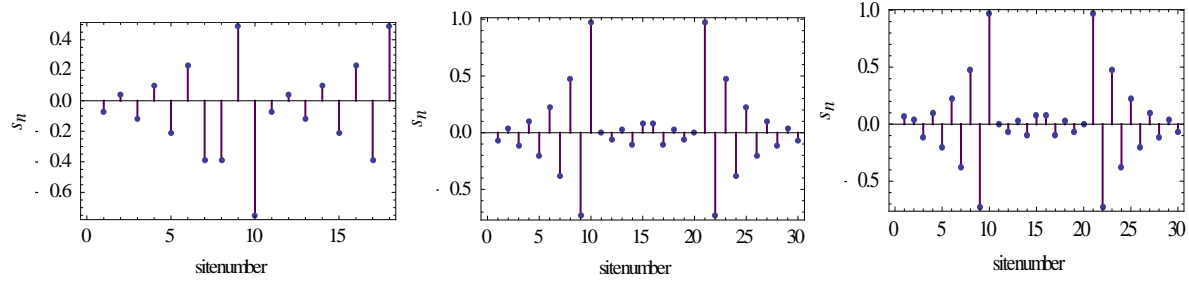
Figure 1:Spin deviation $S_{n, m}$ versus site number for A= 0.1, J= 12, J_2= 8.5, A= 1, J_1= 12 and (a) Ω = -3.95, (b) Ω = -0.5, (c) Ω = 0.5.

Figure: 2 shows the spin deviation when the anisotropic parameter A is varied. In Figure 2(a), the spin deviation is 0.4, the amplitude frequency response shows an irregular variation with repetitive patterns. Further increase in the value of A shows an increased spin deviation. In Figures 2(b), the spin deviation raises to 1. In Figures 2 (c) when A=1 we observe that the peak amplitude appears twice i.e. the system shows more deviation.
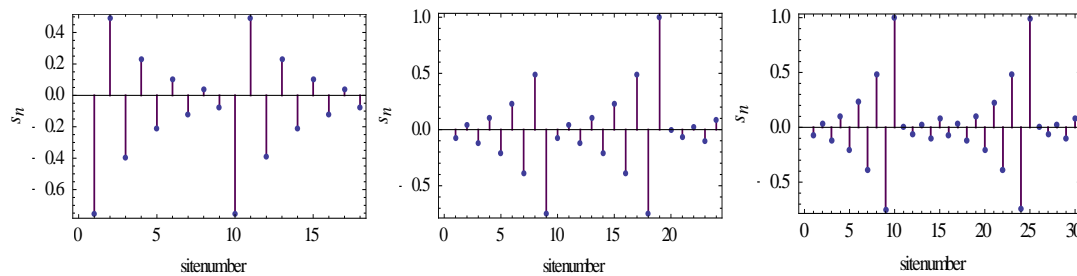
Figure 2:Spin deviation $S_{n, m}$ versus site number for A= 0.1, J= 12, J_2= 8.5, Ω = -3.95, J_1= 12 and (a) A= -0.5, (b) A= 0.5, (c) A= 1.

Figure: 3 shows the spin deviation when the interaction parameter J_1 is varied. When J_1 is increased, the spin deviation increases initially as in Figure: 3 (b) when J_1 is further increased the deviation decreases as in Figure: 3 (c).
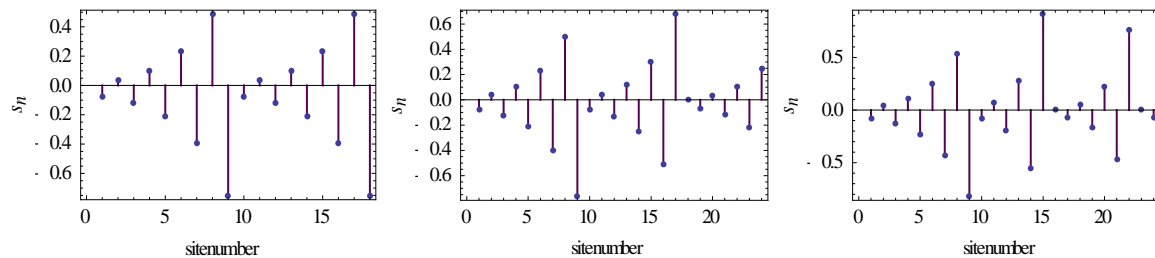
Figure 3:Spin deviation $S_{n, m}$ versus site number for A= 0.1, J= 12, J_2= 8.5, Ω = -3.95 and (a) J_1=12, (b) J_1= 12.5, (c) J_1= 15.

Figure: 4 predicts the influence of interaction parameter J_2 on spin wave. Figure: 4 (a) shows that the oscillation in amplitude is nonlinear. In Figure 4 (b) we observe that when the

interaction parameter J_2 is increased the amplitude increases. In Figure 4 (c) the amplitude becomes periodic but the spin deviation has decreased to 0.4. The frequency amplitude response shows a repetitive pattern.
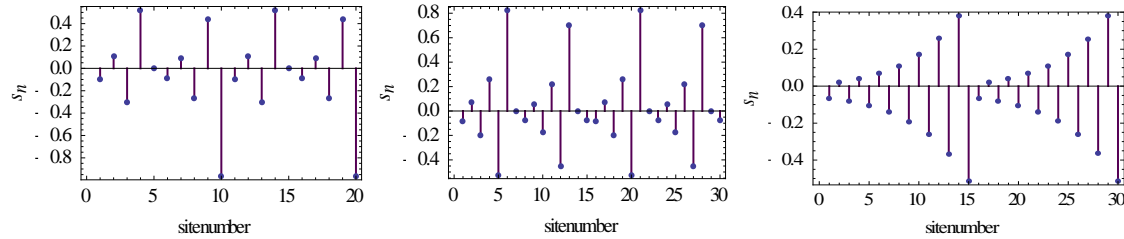
Figure 4:Spin deviation $S_{n, m}$ versus site number for A= 0.1, J= 12, J_1= 12, Ω = -3.95 and

(a) J_2= 6, (b) J_2= 7, (c) J_2= 10.

The above results show attenuation in the spin wave motion which is caused due to dispersive effects that arise due to the variation in the values of interaction parameters.

4. CONCLUSION

A 2-D ferromagnetic system with bilinear exchange interaction and anisotropic interactionis investigated and its nonlinear spin excitations are studied. The variation caused by changing the values of frequency, anisotropic parameter and interaction parameter are mapped. The attenuation in the spin wave motion is observed which occurs due to dispersive effects caused by the variation of parameter values.

REFERENCES

1. S. Strogatz,*Nonlinear dynamics and chaos: With applications to physics,biology,chemistry and engineering*, *Perseus Books Group* (2001).

2. A. Neyfeh, Perturbation Methods, *Wiley, New York* (1973).

3. R. M. Miura, C. S. Gardner and M. D. Kruskal, J. *Math.* **9**(1968)1204.

4. M. M. Latha and T. Anitha, *Soliton Excitations and Stability in a square Lattice Model of Ferromagnetic SpinSystem,*Physica B(2015)149.

5. P. G. Drazin and R. S. Johnson, *Solitons: An Introduction*, *Cambridge University Press, Cambridge* (1989).

SERIES COUPLED MLC CIRCUIT EXHIBITING CHAOS SYNCHRONIZATION

P. Babitha, J.Sheneiga, M. M. Latha[*]

Department of Physics, Women's Christian College, Nagercoil - 629 001, India (Affiliated to Manonmaniam Sundaranar University, Abishekapatti, Tirunelveli-627 012, India)

*Corresponding author: lathaisaac@yahoo.com

ABSTRACT

An experimental circuit simulation for two coupled series Murali – Lakshmanan-Chua (MLC) circuits exhibiting chaos synchronization in their dynamics is presented. The unsynchronized state of the system is converted to a synchronized state by varying the parameters. It is observed through phase portraits obtained from the simulation of the circuit equation characterizing the system.

1.INTRODUCTION

Synchronization of chaos refers to a process wherein two chaotic systems adjust a given property of their motion to common behaviour due to a coupling or to a forcing. To understand the coherent dynamical behaviour of coupled systems, the phenomenon of chaos synchronization in coupled chaotic systems has been studied. In nonlinear electronic circuits the chaos synchronization has been observed in a variety of circuits. The chaos synchronization plays an important role in the application of secure communication and transmission of signals. In identical and nonidentical chaotic system several synchronization phenomena such as complete, phase and lag synchronization have been identified. Among the other types of synchronization complete synchronization is the stronger, it occurs when the states of the coupled systems converge, irrespective of the differences in the initial conditions[1].

The complete synchronization phenomena exhibited by coupled second order dissipative electronic circuits were studied experimentally and numerically. The MLC circuit is a simple second order dissipative nonlinear electronic circuit with Chua's diode as the only nonlinear element was suggested by Murali et al. The period doubling dynamics of the circuit leading to chaotic motion was studied experimentally. An explicit analytical solution to the normalized circuit equation of the MLC circuit was presented. The MLC circuit has the piecewise linear nonlinear element Chua's diode which is linear within the three regions [2,3]. Since the circuit equations describing the MLC circuit is a second order differential equation, the equation is solved for each linear regions of Chua's diode. Similar solutions were given to some second order nonlinear chaotic circuits with piecewise nonlinear element as the active circuit component. The analytical solution thus obtained were used to explain the dynamics of the circuit through phase portraits of the variables. However, this method has not been applied to coupled chaotic circuits [4,5]. Here we present an experimental simulation for coupled MLC circuits and study the phenomena of complete synchronization through phase portraits obtained from the solution.

2. EXPERIMENTAL REALIZATION OF THE CIRCUIT

The circuit realization of simple series LCR network, forced by two sinusoidal voltage generators $F_1 \sin(\omega_1 t)$ and $F_2 \sin(\omega_2 t)$ with the chua's diode N parallel to the capacitor C acting as the nonlinear element. By applying kirchhoff's voltage and the current i_L though the inductor L are given by the following set of two first order coupled nonautonomous differential equations

$$C\frac{dv}{dt} = i_L - g(v) \tag{1a}$$

$$L\frac{di_L}{dt} = -Ri_L - R_s i_L - v + F_1 \sin(\omega_1 t) + F_2 \sin(\omega_2 t) \tag{1b}$$

Where $g(v)$ is the piecewise linear function given by

$$g(v) = G_b v + 0.5(G_a - G_b)[|v + B_p| - |v - B_p|] \tag{2a}$$

$$g(v) = \begin{cases} G_b v_R + (G_b - G_a)B_p, & v_R < -B_p \\ G_a v_R, & -B_p \le v_R \le B_p \\ G_b v_R + (G_a - G_b)B_p, & v_R > B_p \end{cases} \tag{2b}$$

Where G_a=-0.76mS, $G_b = -0.41mS$ and $B_p = 1.0v$ are the respective values of the negative slopes of the inner and outer regions and the breakpoints in the (v-i) characteristic curve of the nonlinear element. The circuit parameters take the values C=10nF, L=18mH, R_s=20Ω, R=1440 Ω, ω_1=23706.61Hz and ω_2=7325.7Hz.

The MLC circuit explained above acting as the drive system is unidirectionally coupled to another MLC circuit which acts as the response system. The drive and the response system operate with different initial conditions and are coupled by a linear resistor and a buffer the buffer acts as a signal driving element, which isolate the drive system variables affected by the response system.

The schematic diagram of the coupled MLC circuit is as shown in Fig.1

The normalized state equation of the response system is given as

$$C\frac{dv'}{dt} = i'_L - g(v') + \epsilon(v - v') \tag{3a}$$

$$L\frac{di'_L}{dt} = -Ri'_L - R_s i'_L - v' + F_3 \sin(\omega_3 t) + F_4 \sin(\omega_4 t) \tag{3b}$$

and the piecewise linear function $g(x')$ is given by

$$g(\upsilon') = \begin{cases} G_b \nu_R' + (G_b - G_a)B_p \,, & \nu_R' < -B_p \\ G_a \nu_R' \,, & -B_p \leq \nu_R' \leq B_p \\ G_b \nu_R' + (G_a - G_b)B_p \,, & \nu_R' > B_p \end{cases} \quad (4)$$

Here $\epsilon = \frac{R_c}{R}$ is the coupling parameter.
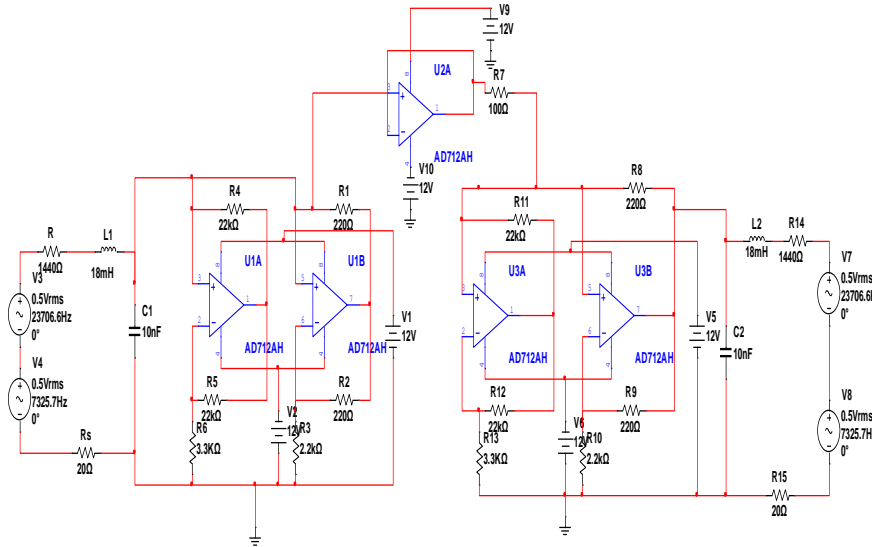
Fig.1 Coupled MLC circuit

For the normalized equations of the response system we could infer that the two circuits are independent of each other when the coupling parameter $\epsilon = 0$ and the explicit analytical solution to the circuit eq.(1) remains the same for all the three piecewise linear regions. For values of the coupling parameter $\epsilon > 0$, the response system is controlled by the drive is unaltered while the dynamics of the response system varies with ϵ.

The circuit parameter of drive and response systems are fixed at C=10nF, L=18mH, R=1440Ω, R_s=20Ω and the parameters of chua's diode are chosen to be G_a=-0.76mS, $G_b = -0.41mS$ and $B_p = 1$v. The frequency of the external periodic force F_1, F_2, F_3, F_4 are fixed at $F_1 = F_2 = F_3 = F_4 = \frac{\Omega}{2\pi} = 8.9$kHz and their amplitudes are varied to fix the drive and response in different dynamical regions. The difference system obtained from eq(1) and (3) is

$$C \frac{d\upsilon^*}{dt} = i_L^* - [g(\upsilon) - g(\upsilon')] + \epsilon(\upsilon^*) \quad (5a)$$

$$L \frac{di_L^*}{dt} = -Ri_L^* - R_s i_L^* - \upsilon^* + F_1 \sin(\omega_1 t) + F_2 \sin(\omega_2 t) - F_3 \sin(\omega_3 t) - F_4 \sin(\omega_4 t) \quad (5b)$$

where $\upsilon^* = (\upsilon - \upsilon')$, $i_L^* = (i_L - i'_L)$ and $g(\upsilon) - g(\upsilon') = g(\upsilon^*)$.

3.RESULTS AND DISCUSSIONS

3. 1 Unsynchronization:
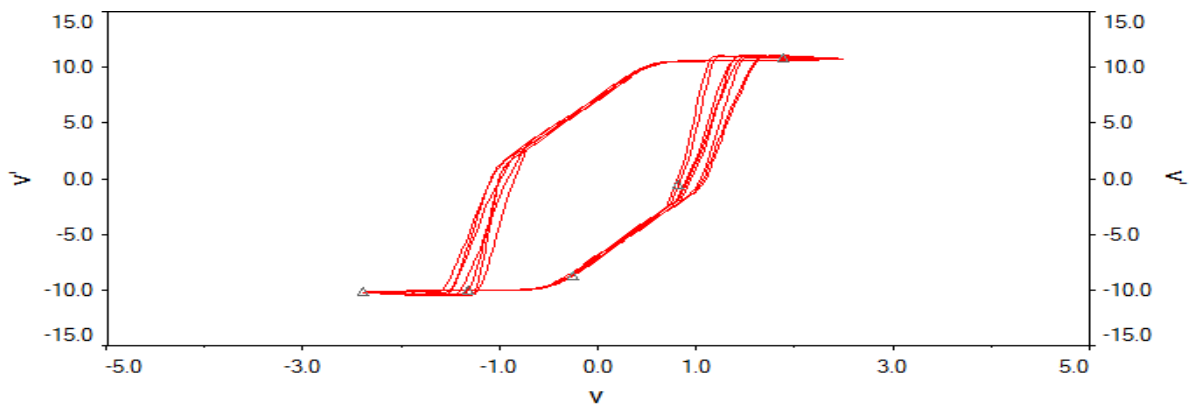
Fig:2a. Phase plot in the (v-v') plane for $\epsilon = 0$ for unsynchronized motion.
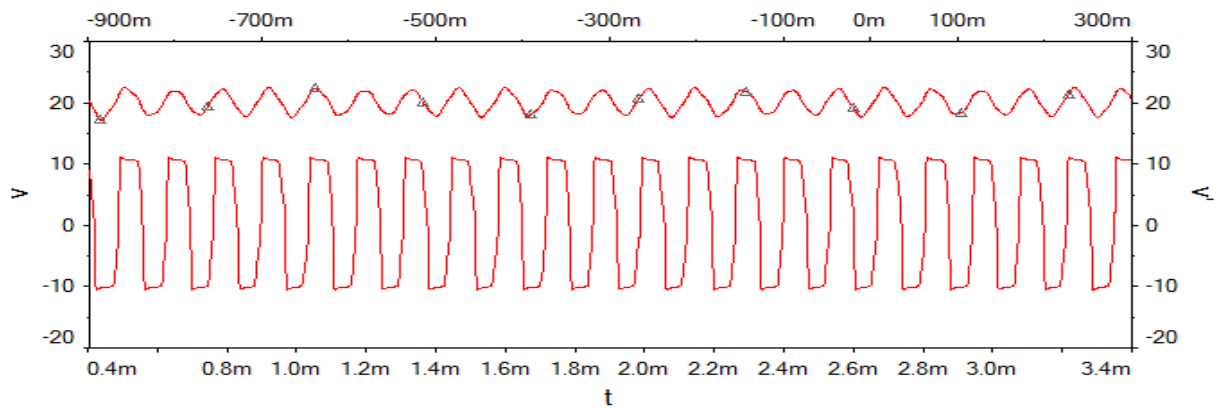
Fig:2b. Phase plot (v-v') versus t for uncynchronized motion.

3.2 Synchronization:
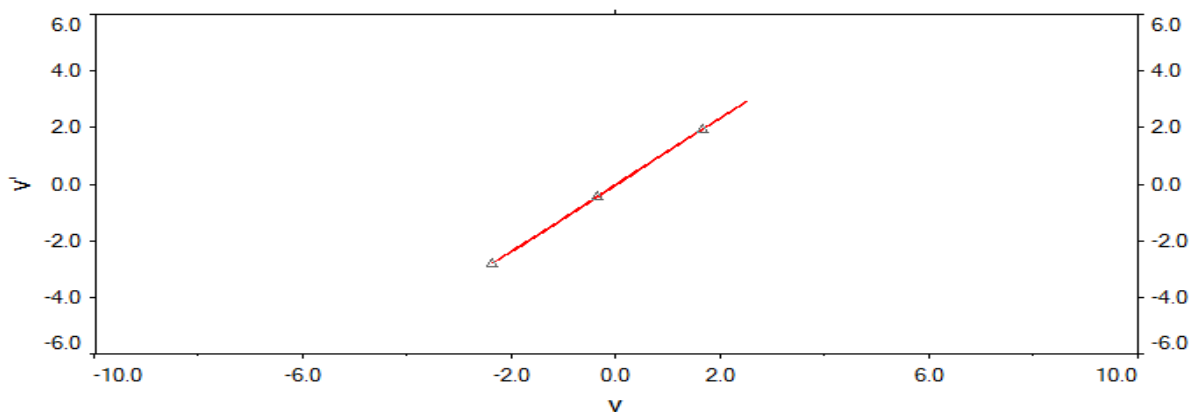
Fig:2c. phase plot in the (v-v') plane for $\epsilon = 1$ for synchronized motion.
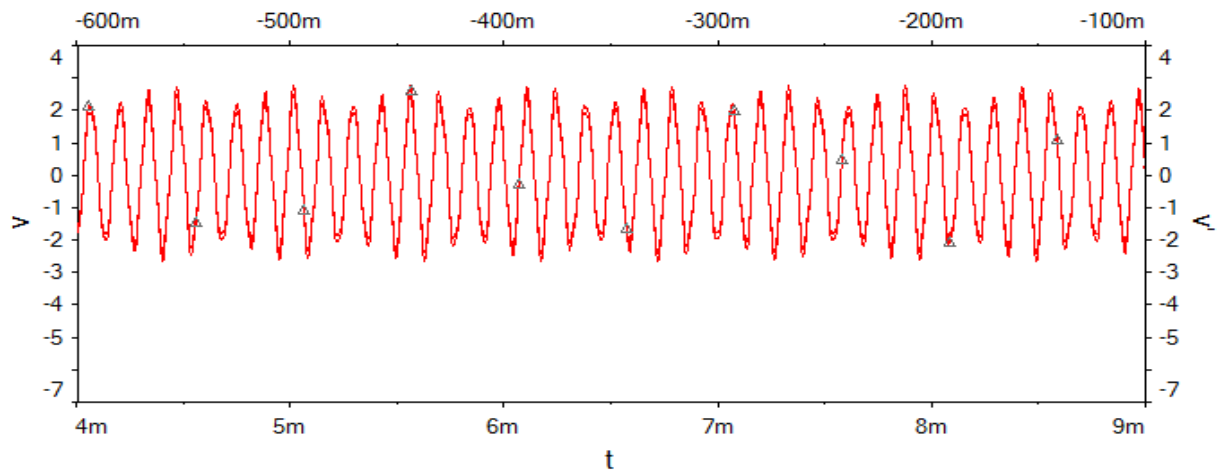
Fig:2d. Phase plot (v-v') versus t for synchronized motion.

From the circuit simulation we notice that the two circuits are independent of each other when the coupling parameter $\epsilon = 0$ and they are synchronized to each other when the coupling parameter $\epsilon = 1$. Which are explicitly shown in the phase plots obtained from the circuit simulation.

4. CONCLUSION

In this paper we have presented an experimental simulation to the normalized state equations of coupled forced systems exhibiting chaotic dynamics. Here the complete synchronization of the drive and response system is based on the value of the coupling parameter. The phase plots thus obtained have been used to explain the phenomenon of complete synchronization in the coupled system.

5. REFERENCES

1. S.Boccaletti, J.Kurths, G.Osipov, D.L.Valladares, C.S.Zhou. The synchronization of chaotic systems, Physics Reports 366(2002)1-101.
2. K. Murali and M. Lakshmanan 1996 controlling synchronization (Singapore:world scientific) chap. 9, p. 239.
3. K. Murali and M. Lakshmanan 1995 Int. J. Bifurcation Chaos Appl. Sci. eng. **5** 563.
4. K. Murali and M. Lakshmanan and Leon O chua 1994 IEEE. Trans. circuits syst.
5. G. Sivaganesh An Analytical study on the synchronization of Murali – Lakshmanan-Chua circuits, CHIN. PHYS. LETT. Vol 32,No.1 (2015) 010503.

EXPLICIT SOLITON SOLUTION USING SINE-COSINE METHOD

G. Addaline Stally[*] and R. Carolin

Department of Physics, Women's Christian College, Nagercoil-629 001, India, Affiliated to Manonmaniam Sundaranar University, Abishekapatti, Tirunelveli-627 012, Tamil Nadu, India.

*Corresponding Author:addalines@gmail.com

ABSTRACT

The Korteweg-de vries equation can be used as model for describing the long wave propagating in a channel. In this work, Sine-Cosine function method is carried out to find the travelling wave solution. The soliton solutions describing its propagation are illustrated graphically.

1.INTRODUCTION

Nonlinear partial differential equations play an important role in nonlinear science, especially in nonlinear physical science since they can provide much physical information and more insight into the physical aspects of the problem. There are many nonlinear equations applicable in engineering, fluid mechanics, biology, hydrodynamics, and physics [1-6]. One of the most exciting advances of nonlinear science and theoretical physics has been development of methods to look for exact solutions of nonlinear partial differential equations. Nonlinear equations are mainly concerned with the study of integrable and non-integrable system. Some of the interesting phenomena that follows from such aspects are soliton and chaos

Soliton refers to a solution of nonlinear partial differential equation. Soliton is a solitary wave whose amplitude, shape, and velocity are conserved after a collision with another soliton. The solitons are the solutions of widespread class of weakly nonlinear dispersive partial differential equations. A soliton is a solitary wave that behaves as a particle.

2. METHODS OF SOLVING NONLINEAR DIFFERENTIAL EQUATIONS:

For a given a nonlinear partial differential equation, there is no general way of knowing whether it has a soliton solution or not, or how the soliton solutions can be found. Many effective methods for obtaining explicit solutions of nonlinear partial differential equations have been presented such as Adomian decomposition method, Differential Transform method, Sine-Cosine method, Hirota's method, Direct algebraic method, Finite difference method, Darboux Transformation method, Inverse scattering method, Pseudo spectral method and Tanh-sech method. In this paper, by means of the Sine-Cosine method, we obtain solutions of Kdv equation. In the following section we have a brief review on the Sine-Cosine method.

The Sine-Cosine Method:

In this section we employ the Sine-cosine function method [4,5]. This method is used to obtain the exact solutions for different types of nonlinear partial differential equations.

1.Consider the nonlinear partial differential equation in the form

$$P(u,u_t,u_x,u_y,u_{tt},u_{xx},u_{yy},u_{xy},\ldots\ldots\ldots) = 0 \tag{1}$$

where $u\ (x,\ y,\ t)$ is a traveling wave solution of nonlinear partial differential equation. We use the transformation.

$$u\ (x,y,t) = q(\xi) \tag{2}$$

where $\xi = x - ct$. This enables us to use the following changes:

$$\frac{\partial}{\partial t} = -c\frac{\partial}{\partial \xi}, \ \frac{\partial^2}{\partial t^2} = c^2\frac{\partial^2}{\partial \xi^2}, \frac{\partial}{\partial x} = \frac{\partial}{\partial \xi}, \frac{\partial^2}{\partial x^2} = \frac{\partial^2}{\partial \xi^2} \tag{3}$$

2.Using Eq. (3) we transfer the nonlinear partial differential equation (1) to nonlinear ordinary differential equation

$$q\ (f, f', f'', f''', \ldots) = 0 \tag{4}$$

3.The ordinary differential equation (4) is then integrated as long as all terms contain derivatives, where we neglect the integration constants. The solutions of many nonlinear equations can be expressed in the form:

$$q(\xi) = \lambda\ (\mu\xi), \qquad |\xi| \leq \frac{\pi}{2\mu}$$

or in the form   (5)

$$q(\xi) = \lambda\ (\mu\xi), \qquad |\xi| \leq \frac{\pi}{2\mu}$$

For this method we use

$$q(\xi)\ = \lambda\ sin^{\beta}\ (\mu\xi) \tag{6}$$

  or

$$q(\xi)\ \ = \lambda\ cos^{\beta}(\mu\xi) \tag{7}$$

 We substitute Eq. (6) or Eq. (7) into the reduced Eq. (4), balance the terms of the sine functions when Eq. (6) are used, or balance the terms of the cosine functions when Eq. (7) are used, and solve the resulting system of algebraic equations by using computerized symbolic packages.

4.Collect all terms with the same power in $sin^k(\mu\xi)$ or $cos^k(\mu\xi)$ and set to zero their coefficients to get a system of algebraic equations among the unknown's α, μ and β, and solve the subsequent system.

3.RESULTS AND DISCUSSION

Nonlinear dispersive equation has been shown to admit the soliton solution the Nonlinear dispersive equations have their potential applications in describing the fluid mechanics, nonlinear acoustics, gas dynamics [6]. Nonlinear equation and the effect of the inhomogeneity on the solitons have been analyzed.

We investigate a Kdv equation given by the following form [6],

$$u_t - \delta u^2 u_x + \delta\ u_{xxx} = 0. \tag{8}$$

In Eq. (8) the variables x and t represent the scaled distance and the scaled time respectively, u represents the probability amplitude of the excitation and the subscripts denote the partial derivatives. We put

$$u = qe^{i\theta} \tag{9}$$

where $\theta = a_{1x} + a_{2x}$. After differentiating Eq. (9) and substituting in Eq. (8) it becomes

$qe^{i\theta}\ ia_2+ q_te^{i\theta} -\delta\ [e^{i\theta}\ (q^3ia_1+q^2q_x)] - ia_1{}^2\ qe^{i\theta} -a_1{}^2q_xe^{i\theta} -2a_1q_xei\ \theta +2ia_1e^{i\theta}\ q_{xx}+ i\ q_{xx}e^{i\theta} + e^{i\theta}\ q_{xxx}\ ] =0$ (10)

The real and imaginary parts of Eq. (10) are separated and are given below:
Real Part:

$$q_t - cq^2q_x - a_1{}^2\ q_x +2a_1q_x+q_{xxx}= 0 \tag{11}$$

Imaginary Part:

$$qa_2 - \delta\ q^3a_1 - a_1{}^2q_x +2a_1\ q_{xx} +q_{xx} =0 \tag{12}$$

Now the travelling wave solutions can be constructed by introducing the wave variable $\xi = x - ct$, where c is the velocity of the wave. Now the ordinary differential equation is expressed as

$$-cq_\xi -cq^2q_\xi - a_1{}^2q_\xi + 2a_1q_\xi +q_{\xi\xi\xi}=0 \tag{13}$$

and

$$qa_2 - \delta q^3a_1 - a_1{}^2q_\xi +2a_1q_{\xi\xi}+q_{\xi\xi} = 0 \tag{14}$$

The solution of nonlinear equation can be expressed in the form

$$q = \lambda \cos^\beta(\mu\xi) \tag{15}$$

Substituting Eq. (15) in Eq (13) and (14), and the parameter β can be found by balancing the higher order derivative term with the nonlinear term.

$-c\mu\lambda \cos^{-2}(\mu\xi)\sin(\mu\xi)\ - \delta\mu\lambda^3 \cos^{-4}(\mu\xi)\sin(\mu\xi) - a_1{}^2\mu\lambda \cos^{-1}(\mu\xi)\ \sin(\mu\xi)$

$+ 2a_1\mu\lambda\cos^{-2}(\mu\xi)\ \sin(\mu\xi)\ -\lambda\mu^3\cos^{-4}(\mu\xi)\ \sin(\mu\xi)\ -\lambda\mu^3\cos^{-2}(\mu\xi)\ \sin(\mu\xi)\ =0$ (16)

and

$a_2\ \lambda\ \cos^{-1}(\mu\xi) -\delta\ a_1\lambda^3\cos^{-3}(\mu\xi) - a_1{}^2\lambda\cos^{-1}(\mu\xi)+ 4a_1\ \mu^2\lambda\cos^{-3}(\mu\xi) -\mu^2\lambda \cos^{-1}(\mu\xi)\ +2\ \mu^2\lambda \cos^{-3}(\mu\xi) - \mu^2\lambda\cos^{-1}(\mu\xi) = 0$ (17)

By solving we obtain a system of algebraic equations as follows:

$\cos^{-1}(\mu\xi)\ \sin(\mu\xi)\ = - a_1{}^2\mu\ \lambda$

$\cos^{-1}(\mu\xi)\qquad = a_2\lambda - a_1{}^2\lambda -2\mu^2\ \lambda$

$\cos^{-2}(\mu\xi)\sin(\mu\xi)\ = -c\mu\lambda + 2a_1\mu\lambda -\lambda\mu^3$

$\cos^{-3}(\mu\xi)\sin(\mu\xi)\ = -\ \delta\ a_1\lambda^3 + 4a_1\ \mu^2\lambda +2\ \mu^2\lambda$

$\cos^{-4}(\mu\xi)\sin(\mu\xi)\ = -\ \delta\mu\lambda^3 - \lambda\mu^3$

 Solving the algebraic equations, we get

$$\lambda = \frac{\sqrt{-c\mu - 2\mu^3 + 2\mu\, a_1 + 4a_1\, \mu^2 - a_1^2 - \mu a_1^2 + a_2}}{\sqrt{\delta\mu + \delta a_1}}$$

$$\mu = \frac{1}{2}\left(2a_1 - \sqrt{2}\sqrt{-c + 2a_1 + a_1^2}\,\right)$$
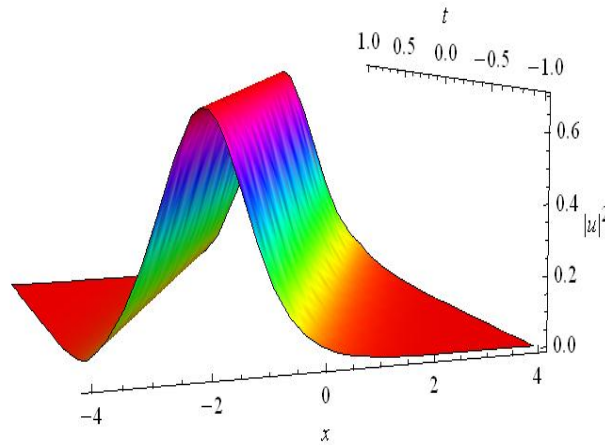
Figure.1 Plot of solitary wave for kdv equation

The figure shows that solitary wave (fig.1) with choice of parameters c=2.1, a_1=0.1, a_2=0.7. Graph clearly shows the soliton propagation varying with x and t. The amplitude of the one soliton is found to constant.

4.CONCLUSION

In this paper we investigate the existence of solitary excitations for Kdv equation. The travelling wave solutions are obtained by employing the sine-cosine method. The solitary wave solution is plotted graphically. From figure we observe the amplitude, shapes and phases of soliton remains the same. Thus, it is expected that when the soliton propagates, the total energy remains constant.

REFERENCES

[1]   B. Kibler, J. Fatome, C. Finot, G. Millot, F. Dias, G. Genty, N. Akhmediev and J. M. Dudley, Nat.

       Phys. 6 (2010) 790.

[2] H. H. Chen and Y. C. Lee, Phys. Rev. Lett. 43 (1979) 264.

[3] A. R. Bishop, Phys. Scr. 20 (1979) 409.

[4] Wazwaz, A.M. Math. Comput. Modelling 40 (2004) 499

[5] Wazwaz, A.M. Appl. Math. Comput 159 (2004) 559
[6] Anwar, A.M. Appl. Math. Comput 216 (2010) 3370

SPIN EXCITATION IN A ONE-DIMENSIONAL ANTIFERROMAGNETIC WITH D-M INTERACTIONS

A. Jarlet Jeyaseeli, M. M. Latha[*]

Department of Physics, Women's Christian College, Nagercoil - 629 001, India (Affiliated to Manonmaniam Sundaranar University, Abishekapatti, Tirunelveli- 627 012, Tamilnadu, India)

* Corresponding author: lathaisaac@yahoo.com

ABSTRACT

We investigate solitary excitations in a model of a one-dimensional antiferromagnet including a single-ion anisotropy and a Dzaloshinsky - Moriya antisymmetric exchange interaction term. Employing the Holstein - Primakoff transformation, the coherent state ansatz and the time variational principle, a discrete set of coupled nonlinear partial differential equations governing the dynamics is derived. By solving these equations intrinsic localized spin excitations in the antiferromagnetic spin chain containing 25 spins have been studied numerically and graphically.

1. INTRODUCTION

The nonlinear excitations in one dimensional magnetic system have attracted a great deal of theoretical and experimental interest in the last few years and continued to be the subject of numerous investigations [1-5]. It is well known that the ferromagnetic (FM) and antiferromagnetic (AFM) chain compounds such as $CsNiF_3$ and TMMC $[(CH_3)_4NMnCl_3]$ are systems exhibiting soliton - like excitations [2]. One of the most interesting methods is that of coherent state treatment. In the spin-coherent treatment. In the spin-coherent state representation, the exact nonlinear equation of motion for the systems is directly with spin operaters without any approximation as regards the Hamiltonian. The other coherent state treatments use a severely truncated Holstein – Primakoff (H-P) expansion for $S_i^{\pm}$ and further approximate the Hamiltonian in the boson operators. Working in the coherent state representation of Glauber [6] and making small-amplitude and long-wave approximations, a solitary wave profile identical to classical solitons can be found, which is known as semi-classical treatment. Experimental investigation of high field neutron scattering measurements and electron paramagnetic resonance investigations have shown that the Dzyaloshinsky-Moria (DM) interaction plays an important role for these materials [7-19].

The plan of the paper is as follows. In section 2, we present the Hamiltonian for Heisenberg antiferromagnetic spin system with bilinear, D-M and anisotropic interactions and study the spin character. In Section 3, we conclude the paper.

2. THE HEISENBERG SPIN CHAIN: MODEL AND EQUATION OF MOTION

The Heisenberg Hamiltonian for an AFM spin system with bilinear and D-M interactions is written as [20]

$$\tilde{\mathcal{H}} = \sum_i \tilde{J}[(\vec{S}_i^A.\vec{S}_i^B + \vec{S}_{i+1}^A.\vec{S}_i^B + \vec{S}_i^A.\vec{S}_{i+1}^B) + \tilde{D}\vec{Z}.(\vec{S}_i^A \times \vec{S}_i^B + \vec{S}_{i+1}^A \times \vec{S}_i^B + \vec{S}_i^A \times \vec{S}_{i+1}^B)$$

$$+ \tilde{A}[(\vec{S}_i^{Az})^2 + (\vec{S}_i^{Bz})^2]], \tag{1}$$

where $\tilde{J}$ represents the bilinear exchange interaction, $\tilde{D}$ is the D-M interaction parameter, and $\tilde{A}$ Corresponds to a crystal field anisotropy interaction. We consider only nearest neighbor interactions. The AFM is divided into two interpenetrating sub lattices A and B, and it is denoted by the superscripts A and B, respectively. Now, we express the spin Hamiltonian (1) in the dimensionless form by introducing the dimensionless spin $\hat{S}_i = \vec{S}_i/\hbar$ and by defining $\hat{S}_i^{\pm} = \hat{S}_i^x \pm i\hat{S}_i^y$. The Hamiltonian now becomes

$$H = -\sum_i \frac{J}{2}[(S_i^{A+}S_i^{B-} + S_i^{A-}S_i^{B+} + S_{i+1}^{A+}S_i^{B-} + S_{i+1}^{A-}S_i^{B+} +$$

$$S_i^{A+}S_{i+1}^{B-} + S_i^{A-}S_{i+1}^{B+} + 2S_i^{Az}S_i^{Bz} + 2S_{i+1}^{Az}S_i^{Bz} + 2S_i^{Az}S_{i+1}^{Bz})$$

$$-\frac{iD}{2}(S_i^{A-}S_i^{B+} - S_i^{A+}S_i^{B-} - S_{i+1}^{A+}S_i^{B-} + S_{i+1}^{A-}S_i^{B+}$$

$$- S_i^{A-}S_{i+1}^{B+} + S_i^{A+}S_{i+1}^{B-}) + A[(\vec{S}_i^{Az})^2 + (\vec{S}_i^{Bz})^2], \tag{2}$$

where the spin operators $S_i^{\pm}, S_i^z$ obey the commutation relations, $[S_i^{\pm}, S_i^z] = \mp S_i^{\pm}$,

$[S_i^{\pm}, S_i^z] = 2S_i^z$.

To investigate spin deviations from the ground state, we define $S_i^{\pm} = \frac{\hat{s}_i^x \pm i\hat{s}_i^y}{S}$, and $S_i^z = \frac{S_i^z}{S}$ in the usual way .The nonlinear equations of motion for the operators S_i^{A+}, S_i^{B-} are found to be

$$i\hbar\frac{\partial S_i^{A+}}{\partial t} = [J(S_i^{AZ}S_i^{B+} + S_i^{AZ}S_{i-1}^{B+} - S_i^{A+}S_{i-1}^{BZ} - S_i^{A+}S_i^{BZ} - S_i^{A+}S_{i+1}^{BZ} - S_i^{A+}S_i^{BZ}) - 2AS_i^{A+}$$

$$- iD(S_i^{AZ}S_i^{B+} + S_i^{AZ}S_{i-1}^{B+} + S_i^{AZ}S_{i+1}^{B+})], \tag{3}$$

$$i\hbar\frac{\partial S_i^{B+}}{\partial t} = [J(S_i^{BZ}S_i^{A+} + S_i^{BZ}S_{i-1}^{A+} - S_i^{B+}S_{i-1}^{AZ} - S_i^{B+}S_i^{AZ} - S_i^{B+}S_{i+1}^{AZ} - S_i^{B+}S_i^{AZ}) - 2AS_i^{B+}$$

$$- iD(S_i^{BZ}S_i^{A+} + S_i^{BZ}S_{i-1}^{A+} + S_i^{BZ}S_{i+1}^{A+})], \tag{4}$$

In the quasiclassical approximation, for these classical spins

$$S_i^Z = \sqrt{S^2 - S_i^+ S_i^-} = \sqrt{S^2 - S_i^+ S_i^+} \tag{5}$$

The equation of motion admits time-dependent solutions which we write as

$$S_i^+ = Ss_i e^{-iwt} \tag{6}$$

With $S_i^Z = S\sqrt{1 - S_i^2}$. It in fact depends on time. Thus, all spins are engaged in a circular precession on a cone that makes the angle $\theta_i = Sin^{-1}(S_i)$ with the Z axis.

We have the time independent equations for the amplitude S_i as

$$\Omega S_i^A = J\left(S_i^B \sqrt{1 - (S_i^A)^2} + S_{i-1}^B \sqrt{1 - (S_i^A)^2} - S_i^A \sqrt{1 - (S_i^B)^2} - S_i^A \sqrt{1 - (S_{i-1}^B)^2} - \right.$$

$$\left. S_i^A \sqrt{1 - (S_{i+1}^B)^2}\right) - D_1\left(S_i^B \sqrt{1 - (S_i^A)^2} + S_{i-1}^B \sqrt{1 - (S_i^A)^2} + S_{i+1}^B \sqrt{1 - (S_i^A)^2}\right) -$$

$$2D_2 S_i^A \sqrt{1 - (S_i^A)^2}, \tag{7}$$

$$\Omega S_i^B = J\left(S_i^A \sqrt{1 - (S_i^B)^2} + S_{i-1}^A \sqrt{1 - (S_i^B)^2} - S_i^B \sqrt{1 - (S_i^A)^2} - S_i^B \sqrt{1 - (S_{i-1}^A)^2} - \right.$$

$$\left. S_i^B \sqrt{1 - (S_{i+1}^A)^2}\right) - D_1\left(S_i^A \sqrt{1 - (S_i^B)^2} + S_{i-1}^A \sqrt{1 - (S_i^B)^2} + S_{i+1}^A \sqrt{1 - (S_i^B)^2}\right) -$$

$$2D_2 S_i^B \sqrt{1 - (S_i^B)^2} \tag{8}$$

where $\frac{\omega}{\hbar S} = \Omega$; $iD = D_1$; $\frac{A}{S} = D_2$. *Eqns.* (7) and (8) determine the envelope of the spin modes. The above said equations are solved for chains containing 25 spins with periodic boundary conditions applied to find the intrinsic localized spin excitations. Eqn.(8) is treated numerically to find the spin deviation. In the numerical calculation, guessing the first set of values and using them in the above equations we may generate the next set of values and so on.

3. RESULTS AND DISCUSSION

A set of 10 sample values of the solution is given in Table 1, and the spin deviation along the site is demonstrated graphically in Figure 1.

Figure 1(a) is the spin deviation curve for Ω = -10.95 which illustrates that as site number increases, the spin deviation also increases. Here the amplitude is 1.0. Also, it is clear that spin deviation associated with A lattice is exactly in phase with that of B lattice. As Ω increases the maximum amplitude increases. Figure 1(b) demonstrates the spin wave for Ω = -15.95. The maximum spin deviation in this case is 0.4.

Table 1: Spin deviation vs Site number for different values of Ω

Ω=-10.95		Ω=-15.95	
S_i^A	S_i^B	S_i^A	S_i^B
0.075	0.026	0.051	0.012
- 0.083	0.026	- 0.085	- 0.021
0.050	- 0.168	0.006	- 0.117
- 0.233	0.109	- 0.075	0.068
0.351	- 0.242	0.159	- 0.004
-0.477	0.519	- 0.089	- 0.142
0.824	- 0.637	0.117	- 0.159
-0.945	0.923	- 0.235	0.062
0.916	- 0.948	0.198	- 0.173
-0.847	0.537	- 0.186	0.253

Arrow: A lattice, **Dot: B lattice**
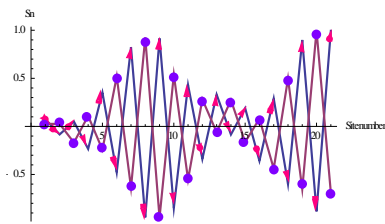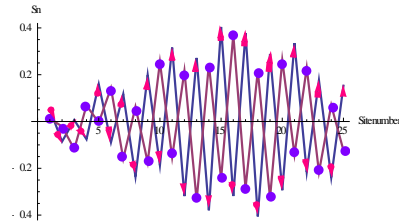
Fig. 1(a)   Fig. 1(b)

Fig.1. Spin deviation S_i verses site number for (a) Ω = -10.95, (b) Ω = -15.95, with J =12, D_0 =3, A= 0.9, S = 0.5.

The intrinsic localized spin excitations occur for frequencies above the linear spin wave bands. When the Ω value increases there is a change in the amplitude of spin wave and an increase in the number of spin waves.

4. CONCLUSION

In this paper, we discuss in detail the existence of the spin excitation and the spin deviations along the site in a 1D AFM with D-M interaction using quasiclassical approximation. Generally, as the Ω value increases, the number of spin wave is increased. Also, a small change in Ω slightly changes the amplitude of spin wave.

REFERENCES

[1] Mikeska H J and Steiner M 1991 Adv.Phys.40 191

[2] Huang G X and Zhiqianng J 1995 Phys. Rev. B 51 613

[3] Leung K M,Hone D W, Mills D L, Mills D L, and Trullinger S E 1980 Phys .Rev.B 21 4017

[4] Pandit R, Tannous C and Krumhansi J A 1983 Phys.Rev.B 28 289

[5] Lemmens L F, Kimura I and de Jonge W J M 1986 J.Phys. C: Solid State Phys. 19 139

[6] Glauber R J, Phys.Rev.131, 2766 (1963)

[7] Shi Z P, Huang G X and Tao R B 1990

[8] Huang G X, Shi Z P, Dai X X and Tao R B 1990 J.Phys. Condense. Matter 2 8355

[9] Huang G X, Shi Z P, Dai X X and Tao R B 1991 J.Phys. Rev.B 43 11197

[10] Liu W M and Zhou B L, J.Phys. Condens. Matter 5, L 149 (1993)

[11] Gouvea M E and Pires A S T, Phys.Rev.B 34, 306 (1986)

[12] Liu W M, He G H and Zhou B L 1993 Phys.Scr. 50 437-41

[13] Liu W M, He G H and Zhou B L 1993 Commun.Theor.Phys. 20 427

[14] Liu W M, He G H and Zhou B L 1994 Phys.Lett.A 1984 487

[15] Kohgi M, Iwasa K 2001 Phys.Rev.Lett. 86 2439

[16] Tsukada I and Masuda T Phys.Rev.Lett. 87 127203

[17] Dender D C and Reich D H 1996 Phys.Rev.B 53 2583

[18] Dzyaloshinsky I 1958 J. Phys. Chem. Solids 4 241

[19] Moriya T 1960 Phys.Rev.120 91

[20] Evangeline Rebecca T and Latha M M Chaos 26,063116 (2016)

AN INHOMOGENEOUS HEISENBERG FERROMAGNETIC SPIN CHAIN: A CHAOTIC STUDY

B. S. Gnana Blessy, M. M. Latha*

Department of Physics, Women's Christian College, Nagercoil - 629 001, India (Affiliated to Manonmaniam Sundaranar University, Abishekapatti, Tirunelveli-627 012, India)
*Corresponding author: lathaisaac@yahoo.com

ABSTRACT

In this paper, a Chaotic dynamical study on an Inhomogeneous Heisenberg Ferromagnetic spin chain is made. A model Hamiltonian is proposed for this system with bilinear, biquadratic and Dzyaloshinskii-Moriya interactions. Hamiltonian equations of motion are constructed. The effect of inhomogeneities of different types on the system is investigated by the characteristic Lyapunov exponent curves.

1. INTRODUCTION

Heisenberg spin chain has presumed much significance in the recent past for various investigations [1-5]. The nonlinear dynamical system which attracts a great deal of interest is the Heisenberg ferromagnetic spin system with the presence or absence of an external magnetic field. By evaluating the nature of the magnetic interactions involved a nonlinear dynamical problem discloses both chaotic and coherent structures. A chaotic system is a system that displays an unpredictable behaviour. The main characteristic response is its excessive sensitivity to initial conditions. From the chaotic dynamical equation, it is impossible to gain its analytical solution, the only most effective method is the numerical analysis with its nonlinear models.

Different kinds of interactions employed with the Heisenberg ferromagnetic system exhibits interesting nonlinear phenomena. In the midst of various magnetic interactions, the notable one is the Dzyaloshinskii-Moriya(D-M) interaction [6,7]. So far there is no work reported in the literature on the chaotic behaviour of an inhomogeneous Heisenberg ferromagnetic system with D-M interactions. Hence in the present study, we construct a Hamiltonian for such a system and study the chaotic dynamics by constructing equations of motion.

2. MODEL HAMILTONIAN

Incorporating bilinear, biquadratic and D-M interactions, the model Hamiltonian for a Heisenberg Ferromagnetic spin chain, it can be written as

$$H = -\sum_i \left[f_i \tilde{J}(\vec{S}_i \cdot \vec{S}_{i+1}) + f_i' \tilde{J}'(\vec{S}_i \cdot \vec{S}_{i+1})^2 + g_i \tilde{D}\vec{Z}.(\vec{S}_i \times \vec{S}_{i+1}) \right.$$
$$\left. -\tilde{A}(S_i^z)^2 - \tilde{A}'(S_i^z)^4 \right]. \tag{1}$$

In Eq. (1) J is the constant coefficient of bilinear exchange interaction, J' is the biquadratic isotropic exchange interaction, D is the D-M interaction parameter between two neighbouring magnetic spins, A is the anisotropic parameter which corresponds to the uniaxial crystal field anisotropy, A' is the higher order uniaxial anisotropic energy and the parameters f_i, f_i', g_i represents site dependent inhomogeneities. To express in the dimensionless form, the Hamiltonian has to be remodelled by introducing $\hat{S}_i = \frac{\vec{S}_i}{\hbar}$. The generated Hamiltonian is now subjected to H-P approximation [8]. The mentioned representation will bosonise the Hamiltonian. It is given as follows:

$$\hat{S}_n^+ = \sqrt{2}S(1 - \frac{\epsilon^2}{4} a_n^\dagger a_n)\epsilon a_n,$$
$$\hat{S}_n^- = \sqrt{2}S\epsilon a_n^\dagger(1 - \frac{\epsilon^2}{4} a_n^\dagger a_n),$$
$$\hat{S}_n^z = S - a_n^\dagger a_n. \tag{2}$$

The rephrased equation requires further expansion in order to study the chaotic dynamics of the system. The related equations are

$$a_n^\dagger = \left(\frac{M\omega}{2\hbar}\right)^{\frac{1}{2}} x - i \left(\frac{1}{2M\hbar\omega}\right)^{\frac{1}{2}} p_x,$$
$$a_n = \left(\frac{M\omega}{2\hbar}\right)^{\frac{1}{2}} x + i \left(\frac{1}{2M\hbar\omega}\right)^{\frac{1}{2}} p_x,$$
$$a_{n+1}^\dagger = \left(\frac{M\omega}{2\hbar}\right)^{\frac{1}{2}} (x+h) - i \left(\frac{1}{2M\hbar\omega}\right)^{\frac{1}{2}} p_x,$$
$$a_{n+1} = \left(\frac{M\omega}{2\hbar}\right)^{\frac{1}{2}} (x+h) + i \left(\frac{1}{2M\hbar\omega}\right)^{\frac{1}{2}} p_x. \tag{3}$$

For the succeeding analysis equations that are coupled with time are essential. It can be uniquely derived using Hamilton's equations of motion.

$$\frac{dx}{dt} = \frac{\partial H}{\partial p_x}, \tag{4}$$
$$\frac{dp_x}{dt} = -\frac{\partial H}{\partial x}. \tag{5}$$

Homogeneous Case

In the case of homogeneous Heisenberg Ferromagnetic Spin system by assuming $f_i' = 0$ and $f_i = g_i = 1$ the Lyapunov Characteristic Exponent analysis is done to predict the stability. The computation is carried out for four sets of values. They are $10^{-6}, 10^{-10}, 10^{-14}$ and 10^{-16}. The curves

derived shows unstable behaviour. Here we could observe all the four curves with positive exponent values thus manifests the nature of chaos.
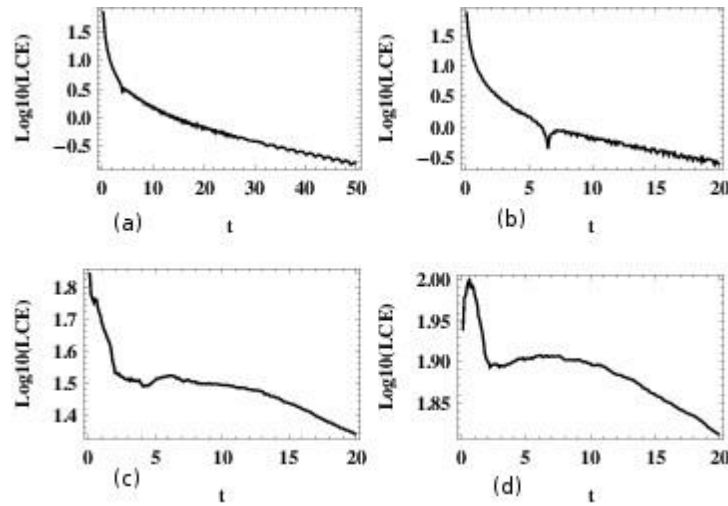
Figure 1: Lyapunov curves for $A = 0.2, J = 12, S = 0.5, \epsilon = 0.5$ at (a) 10^{-6}, (b) 10^{-10}, (c) 10^{-14} and (d) 10^{-16}

Inhomogeneous Case

Inhomogeneous system may have an impact on soliton but here we investigate whether inhomogeneity implies any new effect in chaoticity. The following are the two case studies enforcing four kinds of inhomogeneities with different types such as Localized, Cubic, Biquadratic and Periodic inhomogeneities.

Case 1: For $f'_i = g_i = 1$ and $f_i \neq 1$

Obeying the above prescribed rule here we impose the respective formulae's in the place of f_i. Fig.(2) displays the effect of localized inhomogeneity of the form $f_i = 1 + P tanh(x)$. From the spectra it is noted that the Lyapunov exponent decreases substantially as the inhomogeneity parameter P increases. Subjecting to periodic inhomogeneity i.e. when $f_i = 1 + P sin(x)$, Fig.3(a) and (b) are stable and the rest exhibit chaotic nature. The other two inhomogeneities are not applicable under this case.
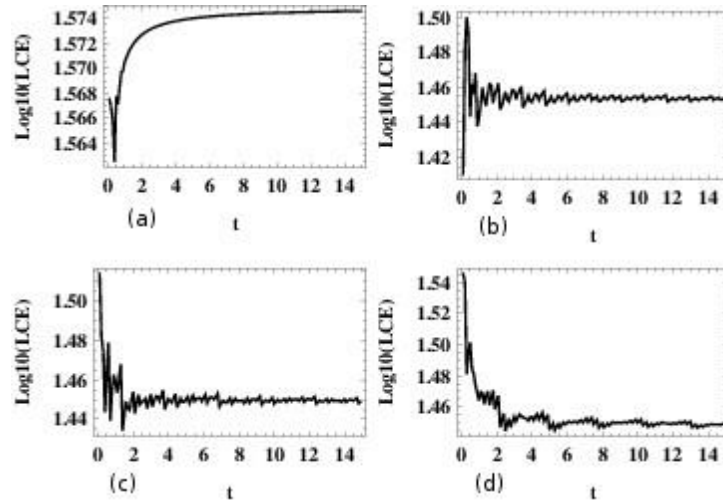
Figure 2: Lyapunov Curves with Localized inhomogeneity for (a) $f_i = 10$ (b) $f_i = 65$ (c) $f_i = 80$ (d) $f_i = 90$
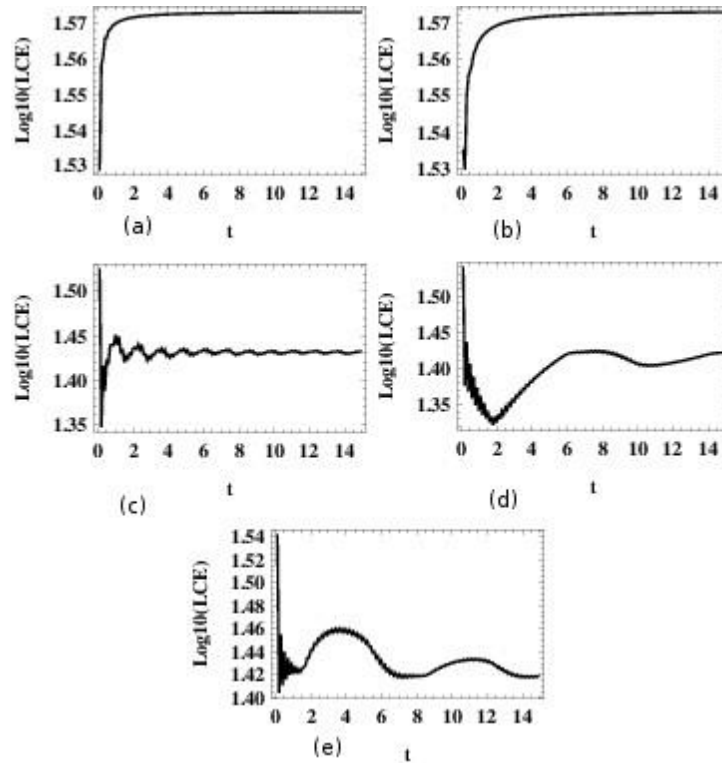
Figure 3: Lyapunov Curves with Periodic inhomogeneity for (a) $f_i = 2$ (b) $f_i = 25$ (c) $f_i = 35$ (d) $f_i = 45$ and $f_i = 50$

Case 2: For $f'_i = f_i = 1$ and $g_i \neq 1$

Enacting the mentioned condition in this system here we find that only the localized and periodic inhomogeneities are effective. Fig.4 represents Lyapunov curves for various values of inhomogeneity parameters. Fig.4(a) shows its linear behaviour. Regarding the other plots they have higher fluctuation in the strength of its stability. Fig.4(f) reveals a dramatic change where the stability falls off to zero then progressing periodically. Considering periodic inhomogeneity, the Lyapunov curves visualise a straight line beginning from zero and reaches a certain point then moving asymptotically. Fig.5(d) curve alone touches the exponent range at 1.55. Subsequently it progresses in a linear manner.
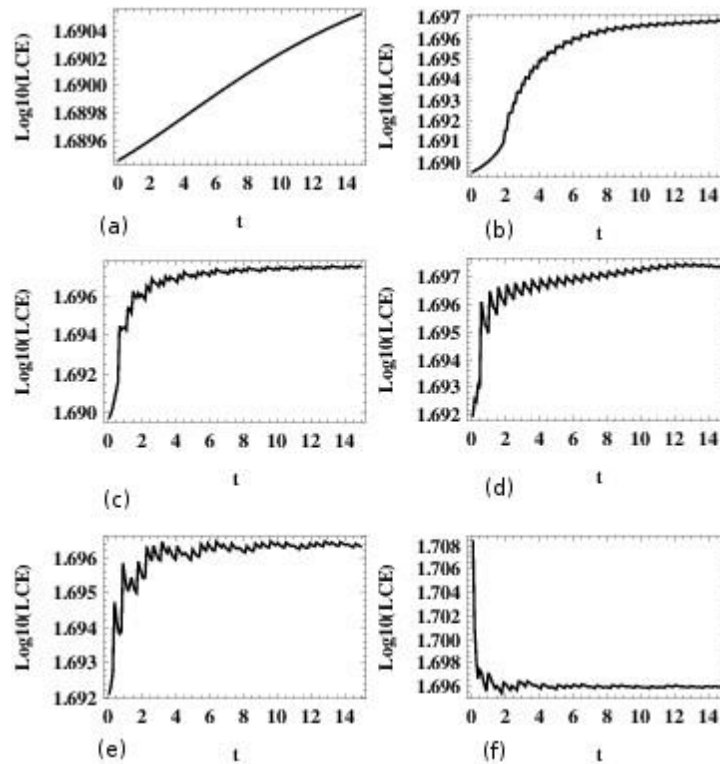
Figure 4: Lyapunov Curves with Localized inhomogeneity for (a) $g_i = 0.2$ (b) $g_i = 120$ (c) $g_i = 460$ (d) $g_i = 2000$ (e)$g_i = 2500$ (f)$g_i = 3000$
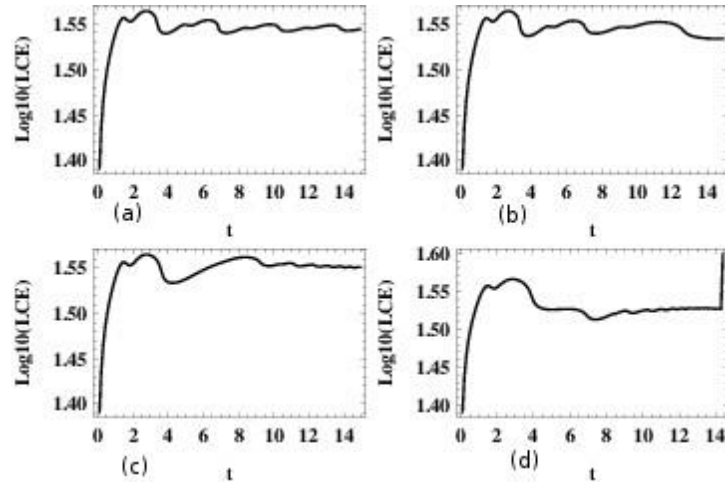
Figure 5: Lyapunov Curves with Periodic inhomogeneity for (a) $g_i = 0.8$ (b) $g_i = 4$ (c) $g_i = 8$ (d) $g_i = 9.5$

3. CONCLUSION

This paper deals with the chaotic behaviour of an inhomogeneous Heisenberg Ferromagnetic spin system. The main criteria behind a chaotic motion is that it must have at least one positive Lyapunov exponent. This criterion goes very well with this study. The Lyapunov exponent characteristic curves constructed under various conditions indicates the presence of chaos for different types of inhomogeneities.

REFERENCES

1. K Porsezian, M Daniel and M Lakshmanan, *J. Math. Phys.* **33**, 1807 (1992)

2. M C Arnesen, S Bose and V Vedral, *Phys. Rev. Lett.* **87**, 017901 (2001)

3. O F Syljua sen, *Phys. Rev. A* **68**, 060301 (2003)

4. D L Deng, S J Gu and J L Chen, *Annals Phys.* **325**, 367 (2010)

5. Asoudeh and V Karimipour, *Phys. Rev. A* **70**, 052307 (2004)

6. I Dzyaloshinskii, *J.Phys.Chem.Solids* **4**, 241 (1958)

7. T Moriya, *Phys.Rev.* **120**, 91 (1960)

8. T Holstein and H Primakoff, *Phys. Rev.* **58**, 1098 (1940)

MODULATIONAL INSTABILITY IN ONE-DIMENSIONAL ANTIFERROMAGNETIC SPIN SYSTEM WITH DZYALOSHINSKI-MORIYA INTERACTIONS

C Christal Vasanthi and M M Latha

ABSTRACT:

We study the stability aspects of one dimensional inhomogeneous antiferromagnetic (AFM) system with bilinear and Dzyaloshinski-Moriya (D-M) interactions in the semiclassical limit. The effect is analyzed by introducing small perturbation in the amplitude and in the phase of the system and the results is illustrated graphically.

Keywords: Antiferromagnetic system, perturbation, stability

INTRODUCTION:

The study of nonlinear spin excitations in terms of solitary waves and solitons in magnetic materials has attracted much interest in the last few years [1-4]. The nonlinear solitary wave excitations in one-dimensional AFM have been intensively investigated by many researchers [4-6]. They use various methods for studying the nonlinear excitations. Moreover, there are extensive studies on the nonlinear spin dynamics of inhomogeneous AFM systems [7,8]. But, to our knowledge the instability aspects of one-dimensional inhomogeneous AFM system with D-M interaction has not yet been analyzed because of the mathematical complexity of their representations in the Hamiltonian and in the governing dynamical equations. Hence in this paper we try to investigate the stability aspects associated with the inhomogeneous partial differential equation (PDE) of one-dimensional AFM system using linear stability analysis.

MODULATIONAL INSTABILITY (MI):

The modulational instability (MI) of waveforms is a fundamental phenomenon in nonlinear media and is closely associated with the concept of self localized waves, or solitons. It signifies the exponential growth of a weak perturbation of the amplitude of the wave as it propagates due to the interplay between nonlinear and dispersive or diffraction effects [9,10]. In most of these cases, MI appears in continuous media where the propagation of nonlinear waves is usually governed by nonlinear Schrodinger (NLS)-type PDEs. These studies of continuum models have shown that the initial amplitude of an unstable modulation wave grows exponentially with the time evolution of a modulated nonlinear plane waves.

In this section we study analytically the MI of the nonlinear plane waves and soliton formation in one dimensional inhomogeneous AFM spin system. The aim of the stability analysis is to perturb the system slightly and then study whether this small perturbation grows or decays with propagation. Now we proceed to discuss the occurrence of MI for the inhomogeneous one-dimensional PDE [7].

$$
i\varphi_1 t = 2S\left(A\eta^2 + Jf\eta^4 - Jf_x\eta^5 + \frac{1}{2}Jf_{xx}\eta^6\right)\varphi_1 + 2A\eta^6|\varphi_1|^2\varphi_1
$$
$$
+ \frac{1}{2}S\left(4\eta^4(Jf - iDg) - 2\eta^5(Jf_x - iDg_x) + \eta^6(Jf_{xx} - iDg_{xx})\right)\varphi_2^*
$$
$$
- S\left(\eta^5(Jf - iDg) - \eta^6(Jf_x - iDg_x)\right)\varphi_{2x}^* + \frac{1}{2}S\eta^6(Jf - iDg)\varphi_{2xx}^*. \quad\longrightarrow\quad (1)
$$

We assume plane wave solutions with constant amplitude of the form

$$
\varphi_1(x,t) = \varphi_0 e^{i(k_1 x - \omega_1 t)}, \qquad\longrightarrow\quad (2)
$$

$$
\varphi_2(x,t) = \varphi_0 e^{i(k_2 x - \omega_2 t)}, \qquad\longrightarrow\quad (3)
$$

where φ_0 is the perturbation amplitude, ω_1 and ω_2 are the frequencies, k_1 and k_2 are the wave numbers. Substituting equations (2) and (3) in equation (1), we get an amplitude dependent relationship

$$
\omega_1 = 2(AS\eta^2 + JSf\eta^4 + A\eta^6\varphi_0^2) - 2JS\eta^5 f_x + JS\eta^6 f_{xx} \qquad\longrightarrow\quad (4)
$$

known as the dispersion relation. Now, we analyze the linear stability of equations (2) and (3) by considering perturbed plane wave solutions of the form

$$
\varphi_1(x,t) = [\varphi_0 + \epsilon u_1(x,t)]e^{i[(k_1 x - \omega_1 t) + \epsilon u_2(x,t)]}, \qquad\longrightarrow\quad (5)
$$

$$
\varphi_2(x,t) = [\varphi_0 + \epsilon v_1(x,t)]e^{i[(k_2 x - \omega_2 t) + \epsilon v_2(x,t)]}, \qquad\longrightarrow\quad (6)
$$

where $\epsilon \ll 1$ is a small parameter which represents the strength of perturbation and

$$
u_1(x,t) = ae^{i(K_1 x - \Omega_1 t)}; \; u_2(x,t) = be^{i(K_1 x - \Omega_1 t)}, \qquad\longrightarrow\quad (7)
$$

$$
v_1(x,t) = ae^{i(K_2 x - \Omega_2 t)}; \; v_2(x,t) = be^{i(K_2 x - \Omega_2 t)}. \qquad\longrightarrow\quad (8)
$$

Using equations (5)−(8) in equation (1) and dropping higher order terms, we get the linearized evolution equation as follows:

$$
\Omega_1 = \frac{1}{4}(4fJS\eta^4 - 2JS\eta^5 f_x + JS\eta^6 f_{xx} + 2gDS\eta^5 k_2 - 2D\eta^6 g_x k_2 - JSf\eta^6 k_2^2 + 8A\eta^6\varphi_0^2
$$
$$
\pm \left[\left(\eta^8\left((4JSf - 2JSnf_x + JS\eta^2 f_{xx} + 2DSg\eta k_2 - 2DS\eta^2 g_x k_2 - JSf\eta^2 k_2^2 + 8A\eta^2\varphi_0^2)^2\right.\right.\right.
$$
$$
+ 4S\eta^2 K_2\left(4JDfSg_x + 2JDfSg_{xx} + 4J^2 f^2 Sk_2 + 4D^2 g^2 Sk_2 + 4D^2 gS\eta g_x k_2 - 4D^2 S\eta^2 g_x^2 k_2\right.
$$
$$
+ 2D^2 S\eta^2 gg_{xx}k_2 - 6JDSf\eta^2 g_x k_2^2 - 2J^2 f^2 S\eta^2 k_2^3 - 2D^2 g^2 S\eta^2 k_2^3 - 6D^2 gS\eta g_x K_2 + 4D^2 S\eta^2 g_x^2 K_2
$$
$$
- D^2 S\eta^2 gg_{xx}k_2 + 10JDS\eta^2 gg_x k_2 K_2 + 5J^2 S\eta^2 f^2 k_2^2 K_2 + 5D^2 S\eta^2 g^2 K_2^3 + 4J^2 S\eta^2 f_x^2(-k_2 + K_2)
$$
$$
+ JS\eta f_{xx}(-2Dg + 2D\eta g_x + 2J\eta f k_2 - J\eta f K_2)
$$
$$
+ 2JSf_x\left(-2Dg - D\eta^2 g_{xx} + 3Dg\eta^2 k_2^2 - 3J\eta f K_2 + 2D\eta^2 gK_2^2 + \eta k_2(2Jf - 5D\eta gK_2)\right)
$$
$$
\left.\left.\left. - 16AD\eta\varphi_0^2(g - \eta g_x) - 8AfJ\eta^2\varphi_0^2(K_2 - 8k_2)\right)\right)\right]^{\frac{1}{2}}. \qquad\longrightarrow\quad (9)
$$

The stability of the nonlinear AFM spin system can be resolved by the imaginary part of Ω_1.

RESULTS AND DISCUSSIONS:

From the above relation, it can be shown that if the terms inside the square root are greater than zero then the eigen value Ω_1 is real for any value of the wave number K_2 and the solution is modulationally stable. When it is less than zero Ω_1 becomes complex and in this case the perturbation increases with time exponentially and the excited AFM system exhibits MI which supports soliton formation.

We have depicted the variation of growth rate amplitude with different values of perturbation wave number k_2 in Fig. 1. From plot it is observed that the growth rate increases with amplitude of the continuous wave and also the stability window grow smaller by decreasing the perturbation wave number k_2, i.e, narrowing of soliton width accompanied by decay of the amplitude can be observed.

The inhomogeneity can have a drastic impact on soliton formation. We here investigate whether nonlinear type of inhomogeneities in the lattice modifies the stability of soliton.
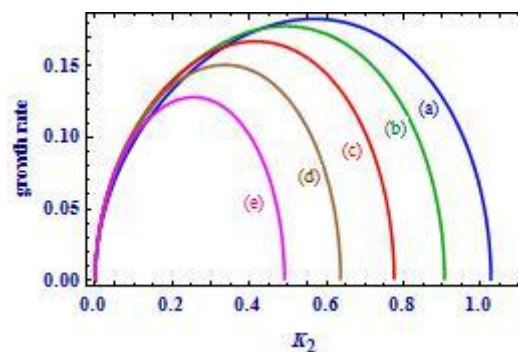
Fig. 1. Variation of growth rate with wave number for J=12, A=0.09, D=1.9, η=0.55, S=0.5, φ_0=1.55, f=g=1, k_2= (a)-1.2, (b)-1.4, (c)-1.6, (d)-1.8, (e)-2.
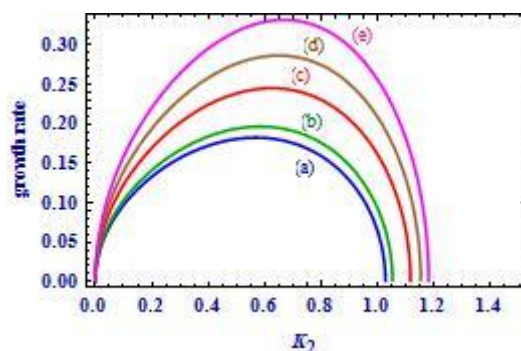
Fig. 2. Variation of growth rate with periodic inhomogeneity for (a) $P_1=P_2=0$; (b) $P_1=0.1$, $P_2=0.02$; (c) $P_1=0.5$, $P_2=0.04$; (d) $P_1=0.9$, $P_2=0.06$; (e) $P_1=1.4$, $P_2=0.08$.
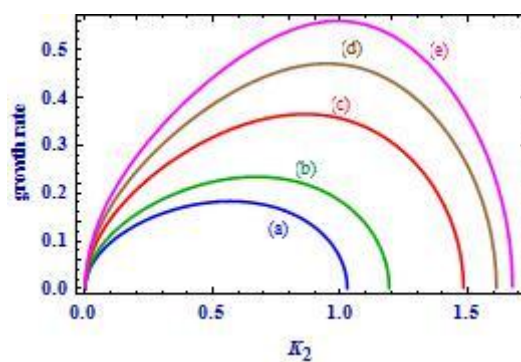
Fig. 3. Variation of growth rate with cubic inhomogeneity for (a) $P_3=P_4=P_5=P_6=0$; (b) $P_3=-0.002$, $P_4=0.1$, $P_5=-0.05$, $P_6=0.02$; (c) $P_3=-0.005$, $P_4=0.4$, $P_5=-0.08$, $P_6=0.05$; (d) $P_3=-0.008$, $P_4=0.7$, $P_5=-0.14$, $P_6=0.08$; (e) $P_3=-0.011$, $P_4=1$, $P_5=-0.14$, $P_6=0.11$.
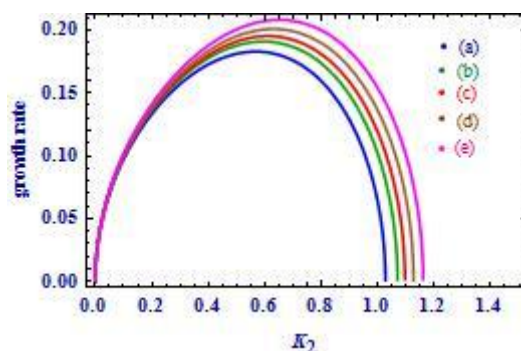
Fig. 4. Variation of growth rate with localized inhomogeneity for (a) $P_7=P_8=0$; (b) $P_7=-0.04$, $P_8=0.7$; (c) $P_7=-0.08$, $P_8=1.1$; (d) $P_7=-0.12$, $P_8=1.5$; (e) $P_7=-0.16$, $P_8=1.9$.

In Fig. 2. we show the growth rate with wave number for periodic inhomogeneity [$f(x) = 1 + P_1\text{Sin}[x]$, $g(x) = 1 + P_2\text{Sin}[x]$]. In the absence of such inhomogeneity, the system supports stable propagation of solitary wave for the choice of parameters $J = 12$, $A = 0.09$,

D=1.9, $\eta = 055$, S = 0.5, f = 1, g=1, $\varphi_0 = 1.55$, x = 1 and $k_2 = -1.2$ (see Fig. 2a). Figures 2b−2e illustrate the growth rate for periodic inhomogeneities with (b) $P_1 = 0.1$, $P_2 = 0.02$; (c) $P_1 = 0.5$, $P_2 = 0.04$; (d) $P_1 = 0.9$, $P_2 = 0.06$; (e) $P_1 = 1.4$, $P_2 = 0.08$. As the inhomogeneity is increased the growth rate amplitude increases. At $P_1 = 1.4$, $P_2 = 0.08$, MI become high and beyond this value the solitonic nature gets distorted. This shows that periodic inhomogeneity affects the MI and hence the formation of soliton. The effect of cubic inhomogeneity [f(x) = 1 + P_3x^3+ P_4x^2, g(x) = 1 + P_5x^3+ P_6x^2] (see Fig. 3) also exhibits the same result as that of periodic inhomogeneity. The threshold values are given by P_3=-0.011, P_4=1, P_5=-0.14, P_6=0.11. For the case of localized inhomogeneity [f(x) = 1 + P_7Tanh[x], g(x) = 1 + P_8Tanh[x]] (Fig. 4) the introduced perturbation shows a little change in width and amplitude of the soliton. The threshold value for localized inhomogeneity are P_7=-0.16, P_8=1.9.

CONCLUSION:

The MI analysis of the inhomogeneous one-dimensional AFM spin system is carried out analytically by introducing small perturbation in the amplitude and phase of the system. The results obtained are illustrated graphically. From the illustrations it is observed that reducing the perturbation wave number k_2 narrows the width and decay the amplitude of the soliton. Moreover, the effect of inhomogeneity plays a vital role in the stability of soliton, i.e. the MI growth rate or the instability of soliton decreases above the given threshold value.

REFERENCE:

[1] Nakamura K and Sasada T 1974 *Phys. Lett. A* **48** 321.

[2] Lakshmanan M and Bullough R K 1980 *Phys. Lett. A* **80** 287.

[3] Daniel M, Kruskal M D, Lakshmanan M and Nakamura K 1992 *J. Math. Phys*. **33** 771.

[4] Gouvea M E and Pires A S T 1986 *Phys. Rev. B* **34** 306.

[5] Takeno S and Kawasaki K 1992 *Phys. Rev. B* **45** 5083.

[6] English L Q, Sato M and Sievers A J 2001 *J. Appl. Phys*. **89** 6707.

[7] Vasanthi C C and Latha M M 2013 *Phys. Scr*. **88** 065012.

[8] Vasanthi C C and Latha M M 2015 *Eur. Phys. J. D* **69** 268.

[9] Benjamin T B and Feir J E 1967 *J. Fluid Mech*. **27** 417.

[10] Witham G B 1965 *Proc. R. Soc*. **283** 238.

ESTIMATION OF RADIONUCLIDES CONCENTRATION OF THE ROCK SAMPLES FROM THE WESTERN GHATS IN KERALA

M.Sheela Udhaya Roselin[a*], G.Shanthi[b]

[a]Department of Physics, Annai Velankanni College, Tholayavattam
[b]Department of Physics and Research Centre, Women's Christian College, Nagercoil

 *Corresponding Author: sheelulin@gmail.com

ABSTRACT

The present study was carried out to examine the gross alpha, gross beta activities and gamma radionuclides from rock samples in Kerala. Eleven samples were collected from different locations in Western Ghats. The gross alpha and gross beta activities were measured by using zinc sulphide scintillation detector and low beta counter. The gamma ray radionuclides were found out using NaI(Tl) gamma ray spectrometer. In this study the gross alpha activity was maximum at L6 (1559.14 $\pm$ 110.70 Bq/kg) and minimum at L4 (752.69 $\pm$ 45.91 Bq/kg), with an average of 1065.49 $\pm$71.07 Bq/kg and the gross beta activity was maximum at L3 (8377.19 $\pm$ 712.90 Bq/kg) minimum at L5 (1315.79 $\pm$ 48.82 Bq/kg) with an average of 4888.36 $\pm$ 354.67 Bq/kg. The average values of activity concentration of ^{238}U, ^{232}Th and ^{40}K would be higher than the world average values of activity concentration of these radionuclides.

Keywords: gross alpha; gross beta; gamma ray; radionuclides

1. INTRODUCTION

Background radiation in the environment arises mainly due to the presence of terrestrial and extraterrestrial radioactive sources. The radiation emitted from both these radioactive sources varies depending on location and altitude. The knowledge of radionuclide distribution and the concentration of radiation in the environment are very essential for assessing the levels of background radiation. The background radiation varies from place to place depending upon the variation of radionuclide concentration in the rock, soil and water. All the rocks contain certain amount of naturally occurring radionuclides such as uranium (^{238}U), thorium (^{232}Th) and potassium (^{40}K). Radio nuclides are present in rocks in varying amounts, and they are easily mobilized into the environment. The concentrations of naturally occurring radionuclides depend on the distribution of rocks from which they originate and the process that is used for the removal of these radionuclides from the parent rocks and transfer to soil. Therefore, the natural environmental radioactivity mainly depends on geological and geographical conditions. The natural rocks such as granite, limestone, dolomite, marble, shale and so on, are widely used as building materials for the measurement of concentration of radionuclides in rocks for assessing the radiological risks to human health. On the point of contribution to radiation dose received by mankind, the most important primordial radionuclides are uranium series, thorium series and ^{40}K (UNSCEAR, 1993).

The most important places among the well documented high natural background (NBR) areas of the world are Guarapuri in Brazil, Yangjiang in China and Chavara and

Manavalakurichi in India (Singh et al., 2007). In India we have high-background radiation areas along the South West coast. According to Paul and Gupta, the Monazite deposits occur throughout the erstwhile south Travancore region comprising parts of Kerala and Kanyakumari district, TamilNadu. The Presence of monazite deposits on the coastal areas of Kerala and TamilNadu is due to the weathering of rocks in Western Ghats (Shanthi et al., 2009), (Manigandan et al., 2014).

2. METHODOLOGY

For the present study, rock samples were collected from 24 places of Western Ghats in Kerala. Basic component of our life support system contains measureable amount of radioactivity. The radio activities due to these components are found out by using different instruments. In this work, the gross alpha and gross beta in the rock samples are measured by using the Zinc Sulphide Scintillation Detector and Low Beta Counter. The activity concentration of gamma ray radionuclides are measured using Gamma Ray Spectrometer.

Zinc Sulphide Scintillation Detector

An alpha counting system comprises of an alpha probe and counting electronics system includes high voltage supply to probe, a preamplifier, an amplifier, timer and scalar. The counter model SP 647A was used for the measurement. The PMT and crystal are placed n a light tight steel housing. So as to have very low background and have an efficiency of about 31.07%. The standard source ^{241}Am was used for detector calibrations.

Low Beta Counter

The Counters consists of two or three G.M counters. The counters have a silver or gold foil window through which the beta particles travels and reach the gas chamber with isopropyl alcohol vapours and ionize the medium. The counter model BCS36A was used for this study. The standard source ^{40}K was used and the corresponding efficiency of the counter was about 38.16%. Twenty Four rock samples were collected from the study region to measure gross alpha and gross beta activities. Each sample nearly 1Kg in weight was washed in distilled water and dried in an oven at nearly 110°C to ensure that moisture was completely removed. Then the samples are grinded as a fine powder. About 0.006gms of powdered samples are spread as a fine layer in a Aluminum planchet and its gross alpha and gross beta activity were measured using alpha and beta counter (Brug, 1997). The samples were counted for 1000s.

NaI (Tl) Scintillation Detector

The scintillation gamma ray spectrometer is one of the most efficient systems for counting gamma rays and measuring their energies. The spectrometer consists of thallium activated sodium iodide as a detector. The dimensions of NaI(TI) crystal is 5"×5". The detector has been coupled to a photo multiplier tube. The preamplifier unit amplifies the signal from the photo multiplier tube. The pulses from the preamplifier are fed to the spectrometer- amplifier. The pulses from the spectrometer - amplifier are analyzed using 2K multichannel analyzer. Standard sources such as standard monazite are used for calibration. To measure an energy spectrum of a radioactive source means to record the pulse height distribution produced by the particles emitted from the source, which is achieved with the use of an instrument called the multichannel analyzer (MCA). The gamma ray spectrum was recorded using a computer based multi channel analyzer and processed using the TMCA32

software. The derivation of K, U and Th concentrations of the samples was performed in two steps. First, it was necessary to identify the peaks from K, U and Th and the energy regions where they are well resolved in the energy spectra of standards and samples.

3. RESULTS AND DISCUSSION

Gross Alpha and Gross Beta activity of the samples

The gross alpha activity of the rock samples was calculated and tabulated in Table 1. The gross alpha activity ranged from 752.69 ± 45.91 Bq/kg to 1559.14 ± 110.70 Bq/kg with an average of 1065.49 ± 71.07 Bq/kg. The lowest activity was observed in L4 (752.69 ± 45.91 Bq/kg), while the highest alpha activity was observed in L6 (1559.14 ± 110.70 Bq/kg).

Table 1: Gross Alpha and Gross beta Activities of the Rock Samples

Sample Location	Gross α Activity (Bq/Kg)	Gross β Activity (Bq/Kg)
L1	1290.32±103.35	7412.28±593.72
L2	860.22±69.68	7017.54±568.42
L3	1021.51±86.93	**8377.19±712.90**
L4	**752.69±45.91**	4298.25±262.19
L5	1290.32±47.87	**1315.79±48.82**
L6	**1559.14±110.70**	4429.82±314.52
L7	967.74±78.39	6973.68±564.87
L8	806.45±49.19	3815.79±232.76
L9	1182.80±72.15	3026.32±184.61
L10	1021.51±62.31	3289.47±200.66
L11	967.74±55.26	3815.79±217.88
Average	1065.49±*71.07*	4888.36±354.67

The gross beta activity of the rock samples was calculated and tabulated in Table 1. The gross beta activity ranged from 1315.79 ± 48.82 Bq/kg to 8377.19 ± 712.90 Bq/kg with an average of 4888.36 ± 354.67 Bq/kg. The lowest activity was observed in L5 (1315.79 ± 48.82 Bq/kg), while the highest beta activity was observed in L3 (8377.19 ± 712.90 Bq/kg). The rock samples contains very high amount of radionuclides, and hence these locations showed very high beta activity.
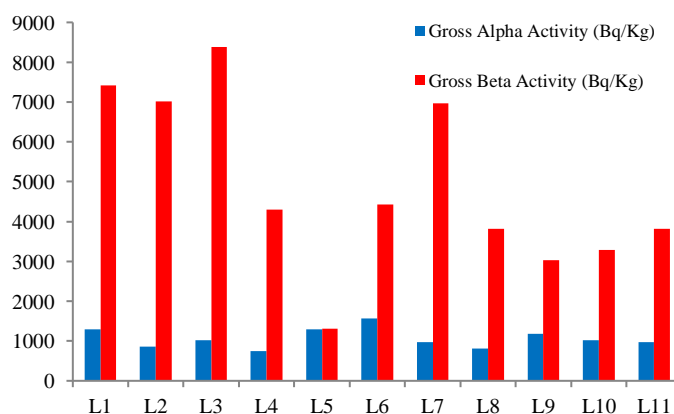
Figure 1. Comparison of Gross Alpha and Gross Beta activities of the Rock Samples

Activity concentration of radionuclides ^{238}U, ^{232}Th and ^{40}K

The gamma ray spectrum was recorded using a computer based multi channel analyzer and processed using the TMCA32 software. The derivation of K, U and Th concentrations of the samples was performed in two steps. First, it was necessary to identify the peaks from K, U and Th and the energy regions where they are well resolved in the energy spectra of standards and samples.

Table: 2 Activity concentrations (Bq kg^{-1}) of radionuclides in the rock samples

Sample Location	Activity Concentration of Radionuclides (Bqkg^{-1})		
	^{238}U	^{232}Th	^{40}K
L1	96.74±7.75	120.93±9.69.	4027.19±322.58
L2	109.04±8.832	81.24±6.58	4189.83±339.38
L3	82±6.9782	158.53±13.49	4708.9±400.73
L4	28.01±1.71	51.38±3.13	3845.16±234.55
L5	39.65±1.47	48.84± 1.81	977.12±36.25
L6	181.07±12.86	165.73±11.77	3803.34±270.04
L7	117.98 ±9.56	140.29±11.36	4336.64±351.27
L8	92.52±5.64	188.46±11.49	2415.58±147.35
L9	54.29±3.31	127.57±7.78	2260.31±137.88
L10	32.27±1.97	69.28±4.23	2441.53±148.93
L11	90.74±5.18	144.08±8.23	2089.68±119.32
Mean	84.03±5.13	117.85±8.14	3190.48±228.03

(a)

(b)
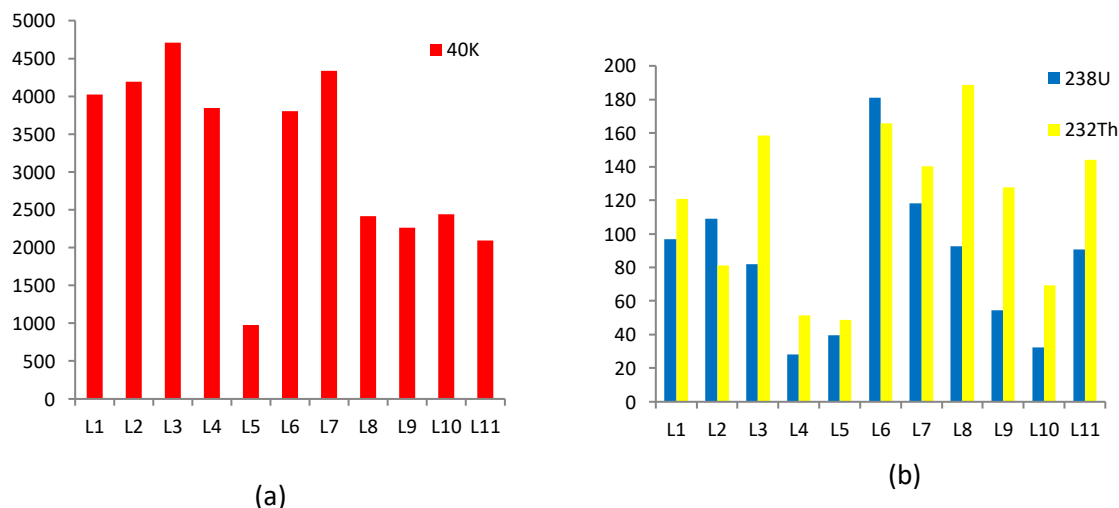
Figure: 2(a) Activity concentrations (Bq kg^{-1}) of ^{238}U and ^{232}Th in the rock samples
Figure: 2(b) Activity concentrations (Bq kg^{-1}) of ^{40}K in the rock samples

The highest activity concentrations of ^{238}U, ^{232}Th and ^{40}K were observed in the location L6, L8 and L3 (181.07±12.86 Bq/kg, 188.46 ±11.50 Bq/kg and 4708.90 ± 400.73 Bq/kg). The average values of activity concentration of ^{238}U, ^{232}Th and ^{40}K would be higher than the world average values of activity concentration of these radionuclides. The average concentrations of ^{238U,} ^{232}Th and ^{40}K were three times, four times and eight times higher than world average values. Thorium and potassium activity concentration is higher than that of

uranium in most of the samples studied. This is due to high mobilization of uranium than thorium. The variation of concentration of radionuclides are $^{238}U < ^{232}Th < ^{40}K$. Thorium and potassium activity concentration is higher than that of uranium in most of the samples studied. This is due to the reason that (a) High mobilization of uranium than thorium and potassium. (b) Thorium is migrating only through the mechanical process, so that it is difficult to migrate due to their high atomic radius.

4. CONCLUSION

In the present study, the data shows that, the gross alpha and beta activities are randomly distributed in Western Ghats in Kerala. The gross beta activity is higher than the gross alpha activity in the collected rock samples. The gross alpha and the gross beta activity values of these locations are very high due to the presence of higher amount of radio nuclides in rock samples. Hence this study will helps to prepare the baseline data for gross alpha and gross beta radioactivity in rock sample which will be used as finger print for the comparison of radioactivity level. The measured concentrations of ^{238}U, ^{232}Th and ^{40}K in the rock samples collected from the studied region are more than that of world average values 30, 35 and 400 Bq/kg. The variations of natural radioactivity levels in the studied region are due to the variation of concentrations of radionuclides in the geological formations. Presence of such higher radioactivity in the rock sample collected from the Western Ghats may be attributed to the presence of such higher amount of accessory minerals such as zircon, iron oxides, fluorite and other radioactive related minerals.

REFERENCES

1. Singh, H.N., Shankar, D., Neelakandan, V.N., Singh, V.P., 2007. Distribution patterns of natural radioactivity and delineation of anomalous radioactive zones using in situ radiation observations in Southern Tamil Nadu, India. Journal of Hazardous Materials. 141, 264-272.

2. Shanthi, G., Manian, C.G., Allan Gnana Raj, G., Thambi Thanka Kumaran, T., (2009). Radioactivity in Food Crops from High Background Radiation Area in Southwest India. Current Science. 97, 9.

3. Manigandan, P.K., Chandar Shekar, B., 2014. Evaluation of Radionuclides in the Terrestrial Environment of Western Ghats. Journal of Radiation Research and Applied Sciences. 7, 310-316.

4. Brug.W.P. (1997). Laboratory Method for Gross Alpha and Beta activity Determination (Los Alamos National Laboratory, Llos Alamos, New Mexico.

5. UNSCEAR (1993), Exposure from natural sources of radiation in United Nations scientific committee on the effect of atomic radiation, United Nations: New York.

NATURAL RADIOACTIVITY IN AGRICULTURE SOIL AND ITS ENVIRONMENTAL IMPLICATIONS IN SOUTH INDIA USING MULTIVARIATE STATISTICAL APPROACH

V.Prabha[1*], G.Shanthi[2]

[1] Rohini College of Engineering and Technology , Palkulam - 629401, TamilNadu, India.

[2] Department of Physics & Research Centre, Women's Christian College, Nagercoil -629001.

 Affiliated to Manonmaniam Sundaranar University, Abishekapatti,Tirunelveli-627012.

*Corresponding author: Prabhanair81@gmail.com.

ABSTRACT

Naturally occurring radionuclides ^{40}K, ^{238}U, ^{232}Th were determined by using NAI detector in agriculture soil samples randomly collected from various locations in Kanyakumari District, at a fertile depth of about 0-10, 10-30 and 30-50 cm. The mean activity concentrations of ^{40}K, ^{238}U, ^{232}Th were found to be 812.395,76.138 and 72.209 Bq/Kg respectively. The absorbed dose rate, annual effective dose rate, radium equivalent activity, excess life time cancer risk, hazard indices (H_{ex} and H_{in}) and annual gonadal dose equivalent were calculated. For the spatial distribution of natural radionuclides in the studied area the ratios between the detected radioisotopes have been calculated. Results were discussed and compared with those reported in similar investigations and with internationally recommended values. The multivariate statistical method was used to study the relationship between the radionuclides and the calculated radiation parameters.

Keywords: Gamma ray spectroscopy, Multivariate, radionuclides, farm soil, hazard index.

1. INTRODUCTION

The naturally occurring radioactive materials (NORMs) are found in various geological formations such as soil, rocks, water, sediments, air and in some building materials (Avwiriet al., 2012). The material containing levels of uranium, thorium and potassium that can be of radiological significance is phosphate rock used as an agricultural fertilizer. 87 % of radiation dose received by humans are from natural radiation doses, which comes from the naturally occurring radioactive isotopes of^{238}U, ^{232}Th and their progency as well as ^{40}K (Isinkaye et al.,

2015). The contribution of radiation from soil to human exposure can either be whole body due to external radiation originating directly from primordial radionuclides present in soil or internal due to inhalation .High levels of uranium and its decay products in rock and soil, and thorium in monazite sands are the main sources of high natural background radiations that have been identified in several areas of the world. Soil and rocks are the major source of radiation exposure to the population and also a means of radionuclide migration into the environment .Measurement of natural radioactivity in soils is very important and monitor the amount of change of the natural background activity with time for environmental protection.(Najamlaith et al.,2011) The usage of chemical fertilizers is increased to increase crop production and to improve the properties of the nutrient deficient lands.

The aim of this study is to measure the natural radioactivity contents, annual effective radiation dose, internal and external hazard indices in the farm soil of kanyakumari district. The data generated inthis study will provide base line values of natural radioactivity in soils and may be useful for studies in future.

2. METHODS AND EXPERIMENTAL TECHNIQUES

Sampling and sample preparation

For the measurement of the natural radioactivity in soil of different depths were collected randomly from different locations in the Kanyakumari district. After collection, samples were crushed into fine powder by using agate motor. The samples were dried in an oven at a temperature of 100^0c for 24 hours before measurement. Each sample was weighed and packed and sealed in an air tight container and kept about a four week period to allow radioactive equilibrium among the daughter products of radon ^{232}Rn, thoron (^{220}Rn) and their short lived decay products. (Dabaynehetal., 2008).

Detection technique

Each sample was measured with a gamma ray spectrometer consisting of a NAI (TI) and a multi- channel analyzer. The detector is shielded in a chamber of a cylindrical lead (100 mm thick). This shield serves to reduce the background radioactivity. The absolute efficiency of the NAI (TI) detector was determined. Each sample was placed in plastic containers as the same size

as that of multi element standard. ^{232}Th activity of the sample were determined from the daughters through the intensity of 1120 Kev gamma line and the ^{238}U activity were determined through the intensity of 1764 Kev gamma line, ^{40}K activity were determined from the 1460 kev emission gamma- lines. The samples were counted for 2000s depending on the concentration of the radionuclides.

Measurement of natural radioactivity

Through calculating the area under the peak and by the detector efficiency curve, the activity concentration was determined using the formula

$$C = \frac{Cn}{\pounds P\gamma Ms} Bq/Kg$$

Where C is the activity concentration of the radionuclide in the sample given in Bq/Kg. C_n is the count rate under the corresponding peak, $\pounds$ is the detector efficiency at the specific γ ray energy. $P\gamma$ is the absolute transition probability of the specific gamma ray and M_s is the mass of the sample.

Table:1 Activity concentrations of ^{40}K, ^{238}U, ^{232}Th in coconut cultivated soil samples

Location	Location Code	Depth cm	Activity concentration of radionuclides(Bq/Kg)		
			^{238}U(Bq/Kg)	^{232}Th(Bq/Kg)	^{40}K(Bq/Kg)
Mondaikadu	MDU	0-10	128.26	124.79	1106.61
		10-30	108.39	107.03	1071.21
		30-50	58.12	74.74	501.31
Karingal	KGL	0-10	64.43	124.74	862.88
		10-30	71.64	115.04	731.03
		30-50	45.76	58.35	316.88
Thingal Nagar	TNR	0-10	91.89	115.31	1489.03
		10-30	52.21	59.6	741.6
		30-50	26.72	50.55	561.25
Paraseri	PRY	0-10	35.74	54.61	648.05
		10-30	19.5	28.39	385.24
		30-50	11.67	27.65	122.38

		0-10	109.44	127.62	1975.96
Manavalakurichy	MKY	10-30	104.38	117.74	1145.15
		30-50	19.91	90.99	527.35

3. RESULTS AND DISCUSSION

Naturally occurring radioactive materials have been investigated in soil used for agriculture in some locations in kanyakumari district about various depths measured using gamma ray spectrometer are shown in table 1. The average values of all radionuclides are higher than the world wide average given by the UNSCEAR 2000. The average values for ^{40}K, ^{238}U, ^{232}Th are 812.395,76.138,72.209 Bq/kg respectively Due to natural radioactivity associated with the soil, the radiation hazard index are determined .The obtained parameters are compared with internationally recommended with safety limits.
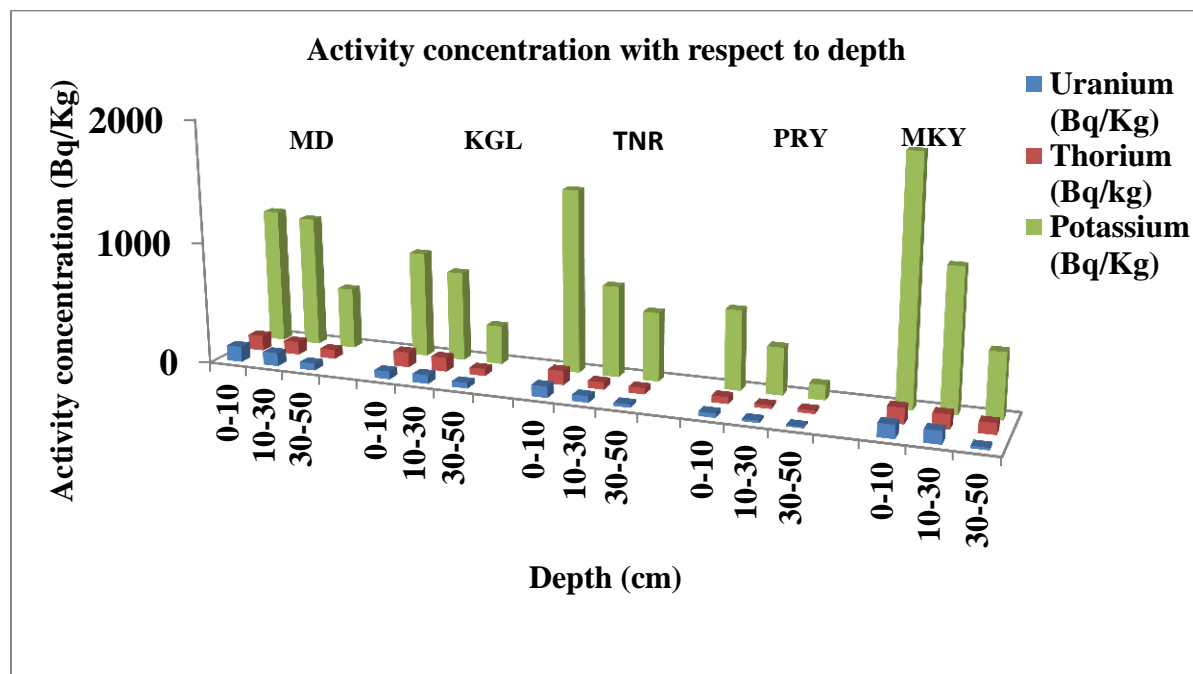
Figure 1: Activity concentration with respect to various depths

Radiological hazard parameters

Calculation of radium equivalent activity (Ra_{eq})

Radium equivalent activity Ra_{eq} (Bq/Kg) is the exposure to radiation which is calculated using the formula

Raeq = C_u + 1.43 C_{th} + 0.07 C_k

Whereas $C_{u,}C_{th,}C_k$ are the specific activity concentrations of ^{238}U, ^{232}Th, ^{40}K in Bq/Kg. The radium equivalent activity concept allows a single index or number to account for the radiation hazards associated with the mixture of uranium,thorium and potassium in agriculture soil samples in different locations (Suresh Gandhi etal.,2013).The mean value of Ra_{eq} is 241.928 Bq/Kg which is lower than the recommended value of about 370 Bq/kg.

Calculation of absorbed dose rate

The external , terrestrial gamma radiation and the absorbed dose rate in air at a height of about 1m above the ground is calculated by using the conversion factor of 0.461 nGyh^{-1}/ Bq/kg for ^{238}U, 0.623 nGyh^{-1}/ Bq/kg for ^{232}Th and 0.0414 nGyh^{-1}/ Bq/kg for ^{40}K (UNSCEAR 2000).

D = 0.461 C_u + 0.623 C_{th} + 0.0414 C_k

$C_u,C_{th,}C_k$ are the activity concentrations(Bq/Kg) of ^{238}U,^{232}Th,^{40}K in agriculture soils respectively. The absorbed dose rate for most of the samples of various depths are higher than the world average value 60 nGy/h is due to the significant of ^{232}Th in that locations.Figure 2 represents the radium equivalent activity and absorbed dose with various depths of different locations in kanyakumari district.

Calculation of annual effective dose equivalent (AEDE)

The annual effective dose equivalent is calculated using a conversion factor of 0.7SvG/y which is used to convert the absorbed rate to human effective- dose equivalent with an outdoor and indoor occupancy of 20% and 80% respectively. (UNSCEAR 2000).

AEDE(mSv/y)= D(nGyh^{-1}) x 8760h x 0.2 x0.7SvGy^{-1}

The average absorbed dose rate is about 0.5681 is higher than the permissible value of 0.48mSv/y.

Table: 2 Radiological hazard parameters in the coconut farm soil in Kanyakumari district

Location Code	Depth Cm	Ra_{eq} (Bq/kg)	D (nGy/h)	AEDE (mSv/y)	H_{ex}	H_{in}	I_γ	ELCR ($\times 10^{-3}$)
MDU	0-10	391.918	182.6857	0.89618	4.8493	0.2240	2.8407	0.78416
	10-30	343.926	160.9956	0.78978	4.6515	0.1974	2.5070	0.69105
	30-50	203.599	94.11057	0.46166	2.1968	0.1154	1.4690	0.40396
KGL	0-10	309.25	143.1385	0.70218	3.6851	0.1755	2.2521	0.61440
	10-30	292.436	134.9606	0.66206	3.1681	0.1655	2.1153	0.57930
	30-50	153.600	70.56624	0.34617	1.4130	0.0865	1.0998	0.30289
TNR	0-10	371.438	175.8453	0.86262	6.3070	0.2156	2.7583	0.75479
	10-30	194.541	91.90185	0.45083	3.1586	0.1127	1.4384	0.39448
	30-50	142.222	67.04632	0.32890	2.3558	0.0822	1.0578	0.28779
PRY	0-10	163.732	77.32744	0.37933	2.7334	0.0948	1.2164	0.33192
	10-30	89.7611	42.62541	0.20910	1.6202	0.0522	0.6707	0.18296
	30-50	60.6327	27.67235	0.13574	0.5294	0.0339	0.4358	0.11878
MKY	0-10	444.085	211.7638	1.03882	8.3357	0.2597	3.3231	0.90897
	10-30	360.924	168.8804	0.82846	4.9416	0.2071	2.6367	0.72490
	30-50	190.631	87.69757	0.43020	2.1995	0.1075	1.3942	0.37643

Calculation of gamma radiation representative level index (I_γ)

Estimation of the level of gamma radiation associated with different concentrations of some specific radionuclides is known as representative level index (Shanthi et al., 2010) is given by

$$I_r = \frac{C_u}{150 Bq-1} + \frac{C_{th}}{100 Bq-1} + \frac{C_k}{1500 Bq-1}$$

Where C_u, C_{th}, C_k are the activity concentrations of $^{232}U, ^{238Th}, ^{40}K$ in Bq/Kg. Gamma representative index average value is 1.8143 mSv and in some locations of various depths the values exceeded unity due to radiologically hazardous.

Table 3: Comparison of average activity concentration of $^{238}U, ^{232}Th, ^{40}K$ and Ra_{eq} in the worldwide agriculture soils.

Location	^{238}U (Bq/kg)	^{232}Th (Bq/kg)	^{40}K (Bq/kg)	Ra_{eq} (Bq/kg)	Reference
Northern Jordan	49.90	26.70	291.10	103.10	Alhamameh and Awadallah (2009)
India Amritsar	50.61	78.31	301.80	189.67	Mehra, and singh (2011)
Malaysia	80.63	116.87	200.66	258.36	Ahmad et.al.(2015)
India	76.138	72.209	812.395	241.928	Present work
Worldwide	32	30	400	370	UNSCEAR(2000)
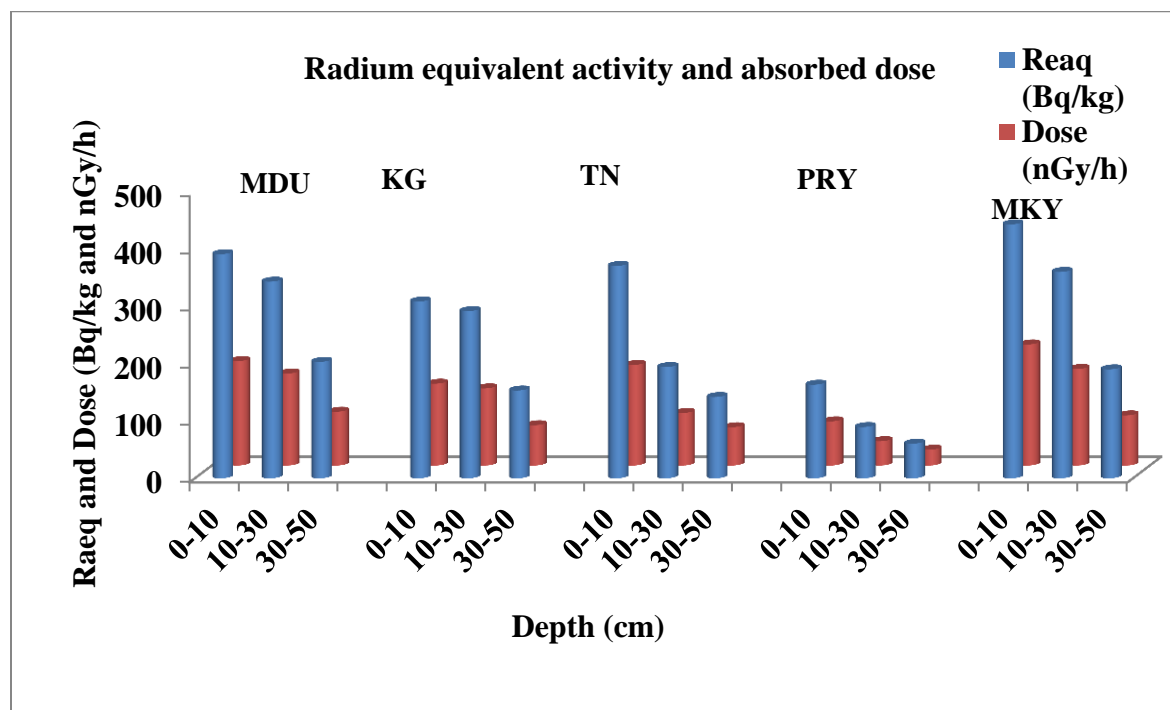
Figure 2: Radium equivalent activity and absorbed dose with respect to depths.

Calculation of External and internal hazard index (H$_{ex}$, H$_{in}$)

External hazard index due to the emitted gamma rays of the samples were calculated using the formula

$$H_{ex} = \frac{C_u}{370Bq-1} + \frac{C_{th}}{259Bq-1} + \frac{C_k}{4810Bq-1}$$

C_u, C_{th}, C_k are the activity concentrations(Bq/Kg) of $^{238}U, ^{232}Th, ^{40}K$ in agriculture soils respectively.

In internal hazard index radon and its short lived products are also hazardous to the respiratory organs. By the internal hazard index, the internal exposure to radon and its daughter products is qualified using the equation (Senthil Kumar et al., 2010)

$$H_{in} = \frac{C_u}{185} + \frac{C_{th}}{259} + \frac{C_k}{4810} \leq 1$$

The mean value of H$_{ex}$ (3.47) is higher than unity and H$_{in}$(0.8932) is lesser than unity.
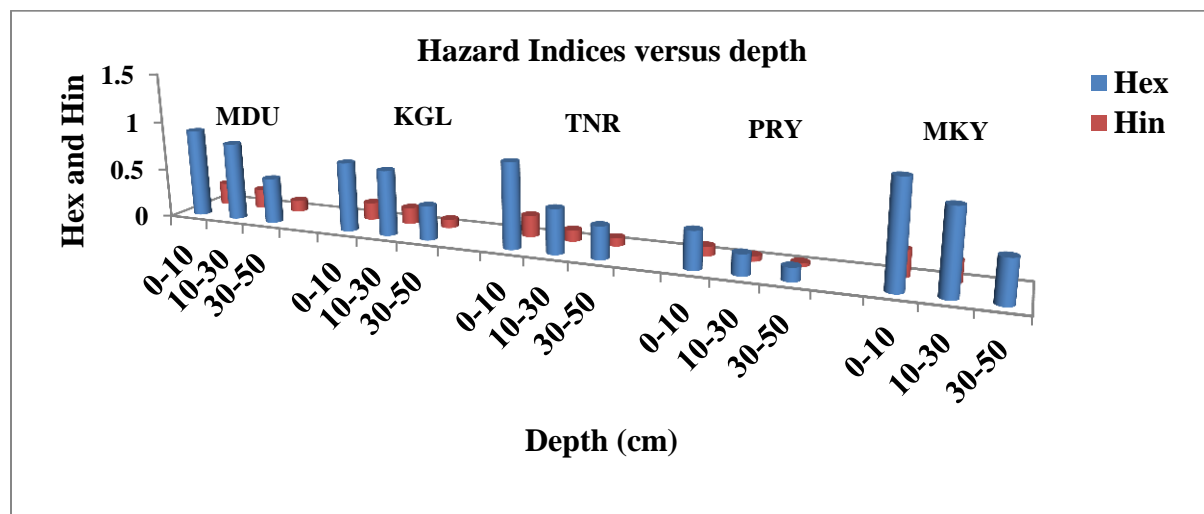
Figure 3: Hazard indices with respect to depth

Excess life time cancer risk (ELCR)

The probability of developing cancer over a life time at a given exposure level. A higher value of ELCR implies higher probability induction of cancer of the individual that was exposed calculated using formula (Taskin et al., 2009)

ELCR= AEDE x DL x RF

DL = Duration of Life, RF= Risk factor (S/v)

The average value of ELCR is 0.4971 x 10^{-3}.ELCR value is greater than the world permissible value 0.29 x10^{-3}.
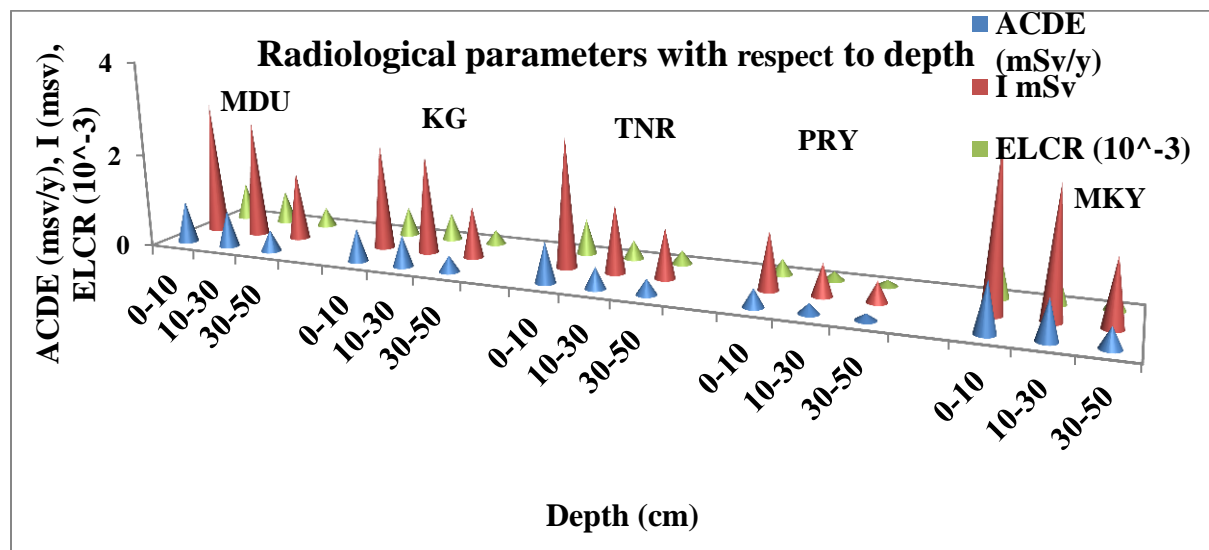
Figure 4: Radiological parameters with respect to various depths

Multivariate Statistical Analysis

Multivariate statistical procedures for data treatment and histograms were performed using the software package SPSS version 16.0 for windows. Pearson correlation and cluster analysis were carried out to clarify the relationship between the variables, the influence of soil parameters on the distribution of natural radionuclides. Multivariate statistical methods are successfully used to interpret the relationships among variables in the environmental studies (Liu et al., 2003). This method can also help to simplify and organize large data sets to provide meaningful insight (Laaksoharjuet al., 1999), and can help to indicate natural associations between samplesand/or variables.

Basic Statistics

The statistical behavior of the measured radionuclide is shown in table 4. "Skewness is a measure of the asymmetry of the probability distribution of a real valued random variables"(Adam and Eltayeb 2012).Positive skewness denotes the distribution with an

asymmetric tail extending towards values that are positive. Kurtosis is a measure whether the data are peaked or flat relative to a normal distribution. Positive kurtosis denotes flat distribution and positive denotes peak distribution.

Table: 4 Basic statistics of the measured data

Variables	^{238}U(Bq/kg)	^{232}Th(Bq/kg)	^{40}K(Bq/kg)
Mean	31.3227	59.2389	782.6187
SD	13.67075	28.47946	458.4244
Variance	186.89	811.08	210152.9
Kurtosis	-0.609	1.433	1.191
Skewness	0.402	1.471	1.012
Maximum	12.84	30.25	143.04
Minimum	58.42	125.21	1881.48
Frequency distribution	Log-Normal	Normal	Normal

Factor Analysis

Factor analysis is to determine the interrelationships among radioactive variables and to describe these variables in terms of their common dimensions (J.C.Davisetal., 1986). Varimax rotation is performed for factor loading (H.F.Kaiser 1958). Component 1 is loaded with ^{238}U and other parameter explains 57.093 % and component 2 is loaded with ^{40}K which explains 42.44% of total variance. Component 1 explains more than the component 2. The two factors extraction in this study explains 99.427% of the total variance of the data set.

Table 5: Rotated factor loading of variables

Variables	Component 1	Component 2
^{238}U(Bq/kg)	1.00	-.140
^{232}Th(Bq/kg)	.931	-.287
^{40}K(Bq/kg)	.937	.347
Raeq (Bq/kg)	.998	-.061

D(nGy/h)	.999	-.036
AEDE (mSv/y)	.999	-.036
Hex	.945	.326
Hin	.999	-.036
Iγ	.999	-.032
ELCR(x10^{-3})	.999	-.036
Percentage of variance explained	57.093	42.344

Pearson Correlation Coefficient Analysis

Person Correlation Analysis is analyzed in order to determine the mutual relationships between the radionuclide and radiological parameters. Positive correlation is observed among the three radionuclides and all the radiation hazard parameters imply very strong relationship with agriculture soil and radiological parameters. It also shows that all radionuclides will contribute the emission of gamma radiation.

Table 6: Pearson correlation between the radioactive variables in agriculture soils

Variables	U	Th	K	Ra$_{eq}$	Iγ	D	H$_{ex}$	H$_{in}$	AEDE	ELCR
U	1									
Th	0.840	1								
K	0.816	0.781	1							
Ra$_{eq}$	0.940	0.948	0.9142	1						
Iγ	0.935	0.943	0.9260	0.999	1					
D	0.939	0.941	0.9242	0.999	0.9999	1				
H$_{ex}$	0.832	0.791	0.9995	0.923	0.9345	0.93	1			
H$_{in}$	0.965	0.932	0.9003	0.996	0.9949	0.99	0.911	1		
ACDE	0.939	0.941	0.9242	0.999	0.9999	1	0.933	0.99	1	
ELCR	0.939	0.941	0.9242	0.999	0.9999	1	0.933	0.99	1	1

Cluster Analysis

The identification and classification of groups with similar characters in a new group. Cluster analysis through axes is used to identify similar characteristics among natural radio isotopes and radiological parameters in the soil. It is also useful to prove for determining the linkages between soil samples from different locations to analyze the data. Cluster I consists of and ^{40}K and their radiological parameters. Cluster II consists of ^{238}U. Cluster III consists of ^{232}Th.
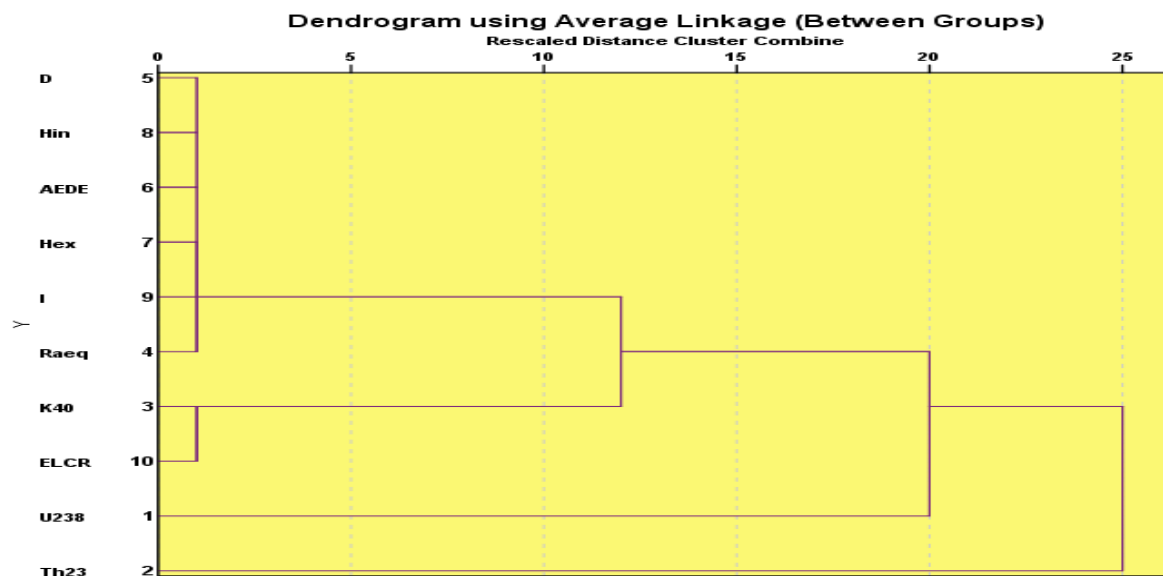
Figure 5: Dendogram of radioactive variables

4. CONCLUSION

The measured average values of ^{40}K, ^{238}U, ^{232}Th are higher than the world wide range given by UNCEAR (2000). Ra$_{eq}$ average value is less than the value identified by UNSCEAR (2000). Due to low cost and more needs phosphate fertilizers are used. The presence of high activity of ^{40}K is due to the potassium containing fertilizers. Due to the accumulation of radioactivity in upper surface of the soil ^{232}Th have the maximum value. At maximum depth the ^{238}U value is minimum due to continuous fertilization. From multivariate statistical analysis as a result of same origin the positive correlation occurs between ^{40}K, ^{238}U, ^{232}Th. The result serves as a reference for the future studies.

REFERENCES

1. Adam AM, Eltayeb MA. Multivariate statistical analysis of radioactive variables in two phosphate ores from Sudan. J Environ Radioact.2012;107:23-43

2. UNSCEAR, (2000). Exposure of natural radiation sources. Annex B. Sources and effects of ionizing radiation , United Nations, Newyork. United Nations scientific Committee on the effects Atomic Radiation.

3. Senthil kumar,B.,Dhavamani, V.,Ramkumar, S. and Philominathan, P. Measurement of gamma radiation levels from Thanjayur, using gamma ray spectroscopy and estimation of populationexplosure. J. Med.Phys., 2010;35, 48-53.

4. Taskin. H., Karavus M., Ay P., Topuzoghi, A., Hindiroglums, S. and karahan, G.Radionuclide concentration in soil lifetime cancer risk due to gamma radioactivity in Kirklaeli,turkey,Journal of environmental Radioactivity,2009;100,49-53.

5. J.C.Davis, Statistics and Data Analysis in Geology,Wiley,Newyork,1986, pp.17.

6. H.F.Kaiser. The varimax criteria for analytical rotation in factor analysis. Psychometrika 1958;23, 187-200.

7. UNSCEAR. Sources and Effects of Ionizing Radiation. United Nations, New York: United Nations Scientific Committee on the Effect of Atomic Radiation; 1993.

8. Liu WX, Li XD, Shen ZG, Wang DC, Wai OWH, Li YS.Multivariate statistical study of heavy metal enrichment in sediments of the Pearl River Estuary. Environ Pollut 2003; 121:377-88.

9. Laaksoharju M, Skarman C, Skarman E. Multivariate mixing and mass balance (M3) calculations, a new tool for decoding hydrogeochemicallin formation. Applied Geochemistry1999;14:861-71.

10. Wenning RJ, Erickson GA. Interpretation and analysis ofcomplex environmental data

Using chemometricmethods.TrendsAnalytChem 1994;13:446-57.

11. K.M. Dabayneh, L.A. Mashal and F.I. Hasan, "Radioactivity Concentration in Soil Samples in the Southern Part of the West Bank, Palestine". Radiation Protection Dosimetry,2008; Vol.131, No. 2, pp.265-271.

12. Avwiri G.O, Ononugbo C.P, Nwokeoji I.E. Radiation Hazard Indices And Excess Lifetime Cancer Risk in Soil, Sediment and Water Around Mini-Okoro/Oginigba Creek, Port Harcourt, Rivers State, Nigeria. Comprehensive Journal of Environment and Earth Sciences,2014; 3(1), 38-50. ISSN-2315-7488 Knowledgebase Publishers.

13. Isinkaye M.O. and Emelue. Natural radioactivity measurements and evaluation of radiological hazards in sediment of Oguta lake, South East Nigeria. Journal of Radiation Research and Applied Sciences,2015;8: 459-469.

14. Shanthi G., Thampi J. T. K. Allen G. G. R.andManiyan C. G. Measurement of activity concentration of natural Radionuclides for the Assessment of Radiological indices. Radiation Protection Dosimetry.2015; 141(1) 90-96.

15. UNSCEAR (1993). United Nations Scientific Committee on effects of Atomic radiation Report to the general assembly, (New York: United Nations)

16. NajamLaith A. ,A.L.JomailyFiras M., ALFarhaEnas M. Natural radioactivity levels of limestone rocks in northern Iraq using gamma spectroscopy and nuclear track detector, J RadioanalNuclChem .2011;289:709 -715.

^{222}Rn, ^{220}Rn MEASUREMENT IN AIR – VALIDATION OF ONLINE RADON MONITOR

G Shanthi[1], Jayaram UK[1,2*], Sreekumar K[3]

[1] Department of Physics & Research Centre, Women's Christian College
Nagercoil, 629001. Affiliated to Manonmaniam Sundaranar University, Tirunelveli

[2] Kudankulam Nuclear Power Project, KKNPP, Tirunelveli

[3]Indian Rare Earth Ltd- IREL, Manavalakurichi

*Corresponding author: jayaramkknpp@gmail.com

ABSTRACT

Presently in earth crust uranium 235, 238 and thorium 232, are the main radioactive elements and they are the parent members of corresponding natural radioactive decay chains viz. (4n+3), (4n+2) and 4n. All three of these natural decay chains include isotopes of radon. Radon-219, or "actinon", in the uranium-235 series, radon-220, or "thoron", in the thorium-232 decay chain and radon-222, or familiar "radon", in the uranium-238 decay chain. Online radon monitor DURRIDGE RAD7 uses alpha spectrometry technique to detect radon and thoron directly. The associated 'capture' software is versatile, can be used for real time data charting and for off line data analysis including related corrections. It is evaluated here using monazite source and emanating radon/ thoron gases. The results are in good agreement with the expected value of ^{222}Rn and ^{220}Rn growth from monazite.

1. INTRODUCTION

When earth was formed, billions of years ago there were probably many radioactive elements included in the mix. Presently when we look at the survivors mainly uranium 235, uranium 238 and thorium 232 are seen. Each has a measured half life of billions of years and they are the parent member of corresponding natural radioactive decay chains viz. (4n+3), (4n+2) and 4n respectively.

All three of these natural decay chains include isotopes of radon. ^{219}Rn (Radon-219), or "actinon", is a link in the uranium-235 chain. We probably never encounter actinon in indoor air, due to its scarcity and short half-life. ^{220}Rn (Radon-220), or "thoron", is part of the thorium-232 decay chain and at times we encounter thoron in air, particularly near southern coast of Tamilnadu and the coast of Kerala, as soil gas. ^{222}Rn (Radon-222), or familiar "radon", is part of the uranium-238 decay chain. We can detect radon-222 in indoor air, outdoor air, and soil gas. The radon isotope is the first element, in each of the decay chains, that is not a metal. It is, in fact, an inert, or "noble", gas, which can escape any chemical compound its parent (radium) was in, and diffuse into the air.

^{222}Rn an inert gas, alpha emitter that does not stick to or react with any materials. It has a half-life of 3.82 days. When the radon nucleus decays, it releases an alpha particle with 5.49 MeV of energy, and the nucleus transforms to polonium-218 and so on. Similarly to ^{222}Rn, every ^{220}Rn (thoron) nucleus eventually decays through a sequence of 5 transformations to Lead-208. The main distinction is the very different half lives involved. Thoron has a half life of only 55.6 seconds. It emits a 6.29 MeV alpha particle and transforms to polonium-216, which in turn has only a 0.15 second half-life before emitting a 6.78 MeV alpha particle and transforming to Lead–212 (^{212}Pb)

There are many methods to monitor radon and several types of continuous radon monitors on the market. Nearly all of these are designed to detect alpha radiation, but not beta or gamma radiation as it is very difficult to build a portable detector of beta or gamma radiation that has both low background and high sensitivity.

Growth and Decay of ^{222}Rn and ^{220}Rn:

$$\frac{dN_1}{dt} = -\lambda_1 N_1$$

N_1 is initial number of radium atoms, λ_1 is the decay constant.

^{222}Rn or ^{220}Rn growth from decay of ^{226}Ra or ^{224}Ra is given by

$$\frac{dN_2}{dt} = \lambda_1 N_1 - \lambda_2 N_2$$

N_2 is Number of radon atoms λ_2 is the decay constant.

Solving above differential equation

$$N_1(t) = N_1^0 e^{-\lambda_1 t}$$

$$N_2(t) = \frac{\lambda_1}{\lambda_2 - \lambda_1} N_1^0 (e^{-\lambda_1 t} - e^{-\lambda_2 t})$$
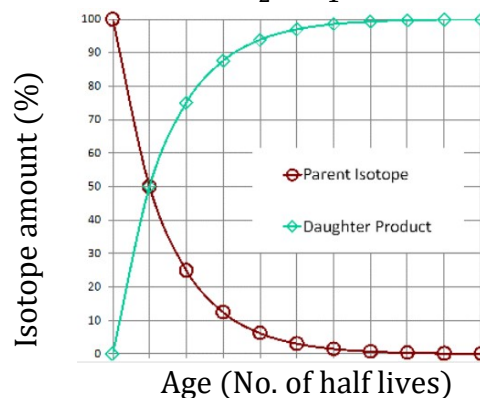
Fig 1. Growth of ^{220}Rn or ^{222}Rn
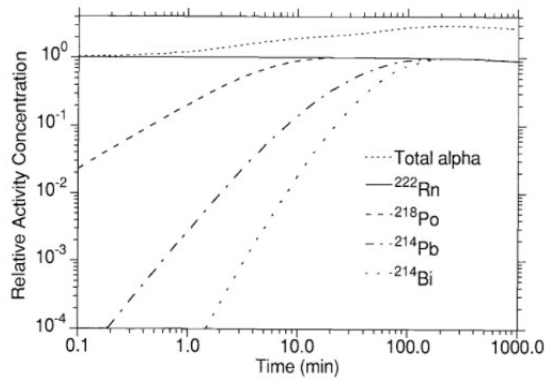
Fig 2. Relative activity concentration of ^{222}Rn and its immediate decay products as a function of time. It is assumed that ^{222}Rn is present initially
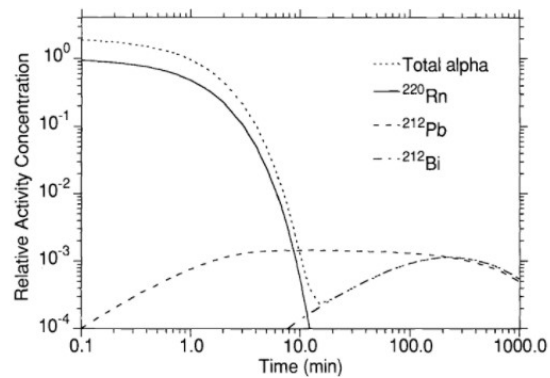
Fig 3. Relative activity concentration of ^{220}Rn and its immediate decay products as a function of time. It is assumed that ^{220}Rn is present initially

2. MATERIALS AND METHOD

Monitoring of radon isotopes (^{222}Rn, ^{220}Rn) in air

Radon measurement techniques are classified based on three characteristics (Table 1): (i) whether the technique measures ^{222}Rn or its daughter products; (ii) time resolution and (iii) radioactive detection of the type of emission - either alpha, or beta particles or gamma radiation resulting from radioactive decay. Most common methods rely on detection of alpha particles. Sometimes a single alpha particle (e.g., ^{218}Po for ^{222}Rn) is detected to measure radon isotopes or by counting all three alpha particles produced in the decay of ^{222}Rn (i.e., ^{222}Rn, ^{218}Po, and ^{214}Po) using scintillation counters. Some methods are based on the detection of gamma-ray emitted radionuclides during radioactive decay of the progeny of ^{222}Rn (^{214}Bi, ^{214}Pb) and only a few methods utilize beta decays.

Table 1. Methods and Instruments to measure radon and its progeny

Radon Gas					Progeny	
Passive methods		Active methods			Pump/filter assembly	
• No power supply • Integral exposure measurement • Analysis after exposure using special equipment		• Electrical power required • Storing the time distribution of radon concentration • Direct data reading				
Track etch	Electret	Silicon detector Alpha spectroscopy	Ionisation chamber	Scintillation chamber Lucas cell	First sample then analyse	Continuous analysis

Radon monitors based on alpha particle detectors presently used are:
1. Scintillation cells or "Lucas cells"

2. Ion chambers
3. Solid state alpha detectors.

Principle of Lucas cells

Lucas Cell is a 150 cc Cylindrical chamber which is internally coated with ZnS(Ag) scintillator powder and one side (usually the bottom side) has transparent flat surface and constitutes a viewing window. The cell typically has two sampling ports, each fitted with a valve, and a photomultiplier tube is coupled to the transparent window of the cell. When an alpha particle produced within the cell strikes the phosphor, a flash of light is produced and is sensed by the photomultiplier tube which is optically coupled to the cell window and associated electronics (preamplifier and multiplexer) and is counted using a multichannel analyzer (MCA) or traditional scalar arrangement. The use of multichannel analyzer advantages include: (i) ability to observe the number of counts above and below the 'window' of the counting region. (ii) the overall shape of the distribution allows easy identification of spurious counts resulting from electrical noise or interference. (iii) changes in the performance caused by voltage drifts or deterioration of the PMTs; and (iv) MCAs can be programmed to make a set number of individual counts during the counting period.

After radon is filled in a Lucas cell and before it is assayed in a scintillation counter, it is usually stored for about 3 h for the daughter products ^{218}Po, ^{214}Pb, ^{214}Bi and ^{214}Po to reach secular equilibrium with 222Rn (governed by the half-life the longest lived daughter, ^{214}Pb, with a half-life of 26.8 min). In this decay of ^{222}Rn, three alphas (from the decay of ^{222}Rn, ^{218}Po, ^{214}Po) and 2 betas (from the decay of ^{214}Pb and ^{214}Bi) along with a number of gamma-ray lines are produced. The background of the Lucas cell is expected to increase due to its repeated use from the decay of ^{222}Rn daughter products during the time between filling and evacuation of the cell (after counting). In this interval, a finite amount of ^{210}Pb would have been produced from the decay of ^{214}Bi via ^{214}Po. With time, ^{210}Pb decay to ^{210}Po (alpha decay) via ^{210}Bi (beta emitter) takes place and thus periodic monitoring the background of each of the Lucas cell is essential.

Principle of ionisation chambers

A 5 MeV alpha particle creates about 10^5 electron ion pairs along its track in a gas of atmospheric pressure, which would give rise to a large electric pulse with a small amplitude variation if this charge could be collected completely. Rare gas filled ionisation chambers in pulse counting mode for alpha particle detection will have good spectral resolution and suitable for the purpose.
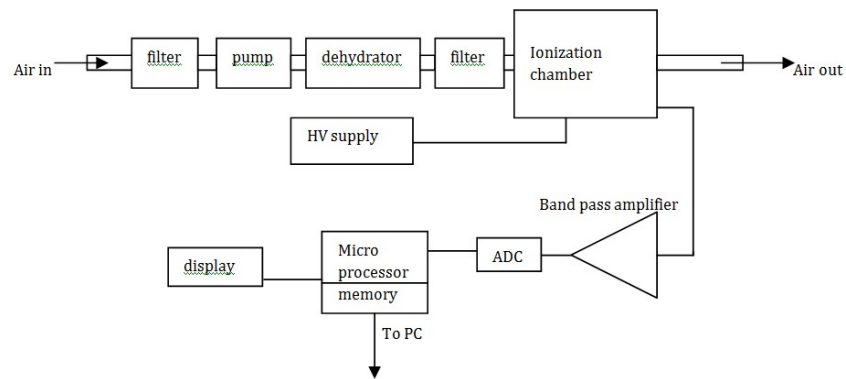
Fig 4. Block scheme of ionisation chamber and the associated equipment.

Each of these types has advantages and disadvantages relative to the others. All of these types can be used for low background alpha particle counting.

Solid state detectors

DURRIDGE RAD7 direct radon monitor uses a solid state alpha detector (usually silicon) that converts alpha radiation directly to an electrical signal. The advantages of solid state devices are ruggedness and the ability to electronically determine the energy of each alpha particle. This makes it possible to tell exactly which isotope (polonium-218, polonium-214, etc.) produced the radiation, so that one can immediately distinguish old radon from new radon, isotopes of radon, and signal from noise. The alpha spectrometry technique is having advantage in sniffing or grab-sampling applications.

The RAD7 uses a high electric field with a silicon semiconductor at ground potential to attract the positively charged polonium daughters, $^{218}Po^+$ ($T_{1/2}$=3.10min; Eα=6MeV) and $^{214}Po^+$ ($T_{1/2}$=164μSec; Eα=7.67MeV) which are then encountered as a measure of the radon activity in air.

Experiment to validate the RAD7

An experiment set up is made with a conical flask containing 20 gm of bulk monazite (figure -5). The emanation from the bottle is directly connected to RAD7 through a moisture absorbing setup as designed in recirculation mode.
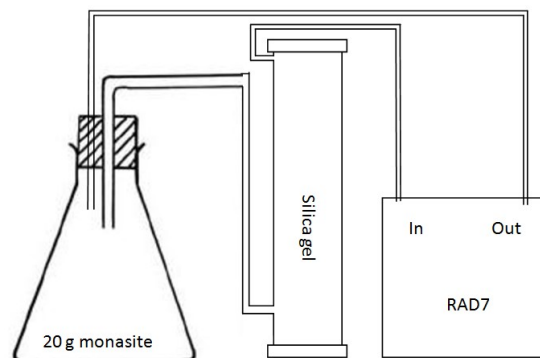
Fig. 5. Experimental setup

3. RESULTS AND DISCUSSION

It is expected to develop ^{222}Rn and ^{220}Rn with respect to the half life of isotopes in each series and readings of ^{222}Rn and ^{220}Rn is taken using the "capture" soft ware of RAD7. In few minutes ^{220}Rn achieves a stable value and radon slowly builds-up and it takes a few days to attain a stable value.

Table 2. RAD 7 readings observed on different dates

RAD 7 online readings observed (average) on different dates		
Day	^{222}Rn (Radon) (Bq/m³)	^{220}Rn (Thoron) (Bq/m³)
Day 1	85±9	591±46
Day 2	92±4.9	650±24
Day 3	84.7±5.9	641±24
Day 4	90.5±7	646±27
Day 5	79.5±11	544±40
Day 6	93.6±6	606±24
Day 7	110±6	677±29
Day 8	84.6±11	587±43
Day 9	107±8	638±28
Day 10	107±13	614±46
Day 11	89.6±7	630±28
Day 12	88.8±8	594±28
Day 13	103±11	652±43
Day 14	83.7±8	566±31
Day 15	100±10	629±28
Day 16	102±8	612±41
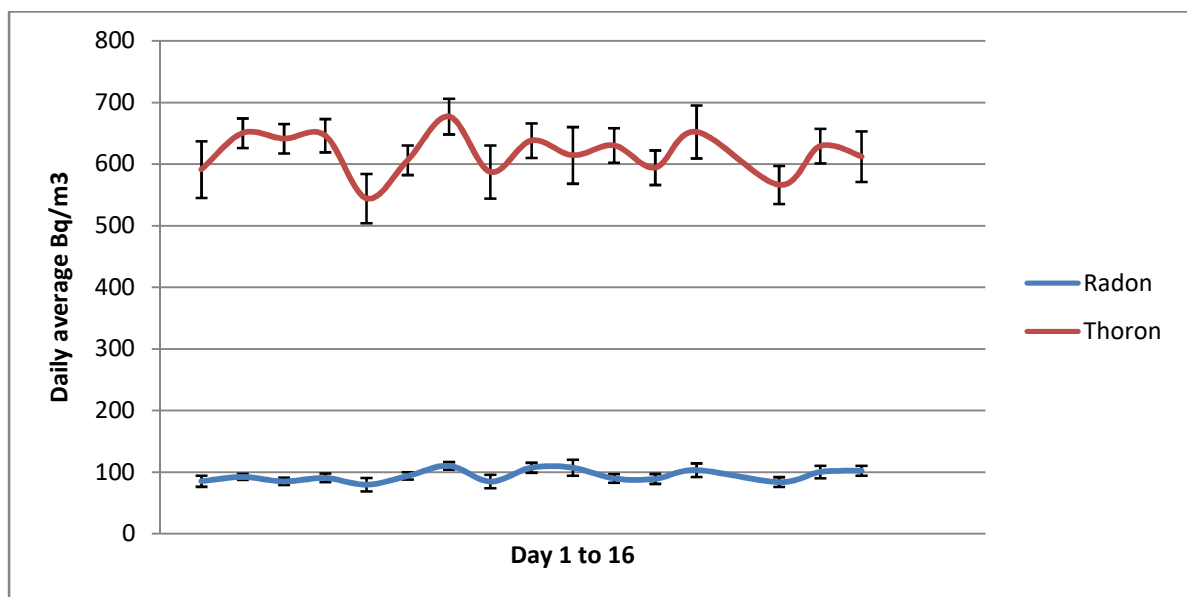
Fig 6. Plot of ^{222}Rn and ^{220}Rn growth from observed RAD 7 readings

Fig 7. Experimental set up
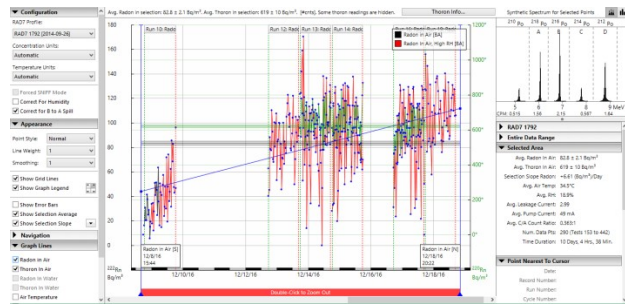
Fig 8. Spectrum of capture software observed

4. CONCLUSION

For many instruments, ^{222}Rn and ^{220}Rn interfere with each other. Generally it is difficult to measure one isotope accurately in presence of the other. Many radon detectors needs to wait for the daughters to decay away (about three hours) before counting another sample. With the RAD7, however, we can go from high to low concentrations in a matter of minutes by counting in SNIFF mode, since the RAD7 distinguishes the different alpha-emitting daughters by their alpha energy. The RAD7 separates ^{222}Rn and ^{220}Rn signals and counts the two isotopes at the same time with little interference. The associated 'capture' software provides a wealth of graphing and data analysis options once the data is downloaded. It is also capable to monitor the real time data in a chart recorder. The results are in good agreement with the expected value of ^{222}Rn and ^{220}Rn growth from monazite.

REFERENCE

1. Radon: Prevalence, measurements health risks and control, ASTM manual series MNL 15.
2. RAD 7 Radon detector user manual.
3. Physics for radiation protection , James E Turner.
4. Radon: A Tracer for Geological, Geophysical and Geochemical Studies. Mark Baskaran. ISBN 978-3-319-21329-3
5. http://www.SARAD.de/

THE MEASUREMENTS OF RADON AND THORON FROM AGRICULTURAL SOIL

S.Sumitha Devi[*], G.Shanthi
Department of Physics & Research Center,
Women's Christian College, Nagercoil 629001.
(Affiliated to Manonmaniam Sundaranar University, Tirunelveli)

* Corresponding Author:sumitha18sumi@gmail.com

ABSTRACT

In the present study Radon and Thoron Concentrations are analyzed from the Agricultural soil at depth 15 cm from different villages in Tirunelveli District of Tamil Nadu. The Concentration of Radon and Thoron is measured using electrostatic solid state alpha detector (RAD7). Thoron is an isotope of the element radon having very similar properties. Both are chemically inert radioactive gases that occur naturally from the decay of radioactive elements in soils and minerals. The result indicates Concentration of Radon is smaller than Thoron. The highest Concentration of Radon and Thoron in the latitude $8^{\circ}37'$ (Mannarpuram) is 1.0 Bq/m^3 and $8^{\circ}30'$ (Kumbilambadu) is 14.0 Bq/m^3. The lowest Concentration of Radon is 0.2 Bq/m^3 in two various places that is in the latitude $8^{\circ}24'$ (Soundarapandipuram) and $8^{\circ}45'$ (Malayadiputhoor). Thoron lowest concentration in $8^{\circ}32'$ (Pushbavanam) is 0.2 Bq/m^3.

1. INTRODUCTION

Radiation is form of energy such as light (or) heat. Radiation is characterizing according to the frequencies of the wavelengths. Radiation has always been present and is all around us in many forms. All living organisms including human beings are exposed to low levels of natural nuclear radiation during their daily lives. Life has evolved in a world containing significant levels of ionizing radiation. Radiation is presented in the soil, Rock, Water and in the Food too. Human body contains radioactive material. Excess of radioactivity is harmful to human life. Natural radiation is played a major role in the evolution of life itself. Biological effects due to natural radioactive substances increase along with the increase of the level of their content in the surrounding media and corresponding with the increase of the background radiation.(1) Background radiation in the environment arises mainly due to the presence of terrestrial and extraterrestrial radioactive sources.

The radiation emitted from both these radioactive sources varies depending on location and altitude. The knowledge of radionuclide distribution and the concentration of radiation in the environment are very essential for assessing the levels of background radiation. The background radiation varies from place to place depending upon the variation of radionuclide concentration in the rock, soil and water. (2) Radiation material is found throughout nature detectable amounts occur naturally in soil, rocks, water, air and food which are inhaled and ingested into the body. Our body constantly exposed to radiation generally does not affect health.(1) ^{222}Rn and ^{220}Rn are the products of ^{238}U and ^{232}Th decay series, and as such both are always present in small concentrations in many geological formations. Both uranium and thorium are commonly found in soils and minerals, sometimes separately, sometimes together. Thoron and Radon and their respective progeny differ very significantly in their half-lives and in the energies of their radiations. Thoron is an isotope of the element radon having an atomic mass of 220. The word "radon" without a mass number almost always refers to radon-222.

Thoron and Radon have very similar properties. They are both chemically inert radioactive gases that occur naturally from the decay of radioactive elements in soils and minerals. (3). When the rocks are disintegrated through natural process, radio nuclides are carried to soil by rain and flows.(5)

^{222}Rn decays with a half-life of 3.83 days by alpha emission to a series of particulate progeny. These particulate progeny (of ^{222}Rn) are also radioactive and decay through a series of alpha and beta emissions. ^{220}Rn also decays by alpha emission with a half-life of 54.6 s to a series of particulate progeny having similar but different half-lives and emissions than the progeny of ^{222}Rn. (4). In view of the fact that radon, thoron and their progeny concentrations contribute the most to the natural radiation dose to general populations, large scale and long-term measurement of radon, thoron and their progeny concentrations has been receiving considerable attention (5). The decay products of the radon are solid elements that get lodged in the inner layers of the lungs during inhalation. Upon decaying onto the inner layers of the tissues of the lungs, they burst small radiations. These radiations damage the sensitive tissues in the lungs and cause harmful effects on body like changes in the respiratory function and occurrence of lung cancer. Much attention, however, has been given to radon as a radiological health hazard, as human beings are continuously exposed to radon and its decay products in the environment they live in. (6)

This work is aimed at studying the Concentration of Radon and Thoron from Agricultural soil for the Samples at 15cm depth in the villages of South Tirunelveli, Tamil Nadu. This type of study has been done for the very first time in this region, so the obtained results will be helpful in mapping the region and for further baseline studies.

2. METHODS AND TECHNIQUES

The present study was carried out in the 30 villages of the South Tirunelveli, Tamil Nadu and it is given in the map (Figure 1) .The whole studied region lies between $8^{o}19^{'}$ to $8^{o}46^{'}$ north latitude and $77^{o}53^{'}$ to $77^{o}81^{'}$ east longitude

1.Vadakangulam
2. Koliyangulam
3. Kavalkinaru
4. Sivakamipuram
5. Azahaneri
6. Mathaganeri
7. Mannarpuram
8. Kalkarai
9. Kumbilambadu
10. Adankargulam
11. East Keelakulam
12. Chithambarapuram
13.Sivasubramaniyapum
14. Pushbavanam
15. Thanakarkulam
16. Rajaputhoor
17. Leppaikudirupu
18. Perungudi
19. Thirukurungudi
20. Rosmiyapuram
21. Malayadiputhoor
22. Sundavilai
23. Thirumalapuram
24. Sembadu
25. Vinayagapuram
26. Arulnathapuram
27. Azahappapuram
28. Vepillangulam
29.Soundarapandipuram
30. Pambangulam
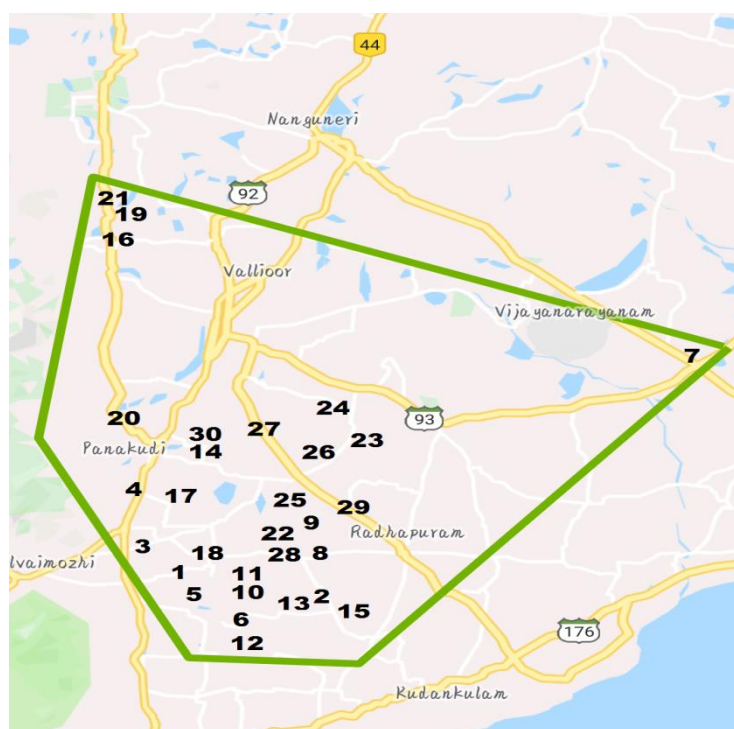
Fig. 1: Studied locations

For the measurement of soil-gas radon concentration, the radon gas has been measured at the depths of 15 cm in 30 villages of the South Tirunelveli, Tamil Nadu. The soil samples have been collected at the depth of 10 –15 cm from the soil profile to obtain undisturbed and pure soil samples. About 1 kg soil samples were collected in a polyethylene bag from each location. The soil samples were not collected from the surface because at the soil surface the radium nuclides might have been flushed away by wind or water. While collecting the soil samples, it was kept in mind that soil samples must be free from gravels and pebbles and named properly. These were dried in open air to remove moisture and humidity totally. These were dried in open air to remove moisture and humidity totally. The dried samples were crushed using a Mortle-pestle.

Experimental technique

In the present study, RAD 7 were used for the measurement of the Radon and Thoron Concentration. The DURRIDGE RAD7 uses a solid state alpha detector. A solid state detector is a semiconductor material (usually silicon) that converts alpha radiation directly to an electrical signal. The RAD7 amplifies, filters, and sorts the signals according to their strength. There are various corrections and calculations that may be applied to calculate more precise radon and thoron concentrations. Some of these corrections are made automatically by the RAD7 itself. DURRIDGE provides a free software utility for Windows and macOS called CAPTURE, which makes it easy to perform these actions, as well as to monitor the RAD7's status , graph radon and Thoron data, apply corrections to account for environmental factors, and export the results for analysis in a spreadsheet program or other software. CAPTURE Software running on Windows (Figure 2) is shown below. (1)
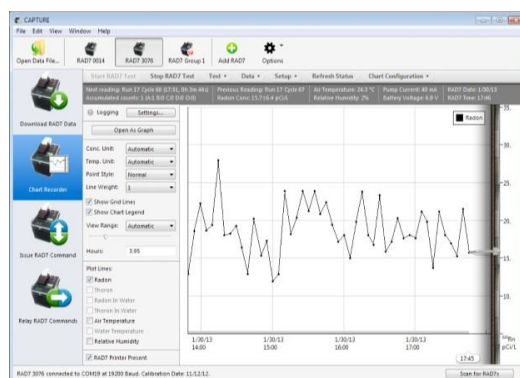
Fig. 2: CAPTURE Software running on Windows

3. RESULTS AND DISCUSSION

The studied values of the Radon Concentration and Thoron Concentration measured for the samples were collected from 30 Villages at South Tirunelveli, Tami Nadu. The Regions of collected area are presented in the Table 1. The values of the Radon Concentration have varied from the lowest value 0.2 to the highest value 1.0 Bq/m^3. The values of Thoron Concentration have been varied from the lowest value 0.2 to the highest value 14.0 Bq/m^3. The results that the highest values of Radon Concentration were for

Sample 7 and the highest values of Thoron Concentration were for Sample 9. The results that the lowest values were for Radon Concentration is on Sample21 and 29 and the lowest values of Thoron Concentration on Sample 14. This may be due to the difference in the concentration of radioactive elements, viz. uranium and radium in the soil and building materials of the study area. As radon is the daughter product of radium therefore low level of radium in soil resulting low level of indoor radon and it is very well reflected in our present study. Table 1 shows the Radon Concentration and Thoron Concentration in the 30 villages.

Table. 1: The Activity concentration of Radon and Thoron

Sample number	Villeges	Radon Bq/m^3	Thoron Bq/m^3
1	Vadakangulam	0.6	6.3
2	Koliyangulam	0.6	5.3
3	Kavalkinaru	0.5	3.6
4	Sivakamipuram	0.5	3.1
5	Azahaneri	0.4	4.0
6	Mathaganeri	0.7	3.2
7	Mannarpuram	1.0	6.3
8	Kalkarai	0.7	4.0
9	Kumbilambadu	0.4	14.0
10	Adankargulam	0.5	6.6
11	East Keelakulam	0.5	10.6
12	Chithambarapuram	0.5	6.0
13	Sivasubramaniyapuram	0.4	0.8
14	Pushbavanam	0.6	0.2
15	Thanakarkulam	0.4	3.3
16	Rajaputhoor	0.5	2.3
17	Leppaikudirupu	0.5	3.3
18	Perungudi	0.5	3.1
19	Thirukurungudi	0.4	2.9
20	Rosmiyapuram	0.3	0.6
21	Malayadiputhoor	0.2	1.3
22	Sundavilai	0.4	2.9
23	Thirumalapuram	0.4	3.8
24	Sembadu	0.5	2.2
25	Vinayagapuram	0.5	6.6
26	Arulnathapuram	0.4	3.5
27	Azahappapuram	0.3	0.5
28	Vepillangulam	0.4	5.6
29	Soundarapandipuram	0.2	10
30	Pambangulam	0.3	6.6

In all the samples surveyed, the maximum annual effective dose is found less than the lower limit of the action level recommended by International Commission on Radiological Protection (ICRP). It is clear from table 1 that the values of Thoron concentration are higher than Radon in the regions; it may be due to the difference in half life of radon and Thoron, which affects the concentration distribution in the ground.

4.CONCLUSIONS

The Radon and Thoron Concentration was measured for the 30 Samples, which were collected from Tirunelveli District of Tamil Nadu. The concentration of the Radon is varied from 0.2 Bq/m^3 at latitude 8º32' (Soundarapandipuram) and 8º45' Malayadiputhoor) to 1.0 Bq/m^3 at latitude 8º37' (Mannarpuram). The value of Thoron Concentration is varied from Bq/m^3 at latitude 8º32' (Pushbavanam) to the 14.0 Bq/m^{3}at latitude 8º30' (Kumbilambadu). The highest concentration values of Radon and Thoron are for Sample 7 (1.0 Bq/m^3)and Sample 9 has the value of 14.0 Bq/m^3. The lowest value of Radon and Thoron concentration of Sample 21, 29 is 0.2 Bq/m^3 and Sample 14 is 0.2 Bq/m^3.

REFERENCES

1. A. Priya Latha. *Statistical Analysis of Gamma Emitting Radionuclide Concentration For The Coastal Region* (7-)
2. UNSCEAR (1993), *Exposure from natural sources of radiation in United Nations scientific committee on the effect of atomic radiation*, United Nations: New York
3. R.Sivakumar (2010) *A study on radon and thoron progeny levels in dwellings in South India*.Department of Physics, Eritrea Institute of Technology, Asmara, Eritrea, North East Africa.8(3)149-154.
4. Durridge Company Inc. (2015). *RAD7 Radon detector. User manual.* Retrieved December 16, 2015, from www.durridge.com Manual.pdf.
5. Mayya, Y. S., Eappen, K. P. and Nambi, K. S. V. (1988). *Methodology for mixed field inhalation dosimetry in Monazite areas using a twin-cup dosimeter with three track detectors*. Rad. Prot. Dosim.*, **77**, 177-184.
6. Manpreet Kaura, b, Ajay Kumar a, Rohit Mehrab, and Rosaline Mishrac(2013) *A Study of radon/thoron exhalation rate, soil-gas radon concentration, and assessment of indoor radon/thoron concentration in Siwalik Himalayas of Jammu & Kashmir.*

THE DISTRIBUTION OF SOLAR WIND PARAMETERS IN 23 & 24 SOLAR MAXIMA

Bidhu S S[1*]*, A Iren Sobia*[2]

[1]*Department of Physics, Nesamony Memorial Christian College, Marthandam, India.*
[2]*Department of Physics, Muslim Arts College, Thiruvithancode, India.*
[*]*Corresponding author: bidhuss@gmail.com*

ABSTRACT

The solar activity and variations can be quantified by several solar wind parameters. This study discussed about the distribution of solar wind parameters during 23 and 24 solar cycle maxima. Data from ACE and WIND spacecrafts were used to analyse the distribution of solar wind plasma parameters. Both spacecrafts observed similar distribution of solar wind parameters in 24 and 23 solar cycle maxima. There was a difference in the space environment between the successive solar maximum years, although the changes from year to year may be gradual. Generally in solar maximum periods, there were often larger solar storms and a greater degree of turbulence in the solar wind. To illustrate the difference in space weather conditions between the 23 and 24 solar maxima, perform this study corresponding to 23 and 24 successive solar maxima periods.

Keywords: solar wind parameters - velocity, density, temperature and magnetic field.

1.INTRODUCTION

The Sun offers a unique laboratory for the study of the fundamental physical process of the interaction between matter and magnetic fields. The combination of vast amounts of ionized gas, strong magnetic fields and enormous interaction length scales constitute physical conditions which are impossible to reproduce on Earth. Applying similarity transformations[1], reducing the solar dimensions down to those of terrestrial laboratories, the scaled values of magnetic field strengths and electric current densities are beyond reach of present-day technology[8]. Even when there are numerous examples of environments in the universe where conditions are even more extreme, the Sun, due to its proximity, offers the unique possibility to study these fundamental processes in great detail[2].

During periods of solar maximum, the dominant component of the solar wind plasma appears to be slow solar wind [9] . The solar wind is basically determined by the sun's magnetic field and responds in various ways to solar activity and the accompanying changes in the magnetic field, which determines the solar wind structure in the entire interplanetary meduim. The evolution of the sun's magnetic field and solar wind prameters, and their influence on the interplanetary medium, have been the subject of continual attention for at leat the last two solar cycles[5] .

In this study, we have analysed the distribution of solar wind parameters; solar wind velocity, temperature, density and mean magnetic field in the solar wind.Various investigators have used these observations to establish statistical relationships between the solar wind parameters [3,6,7] . There was a difference in the space environment between the successive solar maximum years, although the changes from year to year may be gradual. Generally in solar maximum periods, there were often larger solar storms and a greater degree of turbulence in the solar wind. To illustrate the difference in space weather conditions between the 23 and 24 solar maxima, presented below data corresponding to 23 and 24 successive solar maxima periods.

2. DATA

The solar wind parameters and sunspot data of consecutive solar maxima for 23 and 24 solar cycles are taken for the study. These two maximum periods are taken account for the present work.

Data taken from SWEPAM and Mag instrument for ACE and SWE instrument and Magnetic Field Investigation instrument for WIND.

3. RESULTS AND DISCUSSION

Solar wind velocity

The differences in speed of the solar wind vary depending on the number of solar transients occured during investigated period of 23 and 24 solar cycle maximum phase. Fig. 1 and 2 show a histogram of the solar wind speed for the maximum phase of 23 and 24 solar cycle. In 23 solar maximum, solar wind velocity varied from 300 km/s to 740km/s for ACE observation and its varied from 260 km/s to 800 km/s for WIND observations. But in 24 solar maximum, solar wind velocity varied from 280 km/s to 720km/s for ACE observation and its varied from 260 km/s to 820 km/s for WIND observations. Fig. 1 and 2 show that solar wind velocity variations were quiet similar in both solar maximum phase. The distribution was almost uniform with same variations. Both spacecraft observed maximum slow solar wind in these investigated phase.
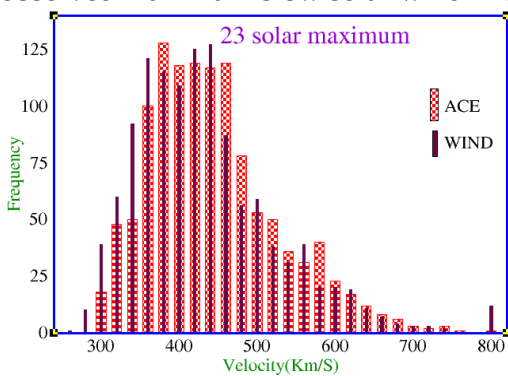
Fig. 1:Solar wind velocity distribution for SC 23 maximum
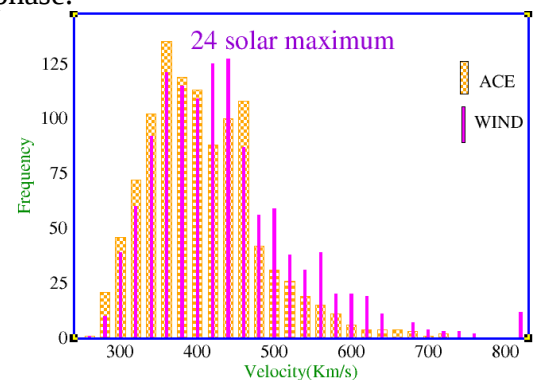
Fig. 2: Solar wind velocity distribution for SC 24 maximum

Solar wind temperature

The temperature of the solar wind was conditional on how fast the stream was moving and how dense it was. Cooler streams tend to be slow, whereas hotter streams tend to be fast. If the solar wind was moving faster, then there were more collisions and more friction, and so the stream got hotter. If the particles were slow-moving, there were less collisions and less friction, giving the stream a cooler temperature. Fig. 3 and 4 show the solar wind temperature distribution histograms over maximum phase of 23 and 24 solar cycles respectively. In maximum phase of SC 23 and 24, temperature of the solar wind varied between 1.0e+04 K and 3.0e+05 K. The distribution showed that most of the solar wind had the temperature, below 1e+05 in both solar maximum phase. The temperature distribution observed during solar cycle 23 and 24 maximum was similar for both ACE and WIND.
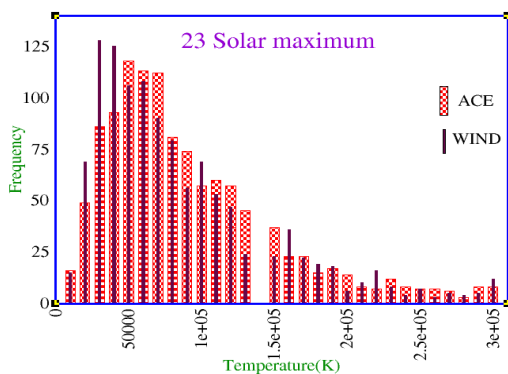
Fig. 3:Solar wind temperature distribution for SC 23 maximum
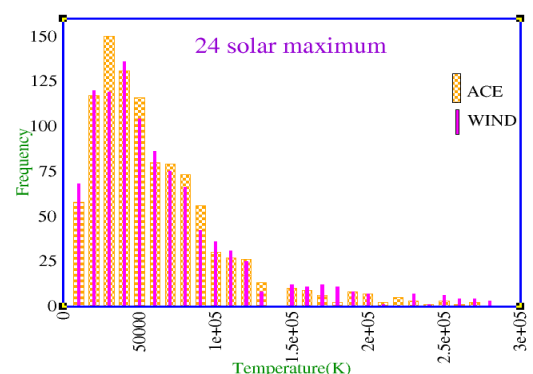
Fig. 4: Solar wind temperature distribution for SC 24 maximum

Solar wind density
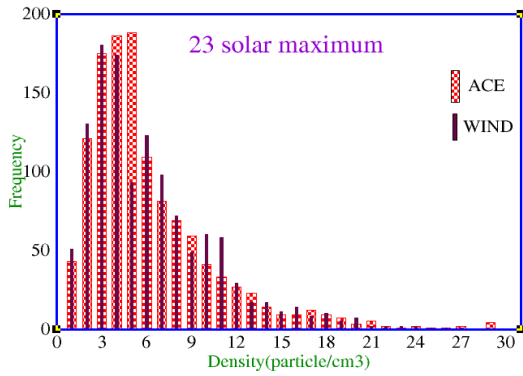
Fig. 5:Solar wind density distribution for SC 23 maximum
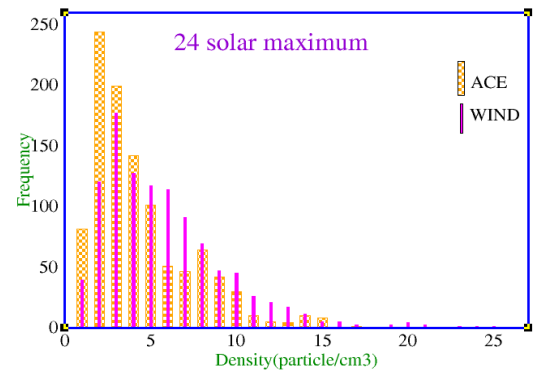
Fig. 6: Solar wind density distribution for SC 24 maximum

Due to the interconnectedness of the solar wind speed, temperature, and density, it come as no surprise that density data from the ACE and WIND spacecraft had similar trait to the analyzes of speed and temperature. Fig. 5 and 6 show a histogram of solar wind density for the maximum phase of 23 and 24 solar cycle. ACE and WIND observed solar wind particle density distribution nearly in a similar manner. The solar wind density was more intensed in 24 solar maximum than in 23 solar maximum. The first thing to note was that the extreme values were not only in the high densities, but rather they appear in the lower densities as well. The densities during the solar maximum range all the way down to one p/cm^3 and all the way up to 180 p/cm^3 in SC 23 and way down to one p/cm^3 and all the way up to 240 p/cm^3 in SC 24. Comparing Solar cycles, 23 SC was characterised by less dense streams than 24 SC. The extremely low values for the density was due to the increased number of high velocity transients emerging from the solar surface at the solar maximum speeds. These caused the particles to spread and the stream become very tenuous. On the contrary, due to the number of active regions on the Sun during the solar maximum.

Solar wind magnetic field
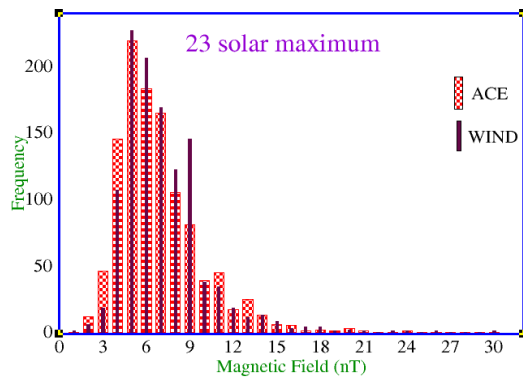
Fig. 7:Solar wind magnetic field distribution for SC 23 maximum
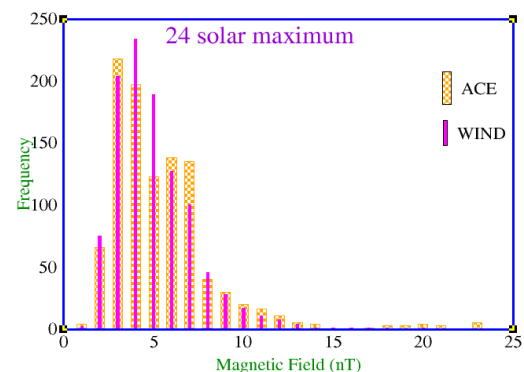
Fig. 8: Solar wind magnetic field distribution for SC 24 maximum

The solar magnetic field played a key role in solar activity. The histogram for distribution of magnetic field over SC 23 and 24 maxima were depicted in Fig. 7 and 8. The magnetic field distribution of solar wind observed by ACE and WIND spacecrafts are in a similar manner. The solar magnetic field values in solar cycle 23 maximum phase varied from 1nT to 30 nT. But in solar cycle 24 maximum, the solar magnetic field varied from 1nT to 23 nT. The distribution for both solar cycle appeared in analogous way and the distribution varied between 1-220 for ACE and 1-240 for WIND. In maximum phase of solar cycle 23, the more solar wind had the magnetic field at 5nT for both spacecrafts and in 24 solar maximum phase,the more solar wind had the magnetic field at 3nT for ACE and 4nT for WIND.

4. CONCLUSION

The distribution of solar wind parameters; solar wind velocity, temperature, density and magnetic field were cross analysed to get the information of solar wind parameters during the 23 and 24 solar maximum phase. The simultaneous observation of ACE and WIND in L_1 orbit, WIND observed solar wind on one phase of solar hemisphere at the same time ACE observed solar wind on another phase of solar hemisphere was similar during these maximum phases. The observations showed that Sun s activity was evenly distributed in all latitude. ACE and WIND spacecrafts observed similar type of variations of solar wind parameters in 23 and 24 solar maximum phase. The solar wind parameters, solar wind velocity, temperature, density and magnetic field had maximum variations in 23 solar cycle maximum phase as these compared with the solar wind parameters in 24 solar cycle maximum phase. The reduced activity was due to the weak nature of solar cycle 24.

REFERENCE
1. Alfvén, H., and C. G. Falthammar, Cosmical Electrodynamics: Fundamental Principles. Fundamental Principles, Clarendon Press (1963).
2. Bidhu S. S, A Iren Sobia, A Dickson Benjamin, Solar wind Parameters Interdependences During Solar Maxima, Journal of Pure Applied and Industrial Physics, Vol.7(3), 101-106, (March 2017).
3. Maezawa K., Solar Terr. Environ. Res. Japan, 2, 103, (1978).
4. Sanderson T.R, K.L Harvey et al., Jn of Geophysical Research, Vol. 108, A1, 1035, doi:10.1029/2002JA009388, (2003).
5. Sanderson T.R, K.L Harvey et al., Jn of Geophysical Research, Vol. 108, A1, 1035, doi:10.1029/2002JA009388, (2003).
6. Smart D.F., Garrett H.B., and Shea M.A., in solar Terrestrial Prediction Proceedings, vol. 2, edited by R.F. Donnelly,733pp., NOAA, Washington D.C., (1979).
7. Snyder C.W., Neugebauer M., and Rao U. R., J. Geophys. Res. 68, 6361, (1963).
8. Stenflo, J. (Ed.), Solar magnetic fields: polarized radiation diagnostics, astrophysics and Space Science Library, Kluwer Academic Publishers, Netherlands (1994).
9. Wang Y., Space Sci.Rev.,DOI:10.1007/s11214-010-9733-0 (2011).

RAINFALL VARIABILITY (DROUGHT) ANALYSIS OVER TWO GEOGRAPHICALLY VARYING LOCATIONS

S.Jeslin Sunitha
Department of Physics and Research Centre,
N.M. Christian College, Marthandam
Email: jeslinsunitha@gmail.com

ABSTRACT

Rainfall is an important agro meteorological parameter. The year to year variability of the annual rainfall causes considerable modifications in the pattern of agriculture, water management etc. of a particular region. Drought is an universally acknowledged phenomenon associated with scarcity of water. It is a normal recurrent feature of climate and is observed in all climatic zones. The problem of drought can also be aggravated by other climatic factors such as high temperature, wind, humidity etc. Thus lack of water for the normal needs of agriculture, live stock industry or human population may be termed as drought. In this study, drought has been analysed and calculated independently for dry months, normal months and above normal months at two selected locations in Kanyakumari and Tuticorin districts of Tamil Nadu with contrast geographical configurations. The study revealed that dry months have been maximum in Tuticorin giving a clue that it swings to drought disaster.

Key words: Drought, Standard deviation, Coefficient of variance, Dry month

1.INTRODUCTION

Water is most essential for the survival of life on our planet Earth. Excess rainfall leads to floods and less rainfall leads to droughts. Indian summer monsoon rainfall shows large scale intra-seasonal and inter - annual variabilities. Satakapan (1951) has studied the usefulness of various statistical analyses with the past rainfall data base to facilitate planners and managers for efficient surface water management. Pramanik and Jagannathan (1953) have found that the probability of occurrence of deficient monsoon rainfall over arid and semi arid regions of India would be comparitively more. Parthasarathy et.al. (1984 and 1987) have studied the probabilities of occurrence of flood/drought over different parts of India. Drought occurs due to inadequate rainfall, late arrival of rains and excessive withdrawal of ground waters. Drought causes hunger, malnutrition, scarcity of drinking water, ground water depletion and adversely affects human inhabitance and initiates desertification. Estimation and predictionof the amount of rainfall in time and space is a problem of fundamental

importance in various fields. Understanding of rainfall pattern and its variability helps in better water resource management.

2. DATA AND METHODOLOGY

In the present work, the data to be analysed was obtained from two locations in Tamilnadu viz, Pechiparai (8^0 46' N and 77^0 5' E) with an altitude of 76 m above MSL of Kanyakumari District along the Western Ghats region and Killikulam (8^0 46' N and 77^0 4' E) with an altitude of 46 m above MSL of Tuticorin District along coastal region. The daily rainfall data for 20 years (1993-2012) were collected from the meteorological observatory from the selected sites. Both sites possess contrast geographical configuration and pattern of rainfall etc.

The Probability pattern of rainfall (Drought statistics) can be analyzed by the classifications of drought, normal and excessive rainfall months/annual. If x be the monthly rainfall/annual rainfall, between $A_1 = x/2$ and $A_2 = 2x$, then a month/year receiving rainfall less than A_1 is defined as drought month/year, between A_1 and A_2 is termed as normal and that above A_2 is

labelled excessive rainfall month/year. The probability pattern has been applied for the experimental locations in order to understand the rainfall patterns (Pimpale and Thiware, 2001). In addition to that, the statistical values of Mean, Standard deviation and Coefficient of variation were also calculated using computational formulae.

Standard Deviation

The square root of the average of the squares of the deviation taken from the mean is defined as the standard deviation. A common measure of dispersion which is preferred in most circumstances in statistics is the standard deviation. The computational formula used for calculating the standard deviation is,

$$s = \sqrt{\frac{\sum d^2}{n}}$$

Where, d is   deviation from mean

n is total number of distributions

Coefficient of Variation (C.V)

Coefficient of variation is defined as the ratio of standard deviation to the mean of the sample. Generally it is expressed in terms of percentage.

$$C.V = \left(\frac{Standard\ Deviation}{mean}\right) * 100\%$$

3. RESULTS AND DISCUSSION

The status of dry, normal and excess rainfall months and years (annual) and the probability patterns (drought statistics) for monthly and yearly rainfall for the period of 20 years from 1993 to 2012 are calculated in both the locations and the pictorial representations are depicted in Figures 1 to 4. Table 1 depicts the calculated values of the drought parameters at Killikulam

Table 1 Drought statistics based on monthly and seasonal rainfall analysis at Killikulam

Month	Mean A (mm)	SD	CV %	A1 mm	A2 mm	Dm	Nm	An m	No Rain Month	Dm %	Nm %	An m %
Jan	18.5	19.7	106.8	9.2	36.9	3	9	3	5	15	45	15
Feb	30.1	39.8	131.9	15.1	60.3	4	3	5	8	20	15	25
Mar	39.8	77.7	195.3	19.9	79.6	6	5	2	7	30	25	10
Apr	81.1	57.1	71.0	40.6	162.3	6	12	2	0	30	60	10
May	25.4	36.6	144.1	12.7	50.9	9	6	3	2	45	30	15
June	3.7	4.8	130.6	1.8	7.3	2	6	4	8	10	30	20
July	8.5	13.4	157.4	4.2	17.0	6	5	3	6	30	25	15
Aug	15.1	27.2	180.9	7.5	30.1	4	5	3	8	20	25	15
Sep	41.0	38.0	92.7	20.5	82.0	7	8	4	1	35	40	20
Oct	139.7	94.4	67.6	69.9	279.4	5	13	2	0	25	65	10
Nov	222.0	95.6	43.1	111.0	444.0	3	17	0	0	15	85	0
Dec	88.3	92.7	105.1	44.1	176.5	6	10	3	1	30	50	15

DM-Dry month, **NM-**Normal month**, ANM-**Above normal month
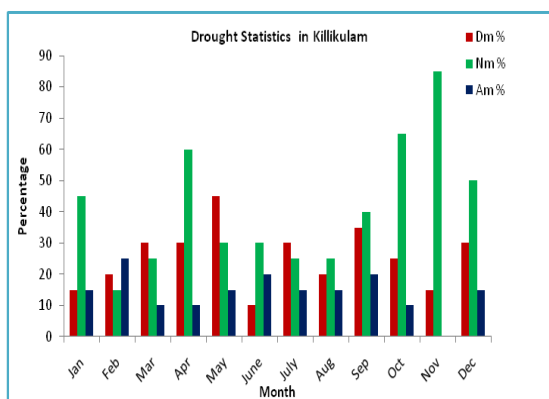
Fig 1 Monthly drought statistics at Killikulam
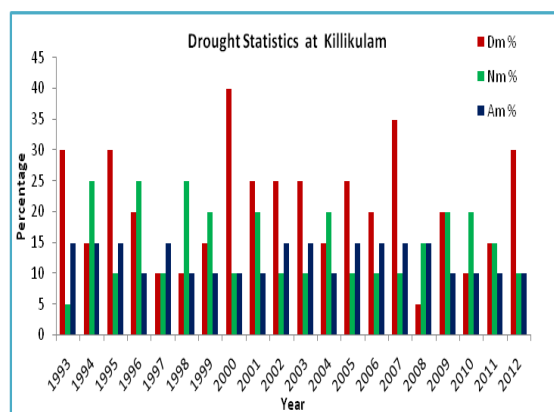
Fig 2   Annual drought statistics at Killikulam
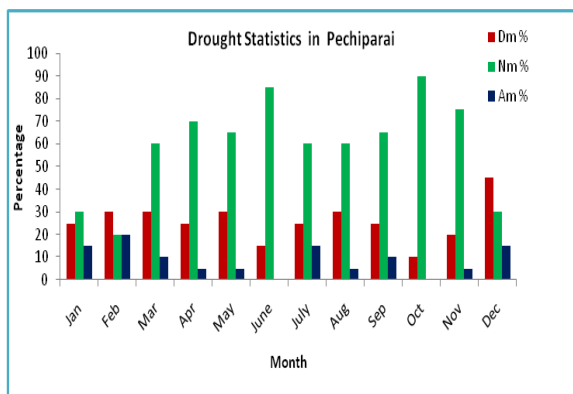
Fig 3 Monthly drought statistics at Pechiparai
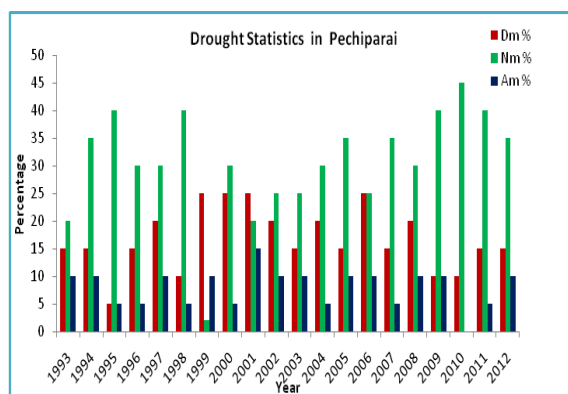
Fig 4 Annual drought statistics at Pechiparai

In the study area of Killikulam in Tuticorin District, the deficient rain occurred during the months of June, July, and August. June is found out as the driest month with a meagre amount of 3.7 mm of average rainfall. It has a coefficient of variation 157.4 % that shows an erratic pattern of rainfall. November is found to be the wettest month which receives an average rainfall of 222 mm with low coefficient of variation 43.1%. The wettest month next to November is October with an average rainfall of 139.7 mm and a coefficient of variation 67.6%. In 20 years of observation, Killikulam received a moderate amount of rainfall except during the months of June and July.

Rainfall variability for the study period revealed that the number of months with deficit, normal and excessive rainfall are 61, 99, 34 months respectively. In a total of 240 months, 194 months have received rain and 46 months have not received any rain. The deficient rain occurred during the years 1994, 1995, 1996, 1999, 2003, 2006, 2010, 2011 and 2012. The years 1995, 2000, and 2007 indicates the driest years that have 6 and 7 dry months. Next to the years 1995, 2000, and 2007 all the successive years received a low amount of rainfall. In the analysis of dry months for the study period the period. During the monsoon period of 20 years, there were about 35% of dry months, 25% of normal months and 21 % of excess rainfall months and 19 % of no rain months. from1993 to 2012, it was seen that it is minimum during 1997, 1998 and 1999 and maximum during the years

from 2000 to 2002. Analysis of normal month reveals that it was maximum during 1996 and 1999 and minimum during 1993.

In Pechiparai, the minimum amount of rainfall occurred during January with an amount of 29.3 mm and has a C.V of 166.6 %. October is observed to be the wettest month which receives an average of 387.1 mm of rainfall with a low C.V of 39.23 %. Over the 20 years of rainfall observations, Pechiparai receives moderate amount of rainfall in all seasons. The numbers of months with deficit, normal and excess rainfall are 62, 142 and 21 respectively. In a total of 240 months, 225 months have received rain and 15 months have not received any rain.

The deficient rain occurred during 1999, 2000, 2001 and 2006 indicates the driest years having 5 dry months each. Analysis of normal month depicts that it was maximum during 1994, 1995, 1998, 2005, 2007, 2011 and 2012 with 7 or 8 normal months. The above normal rainfall in 2010 has 9 months. During monsoon periods of the study period, there exists 28 % of dry, 53 % of normal and 13 % of above normal rainfall and 6% of no rain months.

4. CONCLUSION

From rainfall variability studies, the North East Monsoon (NEM) was found to be the dominant one in Killikulam (Tuticorin) and both South West Monsoon (SWM) and North East Monsoons (NEM) dominant in Pechiparai (Kanyakumari). Pechipparai being an adjacent location to Western Ghats fetches this unique feature. Also it has been revealed that dry months are maximum in Killikulam. This confirms that locational effect on climate is explicit in the chosen sites.

REFERENCES

1. **Adejuwon J O** Balogun E EAdejuwon S A *Intern J Climatol***10** (8) 839-848 **1990**

2. **Parthasarathy B Sontakke N A Kothawale D R** *Curr.Sci.,***53***,94-96* **1984**

3. **Parthasarathy B Sontakke N A Munot A A Kothawale D R** *J Climatol.,***7***,57-70* **1987**

4. **Pimpale A R Thiware S S** *Journal of water management* **9** 1and2 9-12 **2001**

5. **Pramanik S K Jagannathan P** *Indian J. Met.&Geophys.,***4***,291-309* **1953**

6. **Satakapan V** *Indian J. Met.&Geophys.,***2***,9-24* **1951**

ESTIMATING SEASONAL VARIATION OF GLOBAL SOLAR RADIATION USING TEMPERATURE

S.Rathi[*], G.Shanthi

Department of Physics & Research Centre, Women's Christian College, Nagercoil-629001

Affiliated to Manonmaniam Sundanar University, Tirunelveli-627012

[*]*Corresponding author:gbrathijeyakumar@gmail.com*

ABSTRACT

The knowledge of the seasonal variation in global solar radiation reaching a location on the earth is important information for Agriculturists, water sector personnel, electrical power sector, environmentalists, etc. The objective of this work is to determine how global solar radiation of experimental site varies with seasons Hargreaves radiation model of global solar radiation prediction was used for this work, making use of minimum and maximum air temperature data. The result shows that there is variation in global solar radiations in the two seasons, with dry season having radiation than rainy season. It was also observed by them that there is seasonal variation in global radiation, and that the dry months have comparably larger values than wet months

Key words: Agriculture, Hargreaves radiation Model, Maximum Temperature, Seasonal Global Solar Radiation

1. INTRODUCTION

Climate and weather information are important in agriculture, aviation, water resources management, health, electric power generation, road and marine transport etc (Ogolo, 2002). The earth's climate is changing continuously. The changes include both spatial changes and the temporal changes. The sun is the fundamental source of all energy in the climate system. Hence it is reasonable to assume that the variations in the solar output might be one of the causes of the climate changes (Joanna, 2000). The changes in the solar output due to the earth's orbital parameters are responsible for the climate changes over millennial timescales (Hayes et al., 1976). The changes in the solar output over century time scale are partly responsible for the Little Ice Age (Lean et al., 1992).Solar radiation is the main permanent driving force of weather on earth. The periodic movement of the earth around the sun combined with the earth axis inclination, results in a periodic variation in incident solar radiation. This is the origin of the well-known seasonal patterns in weather, occurring every year.

2. MATERIALS AND METHOD

The meteorological parameters like Maximum Temperature, Minimum Temperature for the period of 11 years (2007-2017) were obtained from Horticultural Research Station, Pechippari in Kanyakumari district. The chosen experimental site for the present work is situated in between Northern latitude 8.4 and East longitude 77.3 with an altitude of 76m above MSL.

Solar or shortwave radiation (Rs)

The amount of radiation reaching a horizontal plane is known as the solar radiation (R_s). In this work, the method used is Hargreaves Radiation model of global solar radiation predictions. The model equation makes use of the maximum and the minimum temperature of the study area to predict the global solar radiation of the location. The Hargreave's equation is given as:

$$R_s = K_{Rs}\sqrt{(Tmax - Tmin}\ R_a \quad \text{-------------------------- (1)}$$

Where T_{max} is the maximum temperature, T_{min} is minimum temperature, Ra is the extraterrestrial solar radiation of the area, K_{Rs} is adjustment coefficient. For the 'interior' locations, it is approximately 0.16 and for 'coastal' locations its value is approximately 0.19.

Parameters for Global Solar Radiation

The parameters calculated before finding the global solar radiation of an area based on Hargreave's method are

(a) Relative distance Earth-Sun and Solar declination

The inverse relative distance Earth-Sun, d_r, and the solar declination, δ, are given by

$$d_r = 1 + \cos\left(\frac{2\pi}{365} J\right) \text{-------------- (2)}$$

$$\delta = 0.409 \sin\left(\frac{2\pi}{365} J - 1.39\right) \text{------------------------- (3)}$$

Where, d_r is Inverse relative distance Earth-Sun, J is the Number of the Day in the Year between (January to December).

(b) Sunset Hour angle (ω_s)

The sunset angle of a location is calculated using the formula given as

$$\omega_s = arc \cos\left[-\tan(\varphi)\tan(\delta)\right] \text{------------------ (4)}$$

Where, ω_s is the Sunset hour angle [rad], φ is the Latitude [rad], δ isSolar declination [rad].

(c) Extraterrestrial radiation for daily periods (Ra)

The extraterrestrial radiation, R_a, for each day can be estimated using the formula:

$$R_a = \frac{24\ (60)}{\pi} G_{sc}\ d_r[\omega_s \sin(\varphi)\sin(\delta) + \cos(\varphi)\cos(\delta)\sin(\omega_s)] \text{------------------- (5)}$$

Where, R_a is Extraterrestrial radiation[MJ m^{-2} day^{-1}],G_{sc} is Solar constant = 0.0820 MJ m^{-2} min$^{-1,}$ d_r is Inverse relative distance Earth-Sun, ω_s is the Sunset hour angle [rad], φ is Latitude [rad],δ is the Solar declination [rad].

3. RESULTS AND DISCUSSION

The annual variation of mean solar radiation for the period of 11 years from (2007-2017) was computed using equation (1-5) and it was tabulated in the Table 1.the graphical representation of the solar radiation is depicted in the Fig 1.

Table 1: Annual solar Radiation of pachippari region (2007-2017)

Year	Solar Radiation (MJm^{-2}d^{-1})
2007	18.1496
2008	19.8423
2009	17.8816
2010	18.9209
2011	20.8995
2012	24.1210
2013	21.9661
2014	21.6790
2015	14.5866
2016	12.4326
2017	17.5370
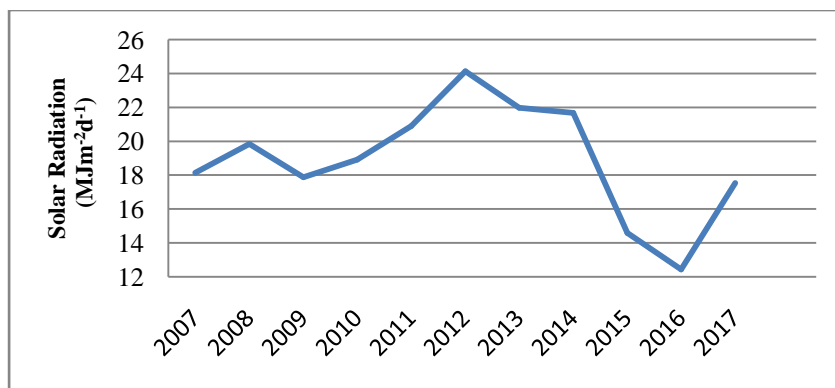
Fig 1: Annual solar Radiation of pachippari region(2007-2017)

 From the Fig1: the annual solar radiation pechippari region it has been found that there is a higher value of solar radiation in the year (24.12107 MJm^{-2}d^{-1}). It also revealed before 2012 there occurs moderate value of solar radiation

Table 2: Monthly mean solar radiation of pachippari region during the year (2007-2017)

Month	Solar radiation (M J m^{-2} d^{-1})
January	21.91667
February	22.00955
March	21.60429
April	19.51866
May	16.57758
June	15.12862
July	16.59098
August	16.63852
September	18.15812
October	19.51945
November	19.91922
December	20.58065
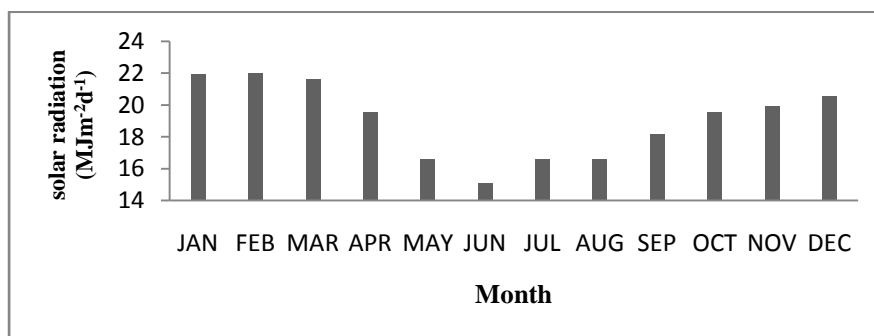
Fig 2: monthly mean solar radiation of pachippari region during the year (2007-2017)
 The above Figure shows the lowest value of solar radiation in the month of June (15.12862 MJm^{-2}d^{-1}) and highest value in the month of January (21.916 MJm^{-2}d^{-1}),February 22.009 (MJm^{-2}d^{-1}),and march 21.60429 (MJm^{-2}d^{-1})

Variation of seasonal solar radiation:
Table 3: variation of seasonal solar radiation pachippari site during the year (2007-2017)

YEAR	WINTER	SUMMER	SWM	NEM
2007	18.1496	22.9354	19.5633	25.4479
2008	19.8423	22.6173	17.6291	17.7850
2009	17.8816	23.0358	18.8192	14.1173
2010	18.9209	23.6663	20.1855	15.4838
2011	20.8995	23.7263	20.4115	17.1089
2012	24.1210	28.0137	24.1361	21.4977
2013	21.9661	24.6865	24.2573	18.4947
2014	21.6790	25.3103	22.4742	18.8305
2015	14.5866	17.5624	14.5440	13.2507
2016	12.4326	13.0755	12.1033	11.9215
2017	17.5370	18.9897	16.1432	17.39122
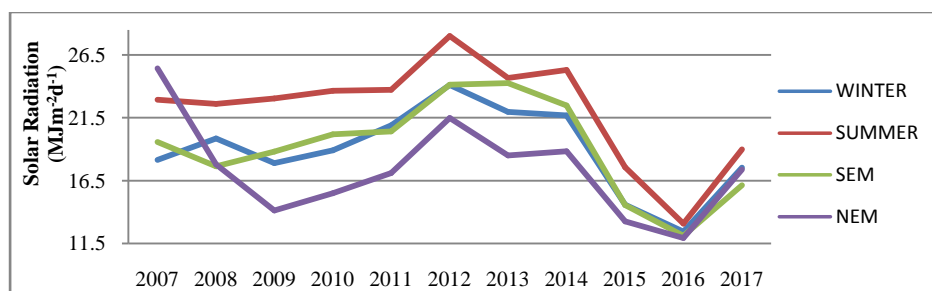
Fig 3: variation of seasonal solar radiation pachippari site during the year (2007-2017)
The above Figure shows the marked variation in summer season 28.01371 $MJm^{-2}d^{-1}$. It is clear that the winter, range of radiation varies from 12.4362 $MJm^{-2}d^{-1}$ to 24.12109 $MJm^{-2}d^{-1}$ The mean radiation value of summer varies from 13.07558 $MJm^{-2}d^{-1}$- 28.01371 $MJm^{-2}d^{-1}$. The mean radiation value of SWM varies from (12.13044 $MJm^{-2}d^{-1}$ – 24.25735 $MJm^{-2}d^{-1}$). The mean radiation value of NEM varies from (11.9215 $MJm^{-2}d^{-1}$-21.4977 $MJm^{-2}d^{-1}$).Overall the year 2016 shows low value in all the seasons. The result shows that there is clear variation between the global solar radiation during rainy and dry seasons. It shows that global solar radiation is very high in dry season (summer) than in rainy season (SEM&NWM) Fig. 2. The global solar radiation in February was seen to be generally high though oscillating, the behaviour which is also observed in that of January and March, except at the middle of January which shows some deviation from its general trend. The maximum global solar radiations are 22.0095 $MJm^{-2}d^{-1}$ for February and 21.91667 $MJm^{-2}d^{-1,}$ 21.620429 $MJm^{-2}d^{-1}$ for January and March. The minimum values are 15.1286 $MJm^{-2}d^{-1}$ and 16.59098 $MJm^{-2}d^{-1}$ and in June and July respectively. Although the global solar radiations for both rainy and dry seasons were oscillating.

4. CONCLUSION

From the results, it can be observed that variation occurs between solar global radiation in rainy season and dry season, with the global solar radiation higher in dry season (March, February, January) than in rainy season (June, July). This is in accordance with the work by S. O. Falodun and E. O. Ogolo (2007), at Akure, South-west, Nigeria, in which it was stated that there is seasonal variation of global radiation, and that the dry months have comparably larger values than wet months. It can also be conclusively stated that although, the global solar radiations for both rainy and dry seasons change in almost the same trend.

REFERENCES

1. Ogolo.E.O, Characterization of Weather Parameters for Ibadan using Bowen ratio as an index of seasonal variation unpublished Ph.D. Thesis", Department of physics, University of Ibadan, Ibadan, Nigeria, (2002).
2. Joanna D Haigh "A GCM study of climate change in response to the 11-year solar cycle", Quarterly Journal of Royal Meteorological Society, 125,871-892(1999).
3. Lean.J, Skumanitch.A and White.O, "Estimating the sun's radioactive output during the Maunder Minimum", Geophysical Research Letter, 19, 1591-1594(1992).
4. Hayes.J.D, Impire.J , Shakleton.N.J, "Variations in the earth's orbit: Pacemaker of the ice ages", Science, 194(1976)
5. S. O. Falodun and E. O. Ogolo (2007). Diurnal and seasonal variation of Global solar radiation at Akure , South-western Nigeria ,
6. Abdullahi, S. Ayegba, Shelbut Nandir Elaine, Abegunde Linda Olukemi, Mba Tochukwu William" Assessing the Seasonal Variation in Global Solar Radiation of Lagos State, Nigeria" JEAS Volume 7, Issue 1, (2017) 2250-3153

EQUATORIAL UPPER ATMOSPHERE DURING

GEO MAGNETIC STORM - A CASE STUDY

Sumod S.G

Space Science Group, Department of Physics, Sacred Heart College, Kochi, Kerala

Emai id: sgsumodh@gmail.com

ABSTRACT

The prime objective of this work is to understand the behavior of the   Equatorial/low latitude ionosphere-thermosphere system in context of the geomagnetic storm of 15th December 2006. For the same, simultaneous observations of Equatorial Electrojet (EEJ) and thermospheric OI 630.0 nm dayglow as obtained using the Proton Precession Magnetometers (PPM) and Multiwavelength Dayglow Photometer (MWDPM) respectively, have been used. The important observations are (i) the reversal of EEJ /electric field during the main phase of the storm due to the combined effect of 'Ionospheric Disturbance Dynamo Electric field' and prompt penetration effect (ii) small scale fluctuations in the EEJ as a result of DP2 fluctuations and (iii) the spatio-temporal variability in the observed dayglow over the equatorial station caused by the large scale Travelling Ionospheric Disturbances (TIDs), associated with the storm.

Keywords: *Equatorial Electrojet, OI 630.0 nm dayglow, geomagnetic storm.*

1. INTRODUCTION

To describe the physical processes underlying several phenomena of geomagnetic storms, many studies have been carried out till date [1].Nevertheless, many aspects concerning the storm and associated effects, particularly over the equatorial upper atmosphere are far from complete. In this context, an attempt is made in this work to understand the behavior of equatorial/low latitude ionosphere in context of geomagnetic storm of 15th December 2006.

2. METHODOLOGY

In the present study, ground based instruments such as Proton Precision Magnetometer (PPM) and Multiwavelength Dayglow photometer (MWDPM) have been used to investigate various effects in the equatorial upper atmosphere [3]. In addition, several satellite measurements have also been used. This mainly includes the interplanetary data from Advanced Composition Explorer (ACE) satellite. Further, data obtained from the World Data Center (WDC), Kyoto University, Japan have also been used for substantiating many of the results.

3. RESULTS AND DISCUSSION

Figure 1 (top panel) shows the time evolution of SYM-H during the period 13-18, December 2006. The sudden storm commencement is indicated by the increase of SYM-H above its normal value at 20.00 IST on 14 December 2006. Sudden Storm Commencement is followed by an abnormal value of SYM-H for 8 hours which started at ~20.00 IST on 14 December and lasted till 04.00 IST on 15 December which is denoted as Initial phase. The initial phase is followed by a sudden decrease of SYM-H lasting for about 4 hours from 04.00 IST on 15 December called the Main phase. During this phase, SYM-H decreased sharply to a minimum of around -200 nT at ~06.00 IST. The main phase is followed by the Recovery phase lasting 1 to 2 days during which the geomagnetic field approaches its pre-storm conditions.
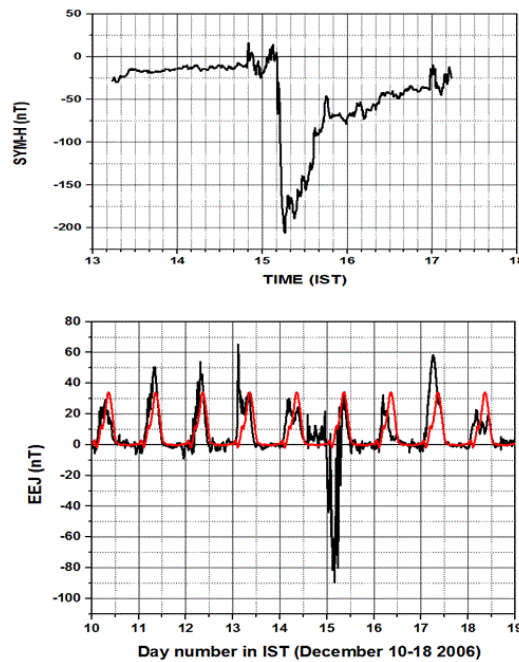
Figure 1: The top panel shows variation of SYM-H during geomagnetic storm and bottom panel shows the EEJ values of December 10-18 2006 with the mean EEJ for quiet days superimposed on each of the days.

For the EEJ measurements, the data obtained from the magnetometers installed at Tirunelveli (an equatorial station) and Alibag (an off- EEJ station) are used. The internationally geomagnetic quiet days i.e., 2, 4, 29, 30 and 31 of December 2006 as mentioned in WDC have been selected as the quiet days. Night time (0-5 IST) mean magnetic field for these days is calculated for Alibag and Tirunelveli separately. These mean values are subtracted from the respective magnetic fields to obtain ΔH_{tir} and ΔH_{abg} respectively. Then the EEJ can be obtained using the equation, EEJ= ΔH_{tir}-ΔH_{abg} (black line).

The time variations of EEJ during the period December 10-18, 2006 are plotted in figure 1. The mean EEJ for quiet days are also shown. As is clear from figure, significant variability has been noticed. These variations occur at EEJ altitudes (~ 106 km), i.e., at E region heights. This can significantly affect F-region dynamics also, because the field lines over E-region at low latitude regions are mapped over the equatorial F-region. Hence in order to investigate this aspect in detail, the OI 630.0 nm dayglow variations are studied.

The 630.0 nm data were obtained from the MWDPM. At present configuration, it scans in the N-S meridian so that it can cover a range of 4-13° N geographic latitudes. Therefore the OI 630 nm intensity variations are plotted as a function of geographic latitude in figure 2. The intensity of dayglow started increasing at around 12.00 IST and it peaks at about 13.00 IST. Although, the dayglow exhibited significant fluctuations due to the ensuing TIDs (Travelling Ionospheric Disturbances), the intensity reached a normal value at about 16.00 IST.

The important observations as far as the EEJ is concerned are (i) the reversal of EEJ electric field during the initial phase of the storm and (ii) small scale fluctuations in the EEJ. The former could be due to the Disturbance dynamo electric field, although the time delay observed here is not as high for the development of the disturbance electric field. It must be mentioned that the effect of prompt penetration electric field also cannot be precluded in this context. The small scale fluctuations as observed in the EEJ could be due to the DP2 fluctuations [3]. DP2 is a global ionosphere equivalent current system proposed to account for quasi-periodic fluctuations in the geomagnetic field that occurs coherently at high latitudes, dayside dip equator and in the IMF B_z [3]. Further, it is understood that the enhancement of DP2 amplitude is conspicuous over dayside dip equator as compared with the low latitudes due to the Pedersen current amplified by the Cowling effect.
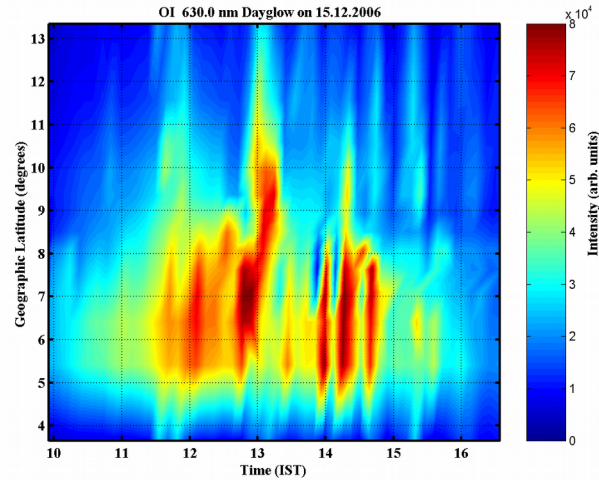
Figure 2: OI 630 nm dayglow on 15 December2006

4. CONCLUSION

In this study, an attempt has been made to investigate the effects of geomagnetic storm occurred on 15 December 2006 over the equatorial/low latitude regions. A large variation in EEJ with a change in direction from east to west has been observed during the main phase of the storm. This can be explained on the basis of the combined effect of 'Ionospheric Disturbance Dynamo Electric field' and prompt penetration effect. The small scale fluctuations observed in EEJ are due to the DP2 fluctuations as detailed. The spatio-temporal variability in the observed dayglow over the equatorial station can be attributed to the large scale TIDs.

REFERENCES

[1] Sumod, S. G., T. K. Pant, C. Vineeth, and M. M. Hossain (2015), Unusual depletion of OI 630.0 nm dayglow and simultaneous mesopause heating during the penetration of interplanetary electric field over dip equator, J. Geophys. Res. Space Physics, 120, doi:10.1002/2014JA020584.

 [2] Sumod S.G (2012), Study of the neutral and electrodynamical coupling processes in the equatorial upper atmosphere. Ph.D Thesis Vikram Sarabhai Space Centre, India.

[3]Sastri, J.H., N. Jyoti, V.V. Somayajulu, H. Chandra, and C. V. Devasia (2000), Ionospheric storm of early November 1993 in the Indian equatorial region. J. Geophys. Res., 105, 18,443.

SPECTROSCOPIC CHARACTERIZATION OF METHYL N-[6-[HYDROXY(PHENYL)METHYL]-1H-BENZIMIDAZOL-2-YL]CARBAMATE BY DFT CALCULATIONS

A.Beta Daniel[*], D.Aruldhas

Department of Physics and Research Centre, Nesamony Memorial Christian College, Marthandam
Affiliated to Manonmaniam Sundaranar University, Abishekapatti, Tirunelveli
*Corresponding auther:betadaniel2009@gmail.com

ABSTRACT

The optimization geometry, intramolecular hydrogen bonding and harmonic vibrational wavenumbers of methyl N-[6-[hydroxy(phenyl)methyl]-1H-benzimidazol-2-yl]carbamate have been investigated with the help of B3LYP density functional theory (DFT) methods. The infrared and Raman spectra were predicted theoretically from the calculated intensities. The various intramolecular interactions have been exposed by natural bond orbital (NBO) analysis. The molecular orbital contributions are studied by density of energy states (DOS). Various reactivity and selectivity descriptors such as chemical hardness, chemical potential, softness, electrophilicity, nucleophilicity and the appropriate local quantities employing natural population analysis (NPA) are calculated.

Keywords: DFT, NBO, DOS, NPA

1. INTRODUCTION

Benzimidazoles show different biological activities such as anticancer, antimicrobial, and antihelmintic activities[1]. Spectroscopic studies of certain benzimidazole derivatives are already reported[2,3]. Several carbamates also have been synthesized as anticancer agents recognizing their inhibiting effects on endothelial cell proliferation in vitro and tumor induced angiogenesis in vivo as well as tumor growth in mice[4]. Density functional theory (DFT) has emerged as a powerful tool for analyzing vibrational spectra of fairly large molecules. The application of DFT to chemical systems has received much attention because of faster convergence in time than traditional quantum mechanical correlation methods[5]. The present work reports a detailed spectroscopic study on methyl N-[6-[hydroxy(phenyl)methyl]-1H-benzimidazol-2-yl]carbamate using IR and Raman spectra. The natural bond orbital (NBO) analysis is carried out to interpret hyperconjugative interaction and intramolecular charge transfer (ICT). The calculated value of HOMO–LUMO energy gap is used to interpret the biological activity of the molecule.

2. COMPUTATIONAL DETAILS

DFT quantum chemical computations have been carried out at the B3LYP/6-311G(d,p) level[6] using Gaussian'09 program package[7] which has proved itself to be extremely useful in treating electronic structure of the molecules and get a clear knowledge of optimized parameters, vibrational wavenumbers, IR intensities, harmonic vibrational frequencies and their intensities which are calculated in order to provide more information for the vibrational assignments of methyl N-[6-[hydroxy(phenyl)methyl]-1H-benzimidazol-2-yl]carbamate. NBO 3.1[8] program has been used to perform NBO calculations as implemented in the Gaussian'09 package at the DFT/B3LYP level. To calculate functional group contributions to the molecular orbitals, the total

density of states (TDOS), the partial density of states (PDOS) and overlap population density of states (OPDOS) spectra are prepared by using the program GaussSum 2.2[9].

3. RESULTS AND DISCUSSION

Optimized Geometry

Molecular structure is depicted in Fig. 1. Selected optimized geometrical parameters are tabulated in Table1. In benzimidazole ring, shortening of C-C and C-N bond lengths are due to the inductive effect caused by electron withdrawing through sigma bond and electron donating through pi bond carbon atoms [10]. Bond length C_{31}-O_{32} (1.345Å) is less than that of persuaded value (1.43Å)[11] due to the presence of carbonyl group and nitrogen leading to redistribution of electron cloud.
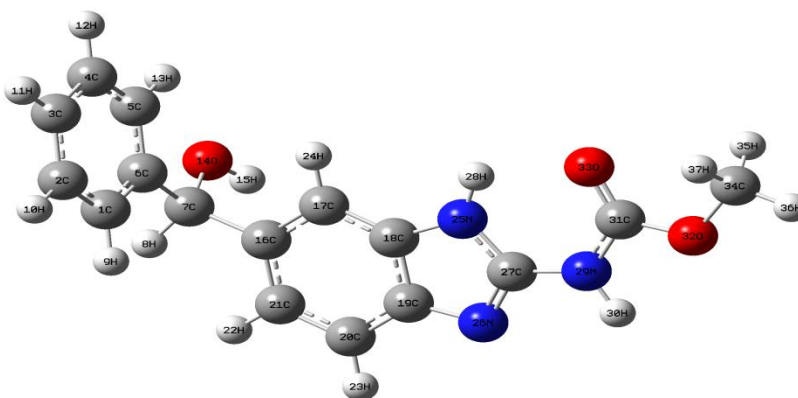
Figure 1 Optimized structure of methyl N-[6-[hydroxy(phenyl)methyl]-1H-benzimidazol-2-yl]carbamate

Table 1

Optimized parameters

Bondlength	Exp. Value (Å)	Cal. Value (Å)
C_1-C_6	1.400	1.399
C_3-C_4	1.386	1.392
C_{31}-O_{32}	1.338	1.345
C_{34}-H_{37}	1.086	1.09
Bond angle	**Exp. Value (°)**	**Cal. Value (°)**
C_2-C_3-C_4	119.1	119.4
C_7-C_{16}-C_{21}	120	120.1
O_{32}-C_{34}-H_{36}	105.7	105.1
N_{29}-C_{31}-O_{32}	112.9	109.8
N_{29}-C_{31}-O_{33}	124.1	124.9
Dihedral angle	**Exp. Value (°)**	**Cal. Value (°)**
C_6-C_1-C_2-C_3	-7.40	0.07
H_9-C_1-C_2-C_3	-176.2	-179.6
C_{18}-N_{25}-C_{27}-N_{29}	178.8	179.9
N_{25}-C_{27}-N_{29}-C_{31}	-0.4	-0.24

The C-H (1.39–1.53 Å) bond lengths are in good agreement with the calculated values. Bond angles N_{29}-C_{31}-O_{32}(109.8°) and N_{29}-C_{31}-O_{33} (125.1°) significantly deviate(5.1°–10.1°) from the expected trigonal angle as a consequence of molecular crowding effect arising as a result of steric effect between carbonyl and methyl groups.

NBO Analysis

Table 2 presents the second-order perturbation theory analyzes of Fock matrix in NBO basis that shows the strength of intramolecular hyperconjugative interactions. Presence of strong intramolecular hyperconjugation interactions LP(1)O_{14}→σ*(C_7-H_8) and LP(1)→σ*(C_{34}-H_{36}) have been observed with energies 31.46kJmol^{-1} and 9.24kJmol^{-1} respectively.

Table 2

Second order perturbation theory analysis

Donor NBO(i)	E.D.(e)	Acceptor NBO(j)	E.D.(e)	$E^{(2)}$ kJmol^{-1}
σ (C_1-C_2)	1.96652 -0.69760	σ*(C_6-C_7)	0.03058 0.33067	21.50
σ (C_6-C_7)	1.97267 -0.68731	σ*(O_{14}-H_{15})	0.02929 0.47809	10.75
σ (N_{26}-C_{27})	1.97535 -0.71788	σ*(C_{19}-C_{20})	0.02335 0.49649	15.15
n_1 O_{14}	1.97740 -0.74040	σ*(C_7-H_8)	0.04005 0.50453	20.58
n_1 O_{32}	1.97740 -0.74040	σ*(C_{34}-H_{36})	0.01934 0.34804	11.21
n_1 O_{33}	1.97412 -0.52515	σ*(N_{25}-H_{28})	0.01614 0.41660	22.76

The carbonyl group attached to benzimidazole ring is electron withdrawing groups, therefore the energy for the lone pair interaction LP(1)O_{33}→σ*(N_{25}-H_{28}) is 2.30kJmol^{-1} and the O_{33}...H_{28}(2.12Å) distance is shorter than the Van der Waal's separation between the O atom and H atom lying within the range <3Å for hydrogen interaction [12]. The shortening of C-N and C=O bonds gives clear evidence that the resonance of the benzimidazole ring is increased by the groups present which contributes to the bioactivity and stability of the molecule.

Spectral Analysis

Simulated FT-IR and FT-Raman spectra are presented in Figs. 2 & 3. calculated IR and Raman frequencies using B3LYP/6-311+G(d,p) level is presented in Table 3 along with detailed assignments as stipulated by the potential energy distribution (PED) calculation.

Benzimidazole ring vibrations

In heterocyclic compounds, N-H stretching vibration occurs in the region 3500–3000cm^{-1}[13]. Band appearing at 3237 and 3306 cm^{-1} in FT-IR spectrum of methyl N-[6-[hydroxy(phenyl)methyl]-1H-benzimidazol-2-yl]carbamate is due to the symmetric N-H stretching vibration.
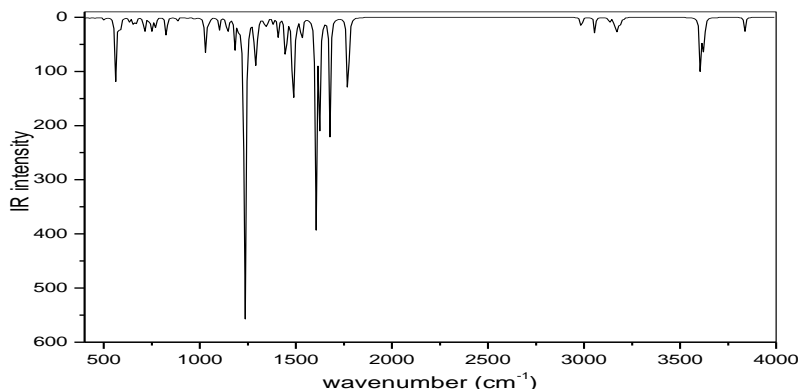
Figure 2 simulated IR spectrum

Intensity of the FT-IR spectral band at 3237 cm^{-1} is very small, and this striking discrepancy is due to the formation of intramolecular N-H...O interaction, since the bands are mixed in the very broad profile in that region and are observed as very weak shoulder [14].
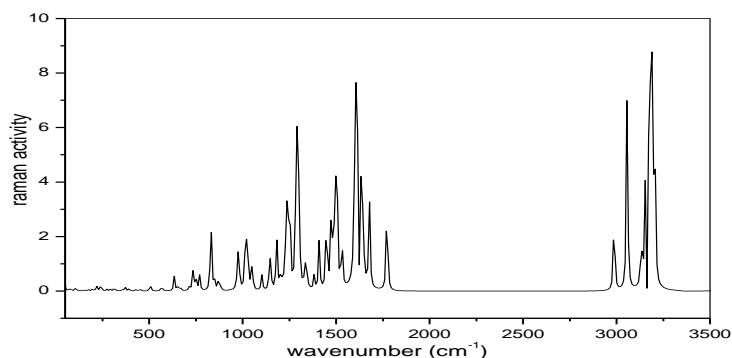
Figure 3 simulated Raman spectrum

Methoxy and carbonyl group vibrations

Methoxy group wavenumbers of the vibrational modes are known to be biased by a variety of interesting interactions such as electronic effects and inter-molecular hydrogen bonding. Position of C-H stretching and bending modes are shifted due to presence of electronic effects such as back-donation and induction, mainly caused by the presence of oxygen atom adjacent to CH_3 group [15,16]. Asymmetric stretching vibrations and symmetric stretching vibrations of CH_3 are expected to occur in the region 3000–2925 cm^{-1} and 2940–2905 cm^{-1} [17,18]. For the title compound, asymmetric stretching vibrations are observed at 2962 cm^{-1} in FT-Raman spectrum and symmetric stretching vibrations are observed at 2957 cm^{-1} in FT-IR spectrum with 94% PED. Carbonyl stretching C=O vibration [19] expected in the region 1715–1680 cm^{-1}, appears at 1712 cm^{-1} and 1706 cm^{-1} in FT-Raman and FT-IR spectra while PED calculations locate it at 1713 cm^{-1}. Formation of hydrogen bonds can increase the intensity of the carbonyl group because of conjugation and so conjugation leads to the intensification of Raman

as well as the infrared band intensities. C=O stretching mode is found to be simultaneously active in both IR and Raman spectra.

Phenyl ring vibration

The allowed C–H stretching modes 2, 20a, 20b, 7a, 7b for monosubstituted phenyl ring are expected in the range 3120–3010 cm^{-1} [20]. The C–H stretching mode 2 is observed at 3079 cm^{-1} as a weak band in IR. The ring mode 20a is observed at 3085 cm^{-1} as a weak band in the Raman spectrum. The mode 7b is observed as a weak band at 3065 cm^{-1} in the IR and as a medium band at 3062 cm^{-1} in the Raman spectrum. There are five C–C stretching vibrations 8a, 8b, 19a, 19b, and 14, which are dependent on the substituents. The degenerate modes 8a and 8b of the phenyl ring are insensitive to the substituents; the intensity of the 8a mode increases with the enhancement of the side chain. The normal mode 8a has been observed in the IR spectrum at 1585 cm^{-1}. The strong band observed at 1572 cm^{-1} in the Raman spectrum is assigned to the 8b mode. The enhanced intensity clearly shows the higher degree of the conjugation in the phenyl ring. The modes 19a and 19b for monosubstituted ring are around 1500 cm^{-1} and 1400 cm^{-1}, respectively. The observed band at 1495 cm^{-1} in the Raman spectrum and 1447 cm^{-1} in the IR spectrum is assigned to the 19b and 19a modes of the phenyl ring.

HOMO-LUMO Analysis

Energy gap between HOMO and LUMO is a vital structure in determining molecular electrical transport properties[21]. The HOMO-LUMO plot is shown in figure 4
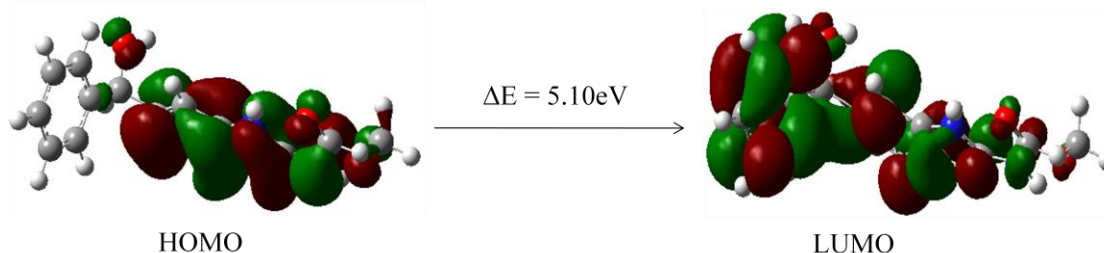
Figure 4 HOMO-LUMO plot

HOMO is localized over the benzimidazole ring, HOMO→ LUMO transition implies an electron density transfer from benzimidazole ring to hydroxy phenyl group. Orbitals significantly overlap near C$_7$ atom and charge transfer occurs through methyl hydroxy group. Atomic orbital compositions of the frontier molecular orbital are sketched in Fig. 2. The energy difference between HOMO and LUMO orbital which is called as energy gap is a critical parameter in determining molecular electrical transport properties because it is a measure of electron conductivity, calculated 5.10eV for title molecule. The low HOMO-LUMO gap indicates the bioactivity of the molecule.

Total, Partial and Overlap Population Density of States

Group contributions of the molecular orbitals to prepare the density of the states DOS, PDOS and COOP (crystal orbital overlap population) spectra are plotted using Gauss-Sum program as shown in figure 5. Contributions to chemical bonding through PDOS plots show percentage contribution of a group to each molecular orbital. Positive value of COOP indicates

bonding interaction, negative value indicates antibonding interaction and zero value indicates nonbonding interactions [22]. COOP diagram reveals that benzimidazole ring and carbonyl group have strong bonding and anti-bonding characters.

DOS

COOP

PDOS
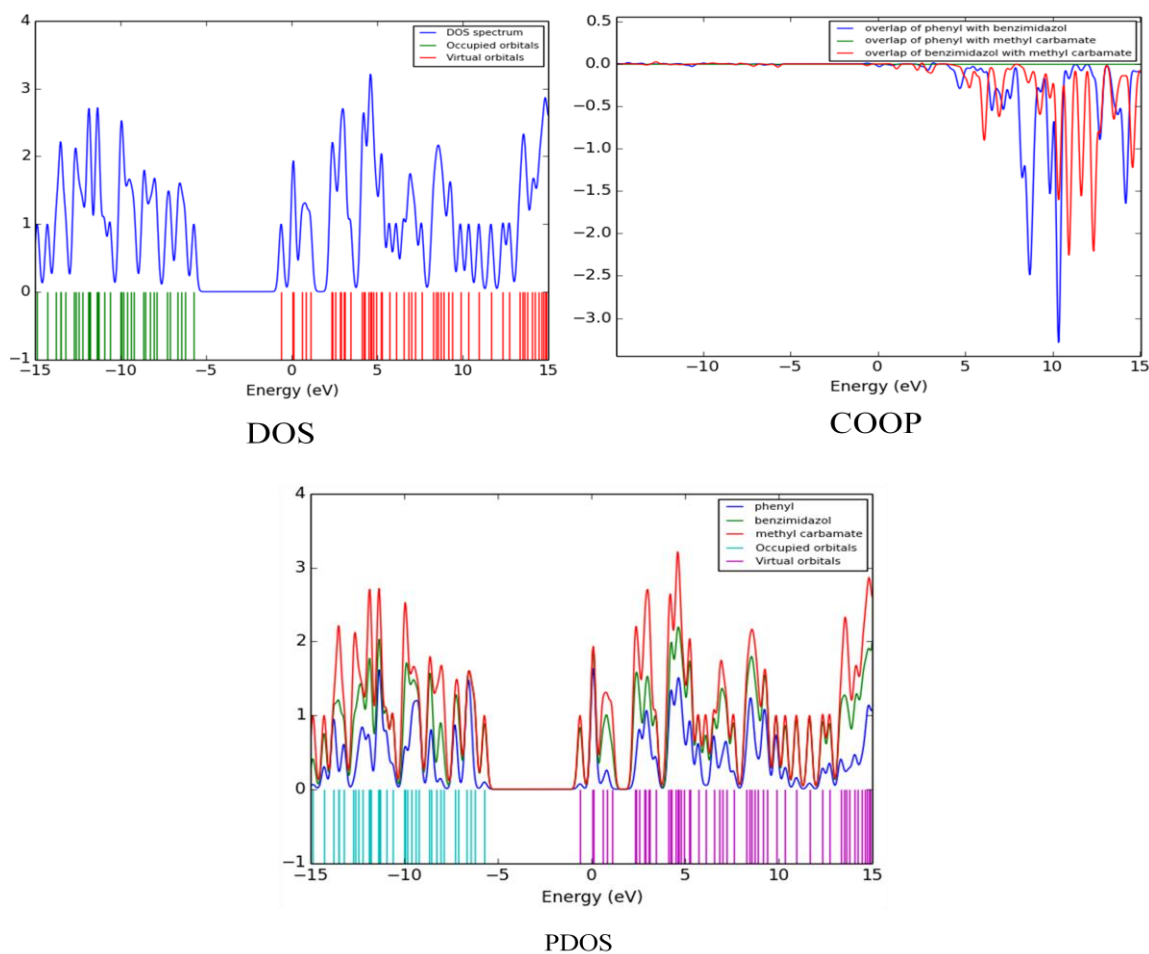
Figure 5 Density of states

4. CONCLUSION

DFT analysis explicates a slight deviation in values which were observed predominantly in benzimidazole ring and carbonyl group. The CH$_3$ group wavenumbers was blue-shifted due to the electronic effects and intramolecular hydrogen bonding. NBO analysis clearly accounts for the increase in energies and the shortening of C-N and C=O bonds due to resonance of the benzimidazole ring which has been increased by the groups present contributing to the stability of the molecule. The HOMO and LUMO energy gap reveals the chemical reactivity of the molecule. Orbital energy interactions between benzimidazol, methyl carbamate and phenoxy groups are analyzed by density of energy states.

REFERENCES

[1] J. Lu, B. Yang, Y. Bai, Synth. Commun. 32 (2002) 3703–3709.
[2] N. Sundaraganesan, S. Ilakiamani, P. Subramani, B. Dominic Joshua, Spectrochim. Acta A 67 (2007) 628–635.

[3] M. Sekerci, Y. Atalay, F. Yakuphanoglu, D. Avci, A. Bas̨ o?glu, Spectrochim. Acta A 67 (2007) 503–508.

[4] S. Ray, D. Chaturvedi, Application of organic carbamates in drug design. Part 1: anticancer agents, Drugs Future 29 (2004) 343-357.

[5] N. Sundaraganesan, S. Ilakiamani, P. Subramani, B. Dominic Joshua, Spectrochim. Acta A 67 (2007) 628–635.

[6] C. Lee, W. Yang, R.G. Parr, Phys. Rev. B 37 (1988) 785.

[7] M.J. Frisch, G.W. Trucks, H.B. Schlegel, G.E. Scuseria, M.A. Robb, J.R. Cheeseman, G. Scalmani, V. Barone, B. Mennucci, G.A. Petersson, H. Nakatsuji, M. Caricato, X. Li, H.P. Hratchian, A.F. Izmaylov, J. Bloino, G. Zheng, J.L. Sonnenberg, M. Hada, M. Ehara, K. Toyota, R. Fukuda, J. Hasegawa, M. Ishida, T. Nakajima, Y.Honda, O. Kitao, H. Nakai, T. Vreven, J.A. Montgomery Jr., J.E. Peralta, F. Ogliaro, M. Bearpark, J.J. Heyd, E. Brothers, K.N. Kudin, V.N. Staroverov, T. Keith, R. Kobayashi, J. Normand, K. Raghavachari, A. Rendell, J.C. Burant, S.S. Iyengar, J. Tomasi, M. Cossi, N. Rega, J.M. Millam, M. Klene, J.E. Knox, J.B. Cross, V. Bakken, C. Adamo, J. Jaramillo, R. Gomperts, R.E. Stratmann, O. Yazyev, A.J. Austin, R. Cammi, C. Pomelli, J.W. Ochterski, R.L. Martin, K. Morokuma, V.G. Zakrzewski, G.A. Voth, P. Salvador, J.J. Dannenberg, S. Dapprich, A.D. Daniels, O. Farkas, J.B. Foresman, J.V. Ortiz, J. Cioslowski, D.J. Fox, Gaussian 09, Revision B.01, Gaussian, Inc., Wallingford, CT, 2010.

[8] E.D. Glendening, A.E. Reed, J.E. Carpenter, F. Weinhold, NBO Version 3.1, Theoretical Chemistry Institute and Department of Chemistry, University of Wisconsin, Madison, 1998.

[9] N.M.O'Boyle, A.L.Tenderholt, K.M.Langner, J.Comput.Chem.29(2008) 839-845.

[10] M. Joseph, Hornback, University of Denver, Organic Chemistry, 2006, p. 94.

[11] R.D. Harcourt, Qualitative Valence-Bond Descriptions of Electron-RichMolecules: Pauling 3-ElectronBonds' and Increased-Valence'Theory, Springer-Verlag, Berlin Heidelberg, 1982, p. 121.

[12] A. Bondi, J. Phys. Chem. 68 (1964) 441.

[13] G. Socrates, Infrared and Raman characteristic group frequencies, tables and charts, third ed., Wiley, Chichewster, 2001.

[14] L.J. Bellamy, R.L. Williams, Spectrochim. Acta 9 (1957) 341.

[15] B. Smith, Infrared Spectral Interpretation, a Systemtic Approach, CRC Press, Washington DC, 1999.

[16] M. Gussoni, C.O. Castiglioni, J. Mol. Struct. 521 (2000) 1.

[17] N.B. Colthup, L.H. Daly, S.E. Wiberly, Introduction of Infrared and Raman Spectroscopy, 3rd ed., Academic Press, New York, 1990.

[18] N.P.G. Roeges, A Guide to the Complete Interpretation of Infrared Spectra of Organic Structures, Wiley, New York, 1994.

[19] M. Barthes, G. De Nunzio, G. Riber, Synth. Met. 76 (1996) 337.

[20] C.Y. Panicker, H.T. Varghese, D.P. Philip, H.I.S. Nogueira, K. Kastkova, Spectrochim. Acta 67A (2007) 1313.

[21] K. Fukui, Science 218 (1982) 747.

[22] M. Chen, U.V. Waghmare, C.M. Friend, E. Kaxiras, J. Chem. Phys. 109 (1998) 6680.

MOLECULAR STRUCTURE, NBO, HOMO-LUMO AND NLO PROPERTIES OF (4-DIMETHYLAMINO-PHENYL)-GLYOXAL NLO MATERIAL BASED ON DFT CALCULATIONS

D.Jaya Reshmi and D. Arul Dhas[*]

Department of Physics and Research Centre, Nesamony Memorial Christian College, Marthandam Affiliated to Manonmaniam Sundaranar University, Abishekapatti, Tirunelveli-627012

*Corresponding author: aruldhas2k4@gmail.com

ABSTRACT

Quantum chemical calculations of molecular structure and vibrational wavenumbers of (4-Dimethylamino-phenyl)-glyoxal have been calculated employing DFT level of theory using the 6-311G (d,p) basis set. The calculations revealed that the optimized geometry closely resembled the experimental XRD data. In addition, DFT calculations of the title compound, Natural Bond Orbital (NBO), dipole moments, and Highest Occupied Molecular Orbital (HOMO) and lowest unoccupied molecular orbital (LUMO) energy were also computed. The relative SHG efficiency was compared with urea by Kurtz powder method The Non-linear optical properties such as dipole moment (μ), polarizability (α_{tot}) and molecular first order hyperpolarizability (β) of the title compound are computed.

Key Words: DFT, Charge Analysis, SHG, Vibrational Analysis, NLO

1. INTRODUCTION

The organic molecules contain both conjugated bonds and acceptor group on one side and a donor group on the other side are known as nonlinear optical materials [1].The most significant features of the molecular structure, such as dipole moment, vibrational frequencies and non-linear optical properties etc., are obtained by studies in the literature [2-4]. The FT-IR spectral investigation of title molecule was performed using DFT. Vibrational spectra of the compound are analyzed on the basis of calculated potential energy distribution (PED). The main objective of this work is molecular structure parameters and vibrational wave numbers. The structure geometry, non- linear optical (NLO) property, Natural Bond Orbital (NBO), (HOMO) and (LUMO) energies are performed.

2. METHODS & METHODOLOGY

Experimental Details

(4-Dimethylamino-phenyl)-glyoxal was purchased from Sigma-Aldrich Company with a stated purity of 99% and it was use without further purification.

Computational details

In the present study, the quantum chemical calculations of the compound is done by applying DFT method with the B3LYP functional and 6–311G (d,p) basis set using Gaussian 09W software [5]. GaussView 4.1 [6] and Chemcraft [7] programs were utilized to draw the structure of the optimized geometry and to visualize the HOMO, LUMO pictures. The

HOMO–LUMO analysis has been carried out to explain the charge transfer within the molecule. The natural atomic charges were calculated using NBO method as implemented in the Gaussian 09W package [8] at the DFT/B3LYP level. The polarizability, hyper-polarizability and dipole moments of the sample have been calculated using the same method.

3. RESULTS AND DISCUSSION

Optimized geometry

Molecular geometries can be specified in terms of bond lengths, bond angles and torsion angles. Fig. 1 shows the optimized molecular structure of the title compound calculated at B3LYP/6-311G (d,p) level. The optimized geometrical parameters calculated are shown in Table 1.
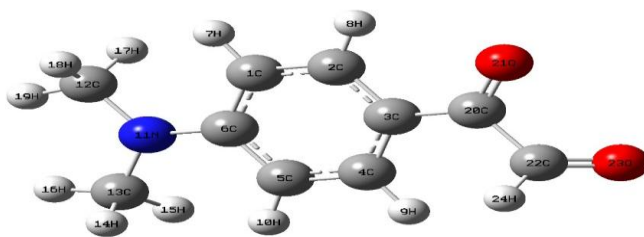
Fig.1. optimized molecular structure of (4-Dimethylamino-phenyl)-glyoxal

The six-membered ring in benzene is a perfect hexagon all carbon-carbon bonds have an identical length of 1.40 Å. The experimental and theoretical data shows that the C-C bond lengths are observed in the range 1.371–1.411 Å. In the ring, the low bond distance measured at C_1-C_2 is 1.382Å, denote the C_2-H_8 …O_{21} inter-molecular hydrogen bonding and C_4-C_5 is 1.384Å indicatingC_4-H_9 …O_{22} inter-molecular hydrogen bonding. The bond lengthof C_2-C_3 is 1.399Å and C_3-C_4 bond length is 1.400Å.C_5-C_6 bond length is 1.415Å and C_1-C_6 is 1.416Å this is due to the substitution of dimethyl amino group in place hydrogen atom in benzene ring. The electronegative oxygen atom affect the bond C_3- C_{20}so it has high value 1.477 Å. Normally, the benzene ring bond angle 120˚. Both endo cyclic and exo cyclic bond angle C_1-C_2-C_3, C_3-C_4-$C_5$and C_4-C_5-C_6 shows the non-aromatic character.C_1-C_5-C_6 and C_2-C_3-C_4 are 117.4˚ and 118.2˚.C_3-C_{20}=O_{21} and C_3-C_{20}-O_{22} is 125.0˚ and 112.1˚ respectively. The dihedral angles C_1-C_6-N_{11}-C_{12} and C_2-C_3-C_{20}-O_{21} are indicating that in the molecule, the glyoxal and dimethylamino groups are essentially nonplanar with the benzene ring. As shown in Table 1, the bond distances calculated by electron correlated methods are longer than the experimental distances.

Table.1. Optimized geometry of (4-Dimethylamino-phenyl)-glyoxal

Bond length	Experimental value	calculated value	Bond angle	Experimental value	calculated value
C_1-C_2	1.371	1.382	$C_1-C_2-C_3$	121.3	121.3
C_2-C_3	1.389	1.399	$C_2-C_3-C_4$	118.2	118.2
C_3-C_4	1.395	1.400	$C_3-C_4-C_5$	121.0	121.0
C_4-C_5	1.372	1.384	$C_1-C_2-C_6$	120.8	120.8
C_5-C_6	1.407	1.415	$C_1-C_5-C_6$	117.4	117.4
C_1-C_6	1.411	1.416	$C_6-N_{11}-C_{12}$	121.4	120.1
$C_{20}=O_{21}$	1.209	1.211	$C_3-C_{20}=O_{21}$	124.5	123.5
$C_{22}-O_{23}$	1.336	1.356	$C_3-C_{20}-O_{22}$	112.5	122.7

Vibrational analysis

The title molecule consists of 24 atoms and they have 66 normal modes of vibrations. All fundamental vibrations are active in IR absorption. The calculated harmonic wavenumbers are usually higher than the corresponding experimental quantities due to electron correlation effects and basis set deficiencies. The implementation of uniform scaling factors to the theoretical calculation makes it coincide with the experimental data. The calculated spectra of FT-IR is shown in Fig. 2
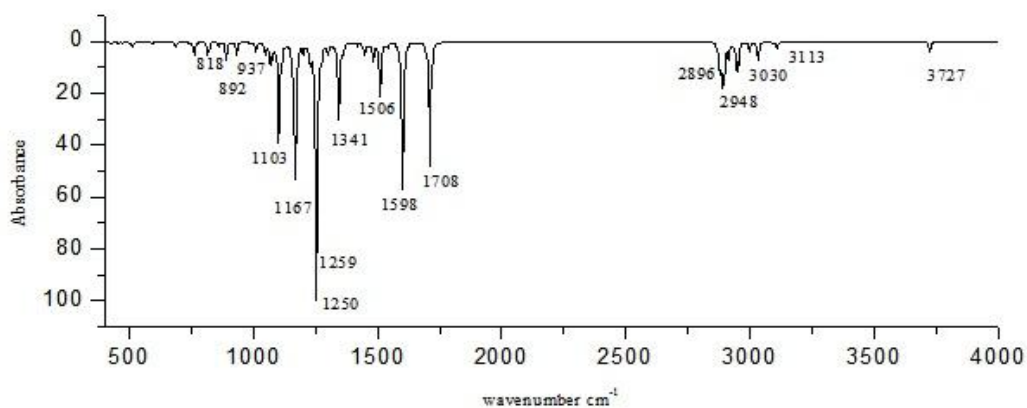
Fig.2. calculated FT-IR spectra of 2-hydroxyethyl 4-dimethylaminobenzoate

C–H and C -C vibrations

In aromatic compounds, the carbon–hydrogen stretching vibrations normally occur at 3100–3000 cm^{-1} [9]. These vibrations are not found to be affected due to the nature and position of the substituent. In this work, the FTIR bands observed at 3113, 3087 and 3030cm^{-1}are assigned to symmetrical stretching. Corresponding calculated values are 3112, 3096 and 3042cm^{-1}. The C- C stretching vibrations in aromatic compounds form characteristic bands in the region of 1430–1650 cm^{-1} [10-11]. The presence of conjugate

substituent such as C-C causes a heavy doublet formation around the region 1200–1350 cm^{-1}. The six ring carbon atoms undergo coupled vibrations called skeletal vibrations and give a maximum of four bands in the region 1660–1420 cm^{-1}. In IR spectra, the C–C stretching vibration of ring appears strongly at 1598 and 1708cm^{-1}. The intra molecular charge transfer (ICT) from the donor to acceptor group through single–double bond conjugated path can induce large variations of both the molecular dipole moment and molecular polarizability making simultaneous activation of C=C stretching modes of the ring. The simultaneous activation of C=C stretching modes of the ring was evident from the very strong IR band at 1598 cm^{-1} provide evidence for the charge transfer interaction between the donors and acceptor groups through the π- system which make the molecule highly polarized enhancing the NLO property.

CH$_3$ vibrations

The anti-symmetric and symmetric stretching modes of the methyl groups generally appear at about 3100 and 2880 cm^{-1}. The bands observed at 3012 cm^{-1} in the IR spectrum and the bands are assigned to the anti-symmetric stretching mode of the methyl group linked to the N atom. The bands located at 2948 and 2896 cm^{-1} in the IR spectrum assigned to the methyl symmetric stretching vibration. CH$_3$ stretching modes were reported in the range between 2912 and 2860 cm^{-1} [12]. The anti-symmetric methyl deformation modes are observed at 1485, 1468, 1432 and 1415 cm^{-1} in the IR. The IR bands located at 1446 and 1393 cm^{-1} are assigned to the symmetrical methyl deformation mode. The values reported in literature for these modes are expected in the range 1506–1341 cm^{-1} and the authors do not discriminate between symmetric and anti-symmetric bending modes of the methyl group. The IR bands located at 1103 and 937 cm^{-1} are assigned to the rocking mode.

CH$_2$ vibrations

The six fundamental CH$_2$ group frequencies include symmetric stretch, asymmetric stretch, scissoring, rocking, wagging and twisting modes [13]. The asymmetrical stretching (ν_{asym}) and symmetrical stretching (ν_{sym}) bands of the methylene group occur near 2926 and 2853cm^{-1}. Due to the blue shift the possibility of weak hydrogen bonding occurs between C$_{23}$-H$_{24}$...O$_{21}$. The calculated values of CH$_2$ asymmetric stretching vibration is 2955cm^{-1}. The calculated value for the symmetric stretching is found to be 2948 cm^{-1}. This symmetry and asymmetry CH stretching vibration indicates the presence of a blue shifting. The four bending vibrations of CH$_2$ group are scissoring, rocking, wagging and twisting. CH$_2$ scissoring band in the spectra of hydro carbons occur at 1455cm^{-1} while CH$_2$ wagging vibration are observed in the region 1307-1304cm^{-1} which are weaker than those resulting from CH$_2$ scissoring. The CH$_2$ scissoring calculated value is found to be 1471 cm^{-1}.

C-N vibrations

The C-N stretching absorption assigned in the region 1382–1266 cm^{-1} for aromatic amines. Primary aromatic amines with nitrogen directly connected to the ring absorbs strongly at 1330–1260cm^{-1} due to stretching for the phenyl C-N band. In our present study, a weak band observed in the FT-IR spectrum at 1259 cm^{-1} is assigned to the C-N stretching

vibration and it is in good agreement with the theoretically computed value of $1267 cm^{-1}$, respectively.

C=O vibrations

The carbonyl stretching C=O vibration is expected in the region $1715-1680$ cm^{-1} and in the present study this mode appears at $1708 cm^{-1}$ in FT-IR as a weak band. The DFT calculations give this mode at 1699 and $1703 cm^{-1}$. The conjugation and influence of intermolecular hydrogen bonding result in the lowering of the stretching wavenumbers.

Atomic charge

Charge distribution has a major deciding role in the application of quantum chemical calculations to molecular system because atomic charges affect varied properties such as dipole moment, molecular polarizability, electronic structure and acidity–basicity behaviour of compound. The C_{20} atom is found to have the highest negative natural charge value. The reason is the high electronegativity of the O-atom attached to it. All the H–atoms are seen to be electropositive. Ring hydrogen (H_8) is more positive compared with other hydrogen atoms. This is due $C_2-H_8 \ldots O_{21}$ hydrogen bonding. C_2 atom has very low negatively charged.

Natural bond orbital (NBO) analysis

NBO analyses were performed using NBO 3.1 program as implemented in the Gaussion '09 package at the DFT level. A useful aspect of the NBO method is that it gives information about interactions in both filled and virtual orbital spaces that could enhance the analysis of intra- and intermolecular interactions. The interaction result is a loss of occupancy from the localized NBO of the idealized Lewis structure into an empty non-Lewis orbital. For each donor (i) and acceptor (j), the stabilization energy $E^{(2)}$ associated with the delocalization ij is estimated as

$$E^{(2)} = \Delta E_{ij} = qi\left(\frac{(F(i,j)2}{\varepsilon j - \varepsilon_i}\right)$$

Where q_i is the donor orbital occupancy, areε_i andεj diagonal elements and F (i,j) is the off diagonal NBO Fock matrix element. The larger the $E^{(2)}$ value shows the more intensive is the interaction between electron donors and electron acceptors, i.e. the more donating tendency from electron donors to electron acceptors and the greater the extent of conjugation of the whole system. The intra molecular interaction is formed by the orbital overlap between σ and π bonding (C–C, C–H, and C–F) and antibonding σ*and π*(C–C, C–H and C–F) orbital's which result intra molecular charge transfer (ICT) causing stabilization of the system. These interactions are observed as an increase in electron density (ED) in C–C antibonding orbital that weakens the respective bonds [14-15]. The bond pair donor orbital π C=C→π*C-C and π C-C→π*C-O give more energy stabilization than σ C-C→ σ*C-C. A very strong interaction has been observed between the lone electron pair LP N_{11} and the σ*C_1-C_6 with an energy of 47.67 kcal mol^{-1}. The lone pair LP O_{21} participates in LP O_{21}→σ*C_3-C_{20} interaction with an important value of energy. The energy value of the interactions π*C_1-C_6→π*C_2-C_3 and π*C_1-C_6→π*C_4-C_5 are 285.2 and 162.2 kcal mol^{-1}, respectively indicating that these interactions produce a great stabilization in the molecule.

Second Harmonic Generation (SHG) test

The SHG efficiency of title molecule is measured by using the Kurtz powder technique and compared with urea. The sample is subjected to a Q-switched Nd:YAG laser emitting 1064nm 10 ns pulse width and 5mJ power. The generated SHG signal at 532nm is split from the fundamental frequency using an IR separator. A detector connected to power meter is used to detect second harmonic intensity and read the energy input and output. The SHG efficiency is compared with urea. From SHG test, the SHG efficiency of the title molecule was found to be nearly 5 times greater than that of urea.

Non-linear optical (NLO) properties

Molecule-based second-order nonlinear optical (NLO) materials have recently attracted much interest because they involve new scientific phenomena and they offer potential applications in emerging optoelectronic technologies, telecommunications, optical switching and signal processing [16].The first hyper-polarizabilities (β) of the title molecule along with related properties (μ, α and $α_°$) are calculated using B3LYP/6-311G(d,p) method. In this paper, the studied molecule was divided into two parts to evaluate the charge distribution, Part A for dimethyl amino and Part B is glyoxal group (Fig. 3). In the study molecule, there is significant intramolecular charge transfer (ICT) from the ring (part A) as electron donor to part B as electron acceptor. Such ICT is responsible for the high hyper-polarizability of the studied system. Also the studied compound has lower energy gap (ΔE) compared to urea. Based on these calculations, the studied molecule is considered as better NLO material than urea which is used as reference molecule for comparison of the NLO activity [17].

The values of the polarizabilities (α) and first hyper-polarizability (β) of the GAUSSION '09W output are reported in atomic units (a.u) the calculated values have been converted into electrostatic units (esu). The polarizability and the first hyper polarizabilities of the compound is 14.849×10^{-30}, based on these facts, it could be concluded that the present material has a reasonably good propensity for non- linear optical activity. The molecular orbital of HOMO and LUMO of shown in Fig.3 The frontier molecular orbitals of the title molecule have greater hyperpolarizability and lower HOMO-LUMO energy gap which indicates greater NLO properties of title molecule.

$$\Delta E_{HOMO\text{-}LUMO} = 0.11631eV$$
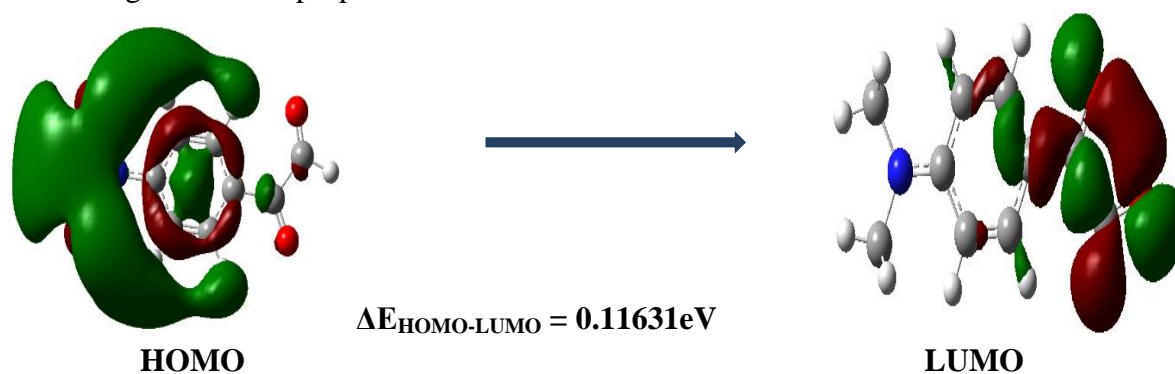
HOMO   **LUMO**

Fig.3. Homo-Lumo structure of (4-Dimethylamino-phenyl)-glyoxal

4. CONCLUSION

All theoretical calculations is performed at the B3LYP methods with the 6-311 G(d,p) polarized basis set. Comparison between the calculated and experimental parameters shows that the B3LYP method results are in good agreement with experimental values. The atomic charge distribution of the title compound has been calculated by the natural population analysis. The NBO analysis reveals that the electron density transfer and the second order perturbation theory of Fock matrix shows strong intra-molecular hyperconjugative interactions within the molecule. The movement of π-electron cloud from donor to acceptor i.e. intramolecular charge transfer can make the molecule more polarized and the HOMO–LUMO energy gap must be responsible for the NLO properties of molecule. The calculated NLO values increased with the polarity of the solvent. NLO properties of the title compound are much greater than those of urea. Therefore, the title compound may be a potential applicant in the development of NLO materials.

REFERENCES

[1] C.G. Liu, Y.Q. Qui, S.L. Sun, H. Chen, N. Li, Z.M. Su, Chem. Phys. Lett. 429 (2006)

[2] G. Alpaslan, M. Macit, A. Erd€ onmez, O. Büyükgüng€ or, J. Mol. Struct. 997 (2011)

[3] S. Yazıcı, Ç. Albayrak, I.E. Gümrükçüoglu, I. S¸ enel, O. Büyükgüng€ or, Spectrochim. Acta A 93 (2012) 208e213.

[4] Y. Bing olAlpaslan, G. Alpaslan, A. Alaman A gar, N. OcakIskeleli, Emin €Oztekin, J. Mol. Struct. 995 (2011) 58e65.

[5] T. Sundius, Vib. Spectrosc. 29 (2002) 89.

[6] R. Dennigton II, T. Keith, J. Millam, GaussView, Version 4.1.2, Semichem, Inc., 2007. Shawnee Mission, KS.

[7] Zhurko GA, Zhurko DA, Chemcraft. Lite version build 08, 2005.

[8] M. Szafran, A. Komasa, E.B. Adamska, J. Mol. Struct. (Theochem.) 827 (2007)101.

[9] F.R. Dollish, W.G. Fateley, F.F. Bantley, Characteristic Raman Frequencies of Organic Compounds, Wiley, New York, 1974. 170.

[10] G. Varsanyi, Vibrational Spectra of Benzene Derivatives, Akademiai Kiado, Budapest, 1969.

[11] V. Krishnakumar, V. Balachandran, Spectrochim. Acta 63 A (2006) 464.

[12] B.J. Coe, J.A. Harris, L.A. Jones, B.S. Bruschwig, K. Song, K. Clays, J. Garın, J. Orduna, S.J. Coles, M.B. Hursthouse, J. Am. Chem. Soc. 127 (2005) 4845–4859.

[13] J.B. Lambert, H.F. Shurvell, R.G. Cooks, Introduction to Organic Spectroscopy, Macmillan Publish, NewYork, USA, 1987.

[14] C. James, A. Amal Raj, R. Rehunathan, I. Hubert Joe, V.S. Jayakumar, J. Raman Spectrosc. 37 (2006) 1381.

[15] Liu Jun-na, Chen Zhi-rang, Yuan Shen-fang, J. Zhejiag, University Sci. 6B (2005)584.

[16] D.A. Kleinman, Phys. Rev. 126 (1962) 1977.

[17] Y.X. Sun, Q.L. Hao, W.X. Wei, Z.X. Yu, L.D. Lu, X. Wang, Y.S. Wang, J. Mol. Struct.: Theochem 904 (2009) 74.

STRUCTURAL ANALYSIS, MESP AND 2D FINGER PRINT PLOT ANALYSIS OF 2-(4-AMINO- 3, 5-DICHLORO-6-FLUOROPYRIDIN-2-YL) OXYACETIC ACID (ADF)

N. Suma[*], D.Aruldhas

Department of Physics and Research Centre, Nesamony Memorial Christian College, Marthandam
Affiliated to Manonmaniam Sundaranar University, Abishekapatti, Tirunelveli-627 012
*Corresponding author:harshram26@gmail.com

ABSTRACT

The spectroscopic investigations along with theoretical quantum chemical studies on 2-(4-amino- 3, 5-dichloro-6-fluoropyridin-2-yl) oxyacetic acid (ADF) have been consummated. The fundamental vibrational transitions were explained by experimental FTIR technique. The HOMO-LUMO analysis is used to determine the Charge transfer within the molecule. Stability of the molecule arising from hyperconjugative interactions and charge delocalization has been analyzed using natural bond orbital (NBO) analysis. NBO showed that the intramolecular C-H…N hydrogen bond in this crystal structure. The structural and spectroscopic data of the molecule were calculated by using density functional theory (DFT) employing B3LYP methods with the 6-311G (d, p) basis set. The geometry of the molecule was fully optimized. As a result, the optimized geometry and calculated spectroscopic data show a good agreement with the experimental result. Using 2d finger print plot analysis confirms the existence of intramolecular interactions.

Keywords: DFT, NBO, HOMO-LUMO

1. INTRODUCTION

2-(4-amino-3, 5-dichloro-6-fluoropyridin-2-yl) oxyacetic acid(ADF) is a selective systemic pyridine herbicide. It is widely used on cereal crops, olive trees and fallow croplands to control broad-leaf weeds [1] .The present work reports a study on ADF using spectroscopic techniques. The natural bond orbital (NBO) analysis has been carried out to interpret hyperconjugative interaction and intramolecular charge transfer (ICT) [2]. The calculated value of HOMO-LUMO energy gap is used to interpret the biological activity of the molecule. Intramolecular hydrogen bonding interactions have received much attention from both practical and theoretical perspectives.MESP can be used to determine the structures and activities of biological molecule. The program crystal explorer (wolft et al., 2012) enables the analysis and visualization of crystal contacts through the Hirshfield surface (2d plot).The optimized molecular structure of the compound with atom numbering scheme adopted in the computation is shown in Figure 1.

2. COMPUTATIONAL DETAILS

We have utilized DFT theory for the computation of molecular structure,vibrational frequencies and energies of optimized structures by using Gaussian 09 program package[3] at the B3LYP level with standard 6-311G (d,p) basis set. The corresponding X-ray diffraction values are also used for comparision.

3. RESULTS AND DISCUSSION

Optimized Geometry

The optimized geometry parameters of ADF at DFT level of computations are listed in Table1.The small deviations are probably due to the intramolecular interactions of the molecule.

Figure 1 Optimized structure of ADF

Table 1

Optimized bond length and bond angle

Bond Length / (Å)			Bond Angle / (°)		
Exp. Value	ADF	Cal. Value	Exp. Value	ADF	Cal.Value
1.319	C_1-N_2	1.327	117.9	C_1-O_{11}-C_{12}	117.6
1.391	C_1-C_6	1.394	118.9	C_1-N_2-C_3	118.0
1.341	C_1-O_{11}	1.347	118.2	C_3-C_4-C_5	118.4
1.728	C_3-F_{10}	1.335	119.2	C_4-C_5-C_6	116.5
0.840	O_{17}-H_{18}	0.969	109.5	C_{15}-O_{17}- $_{18}$	107.0

The experimental C-H and N-H bond lengths are lower than the computed values. Increase in bond length is observed for C-C and C-N bond due to the reason that the calculation is performed in gaseous state and experiment in solid state. The bond length O_{17}-H_{18} **is** lengthened. This variation in O-H bond shows an extended conjugation due to the attachment of CH_2 and COOH group. The increase in bond angle C_{15}-O_{17}-H_{18} (107.0°) is due to the redistribution of partial charges on O_{17} atom. This is due to strong conjugation of ring π-electron system with carboxyl group which stabilizes the molecule. The experimental C-N-C bond angles of pyridine rings are 118.9[0] which is slightly greater than the calculated one.The calculated value of C-C-C

bond angles (**C$_3$-C$_4$-C$_5$ and C$_4$-C$_5$-C$_6$**) are less than 120^0, the differences in the values arises due to acetic acid group substitution.

Spectral Analysis

Secondary amine vibration

The amino groups are generally considered as electron-donating substituents in aromatic ring systems[4]. Generally N-H group share its lonepair of electron with the σ electrons in the ring. The H bonding leads to a reduction in NH stretching wavenumber and an increase in IR intensity [5]. For secondary amine N-H stretching vibration occurs in the range 3500-3300 cm^{-1}
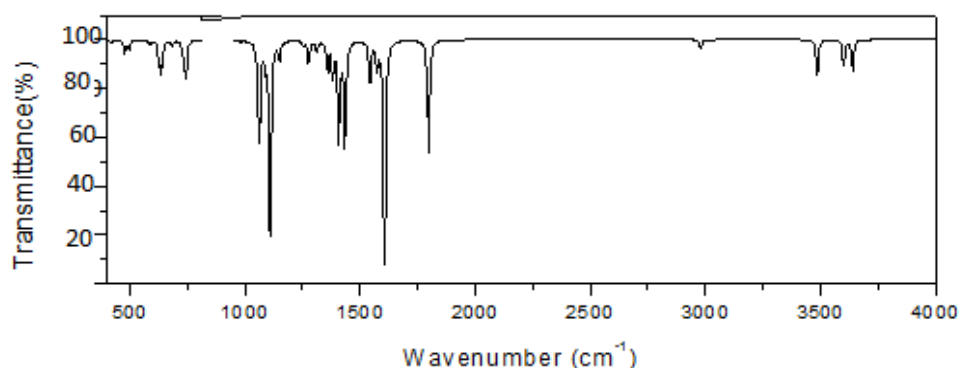
Figure 2 FT-IR Spectrum

COOH vibration

If a compound contains a carbonyl group, the absorption caused by the C-O stretching is generally strongest [7]. The appearance of weak bands in IR 1770-1730 cm^{-1} in aromatic compounds shows the presence of carbonyl group and is due to C=O stretching motion. The calculated C=O stretching mode at 1785 cm^{-1} with PED value of 87%. The wave number due to C=O stretching mainly depends upon conjugative, and steric effect. Vibrational analysis of C=O group is significant because of bioactivity of the compound.

Methylene group vibration

The CH$_2$ Symmetric Stretching vibrations are observed at 3029cm^{-1} as very weak band in IR Spectrum. The asymmetric CH$_2$ Stretching vibrations are generally observed in the region 3100-3000 cm^{-1}, while the symmetric stretch will appear in the region 2909 cm^{-1}[8].

NBO Analysis

NBO analysis provides a description of the structure of a compound based on a set of localized bond, and antibond that can be used to identify and confirm possible intra and intermolecular interactions between the units that would lead to proper and improper hydrogen

bonding. The second order perturbation theory analysis of Fock matrix was carried out to evaluate the donor-acceptor interactions in the NBO analysis [9]. The intramolecular interaction are formed by the overlap between σ (C-C), σ (C-N), σ* (C-N), σ* (C-H), σ* (N-H) bond orbital which results in an intramolecular charge transfer causing stabilization of the system. These interactions are observed as an increase in electron density in C-N bonding orbital that weakens the respective bonds. NBO showed that the intramolecular C-H…N hydrogen bond in this crystal structure.

Table 2

Second order perturbation theory analysis

COMPOUND	DONOR NBO(i)	E.D/e	ACCEPTOR NBO(j)	E.D/e	$E^{(2)}$/kJmol^{-1}
ADF	$\sigma(C_1 - N_2)$	1.976 -0.865	$\sigma^*(C_1 - C_6)$	0.045 0.519	17.70
	$\sigma(C_4 - C_5)$	1.964 --0.739	$\sigma^*(N_8 - H_{20})$	0.011 0.402	8.87
	$n_1(O_{11})$	1.963 --0.561	$\sigma^*(C_{12}-H_{13})$	0.015 0.383	11.20

NBO of the compound shows strong intramolecular hyper conjucative interaction. These interactions are observed as increase in electron density(ED) in C-C, C-N antibonding orbital that weakens the respective bonds [10]. The strong stabilization energy $E^{(2)}$ associated with such hyperconjucative interactions $n_1(O_{11}) \rightarrow \sigma^*(C_{12}-H_{13})$ and $n_1(N_2) \rightarrow \sigma^*(C_{12}-H_{13})$ are obtained as 11.20 kJ/mol. This results the strong intermolecular charge transfer (ICT), stabilizing the system. The weakening and elongation of N-H bonds occur due to hyperconjugation.

HOMO-LUMO Analysis

In the frontier region, neighbouring orbitals are being often closely spaced. In such cases, consideration of only the HOMO and LUMO may not yield a realistic description of the frontier orbitals. The HOMO-LUMO energy gap of title compound as calculated at the B3LYP/6-311G (d,p) level(Figure3), which reveals that the energy gap reflects the chemical activity of the molecule. The LUMO as an electron acceptor represents the ability to obtain an electron, and HOMO presents the ability to donate an electron. The energy gap is **0.14863eV**.The energy gap of HOMO-LUMO explains the eventual charge transfer interaction within the molecule, which influences the biological activity of the molecule. Consequently, the lowering of the HOMO-LUMO band gap is essentially a consequence of the large stabilization of the LUMO due to the strong electron accepting ability of the electron acceptor group[12].The HOMO-LUMO energy separation can be used as a sign of kinetic stability[13].

Figure 3   HOMO   ΔE=0.14863eV   LUMO

Molecular electrostatic potential (MESP)

Molecular electrostatic potential (MESP) is related the electronic density and can be used to predict binding sites for electrophilic (electron rich region) and nucleophilic attack (electron poor region) [14]. In the present case, the lone pair oxygen present in the acid group shows more negative charge, and hydrogen exhibits more positive charge (Figure4). It is worth mentioning that the bioactivity of the compound.
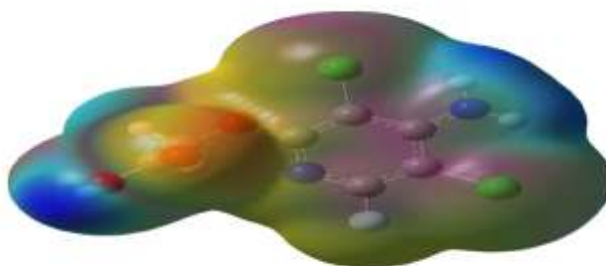
Figure4 mesp of ADF

2D Finger print plot Analysis

The Hirshfeld surface is becoming a valuable tool for analyzing intermolecular interactions while maintaining a whole of the molecule approach. The normalized contact distance d_{norm} based on both d_e (distance from the point due to the nearest nucleus external to the surface) and d_i(distance to the nearest nucleus internal to the surface). The combination of d_e and d_i in the form of a 2D finger print plot [15] provides summary of intermolecular contacts. Figure5 shows the contribution to the new hirshfeld surface area for each type of intramolecular contact of the title molecule O…H contacts comprise 10.3% of the surface area which indicates the spike. Cl...H contacts comprise 10.4% of the surface area and H…H contacts comprise 9.6% of the surface area.Which clearly reveals that the intramolecular hydrogen bonding.

O-H(10.3%)   **Cl-H(10.4%)**   **H-H(9.6%)**

H-Cl(6.0%)   **F-H(4.0%)**   **Cl-O(6.1%)**
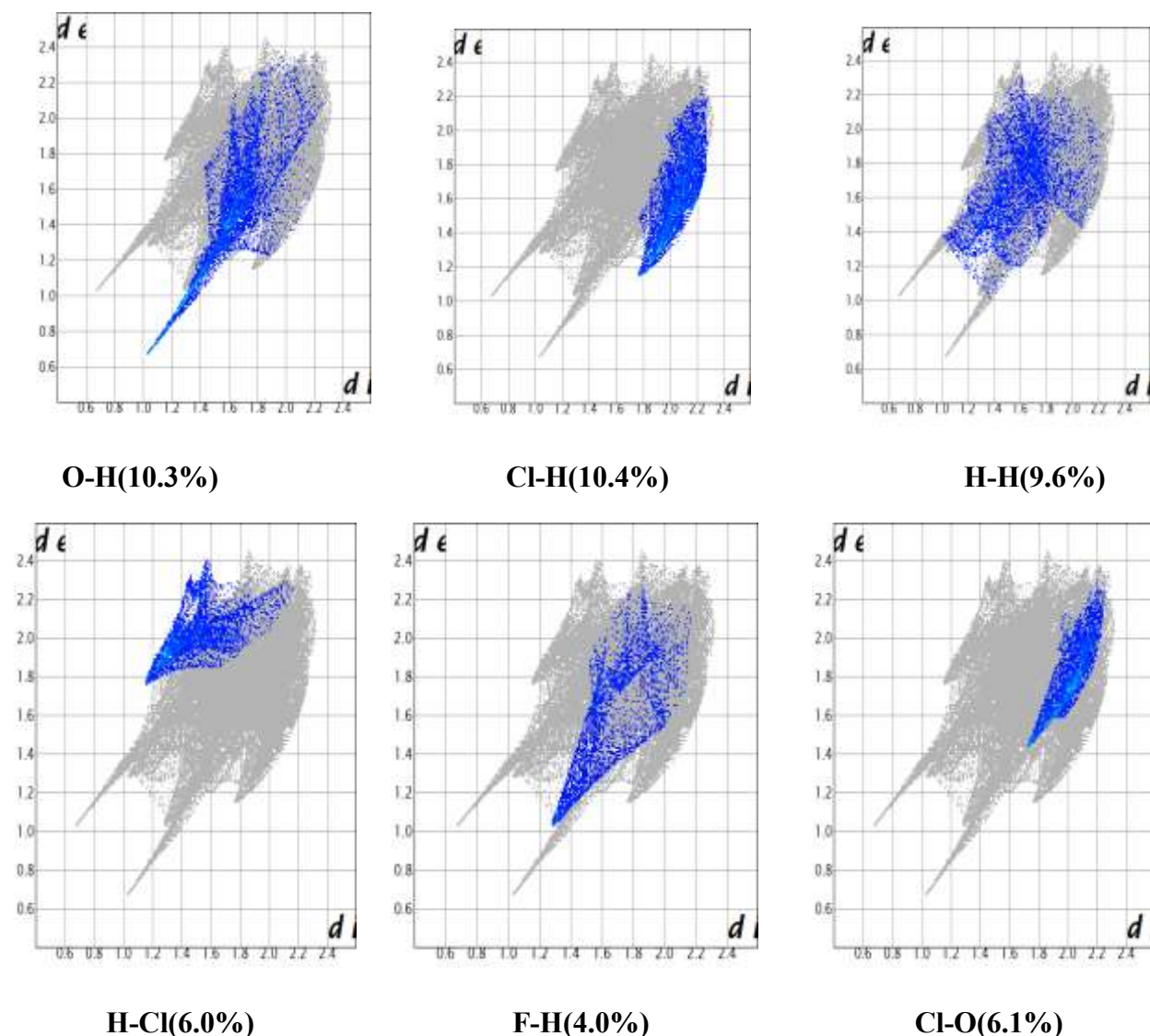
Figure5   : 2D Finger Print Plots

4. CONCLUSION

In the present work, complete vibrational analysis has been made for proper frequency contributions of ADF. The IR frequencies of the title compound have been theoretically computed using DFT methods. The optimized parameters have also been determined and compared with experimental data. From the optimized parameters, it was concluded that due to hyperconjucation, the C=O bond length increases .NBO result reflects the charge transfer within the molecule. NBO analysis reveals that the redshifting of the N-H stretching wave number exhibits the decrease in N-H bond order values that occurs due to donor-acceptor interactions. This leads to the stability and increase in herbicidal activity of ADF. Due to intra molecular C-H…..N hydrogen bonding there is an increase in the electron density of the antibonding orbital

of the C-H bond. The electron density delocalization, decrease in the C-H distance, and an increase in the vibrational stretching wavenumber. The lowering of the HOMO-LUMO energy gap value has substantial influence on the intramolecular charge transfer and bioactivity of the molecule.MESP denotes the active site.2d finger print plot indicates the more contribution of O-H,and Cl-H.Thus from above investigations, it can be concluded that ADF is a good herbicide to treat weeds and further work can be responsible for biological activity.

REFERENCES

[1] Moreno-Castilla, C., Lo´pez-Ramo´ n, M. V., Pastrana-Martı´nez, L. M., A lvarez-Merino, M. A. & Fontecha-Ca´mara, M. A. (2012).Adsorption, 18, 173–179

[2] T.S.Xavier,Naghmana Rashid,I.Hubert Joe," Vibrational spectra and DFT study of anticancer active mole 2-(4-bromophenyl),-1H-benzimidazole by normal co-ordinate analysis",Spectrochimica Acta Part A78,319-326,(2011).

[3] M.J. Frischa, G.W. Trucks, H.P. Schlegel, G.E. Scuseria, M.A. Robb, J.R. Cheesman.et.al. Gaussian '09, Gaussian, Inc., Wallingford CT, (2009).

[4] Colthup NB, Daly L H,Wiberly S E, "Introduction to infrared and spectroscopy", (1990).

[5] Smith B,"Infrared spectral interpretation a systematic approach CRC", Washington, DC, (1999).

[6] R.M.Silverten,G.C.Bassler, and T.C.Morrill,"Spectromeric identification of organic compound",5th ed,Wiley,Ny,pps 158-164, (1991).

[7] T.Joseplin, Beaula,D.Manimaran, I.HubertJoe V.K.Rastogi, V.Beena Jothy, B.C.Smith,Infra red spectral Interpretation.,A systematic Press,Washiington Dc(1999)

[8] R.M.Silverstein, F.X.Webster, Spectrometric identification of organic compounds.JohnWileyan ,New York.,(2003)

[9] M.Sarafran,A.Komasa,E.B.Adamska,JMolStruc(THEOCHEM),827,101, (2007).

[10] Akhil.R.Krishnan,H.Saleem,S.SubashChandraBose,N.Sundaraganesan, S.Sebastian,"Molecularstructure,VibrationalSpectroscopic(FT-IR,FT-Raman),UV and NBO analysis of 2-chlorobenzonitrile by density functional method", Spectrochimica Acta Part A 78,582-589,(2011).

[11] D.Aruldhas, I.Hubert Joe, S.D.D.Roy, S.Balachandran,"Spectroscopic investigation and hydrogen bonding analysis of triazinones",J.mol model ,18, 3587-3608,(2012).

[12] R.M.Silverten,G.C.Bassler, and T.C.Morrill,"Spectromeric identification of organic compound",5th ed,Wiley,Ny,pps 158-164, (1991).

[13] Kini.K.H, Han.Y.K, Jung.J, Theor.Chem.Acc.113, 233,(2005).

[14] Scrocco E, Tomasi J Electronic Molecular structure, Reactivity and intermolecular forces: An Euristic Interpretation by means of chem. (1978)103:115-193.

[15] Joshua.J. MC Kinnon, Wylan. Jayatilalka and Mark A. Spackman chem. Comm.(2007).

DFT CALCULATIONS OF MOLECULAR STRUCTURE, SPECTROSCOPIC CHARACTERIZATION AND NBO ANALYSIS OF PROPAN-2-YL N-[2-(4-PHENOXYPHENOXY)ETHYL]CARBAMATE

L.S.Anju[*], D.Aruldhas
Department of Physics and Research Centre, Nesamony Memorial Christian College, Marthandam
Affiliated to Manonmaniam Sundaranar University, Abishekapatti, Tirunelveli-627 012
*Corresponding author: anju.ls2007gmail.com[a]

ABSTRACT

The DFT method employed to predict electronic properties such as electronic transitions by HOMO-LUMO energies, various global reactivity and selectivity descriptors (chemical potential, electronegativity, chemical hardness, softness and electrophilicity index). Quantum chemical calculations of energies, geometrical structure of Propan-2-yl N-[2-(4-phenoxyphenoxy)ethyl]carbamate were carried by B3LYP/6-31G(d) basis set. NBO analysis was used to find the presence of Hydrogen bonding.

Keywords: DFT, HOMO-LUMO, NBO Charge analysis

1. INTRODUCTION

Carbamates are used as pesticides. They offer certain environmental and toxicological properties which are especially important in public health use. Density functional theory (DFT) is widely used quantum chemical method for geometry optimization and calculation of molecular properties [1,2]. Most are highly toxic to humans and other mammals by all routes of exposure. When inhaled, the effects are usually respiratory and may include bloody or runny nose, coughing, chest discomfort, difficult or short breath and wheezing due to constriction or excess fluid in bronchial tubes. Spectral analysis have been carried out using computation and experimental methods. DFT with the B3LYP method using Guassian '09 programs package is used for calculation.
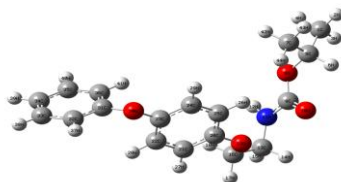
Fig1: Structure of Propan-2-yl N-[2-(4-phenoxyphenoxy)ethyl]carbomate

2. COMPUTATIONAL DETAILS

The DFT computations for the Propan-2-yl N-[2-(4-phenoxyphenoxy)ethyl]carbamate was carried out in the Gaussian 09 program package using "ultrafine" integration grids [3]. The calculations were performed at the B3LYP level with the standard 6-31G(d) basis set in order to derive the optimized geometry, vibrational wave numbers and natural bond orbital analysis of the title compound.

3. RESULTS AND DISCUSSION

Optimized Geometry

The calculated data of Propan-2-yl N-[2-(4-phenoxyphenoxy)ethyl]carbamate are in close agreement with the experimental values [table1]. The bond length C_{20}-C_{25} is increased by 1.399A° because of the substitution of propyl carbamate[4].The various bond angles and dihedral angles are found to be satisfactory agreement with the reported standard values.

Table 1: Selected optimized parameters of Propan-2-yl N-[2-(4- phenoxyphenoxy)ethyl] carbamate

Parameter	Experimental value	Calculated value
C_1-C_5	1.497	1.515
N_{11}-H_{12}	0.86	1.008
C_{20}-C_{25}	1.386	1.399
C_{30}-C_{31}	1.392	1.428
N_{11}-C_{13}-H_{15}	109	107.2
C_{16}-O_{19}-C_{20}-C_{21}	-5.6	0.3
C_{24}-C_{23}-O_{30}-C_{31}	177.3	179.7

Frontier Molecular Orbitals

The highest Molecular orbital (HOMO) represents the outermost orbital filled by electrons and behaves as an electron donor, while in the lower unoccupied molecular orbital (LUMO) considers as the first empty innermost orbital unfilled by electron behaves as an electron acceptor. The energy gap between HOMO and LUMO indicates the molecular chemical stability and is a critical parameter to determine molecular electrical transport properties. In this study, HOMO-LUMO energies and their 3D plots of the title compound are shown in fig.2

LUMO Plot First Excited State

LUMO=-0.1848

E=0.128eV

HOMO=0.3128

HOMO Plot Ground State
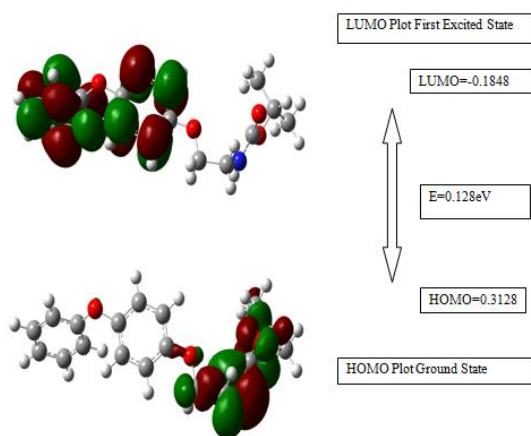
Fig.2.Highest occupied and Lowest unoccupied molecular orbital orbital Propan-2-yl N-[2-(4-phenoxyphenoxy)ethyl]carbamate obtained by B3LYP/6-31G(d).

The narrow energy gap between HOMO and LUMO facilitates intramolecular charge transfer which makes the material to be bioactive [5].

Global Reactivity Descriptors

The global reactivity descriptors like chemical potential, electronegativity, chemical hardness, softness and electophilicity index and local reactivity descriptor like Fukui functions can be calculated on Propan-2-yl N-[2-(4-phenoxyphenoxy)ethyl]carbamate   using DFT. In simple molecule theory approaches, the HOMO energy is related to the ionization potential (I) by Koopman's theorem and LUMO energy has used to estimate the electron affinity (A)[6].

$$\text{Electron affinity (A)} = -E_{LUMO}$$

The average value of HOMO and LUMO energies is related to electronegativity(χ) defined by Mulliken.

$$\text{Electronegativity } (\chi) = (I+A)/2$$

Electro negativity is described as negative of the electornic chemical potential. Where μ is chemical potential takes the average value of ionization potential (I) and electron affinity (A) [7].

$$\text{Chemical Potential} = -(I + A)/2$$

The electronic Chemical Potential is the parameter which describes the escaping tendency of electrons from an equilibrium system. Thus the frontier molecular orbital analysis also provided the details on chemical stability, chemical hardness and electronegativity of the molecule in B3LYP methods with 6-31G(d) basis set are presented in table 1. In addition, the HOMO and LUMO energy is related to the hardness(g) and softness(r)[8].

$$\text{Global hardness } (\eta) = (I - A)/2$$
$$\text{Global softness(S)} = 1/2\ \eta$$
$$\text{Electrophilicity Index } (\omega) = \mu^2/2\eta$$

Electrophilicity index is one of the important quantum chemical descriptors in describing toxicity or biological activities of the molecules in the context of development of Quantitative Structure Activity Relationship (QSAR) analysis.

Table 1: Selected optimized parameters of Propan-2-yl N-[2-(4-phenoxyphenoxy)ethyl] carbamate.

E_{HOMO}	-0.2676 eV
E_{LUMO}	-0.1226 eV
Chemical hardness(η)	0.0725 eV
Softness(s)	0.0363 eV
Chemical Potential(μ)	0.1951 eV
Electronegativity(χ)	0.1951 eV
Electrophilicity(ω)	0.2625 eV

The electrophilicity of Propan-2-yl N-[2-(4-phenoxyphenoxy)ethyl]carbamate describes the biological activity. Considering the chemical hardness, if one molecule has large HOMO-LUMO gap, it is a hard molecule; small HOMO-LUMO gap, it is a soft molecule. We can also relate the stability of molecule of hardness, which means that the molecule with least

HOMO- LUMO gap means, it is more reactive. This shows that the title compound shows more bioactive. The local reactivity descriptor like Fukui function indicates the preferred regions where a chemical molecule will amend its density when the numbers on electrons are modified or indicates the tendency of the electronic density to deform at a given position upon accepting or donating electrons.

4. CONCLUSION

The equilibrium geometries of Propan-2-yl N-[2-(4-phenoxyphenoxy)ethyl]carbamate were determined and analyzed at the DFT level. The DFT calculated values agrees well with experimental data. The HOMO–LUMO energy gap clearly reveals the structure activity relation of the molecule. The result shows the bioactive nature of the molecule. The electronic properties such as electronic transitions by HOMO and LUMO energies, various global reactivity such as chemical hardness, chemical potential, softness, electrophilicity index of the title molecule precisely.

REFERENCES

[1] R.G. Parr, W. Yang, Density functional theory of atoms and molecules, OxfordUniversity Press, New York, 1989.
[2] Z. Zhou, Dongmei Du, Y. Xing, S.U.M. Khan, J. Mol. Struct.(Theochem) 505 (2000) 247–255.
[3] D. Arul Dhas; I. Hubert Joe; S.D.D. Roy; S. Balachandran Spectrochimica Acta Part A: Molecular and Biomolecular Spectroscopy, 79 (2011) 993-1003.
[4] M.Karabacak, Z.Cinar,Spectrochemica acta Part A:Molecular and Biomolecular spectroscopy 85 (2012)179-189.
[5] P.Politzer, F.Abu-Awaad,Thor.Chim.Acta 99(1998) 83-87.
[6] R.S.Mulliken, J.Chem.Phys.2 (1934)782-793.
[7] J.Padmanabhan, R.Parthasarathi, J.Phys. Chem. A111(2007)1358-1361.
[8] R.G.Pearson,Chemical Hardness,John Wiley-VCH, Weinheim(1997).

SPECTROSCOPIC STUDIES, CHARGE TRANSFER AND HYDROGEN BONDING INTERACTION IN (E)-3- (7-HYDROXY-1,3-BENZODIOXOL-5-YL) -N-(2-METHYL PROPYL) PROP-2-ENAMIDE WITH WATER COMPLEXES

J.Priscilla [a], D. Arul Dhas [a*], S.Balachandran [b],I.HubertJoe [c]

[a]Department of Physics, Physics Research Centre, Nesamony Memorial Christian College, Marthandam - 629 165, Kanyakumari District. Affiliated to Manonmaniam Sundaranar University, Abishekapatti, Tirunelveli - 627 012, Tamil Nadu, India,

[b] Department of Chemistry,M.G.College, Thiruvananthapuram 695004, Kerala,India.

[c]Centre for Molecular and Biophysics Research, Department of Physics & Research Centre, Mar Ivanios College, Thiruvananthapuram 695015, Kerala, India.

* Corresponding author: aruldhas_2k4@gmail.com

ABSTRACT

The hydrogen bonding interaction in the (E)-3-(7-hydroxy-1,3-benzodioxol-5-yl)-N-(2-methyl propyl)prop-2-enamide with water complexes studied using density functional theory calculations. The optimized geometry and vibrational frequencies was calculated by B3LYP methods using 6-31G(D,P) basis set. Natural Bond Orbital(NBO) theory applied to quantify the relative strength of hydrogen bond interactions and to account their effect on the stability of molecular arrangements. Density plot over the HOMO and LUMO energy surface provide the information about the donor and acceptor atoms in the molecule.

Keywords: DFT, NBO, HYDROEN BONDING, HOMO-LUMO

1. INTRODUCTION

The major uses of title compound is antioxidant, antiinflammatory and cytotoxicity against PC-3 prostate cancer cells[1].The study of the interaction with water complexes is important because it play an important role on chemical reactions and change many structural parameters related to chemical and physical properties of molecule. The molecular structure and interaction energy, vibrational spectra and assignments of the compound have been studied at the B3LYP/6-31G(D,P) level. The HOMO and LUMO analysis have been used to elucidate information regarding charge transfer within the molecule.

2. COMPUTATIONAL DETAILS

Geometry optimization of the (E)-3-(7-hydroxy-1,3-benzodioxol-5-yl)-N-(2-methyl propyl)prop-2-enamide in the ground state with three water molecule have been performed in Density Functional Theory using Gaussian 09 program package.NBO calculation performed using NBO3.1 program[2] as implemented in Gaussian 09. The electronic properties such as HOMO and LUMO energies had been decided by using TD-DFT approach.

3. RESULTS AND DISCUSSION

Optimized Geometry

The geometry of the (E)-3-(7-hydroxy-1,3-benzodioxol-5-yl)-N-(2-methyl propyl)prop-2-enamide with three water molecule have been optimized by DFT using B3LYP/6-31G(d,p) basis set.The optimized structure of compound with water molecules with atom numbering have been shown in Fig 1.
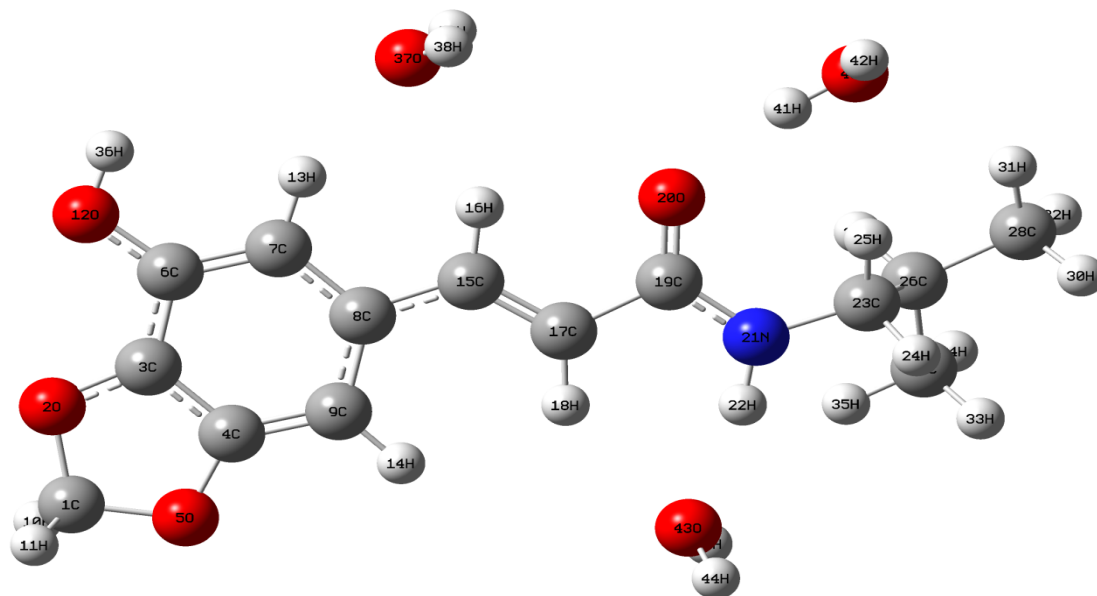
Fig 1: Optimized structure of (E)-3-(7-hydroxy-1,3-benzodioxol-5-yl)-N-(2-methyl propyl)prop-2-enamide with three water molecule

In compound with water complexes, hetronuclear intermolecular hydrogen bonding O-H...O,N-H...O and C-H...O occur between water complex and carbonyl ,amide group present in molecule. The N-H bond length 1.02Å and C=O bond length 1.238 are elongated due to intermolecular hydrogen bonding in molecule.The bond angles of the benzene ring (C-C-C) are observed in the range of 119.65°-123.22° ,which is deviated from normal value to the influence of attached dioxole ring and hydroxyl group in the ring. The dihedral angles of methylenedioxolphenyl ring shows is in planar structure.

Table 1:Selected geometrical parameters of (E)-3-(7-hydroxy-1,3-benzodioxol-5-yl)-N-(2-methyl propyl)prop-2-enamide with three water molecule

Bond Length (Å)	Experimental	compound	Compound with water
C7-H13	0.931	1.088	1.089
C15-H16	0.930	1.089	1.088
C19-O20	1.239	1.231	1.238
N21-H22	0.860	1.008	1.02
Bond Angle(°)			
C4-C3-C6	121.65	121.07	122.14
C3-C4-C9	122.54	123.22	122.69
C6-C7-C8	122.89	122.55	122.23

C7-C8-C9	118.95	119.65	121.18
Dihedral Angle (°)			
O2-C3-C4-O5	0.55	-0.16	0.00
C4-C3-C6-C7	-0.75	-0.28	-0.12
C3-C6-C7-C8	0.69	0.33	0.12
C6-C7-C8-C9	-0.15	-0.15	-0.04
C7-C8-C9-C4	-0.33	-0.08	-0.06

Vibrational Spectral Analysis

The vibrational frequencies were calculated for the optimized molecular structure of the molecule by the DFT/B3LYP method with 6-31G(D,P) basis set. The infrared spectra for the compound in the solid phase are shown in Fig.2.
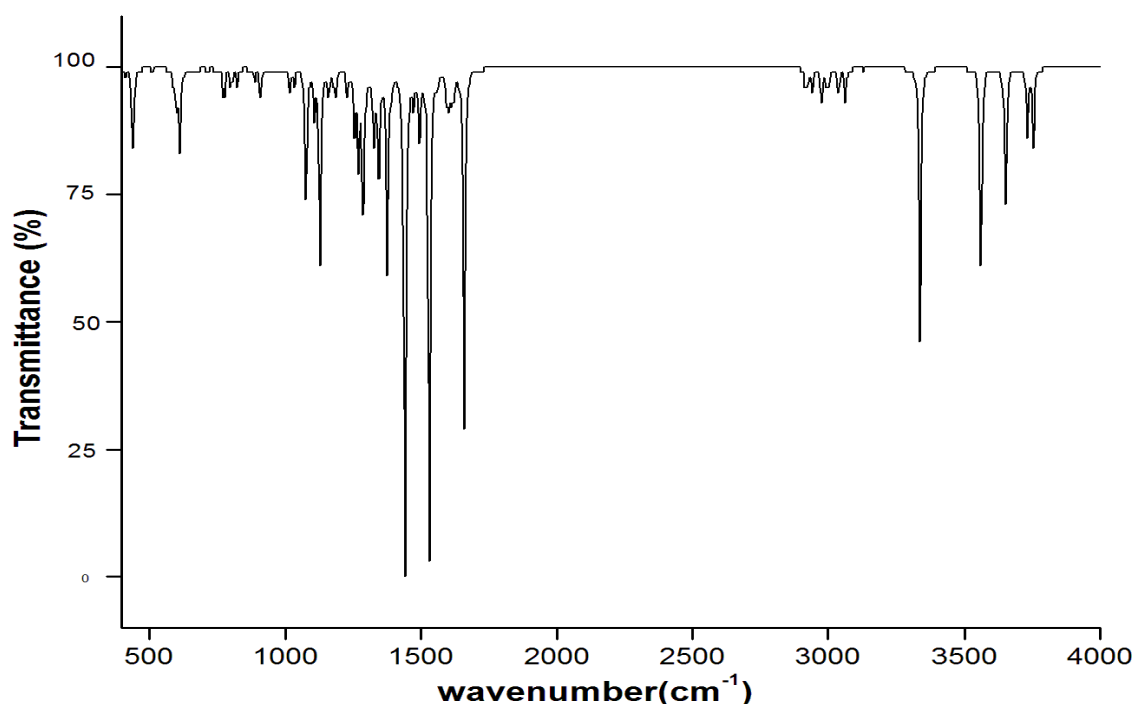
Fig 2: Calculated FTIR spectrum of (E)-3-(7-hydroxy-1,3-benzodioxol-5-yl)-N-(2-methyl propyl)prop-2-enamide with three water molecule

The C-H stretching vibration occur in 3100-3000cm^{-1}[3-5]. The calculated CH stretching vibration is 3089,3051 and 3008cm^{-1}. The stretching vibrational mode free hydroxyl group or non-hydrogen bonded hydroxyl group absorb in the range 3700-3500cm^{-1}. The calculated OH stretching vibration obtained at 3650cm^{-1} .The carbonyl stretching vibration is occured in the region 1725±65cm^{-1}. The strength and position of C=O stretching vibrations depend upon the degree of conjugation, intermolecular interaction and hydrogen bond formation of the molecule.The calculated C=O stretching vibration of the molecule was obtained at 1658cm^{-1}. The observed C=O stretching vibrational mode was shifted towards the lower wavenumber(red shift), Which indicates the presence of O-H...O hydrogen bonding between the compound and water complex.

NBO Analysis

NBO analysis provides the information about interactions in both filled and virtual orbital spaces that could enhance the analysis of inter molecular interactions. The Second-order Fock matrix was carried out to evaluate the donor-acceptor interaction in the NBO nalysis[6].The n1(O43)andn2(O43)→σ*(N21-H22) stabilization energy of the molecule 20.52KJmol^{-1} confirms the presence of N-H...O hydrogen bonding interaction in the compound with water.

Atomic Charges

The calculations of partial atomic charges are useful part of quantum mechanical calculations because of atomic charges explain the changes of dipole moment, molecular electronic structure as well as molecular polarizability. The natural atomic charge of title compound without and with water complexes computed by using B3LYP 6-31G(d,p) basis set. The histogram of calculated natural charge of (E)-3-(7-hydroxy-1,3-benzodioxol-5-yl)-N-(2-methyl propyl)prop-2-enamide without and with water complexes as shown in Fig.3.The C8 atom becomes negative charge in compound with water complexes due to the effect of hydrogen bonding occur in the molecule.
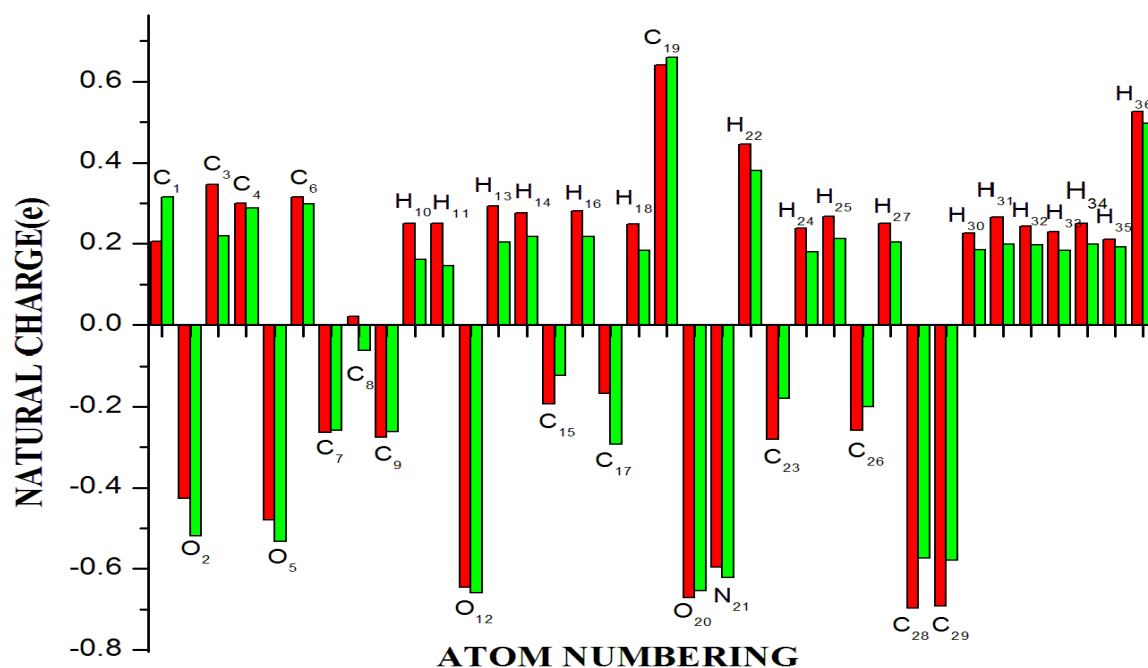
Fig 3: The histogram of calculated natural charge of (E)-3-(7-hydroxy-1,3-benzodioxol-5-yl)-N-(2-methyl propyl)prop-2-enamide without(red) and with(green) water complex

HOMO-LUMO analysis

The total energy ,energy gap and frontier molecular orbital energies of title compound have been computed with B3LYP/6-31G(d,P) level. The HOMO energy characterizes the ability of electron giving, LUMO characterizes the ability of electron accepting, and the gap between HOMO and LUMO explains the molecular chemical stability[7].The energy value of HOMO is -0.33208eV,LUMo is -0.28738eV and the energy gap value is 0.0447eV.The HOMO-LUMO transition implies an electron density transfer to dioxole ring and carbon atom in the middle part of the molecule from the hydroxyphenyl ring.
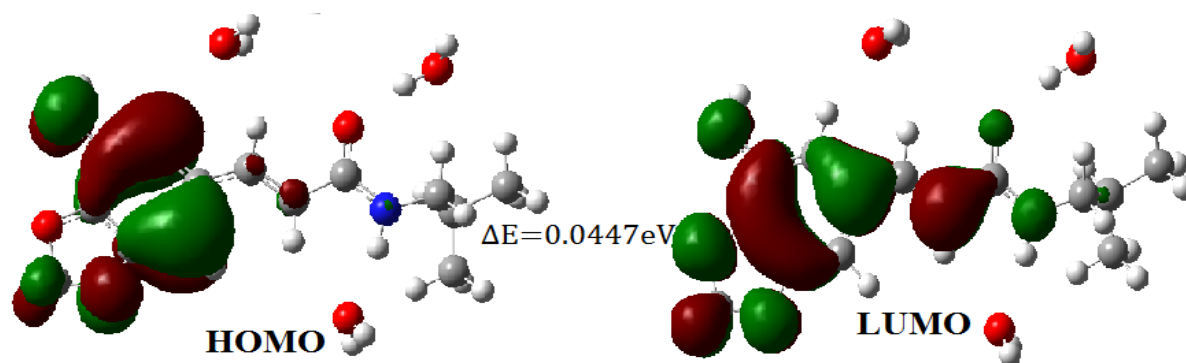
Fig.4: Atomic orbital compositions of the frontier molecular orbital for (E)-3-(7-hydroxy-1,3-benzodioxol-5-yl)-N-(2-methyl propyl)prop-2-enamide with water complex

4. CONCLUSION

The ground state geometries and vibrational spectra of (E)-3-(7-hydroxy-1,3-benzodioxol-5-yl)-N-(2-methyl propyl)prop-2-enamide and its hydrogen-bonded complexes with molecules of water have been optimized. A detailed molecular picture of the title compound and its interactions were obtained from NBO analysis. Natural atomic charge distribution analysis explains the ICT interaction between the atoms , indicating the formation of hydrogen bond in the molecule. The lowering of HOMO-LOMO energy gap value substantial influence on the intramolecular charge transfer within the molecule.

REFERENCES

1. Luc Meva Mbaze,Jean Alexandre Lado,Jean Duplex Wansi, Tze Chieh Shiao,
   Phytochemistry, 2009

2. E.D.Glending,A.E.Reed,J.E. Carpender,NBO version 3.1,TCI(Madison) 1998.

3.Rastogi V.K, Palafox M.A, Tanwar R.P,Mittal L,spectrochem Acta A 58 (2002)1987-2004.

4.Silverstein M,Basseler G.C, Morill C, Spectrometric Identification of Organic Compounds,
   Wiley, New York, 1981 21.

5.Krishnakumar V, Dheivamalar S, Spectrochim Acta71A (2008) 465-470.

6.M.Szafron,A.Komano,E.Bartiosak-Adamka,J.Mol.Struc. 827 (2007) 101-107.

7.K.Fukui,Science 218 (1982) 747.

PESTICIDAL COMPOUND PIRIMICARB: MOLECULAR DOCKING STUDY AND *IN VITRO* BIOACTIVITY

P. Divya, V. Bena Jothy*

Department of Physics and Research Centre, Women's Christian College, Nagercoil -629 001, TamilNadu, INDIA.

*Corresponding author: benaezhil@yahoo.com

1. INTRODUCTION

Pyrimidine and its derivatives are renowned for their biological and pharmaceutical importance [1-2].Pirimidine belongs to the family of nucleic acids and are of great interest, since, they control the manufacture of proteins and the functions of the cells in living organisms [3].Theyshow several biological activities includinganti-malarial, anti-bacterial and anti-fungal activity [4-5]. Calculations have been performed using Gaussian'09 software at Becke's three-parameter hybrid functional B3LYP with a large basis set 6-311G(d, p). Auto docking has alsobeen performed andthe best binding score of Pirimicarb was obtained with protein 5LM8 (-6.95kcal/mol). Antimicrobial activity of Pirimicarbhas been tested against four human pathogenic microorganisms.

2. EXPERIMENTAL AND COMPUTATIONAL DETAILS

Antimicrobial activity of Pirimicarbhas been screened by Kirby-Bauer method and it was tested against four human pathogens, two fungal strains and two bacterial strains.Quantum chemical density functional computations have been carried out using the Gaussian'09 software package at Becke's three-parameter hybrid density functional (B3LYP) [6-7] level supplemented with the standard 6-311G(d, p) basis set.Optimized molecular structure of Pirimicarb has been docked using AutoDock Tools (ADT) Version 1.5.4 revision 30 [8] with Rigid docking method.

3. RESULTS AND DISCUSSION

Structural conformation

Optimized structural parameters of Pirimicarbhas beencalculated using B3LYP/6-311G(d,p)along with the available experimental parameters obtained from the X-ray diffraction study [9] in accordance with the atom numbering scheme in Figure 1.

Atoms O_8, N_7 and O_{18} interact with the protonated pyrimidine ring through C-H…O hydrogen bonds. Bond lengths of C-H (methyl groups) which are shortened due to electron delocalization infer transfer of electrons through sigma bond and pi bond. Intramolecular contacts $H_{10}…O_{18}$, $H_{11}…O_8$, $H_{25}…O_8$ and $H_{21}…O_{18}$ occur with H…O distances of 2.3, 2.54, 2.1 and 2.31 Å respectively, which are significantly shorter than the van der Waals separation between the O atom and H atom (<3 Å) [10] indicating the existence of the intramolecular C–H…O hydrogen bonding interaction in pirimicarb.
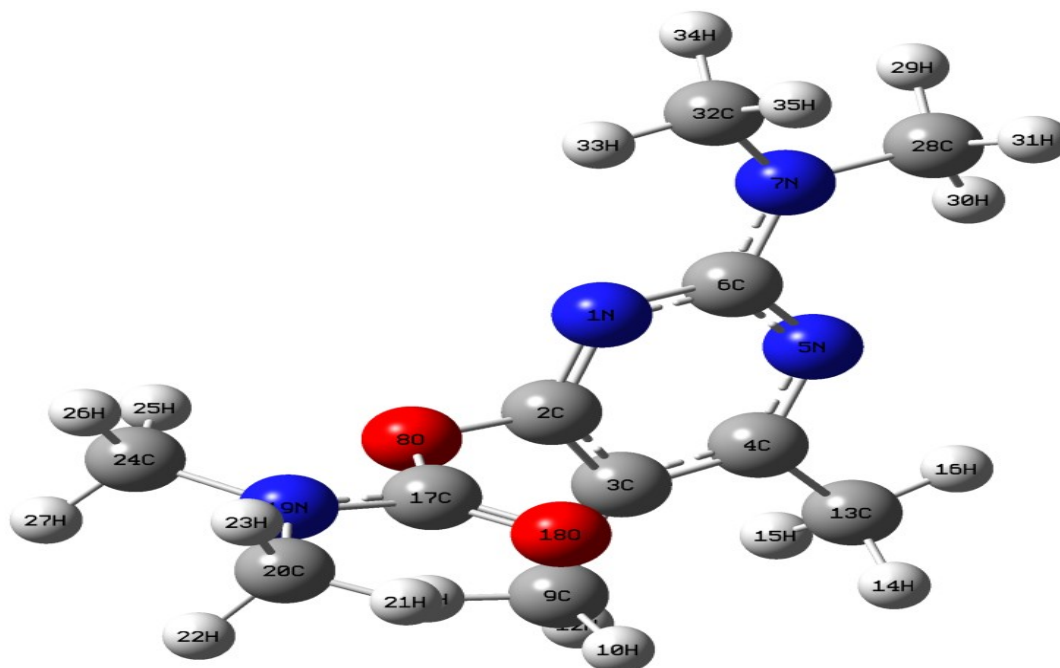
Figure 1: Optimized molecular structure of Pirimicarb with 6-311G (d, p)

Biological activity

Docking

Crystal structure of antimicrobials for two fungal strains and two bacterial strains has been obtained fromProtein Data Bank (PDB ID: 5LM8, 5DXF, 2W7Q, 2X75). Ligand was prepared for docking byminimizing its energy with B3LYP/6-311G(d,p).

Bond formation happens between carbonyl and nitro group with residues in target protein. Pirimicarb is docked with the pocket 5LM8; Primidine ring is embedded and surrounded by amino acids TYR 156, Ser 156 by forming two hydrogen bonds. The best binding score of Pirimicarb has been obtained with protein 5LM8 (-6.95kcal/mol). This may result in the formation of antimicrobial compound, wherein, in Pirimicarb, Pirimidine ring plays the important role in antimicrobial activity

In-Vitro Antimicrobial Activity

Two bacterial strains andfungal strains have been used for studyingtheantimicrobial activity of Pirimicarb.Activity photograph is portrayed in Figure 2 in which it is found that the fungal strain *Aspergillusniger and Candida albicans*exhibits highest inhibition zone in all the three concentrations (10mm, 10mm, 14mm and 12mm, 12mm, 12mm) where the activity increases with increase in concentration. Results clearly reveal that for fungal strains, activity increases with increase in compound concentration and the inhibition of the strains also increases but in bacterial strain there is less inhibition.
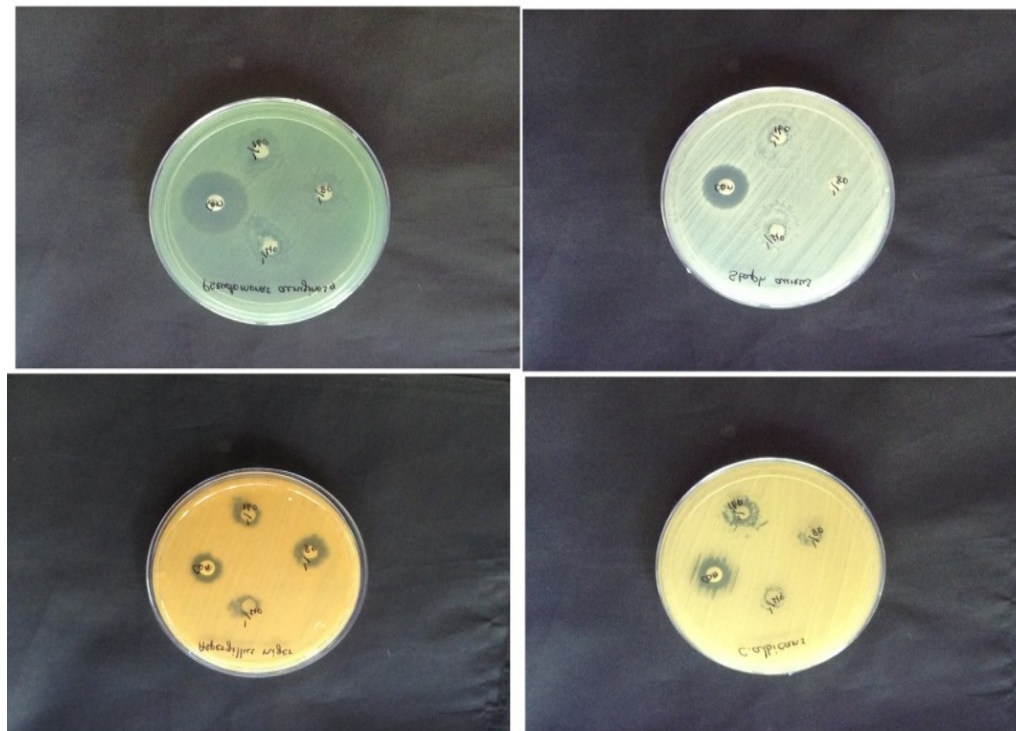
Figure 2: Antimicrobial activity of Pirimicarb

4. CONCLUSION

Molecular docking output shows that the lowest binding energy of 5LM8 is -6.95kcal/mol and most docked inhibitors interact with the ligand within 5LM8 binding site. From the In-vitro Antimicrobial activity, it is found that the fungal strain *Aspergillusniger and Candida albicans*exhibits highest inhibition zone in all the three concentrations.

REFERENCES

[1] É.A. Shokova, V.V. Kovalev, Pharmaceutical Chemistry Journal 50(2) (2016) 63.

[2] S.M. Roopan, R. Sompalle, Synthetic Communications, 46 (2016) 645.

[3] M. Arivazhagana, J. Senthilkumar, SpectrochimicaActa Part 82 (2011) 228.

[4] SeekarajapuramDinakaranVachala, Keloth Kothari Srinivasan, PeralamYegneswaranPrakash, Medicinal Chemistry Research 21 (2012)2998.

[5] K.S Jain, T.S. Chitre, P.B. Miniyar, M.K. Kathiravan, V.S. Bendre, V.S. Veer, S.R. Shahane, C.J. Shishoo, Current Sci., 90 (2006) 793.

[6] A.D. Becke, J. Chem. Phys. 98 (1993) 5648.

[7] C. Lee, W. Yang, R.G. Parr, Phys. Rev. B37 (1988) 785.

[8] G. M. Morris, R. Huey, W. Lindstrom, M. F. Sanner, R. K. Belew, D. S. Goodsell, A. J. Olson, J Comput. Chem., 16 (2009) 2785.

[9] V. Krishnakumar, M. Arivazhagan, Asian J. Chem. 13 (2001) 383.

[10] A. Bondi, van der Waals Volumes and Radii. J. Phys. Chem. 68 (1964) 441

VIBRATIONAL STUDIES OF BIOACTIVE 2-SULFONAPHTHALENE:A DFT APPROACH

R. Mini, T. Joselin Beaula, V. Bena Jothy[*]

Department of Physics and Research Centre, Women's Christian College, Nagercoil 629 001, TamilNadu, INDIA
* Corresponding author: benaezhil@yahoo.com

ABSTRACT

Bioactive natural products are compounds produced by living organisms that exerts biological effect on other organisms. 2-Sulfonaphthalene(NSA) is a biological compound which is used in pharmaceutical industry. Vibrational studies on the bioactive molecule NSA have been performed by means of Density Functional Theoretical (DFT) method using standard B3LYP/6-311G(d,p) basis set implemented with Gaussian'09 software package. Optimized geometric bond length, bond angle and dihedral angle of the molecule have also been calculated.Detailed vibrational assignments have been carried out with the aid of Normal Co-ordinate Analysis (NCA) and discussed in detail. Comparison of simulated spectra with the experimental spectra provides important information about the ability of the computational method to describe the vibrational modes.

Keywords: Vibrational spectra;DFT;NCA.

1. INTRODUCTION

Bioactive substances are of growing interest with a wide range in agrochemicals pharmaceuticals and polymers. This serves as an encouraging area with full refinement, which has emerged in modern research yielding more and more novel results, designed to change the resources of bioactive substances and improve their synthesis [1].NSAserves as an important product for industrial chemical processes and is applied widely in concrete finishing, industrial textile processing, tanning of hides and in the manufacture of agrochemicals and pharmaceuticals [2]. Structuralanalysishave been carried out byDFT methodand vibrationalassignments with the aid of NCA.

2. EXPERIMENTAL AND COMPUTATIONAL DETAILS

FT-IR spectrum in the region 4000-400 cm^{-1} has been recorded using Perkin Elmer one: FT-IR Spectrometer with a typical resolution of 1.0 cm^{-1}.FT-Raman spectrum was recorded in the region 4000-2 cm^{-1}using Bruker RFS 27: Stand alone FT-Raman Spectrometer with Nd: YAG laser source at 1064 nm and resolution 2 cm^{-1}.

Quantum chemical density functional computations were carried out using the Gaussian'09 software package [3]. Optimized structural parameters havebeen obtained by using B3LYP 6-311++G(d,p) basis set. Normal coordinate analysis has been performed in order to obtain a detailed interpretation of the fundamental modes using the MOLVIB program version 7.0 written by Sundius. Natural coordinate analysis as suggested by Pulay*et.al.*have been written as input for the MOLVIB program. Scaling factors have been refined with an RMS error of 12 cm^{-1} between the experimental and SQM wave numbers.

3. RESULTS AND DISCUSSION

Optimized geometry

Optimized molecular structure of NSA is presented in Fig.1.Bond length of S_{18}-O_{21} (1.6497Å) is higher than other S-O bond lengths S_{18}-O_{19} (1.4575Å) and S_{18}-O_{20}(1.4643Å) which is due to the attachment of hydrogen atom with it. Sulfonic acid is highly distorted from its tetrahedral arrangement which is manifested from its bond angles O_{19}-S_{18}-O_{20} (121.07°), O_{19}-S_{18}-O_{21}(108.43°), S_{18}-O_{21}-O_{22}(106.04°) and O_{20}-S_{18}-O_{21}(106.19°). Bond angles O_{19}-S_{18}-O_{21} and O_{20}-S_{18}-O_{21}indicates the pyramidal configurations of sulfonamide with benzene ring.
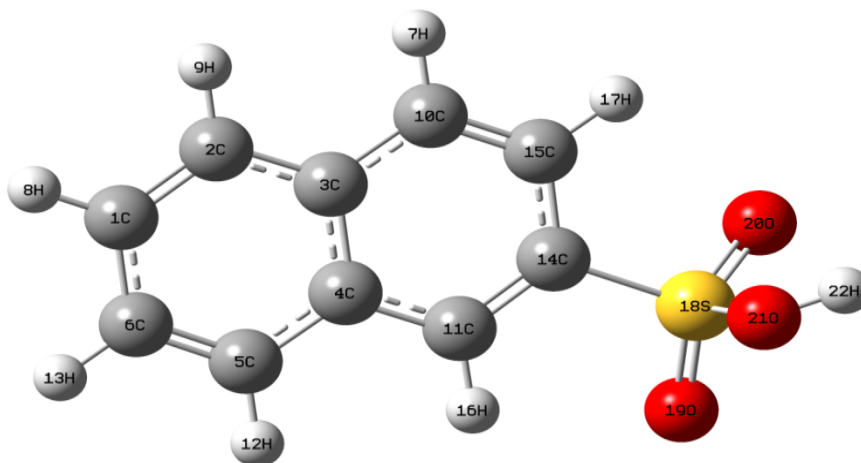
Fig.1: Optimized molecular structure of NSA

Spectral analysis
Sulfonic acid vibrations

Normally, SO_3 stretching vibrations are strongly IR active andappear in the region 1080-1209cm^{-1}, whereas the SO_3symmetric deformation mode gives strong bands in the region 550-660cm^{-1}. [4] Symmetric stretching mode of SO_3 is observed as a very strong band at1084 cm^{-1}in IR and as a weak intensity band at 1097 cm^{-1}inRaman with the computed band at 1082 cm^{-1}which is in goodagreement with the observed values.

Skeleton vibrations

Naphthalene ring stretching vibrations are expected in the region 1620-1390 cm^{-1}. [5]Ring C-C stretching vibrations in the benzene ring appears in the range 1430-1625 cm^{-1}.The in-plane deformation vibrations are at higher wavenumber than the out-of-plane vibrations and computed valuesof ring vibrations shows good agreement with the recorded spectraldata.

Ring vibrations

Aromatic ring modes have more influenced C-C vibrations that are expected to arise within the region1650-1200 cm^{-1} [6] are observed as weak bands at 1505 cm^{-1} in IR and 1627,1592and 1535cm^{-1} in Raman. C-H stretching vibrations commonly exhibit multiple weak bands in the region 3100-3000 cm^{-1}which is observed as a very strong band at 3063cm^{-1}in Raman.
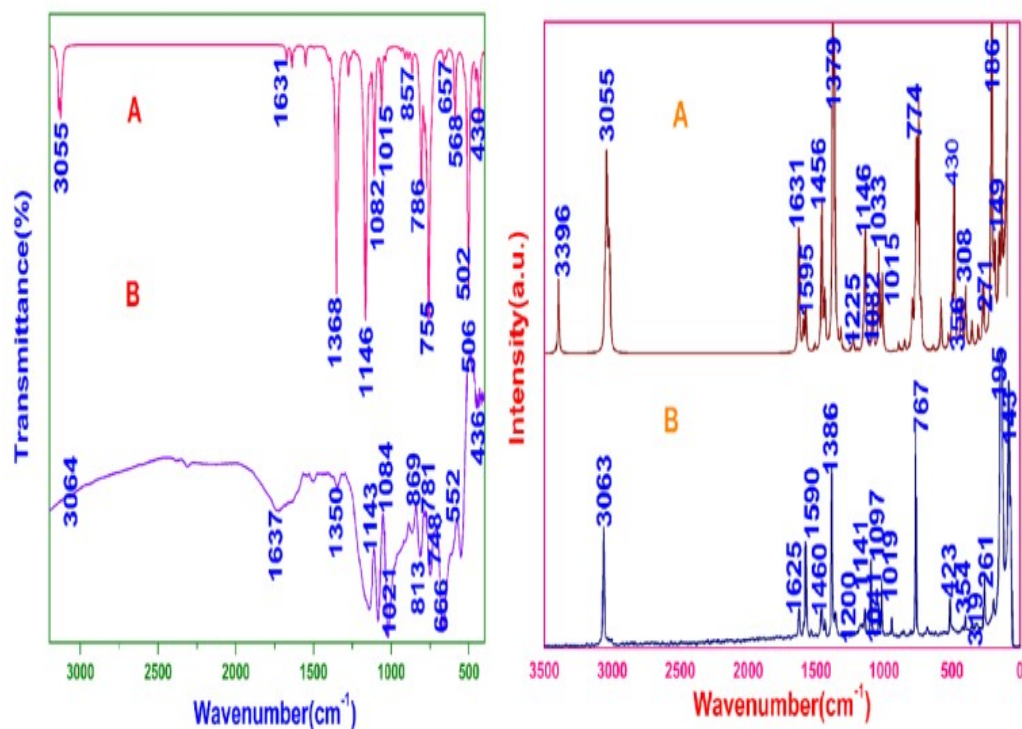
Fig.2 : Experimental and simulated FT-IR and FT-Raman spectra of NSA.

4.CONCLUSION

Structural studies have been analyzed with the aid of DFT and detailed vibrational assignments have been carried out with Normal Coordinate Analysis (NCA). Broadeningand red shifting of O-H stretching band depicts the levelof intra-molecular O-H…O hydrogen bonding effect.

REFERENCES

[1] AbdelkarimGuaadaoui, SoumayaBenaicha, NaimaElmajdoub, Mohammed BellaouI,

AbdellahHamal ,International Journal of Nutrition and Food Sciences 2014; 3(3): 174-179

[2] Storm, T., Reemtsma, T., Jekel, J.,. J. Chromatogr. A 854, 175–185(1999).

[3]. M. J. Frisch *et al*. Gaussian 09, Revision D.01, Gaussian, Inc., Wallingford CT,(2004).

[4] Sperline R, Song Y, Freiser H. Langmuir; 10: 37(1994).

[5] C. Surisseau, P. Marvel, J. Raman Spectrosc. 25, 447–455(1994).

[6]. C. Surisseau, P. Marvell, J. Raman. Spectrosc.25 (1994) 447.

SPECTROSCOPIC INVESTIGATION AND DENSITY FUNCTIONAL THEORY OF 3-[6-DIAMINO METHYLIDENE) CYCLO HEXA-2,5-DIEN-1YLIDENE] PROPANE DINITRILE

V.K.Suma[*], *D. Arul Dhas*

Department of Physics and Research Centre, Nesamony Memorial Christian College, Marthandam

Affiliated to Manonmaniam Sundaranar University, Abishekapatti, Tirunelveli-627 012

*Corresponding author: vksumamsc@gmail.com

ABSTRACT

Vibrational analysis of the 3-[6-diamino methylidene) cyclo hexa-2,5-dien-1ylidene] propanedinitrile was carried out using IR spectroscopic techniques. The equilibrium geometry, various bonding features, harmonic vibrational wave numbers and potential energy surface (PES) scan studies have been computed using density functional theory method. The detailed interpretation of the vibrational spectra has been carried out with the aid of VEDA.4 program. Vibrational spectra, natural bonding orbital (NBO) analysis and optimized molecular structure show the clear evidence for electronic interaction of amino group with aromatic ring. The population analysis on atomic charges and the HOMO–LUMO energy were also calculated. Vibrational analysis reveals that the simultaneous IR of the C–C stretching mode in the phenyl and amino group provide evidence for the charge transfer interaction between the donor and acceptor groups and is responsible for its nlo activity..

Key Words: DFT, NBO, HOMO LUMO, Vibrational Analysis, NLO

1. INTRODUCTION

Non linear optical (NLO) materials have recently engaged a lot of concentration due to their potential use in the fields like laser technology, optical communication, optical data storage and optical signal processing [1–3]. In this respect organic nonlinear optical materials are found to have high nonlinear coefficient equated to those of inorganic materials [4,5]. In the present study the spectroscopic feature of 3-[6-diamino methylidene) cyclo hexa-2,5-dien-1ylidene] propane dinitrile (com.1) was investigated theoretically by computational methods. The bonding features, nature of hydrogen bonding, frontier orbital energy and nonlinear optical property of the title compound. The structure activity is compared with benzene (com.2) by computational method.

2. EXPERIMENTAL METHODS

3-[6-diamino   methylidene)   cyclo   hexa-2,5-dien-1ylidene]   propane   dinitrile   was purchased from Sigma-Aldrich   Company with a stated purity of 99%   and it was use without further purification.

The experimental computation for the 3-[6-diamino methylidene) cyclo hexa-2,5-dien-1ylidene] propane dinitrile was carried out in the Gaussian '09 program package[6] at the

B3LYP level with standard 6-311G (d,p) basis set. This has been successfully applied in order to derive the optimized geometry and vibrational wave number of the normal modes.

4. RESULTS AND DISCUSSION

Optimized geometry

The optimized molecular structure of the compounds com.1, and com.2 with atom numbering scheme adopted in the computation using B3LYP/6-311G(d,p) basis set was shown in Fig 1a-1b and the corresponding structural parameters are given in table1. The optimized structure of title compound consists of phenyl ring, cyano group and amino group. In com.1 the calculated bond length of C-C(C_2-C_3)(Table.1) is lengthened comparing with benzene due to the substitution of amino group. The same deviation is observed in the bond length of C_5-C_6.Another one important calculated C-C (C_3-C_4) bond length in comp1is 1.445 Å and its corresponding bond length of benzene is 1.396Å. The variation is observed due to the substitution of cyano group.
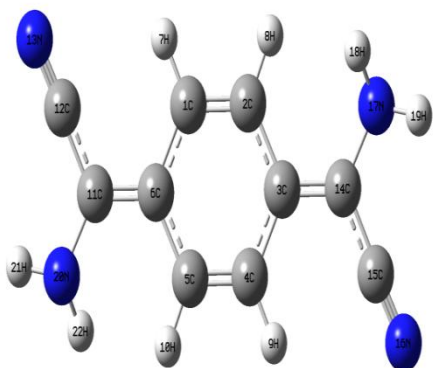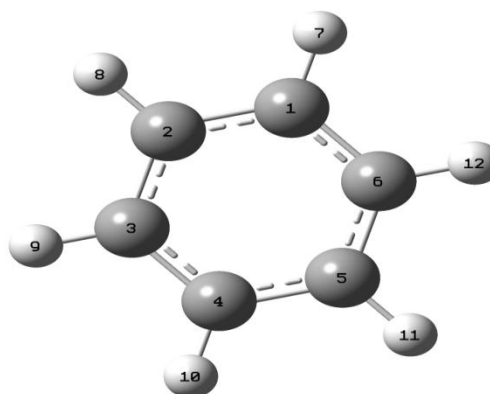
Figure 1   Figure 2

Figure1,2: shows the optimized structure of 3-[6-diamino methylidene) cyclo hexa-2,5-dien-1ylidene] propane dinitrile   and benzene.

The C-C-C bond angle of benzene ring is 120^0 and is said to be aromatic , but in this present work 3-(methyl phenyl)propane dinitrile show slight deviation in the C-C-C (C_1-C_2-C_3=121.3^0 , C_3-C_4-C_5= 121.8^0) bond angle because of this the aromatic character deviates due the substitution of methane and cyano group.

NBO Analysis

The natural bond orbital (NBO) analysis was performed at the B3LYP/6-311G(d,p) level basis set. The stabilizing interactions between filled and unoccupied orbitals and destabilizing

interactions . between filled orbitals can be obtained from this analysis [6-8]. The stabilization energy contribution from the $\sigma(c_1\text{-}c_2)\rightarrow \sigma^*(c_6\text{-}c_{11})$ (Table.2) interaction energy 11.3kJ Mol^{-1}.The most interaction energy in σ bond molecule σ $(c_6\text{-}c_{11})$bond to antibonding $\sigma^*(c_{11}\text{-}c_{12})$ leads to stabilization energy of 18.1KJ/mo^{-1} respectively .

Table.1 Optimized parameters

Bond Length / (Å)			Bond Angle / (°)			
Bond	Experimental Value	Calculated Value		Bond	Experimental Value	Calculated Value	
		Com.1	Com.2			Com.1	Com.2
$C_2 - C_3$	1.480	1.445	1.396	$C_1- C_2 - C_3$	121.3	121.3	120
$C_3- C_4$	1.480	1.442	1.396	$C_2- C_3 - C_4$	121.8	121.2	120
$C_4\text{-}C_5$	1.345	1.355	1.396	$C_3- C_4 - c_5$	120.5	121.5	120
$C_5- C_6$	1.402	1.450	1.396	$C_4- C_5 - C_6$	121.6	121.2	120

Vibrational Analysis

The vibrational spectral analysis of 3 -[6-diamino methylidene) cyclo hexa-2,5-dien-1ylidene] propane dinitrile is performed based on the potential energy distribution analysis.The CH stretching 20b mode vibration of di substituted   phenyl ring normally occurs at 3020-3120cm^{-1}[9]. The present work mode 20b is active in IR with a very weak band at 3108 cm^{-1}. The 8a mode of C-C stretching vibration are expected in the range 1570-1628 (10). In compound 1, 8a mode is observed in IR as a strong band at 1599cm^{-1}.

Cyano group vibration

The C≡N stretching vibration is expected in the range 2240-2220 cm^{-1} [10]. The very strong band   observed at 2229cm^{-1}(IR) are assigned to stretching mode. The calculated value found to be at 2260cm^{-1}. The C≡N stretching vibration is expected in the range 2240-2220 cm^{-1} (11). But in IR is inactive.

Table2. second order perturbaction theory of 3 -[6-diamino methylidene) cyclo hexa-2,5-dien-1ylidene] propane dinitrile.

Donar NBO(i)	E.D(e)	Acceptor NBO(j)	E.D(e)	$E^{(2)}$ kJ mol^{-1}
$\sigma(c_1-c_2)$	1.978 -0.737	$\sigma^*(c_6-c_{11})$	0.0283 0.567	11.3
$\sigma(c_6-c_{11})$	1.966 -0.737	$\sigma^*(c_{11}-c_{12})$	0.033 0.489	18.1

Amino group vibration

The asymmetric NH_2 stretching mode appears from 3500 to3420cm^{-1} and symmetric NH_2 stretching is observed in the range 3420–3340cm $^{-1}$. The asymmetric stretching mode in strong band observed in IR at 3485cm^{-1}.

Non Linear Optical effects

        Quantum chemical calculations have been shown to be useful in the description of the relationship between the electronic structure of the systems and its NLO response . The NLO activity provide the key functions for frequency shifting, optical modulation, optical switching and optical logic for the developing technologies in areas such as communication, signal processing and optical interconnections The polarizability (a) and the hyper polarizability (b) and the electric dipole moment (l) of title compound are calculated by finite field method using b3lyp/6-311G (d,p) basis set. The static polarizability α_o and dipolemoment μ are calculated using Gausian '09 program software is found to be 2.760 x10^{-23} esu and 5.67 D respectively (Table 4). The calculated first order hyper polarizability is 2.789 times greater than that of urea [β of urea = 3.78 x 10^{-30} esu].

Figure.3 shows the IR spectrum of 2-[6-diamino methylidene) cyclo hexa-2,5-dien-1ylidene] propane dinitrile
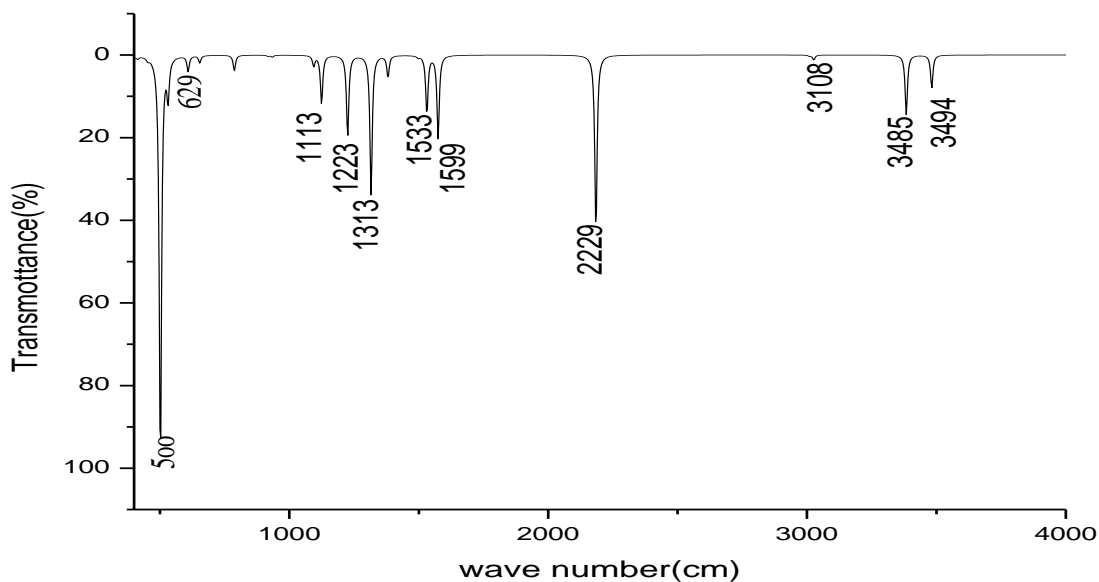
Fig:3 IR spectrum of 2-[6-diamino methylidene) cyclo hexa-2,5-dien- 1ylidene] propane dinitrile

HOMO-LUMO

In the frontier region, neighbouring orbital's are being often closely spaced. In such cases, consideration of only the HOMO and LUMO may yet yield a realistic description of the frontier orbital's. The HOMO-LUMO energy gap of compound 1-14 are calculated at the B3LYP/6-311G(d,p) level ,which reveals that the energy gap reflects the chemical activity of the molecule. The LUMO as an electron acceptor represents the ability to obtain an electron, and HOMO presents the ability to donate electron. The energy gap of compound 1 is 0.1384eV .

$\Delta E = 0.128eV$
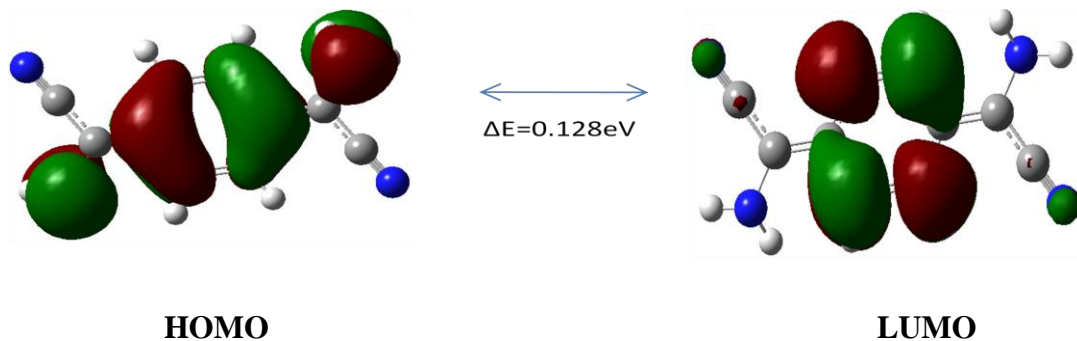
HOMO   **LUMO**

Fig 4. Shows the Homo Lumo plot of 2-[6-diamino methylidene) cyclo hexa-2,5-dien-1ylidene] propanedinitrile   .

The energy gap of HOMO-LUMO explains the eventual charge transfer interaction within the molecule. The atomic orbital components of the frontier molecular orbitals as shown in the figure[4]

4. CONCLUSION

In the present work, complete vibrational analysis has been made for proper frequency contributions of 3-[6-diamino methylidene) cyclo hexa-2,5-dien-1ylidene] propane dinitrile.The IR spectra has been taken and the frequencies of the title compound have been theoretically computed using DFT methods. The optimized parameters have also been analysed. Vibrational frequencies, infrared intensities and Raman activities calculated by DFT level of theory utilizing 6-311G(d,p) method agree well with experimental results. In addition the calculated first hyperpolarizability value of 2-[6-diamino methylidene) cyclo hexa-2,5-dien-1ylidene] propanedinitrile 2.789 times larger than the magnitude of urea. Therefore the investigated compound can be indicate the non linear optical nature of the compound.

References

[1] H.O. Marcy, L.F. Warren, M.S. Webb, C.A. Ebbers, S.P. Velsko, G.C. Kennedy, G.C. Catella, Appl. Opt. 31 (1992) 5051–5060.

[2] D.S. Chemla, J. Zyss, Nonlinear Optical Properties of Organic Molecules andrystals, Academic Press, New York, 1987.

[3] H.O. Marcy, M.J. Rosker, L.F. Warren, P.H. Cunningham, C.A. Thomas, L.A.DeLoach, S.P. Velsko, C.A. Ebbers, J.H. Liao, M.G. Kanatzidis, Opt. Lett. 20 (1995) 252–257.

[4] H.A. Petrosyan, H.A. Karapetyan, M.Yu. Antipin, A.M. Petrosyan, J. Cryst.Growth 275 (2005) 1919–1925.

[5] D. Xue, H. Ratajczak, J. Mol. Struct. Theochem. 716 (2005) 207–210. [6] Tsonko M. Kolev, Denitsa Y. Yancheva, Bistra A. Stamboliyska, Momtchil D.

[6] A.E. Reed, L.A. Curtiss, F. Weinhold, Chem. Rev. 88 (1988) 899-926.

[7] J.P. Foster, F. Weinhold, J. Am. Chem. Soc. 102 (1980) 7211-7218.

[8] F. Weinhold, C.R. Landis, Valency and Bonding: A Natural Bond orbital Donor-

Acceptor Perspective, Cambridge University Press, New York, 2005.

[9] G.Varsanyi D.sc,Vibrational spectra of Benzene derivatives,Acadamic press Newyork and London(1969)

[10] L.J Bellany, The infra red spectra of complex molecule vol 2,1975

PREDICTION OF COD VALUE IN ENGINEERING WORK INDUSTRIAL EFFLUENTS BY ANFIS MODELLING

H.Adline Mahiba[1] , S.Akilandeswari[2]

[1] Department of Physics and Research Centre, Scott Christian College (Autonomous), Nagercoil-629003

[2] Department of Physics, Govt. College for Women (Autonomous), Kumbakonam-612001

Abstract

The quality of water is characterized by various physico chemical parameters. These parameters of water change widely due to pollution, seasonal fluctuations etc. Several techniques are used to predict the parameters of water quality. The new adaptive neuro fuzzy inference system (ANFIS) is an intelligent technique which can be used to predict the chemical oxygen demand (COD) from the characteristic parameters of the effluents. The COD values of the engineering work industrial effluents are predicted by ANFIS and statistical modelling and the results are compared with experimental value.

Keyword: *COD, Industrial effluent, ANFIS modelling, Regression analysis.*

Introduction

Chemical Oxygen Demand (COD) indicates the amount of oxygen required for the oxidation of all organie substances in water. COD is one of the pollution parameter of effluents. The higher the COD of the sample, the higher is the level of pollution. The standard few hours COD test is time consuming. Many computational intelligence models are being increasingly employed for the prediction of COD such as ANFIS, ANN etc. Many investigations have been made to decrease the time required for determining these parameters. In the present work ANFIS and statistical modelling are used to predict COD values of engineering work industrial effluents. The predicted values are compared with the observed COD values.

Materials and methods

The effluent samples were collected from engineering works industry over a period of 1 year in pre-cleaned acid washed and dried polyethylene containers of 2 liters capacity. The samples were analysed for various physico chemical characteristics parameters of the effluents estimated as per the standard procedure (1,2).

ANFIS and statistical modelling are used to predict COD values from industrial effluents. ANFIS modelling is purely an empirical approach. ANFIS modelling incorporates the Fuzzy Logic Theory and Artificial Neural Networks Architecture.

ANFIS is a so designed technique that can be used in modelling decision – making and process control applications (3, 4). The integration of fuzzy systems and neural networks can combine the merits of both systems and offers a more powerful tool for modelling. The detailed architecture and learning procedure of ANFIS can be found in literature (5).

The exclusive feature of ANFIS is that itself - learns and recognizes that exact input - output relationship from the fuzzy inference rules and so acquires enough intelligence in predicting a new situation. The learning process of ANFIS consists of training the FIS to understand the input–output relations using a set of data called 'Training Data' (trnData) comprising of input - output parameters of a system under study. Then the validity of the FIS can be tested by using another set of data known as 'Check Data' (chkData) which comprises of identical input - output parameters but having different values. ANFIS generates automatically the fuzzy rules and selects the rules with maximum firing strength. Now the FIS is capable of predicting the output of a new environment of inputs. If a third data set called 'Test Data' (testData)

comprising of input parameters alone is given, the ANFIS will predict the output parameter (User's Guide, 1998).

In statistical modelling, regression analysis is a statistical process for estimating the relationships among variables. In regression analysis the dependent variable is a function of the independent variables and the degree of contribution of each variable to the output is represented by the regression co efficient on these variables.

The statistical multiple regression analysis was carried out using statistical package SPSS version 13.0. The characteristic parameters of effluent used as training data is given in table. 1. The predicted values of COD obtained from ANFIS and statistical modelling using characteristics parameters TA, EC, OG, TH as inputs are given in table 2 and DO, F, SO_4 and TH as inputs are given in table 3.

The average percentage error can be calculated using the relation

$$APE = \frac{1}{n}\sum_{i=1}^{n}\left|\frac{COD_{(obs)} - COD_{(pred)}}{COD_{(obs)}}\right| \times 100\%$$

Where, n represents number of data pairs, COD (obs) represents observed values of COD, COD (pred) represents predicted values of COD (6,7).

The accuracy in the predicted values of COD be also estimated by finding the Worst-case error (WE) using the relation.

$$WE = COD_{(pred)} - COD_{(obs)}$$

A very powerful test for testing the significance of the discrepancy between observed and predicted values is the chi-square test of goodness of fit.

$$X^2 = \sum_{i=1}^{n} \left[\frac{(O_i - P_i)^2}{P_i} \right]$$

Where O_i (i=1,2,3, ... n) is set of observed values and P_i (i=1,2,3, ... n) is the corresponding set of predicted data.

Table 1. Characteristic parameters of engineering works used as 'Training Data Set' in the present work

Sample Number	Inputs (selectively used to train ANFIS)										Output
	pH	EC (μmhos/cm)	TUR (mg/l)	OG (mg/l)	Cl (mg/l)	F (mg/l)	SO₄ (mg/l)	TH (mg/l)	DO (mg/l)	TA (mg/l)	COD (mg/l)
1	6.86	800	64	7	800	2	750	233	7.2	211	236
2	7.71	722	75	9	1000	1.2	900	198	6.3	365	142
3	7.11	685	71	8	950	1.8	470	236	6.8	389	391
4	8.74	1100	100	10	750	2.2	385	440	4.3	356	132
5	8.86	773	79	9	930	2.4	510	464	12.1	489	146
6	7.54	900	80	8	750	0.8	400	360	10.6	371	198
7	7.02	1485	74	11	240	2.2	810	253	8	367	211
8	8.61	1140	95	10	950	3.4	750	223	9.8	412	145
9	6.96	944	89	9	185	1.4	760	218	9.1	879	362
10	7.45	910	87	8	178	1.1	850	212	14.3	697	324
11	6.98	1410	97	9	201	1.3	960	350	2.3	625	169
12	8.41	1084	91	7	388	1.0	800	238	3.8	642	275
13	7.42	1247	99	8	494	1.1	860	241	3.4	589	246
14	6.48	851	77	9	137	1.7	690	116	8.2	635	385
15	7.54	910	105	12	860	1.8	720	136	5.6	246	241
16	6.22	923	98	10	749	1.5	660	533	5.9	287	145
17	6.69	680	36	15	928	3.2	590	394	6.4	389	285
18	7.20	640	32	14	1020	4.2	520	284	5.7	347	236
19	7.2	710	32	7.6	112	4.5	560	220	11.2	258	362
20	6.96	868	40	8.8	120	4.4	640	210	12.7	269	314
21	7.19	970	38	8.4	340	4.2	520	502	12.9	124	297
22	6.86	715	42	10	705	5.8	470	303	3.1	148	324
23	7.28	710	65	9.5	900	1.9	500	280	15.6	356	221
24	8.5	850	70	9	1200	2.4	740	245	14.2	391	253
25	6.88	765	80	7	1100	2.0	680	250	8.6	587	387
26	7.51	718	60	9	1050	2.3	690	279	8.7	569	365
27	6.42	680	70	10	1200	3.2	500	250	6.4	543	125
28	7.10	925	40	14	1420	4.0	480	186	5.8	521	98
29	8.20	690	50	16	1320	3.4	550	176	5.6	876	145
30	9.1	725	35	10	1055	2.4	325	190	9.1	632	321

Table 2.   **Characteristic parameters (TA, EC, OG and TH) of engineering works industry effluents used as 'check data' and the observed and predicted values of COD**

Sample number	TA (mg/l)	EC (µmhos/cm)	OG (mg/l)	TH (mg/l)	COD (mg/l)			Multiple regression parameters and coefficients
					Observed	Predicted		
						ANFIS model	Statistical model	
1.	349	723	9	236	233	231.7660	263.41	R^2 = 0.1372
2.	350	911	10	441	199	199.4597	348.71	P = 0.0920
3.	328	680	8.3	352	274	271.6396	304.61	F = 2.153
4.	355	716	10	279	292	299.5566	272.86	
5.	760	1085	7.1	188	486	486.1119	318.37	
6.	750	687	12.1	211	368	365.3624	260.83	β_0 = 143.23
7.	314	710	8.8	533	318	322.4260	367.23	β_1 = 0.0707 β_2 = 0.08815
8.	367	924	7.6	117	314	316.4329	247.49	β_3 = -6.024
9.	482	1410	14	251	282	282.9621	308.73	β_4 = 0.093566
10	488	851	16	199	267	263.7166	228.88	
				APE (%) =		0.87	23.07	
				WE =		7.6	167.6	
				Chi-Sq. =		0.361443	238.144241	

Table 3.   **Characteristic parameters (DO, F, SO₄ and TH) of engineering works industry effluents used as 'check data' and the observed and predicted values of COD**

Sample number	DO (mg/l)	F (mg/l)	SO₄ (mg/l)	TH (mg/l)	COD (mg/l)			Multiple regression parameters and coefficients
					Observed	Predicted		
						ANFIS model	Statistical model	
1.	3.0	1.8	470	236	233	233.2945	207	R^2 = 0.5008
2.	10.55	2.1	511	441	199	205.1866	351.59	P = 0.1468
3.	8.07	2.4	850	852	274	274.5209	332.54	F = 1.813
4.	4.0	0.9	751	279	292	293.9276	250.25	
5.	0.23	3.3	901	188	486	479.7602	222.81	
6.	12.12	4.2	639	211	368	374.1586	302.25	
7.	9.164	1.6	500	533	318	321.8386	372.78	β_0 = 29.820
8.	7.75	3.5	742	117	314	312.9922	235.85	β_1 = 7.2746 β_2 = 9.3372
9.	6.19	2.6	640	251	282	283.6912	260.34	β_3 = 0.094277 β_4 = 0.40190
10	2.52	1.3	326	199	267	262.9229	171.00	
				APE (%) =		1.07	28.10	
				WE =		6.2	263.2	
				Chi-Sq. =		0.505398	501.432922	

Result and Discussion

From table 2 and 3, it can be observed that the COD values predicted by statistical modelling shows more deviation from the observed values due to the fact that the input parameters have low correlations with COD. But COD values predicted by ANFIS modelling provides more accurate values irrespective of the low correlation between input parameters and COD. The APE values in tables 2 and 3 confirm that ANFIS modelling is superior to statistical modelling. The graphical representation for these datas are shown in figures 1 and 2 respectively. These figures confirm the accuracy of ANFIS modelling.
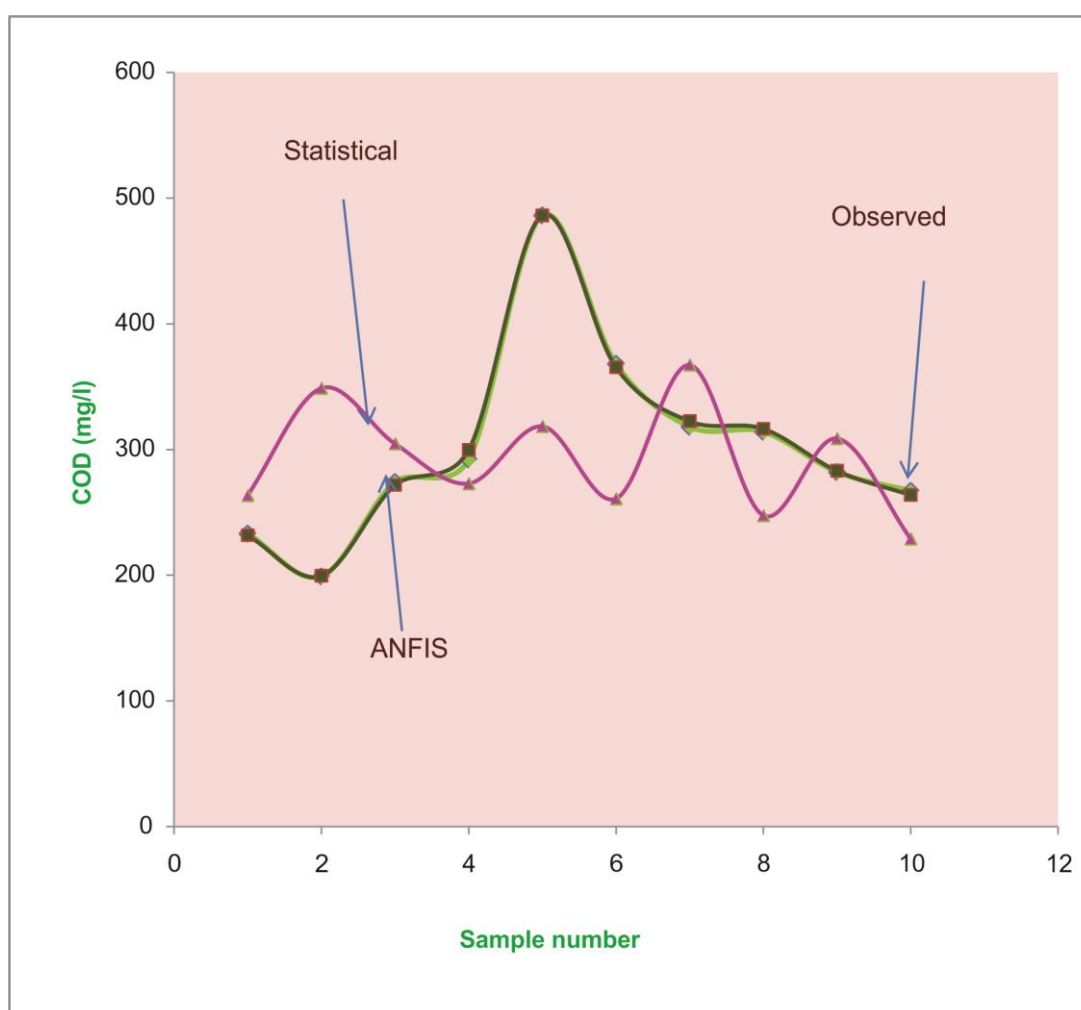
Fig. 1.   **Plot of COD *versus* sample number (with TA, EC, OG and TH as inputs) of engineering works industry**
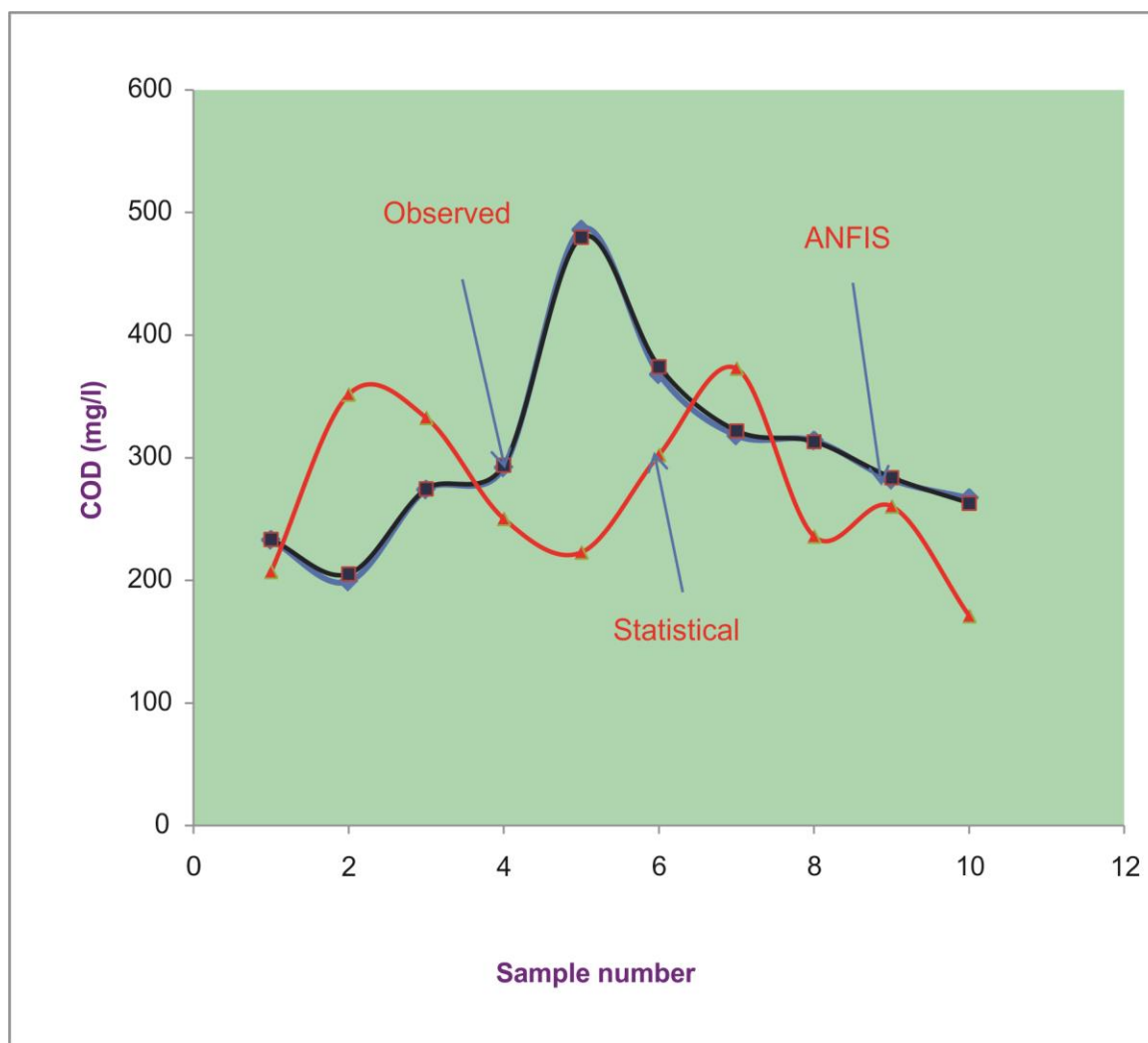
Fig. 2.   Plot of COD *versus* sample number (with DO, F, SO$_4$ and TH as inputs) of engineering works industry

Conclusion

In the present study ANFIS modelling was successfully applied for predicting the COD values of effluents. Prediction of COD values is useful to assess strength of wastes which contain toxins and biologically resistant organic substances. The developed ANFIS model provides accurate prediction of COD than the statistical model.

References

1. APHA, 1998 standard methods for the examination of water and waste water (21st edn.) Washington, D.C

2. Trivedy R.K. and P.K. goel 2005 chemical and Biological methods for water pollution studies environmental publications, Karad.

3. Tyh-Shing Roger tang. 1993 ANFIS: Adaptive Network based Fuzzy Inference System. IEEE trans. on systems, man and cybernetics (Vol. 23, No.3)

4. MWI, 2009 User's Guide Fuzzy Logic Tool Box, for use with MATLAB version 5.3. The Mathworks Inc.

5. Jang. J.S.R. 1993, ANFIS. Adaptive Network based Fuzzy Inference System. IEEE Trans. syst. Man cyber. 23(3), 665-685.

6. S.B. Kalyanaraman and S. Akilandeshwari, Prediction of COD in tannery effluents – ANFIS modelling Poll.Res. 25(5), 417-420.

7. S.Akilandeshwari A. Julie, Application of Adaptive Neuro Fuzzy Inference system in prediction of COD from sugar Industry Effluents, International journal of chemical Engineering   and Applied Science 2012, 2(4): 27-30.

THE OPEN-SOURCE THEORETICAL PREDICTIONS OF THE PHARMACOLOGICAL PROPERTIES OF EIGHT FLUOROQUINOLONE ANIMAL-HUSBANDRY AGENTS.

P. Yowan Jeba Raj*

Doctorate in Chemistry, Manjuvilai, Kalakad - 627 501, Tirunelveli, Tamilnad, India.
* E-mail: yowanjebaraj@gmail.com, Cell: +91 9500663180.

ABSTRACT

The theoretical prediction of pharmacological properties of eight fluoroquinolone-typed animal-husbandry agents, *viz.*, Danofloxacin (**1**), Difloxacin (**2**), Enrofloxacin (**3**), Ibafloxacin (**4**), Marbofloxacin (**5**), Orbifloxacin (**6**), Pradofloxacin (**7**) and Sarafloxacin (**8**) were achieved from online tools and open-source softwares. The chemical structures for the subjected candidates were drawn using ChemSketch software. The components of the Lipinski's rule (Rule-of-five or RO5) were predicted using molinspiration online server. The efficient predictions of pharamacological properties such as: (*i*) Physicochemical properties, (*ii*) Lipophilicity, (*iii*) Water solubility, (*iv*) Pharmacokinetics, (*v*) Drug-likeness and (*vi*) Medicinal chemistry for the candidates were studied using SwissADME online tool. The Boiled-Egg diagram and the Bioavailability Radar plots for all- and individual- candidates were also developed. The extended predictions of Absorption, Distribution, Metabolism, Excretion and Toxicity (ADMET) properties were computed using pkCSM, an online-running program tool.

KEYWORDS Lipinski's Rule, Pharmacokinetics, ADMET, Boiled-Egg diagram, Bioavailability Radar, Log P and Log S.

1. INTRODUCTION

Flouroquinones[1-7] are the significant family of organic drugs was designed in a way that to employ as an oral antibiotics for human as well as animals. Ciprofloxacin[1-2] is a well known candidate of fluoroquinone family, which will work as the broad spectrum antibiotics against gram-positive and gram-negative bacteria. However, the drug resistances also arise for them due to the mutation of bacterial enzymes: topoisomerase II and topoisomerase IV[3]. Moreover, some members of fluoroquinolone family were served only as the animal husbandry agents by their long term-services to heal the wounds in animals and some bacterial infections on animals. Such fluoroquinolone drugs which caring the pet-animals, goats and cattle are classified as animal-husbandry agents[8-15]. The present study explores the

pharmacological study of the known eight fluoroquinolone animal husbandries, *viz.*, Danofloxacin[8], Difloxacin[9], Enrofloxacin[10], Ibafloxacin[11], Marbofloxacin[12], Orbifloxacin[13], Pradofloxacin[14] and Sarafloxacin[15] using online running tools[16-20] and open-source softwares[21].

2. COMPUTATIONAL METHODS

The online tools and open-source softwares were used for this study are:

Sl. No.	Purpose	Online tool / software used
1	Structure draw	ACD/ChemSketch[21]
2	Lipinski's rule (RO5)	Molinspiration[16] (+pkCSM)[17]
3	Pharmacological properties	SwissADME[18]
4	ADMET profile	pkCSM[17]
5	Site of metabolism prediction	SOMP[19]
6	Toxicity predictions	Way2Drug server tools[20]

3. RESULTS AND DISCUSSION

⊕ Structures

The chemical structures for all the eight fluoroquinolone animal-husbandry agents can be drawn using ChemSketch software.

⊕ Components of Lipinski's Rule for Drug-like Behavior

The detailed computations of the components of Lipinski's rule (RO5) for the selected fluoroquinolones were carried out using Molinspiration, an online tool. The computed values for the components of Lipinski's rule were presented in **Table 1**. The number of violations for the rule (RO5) is afforded individually by the candidates is "zero", which proving all the candidates are having drug-like behavior.

Table 1. Components of Lipinski's rule of Drug-likeness computed by molinspiration online tool for the fluoroquinolone animal husbandries (1-8).

Sl. No.	Descriptor	1	2	3	4	5	6	7	8
1	Molecular weight	357.38	399.40	359.40	275.30	362.36	395.38	396.42	385.37
2	miLog P	0.00	-0.02	0.27	0.83	-0.63	2.31	0.09	-0.62
3	No. of Rotatable Bonds	3	3	4	1	2	3	3	3
4	No. of Acceptors (**O, N**)	6	6	6	4	8	6	7	6
5	No. of Donors (**OH, NH**)	1	1	1	1	1	2	2	2
6	No. of violations	0	0	0	0	0	0	0	0

⊕ Pharmacological Properties

The full pharmacological predictions of the fluoroquinolone type animal husbandry agents were studied under five categories: (*i*) Physicochemical properties, (*ii*) Lipophilicity, (*iii*) Water solubility, (*iv*) Pharmacokinetics, (*v*) Drug-likeness and (*vi*) Medicinal chemistry for the candidates which were studied using SwissADME online tool[18]. All those above properties computed were displayed in **Table 2**.

All the physicochemical properties encompassing many pharmacological properties were applicable for framing the bioavalability radar plot for/with individual structures. Moreover, most of these physicochemical properties also contributed for the drug-likeness predictions. Under lipophilicity predictions, there are six different methodologies serving for the computation of the octanol-water partition coefficient. Out of them, the two are significant: (*i*) XLogP3 and (*ii*) WLogP were serving for the prediction of (*i*) Bioavailability Radar plot and (*ii*) Boiled-Egg diagram for vivid representation of drug pharmacological properties. There are three methods were voluntarily serving for the SwissADME - water solubility predictions. Also, the sets of categorical outcomes for the identification of pharmacokinetics and drug-likeness were computed for the selected candidates using SwissADME online tool. Those properties can also be calculated by pkCSM online tool.

Table 2. List of Pharmacological properties, *viz.*, (*i*). Physicochemical properties, (*ii*). Lipophilicity, (*iii*). Water solubility, (*iv*). Pharmacokinetics, (*v*). Drug-likeness and (*vi*). Medicinal chemistry of the fluoroquinolone animal-husbandries (1-8).

i.	Physicochemical properties								
Entry	Candidate	Mol. wt. (g/mol)	No. Heavy Atoms Arom.	No. Heavy Atoms Total	Csp3	NRB	NHBA	NHBD	μ	TPSA
1	Danofloxacin	357.38	10	26	0.47	3	5	1	102.84	65.78 Å^2
2	Difloxacin	399.39	16	29	0.24	3	6	1	112.68	65.78 Å^2
3	Enrofloxacin	359.39	10	26	0.47	4	5	1	104.95	65.78 Å^2
4	Ibafloxacin	275.27	10	20	0.33	1	4	1	73.82	59.30 Å^2
5	Marbofloxacin	362.36	10	26	0.41	2	6	1	103.84	78.25 Å^2
6	Orbifloxacin	395.38	10	28	0.47	3	7	2	104.78	74.57 Å^2
7	Pradofloxacin	396.41	10	29	0.48	3	6	2	112.27	98.36 Å^2
8	Sarafloxacin	385.36	16	28	0.20	3	6	2	107.78	74.57 Å^2

ii.	Lipophilicity						
Entry	Candidate	Log P$_{(o/w)}$ iLog P	XLog P3	WLog P	MLog P	Silicos-IT	Consensus
1	Danofloxacin	2.31	-0.35	1.66	1.75	1.66	1.41
2	Difloxacin	2.66	0.89	2.80	2.61	2.85	2.36
3	Enrofloxacin	2.58	-0.25	1.91	1.75	2.21	1.64
4	Ibafloxacin	1.81	1.96	3.07	2.17	3.03	2.41
5	Marbofloxacin	2.15	-0.49	-0.21	1.45	0.36	0.65
6	Orbifloxacin	2.41	0.89	3.07	2.51	2.93	2.36
7	Pradofloxacin	2.31	0.36	1.83	1.32	2.21	1.60
8	Sarafloxacin	2.33	0.42	2.46	2.39	2.90	2.10

iii.	Water Solubility								
Entry	Candidate	ESOL Log S	ESOL Solubility	ESOL Class	Ali Log S	Ali Solubility	Ali Class	Silicos-IT Log S	Silicos-IT Solubility	Silicos-IT Class
1	Danofloxacin	-1.92	4.28 x 10^0	V.S.	-0.57	9.63 x 10^1	V.S.	-2.97	3.82 x 10^{-1}	S.
2	Difloxacin	-3.09	3.27 x 10^{-1}	S.	-1.86	5.56 x 10^0	V.S.	-5.32	1.90 x 10^{-3}	M.S.
3	Enrofloxacin	-1.93	4.21 x 10^0	V.S.	-0.67	7.63 x 10^1	V.S.	-3.56	9.83 x 10^{-2}	S.
4	Ibafloxacin	-3.09	2.26 x 10^{-1}	S.	-2.83	4.07 x 10^{-1}	S.	-3.81	4.27 x 10^{-2}	S.
5	Marbofloxacin	-1.93	4.25 x 10^0	V.S.	-0.69	7.47 x 10^1	V.S.	-2.29	1.85 x 10^0	S.
6	Orbifloxacin	-2.92	4.77 x 10^{-1}	S.	-2.04	3.60 x 10^0	S.	-4.33	1.85 x 10^{-2}	M.S.
7	Pradofloxacin	-2.58	1.04 x 10^0	S.	-1.99	4.05 x 10^0	V.S.	-3.91	4.85 x 10^{-2}	S.
8	Sarafloxacin	-2.72	7.36 x 10^{-1}	S.	-1.08	1.08 x 10^1	V.S.	-5.66	8.37 x 10^{-4}	M.S.

iv.	Pharmacokinetics									
Entry	Candidate	HIA	BBB	P-GP	CYP inhibitor 1A2	2C19	2C9	2D6	3A4	Log K_p (cm/s)
1	Danofloxacin	High	Yes	Yes	No	No	No	Yes	No	-8.73
2	Difloxacin	High	Yes	Yes	No	No	No	Yes	No	-8.10
3	Enrofloxacin	High	Yes	Yes	No	No	No	Yes	No	-8.67
4	Ibafloxacin	High	Yes	No	No	No	No	No	No	-7.59
5	Marbofloxacin	High	No	Yes	No	No	No	No	No	-8.86
6	Orbifloxacin	High	Yes	Yes	No	No	No	Yes	No	-8.08
7	Pradofloxacin	High	No	Yes	No	No	No	Yes	No	-8.46
8	Sarafloxacin	High	Yes	Yes	No	No	No	No	No	-8.35

v.		**Drug-likeness**						*vi.*	**Medicinal Chemistry**	
Entry	**Candidate**	**Lipinski**	**Ghose**	**Veber**	**Egan**	**Muegge**	**Bioavail. Score**	**PAINS /Brenk**	**Lead-likeness**	**Synth. Access.**
1	Danofloxacin	Yes; 0	Yes	Yes	Yes	Yes	0.55	0 alert	No; 1	4.10
2	Difloxacin	Yes; 0	Yes	Yes	Yes	Yes	0.55	0 alert	No; 1	2.81
3	Enrofloxacin	Yes; 0	Yes	Yes	Yes	Yes	0.55	0 alert	No; 1	2.73
4	Ibafloxacin	Yes; 0	Yes	Yes	Yes	Yes	0.56	0 alert	Yes; 0	2.95
5	Marbofloxacin	Yes; 0	Yes	Yes	Yes	Yes	0.55	0 alert	No; 1	3.37
6	Orbifloxacin	Yes; 0	Yes	Yes	Yes	Yes	0.55	0/1alert	No; 1	3.70
7	Pradofloxacin	Yes; 0	Yes	Yes	Yes	Yes	0.55	0 alert	No; 1	3.77
8	Sarafloxacin	Yes; 0	Yes	Yes	Yes	Yes	0.55	0 alert	No; 1	2.70

♦ Boiled-Egg Diagram

The Boiled-Egg diagram[18] were optionally predicted by SwissADME tool by plotting the TPSA against WLogP which shows that: "whether the distribution of the drug candidates entered with high degree in HIA or BBB?" (**Fig. 1**)

Fig. 1. Boiled-Egg diagram for the distribution strategy of fluoroquinolones (1-8).
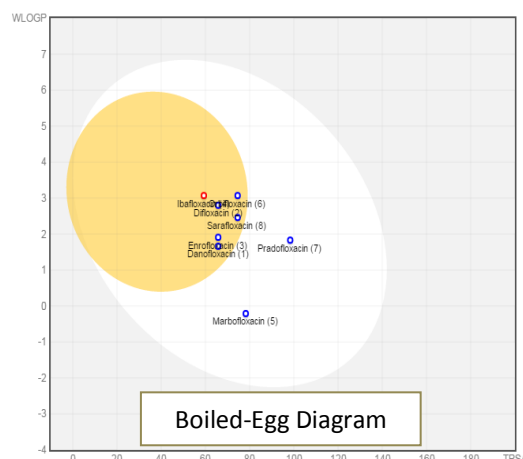
♦ Bioavailability Radar plots

The Bioavailability Radar plots[18] were also optionally computed with the combination of all the six category of predicted pharmacological properties, *i.e.*, combination of six pharmacological components, *viz.*, (*i*) **LIPO:** Lipophilicity (XLogP3), (*ii*) **SIZE:** Molecular weight (in g/mol), (*iii*) **POLAR:** Polarity (TPSA), (*iv*) **INSOLU:** Insolubility (LogS by ESOL), (*v*) **INSATU:** Insaturation (Fraction C$_{sp3}$) and (*vi*) **FLEX:** Flexibility (No. of rotatable bonds) for the all the individual candidates were made using SwissADME online tool and were displayed in **Fig. 2**.

Danofloxacin (**1**)   Difloxacin (**2**)   Enrofloxacin (**3**)   Ibafloxacin (**4**)

Marbofloxacin (**5**)   Orbifloxacin (**6**)   Pradofloxacin (**7**)   Sarafloxacin (**8**)
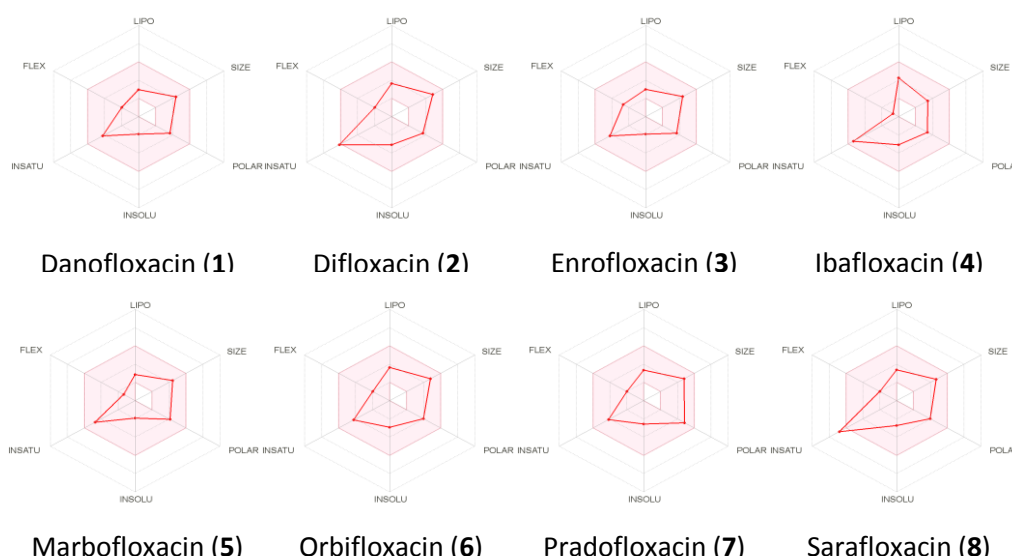
Fig. 2. Bioavailability radar diagram for the single-sight understanding of Pharmocokinetics (or bioavailability) of the fluoroquinolones (1-8).

The colored zone is the suitable physicochemical space for oral bio-activities as:

Sl. No.	Component	Description	Range
i.	LIPO:	Lipophilicity	$-7 < $ **XLogP3** $ < +5$
ii.	SIZE:	Molecular weight (in g/mol)	$150 < $ **Mol. Wt.** <500
iii.	POLAR:	Polarity (TPSA; in Å^2)	20 Å$^2 < $ **TPSA** < 130 Å^2
iv.	INSOLU:	Insolubility (LogS by ESOL)	$0 < $ **LogS (ESOL)** < 6
v.	INSATU:	Insaturation (Fraction C$_{sp3}$)	$0.25 < $ **Fraction C$_{sp3}$** < 1
vi.	FLEX:	Flexibility (No. of rotatable bonds)	$0 < $ **No. Rot. Bonds** < 9

The bio-availability radar plots expel the quick-conclusion by single-sight observation.

⬛ ADMET Predictions

The extended predictions of Absorption, Distribution, Metabolism, Excretion and Toxicity (ADMET) properties were computed using pkCSM, an online-running program tool. The complete ADMET predicted profile with calculated values of Absorption, Distribution, Metabolism, Excretion and Toxicity parameters under the "numerical" and "categorical" criteria were presented in **Table 3**. The random observations of metabolism for CYP substances were observed, but, the unavailability of CYP inhibitors were computed for the selected candidates.

9a (substituted) piperazin-1-yl-

9b (1R,4R)-2,5-diazabicyclo[2.2.1]heptan-2-yl-

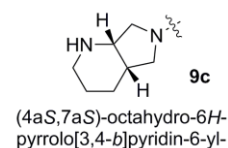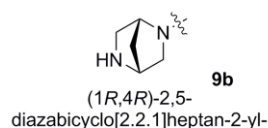**9c** (4aS,7aS)-octahydro-6H-pyrrolo[3,4-b]pyridin-6-yl-

Table 3. Prediction of ADMET Properties (Absorption, Distribution, Metabolism, Excretion and Toxicity) calculated from pkCSM tool for the fluoroquinolones (1-8).

	Sl. No.	Parameter	1	2	3	4	5	6	7	8
A	1	Water solubility	-3.231	-4.057	-3.441	-3.621	-3.151	-3.641	-3.656	-3.96
	2	Caco2 permeability	1.152	1.05	1.163	1.24	1.274	1.23	0.73	1.03
	3	Human intestinal absorption	97.225	97.239	96.667	97.607	81.948	96.354	79.202	97.449
	4	Skin permeability	-2.712	-2.714	-2.709	-2.689	-2.719	-2.724	-2.72	-2.714
	5	P-glycoprotein substrate	Yes	Yes	Yes	No	Yes	Yes	Yes	Yes
	6	P-glycoprotein I inhibitor	No	No	No	No	No	No	No	No
	7	P-glycoprotein I inhibitor	No	No	No	No	No	No	No	No
D	1	Human VDss	0.16	-0.232	0.089	-0.763	-0.195	-0.111	-0.027	-0.297
	2	Human fraction unbound	0.436	0.172	0.425	0.288	0.438	0.381	0.366	0.175
	3	BBB permeability	-0.161	-0.243	-0.174	-0.039	-0.757	-0.795	-0.535	-0.595
	4	CNS permeability	-3.027	-2.435	-3.004	-2.873	-3.118	-3.042	-3.039	-2.525
M	1	CYP2D6 subatrate	Yes	No	Yes	No	No	No	No	No
	2	CYP3A4 subatrate	No	Yes	No	No	No	No	Yes	Yes
	3	CYP1A2 inhibitor	No	No	No	No	No	No	No	No
	4	CYP2C19 inhibitor	No	No	No	No	No	No	No	No
	5	CYP2C9 inhibitor	No	No	No	No	No	No	No	No
	6	CYP2D6 inhibitor	No	No	No	No	No	No	No	No
	7	CYP3A4 inhibitor	No	No	No	No	No	No	No	No
E	1	Total clearance	0.604	0.052	0.198	0.441	0.033	0.235	0.36	0.129
	2	Renal OCT2 substrate	No	No	No	No	No	No	No	No
T	1	Human max. tolerated dose	0.128	0.263	0.154	0.588	0.176	0.485	0.193	0.243
	2	Oral Rat Acute Toxicity (LD50)	2.285	2.579	2.247	2.55	2.271	2.373	2.216	2.559
	3	Oral Rat Chronic Toxicity (LOAEL)	0.744	1.532	0.739	1.292	1.598	1.798	0.849	1.65
	4	*Tetrahymena pyriformis* toxicity	0.295	0.29	0.3	0.31	0.288	0.287	0.296	0.291
	5	Minnow toxicity	0.996	-0.245	0.852	0.596	1.369	1.548	1.58	-0.133
	6	AMES toxicity	No	No	No	No	Yes	No	No	No
	7	hERG I inhibitor	No	No	No	No	No	No	No	No
	8	hERG II inhibitor	No	No	No	No	No	No	No	No
	9	Hepatotoxicity	Yes	Yes	Yes	No	Yes	Yes	Yes	Yes
	10	Skin sensitization	No	No	No	No	No	No	No	No

4. CONCLUSION

All the investigated fluoroquinolone animal-husbandry agents (**1**-**8**) obey the Lipinski's rule of drug-likeness (RO5) without any violations. Except, Ibafloxacin, all the other candidates were predicted as hepatotoxicity, and hence, the hepatotoxicity associated with those candidates may be due to the presence of the *hetero-alicyclic ring* (**9a** / **9b** / **9c**) attached at the 7th position of the fluoroquinolone animal husbandries and which were also contributed by the drug-absorption takes place at various P-glycoprotein substrate (explained by pkCSM predictions). The efficiency order was understood from the bio-availability radar plots (bio-availability sense) as: Difloxacin (**2**) ≈ Sarafloxacin (**8**) > Marbofloxacin (**5**) > Orbifloxacin (**6**) ≈ Pradofloxacin (**7**) > Danofloxacin (**1**) ≈ Enrofloxacin (**3**) > Ibafloxacin (**4**); but from the Boiled-Egg diagram with HIA criteria and BBB penetration concerns (drug distribution trending) as: Marbofloxacin (**5**) > Pradofloxacin (**7**) > Sarafloxacin (**8**) > Orbifloxacin (**6**) ≈ Danofloxacin (**1**) > Enrofloxacin (**3**) > Difloxacin (**2**) > Ibafloxacin (**4**).

REFERENCES

1. A.M. Emmerson, A.M. Jones, *J. Antimicrob. Chemother.*, **2003**, *51*, 13-20.

2. K.J. Aldred, R.J. Kerns, N. Osheroff, *Biochem.*, **2014**, *53*, 1565-1574.

3. G.G. Zhanel, S. Fontaine, H. Adam, K. Schurek, M. Mayer, A.M. Noreddin, A.S. Gin, E. Rubinstein, D.J. Hoban, *Treat. Respir. Med.*, **2006**, *5(6)*, 437-465.

4. Y. Mouton, O. Leroy, *Int. J. Antimicrob. Agents*, **1991**, *1(2-3)*, 57-74.

5. V.R. Anderson, C.M. Perry, *Drugs*, **2008**, *68*, 535-565.

6. R.C. Owens, P.G. Ambrose, *Clin. Infect. Dis.*, **2005**, *41*, S144-S157.

7. G.G. Zhanel, S. Fontaine, H. Adam, K. Schurek, M. Mayer, A.M. Noreddin, A.S. Gin, E. Rubinstein, D.J. Hoban, *Treat. Respir. Med.*, **2006**, *5(6)*, 437-465.

8. P. Lees, F.S. Aliabadi, *Int. J. Antimicrob. Agents*, **2002**, *19(4)*, 269-284.

9. C. Chidiac, Y. Mouton, *Infection*, **1991**, *19(7)*, S365-S371.

10. H.G. Wetzstein, N. Schmeer, W. Karl, *Appl. Environ. Microb.*, **1997**, *63*, 4272-4281.

11. L.J. Horspool, P. van Laar, R. van den Bos, I. Mawhinney, *J. Vet. Pharmacol. Therap.*, **2004**, *27(3)*, 147-153.

12. M. Spreng, J. Deleforge, V. Thomas, B. Boisrame, H. Drugeon, *J. Vet. Pharmacol. Therap.*, **1995**, *18*, 284-289.

13. E. Heinen, *J. Vet. Pharmacol. Therap.*, **2002**, *25*, 1-5.

14. P. Silley, B. Stephan, H.A. Greife, A. Pridmore, *J. Antimicrob. Chemother.*, **2007**, *60(5)*, 999-1003.

15. J.M. Stamm, *J. Aquat. Animal Health*, **1989**, *1*, 135-141.

16. Molinspiration Cheminformatics, http://www.molinspiration.com//cgi-bin/properties.

17. D.E.V. Pires, T.L. Blundell, D.B. Ascher, *J. Med. Chem.*, **2015**, *58*, 4066-4072.

18. (a). A. Daina, O. Michielin, V. Zoete, *Sci. Rep.*, **2017**, *7*, 42717. (b). A. Daina, O. Michielin, V. Zoete, *J. Chem. Inf. Model.*, **2014**, *54(12)*, 3284-3301. (c). A. Daina, V. Zoete, *Chem. Med. Chem.*, **2016**, *11(11)*, 1117-1121.

19. SOMP online tool, http://www.way2drug.com/SOMP/index.php.

20. Way2Drug online server, http://www.way2drug.com.

21. ACD / ChemSketch 12.01, www.acdlabs.com/resources/freeware/chemsketch/